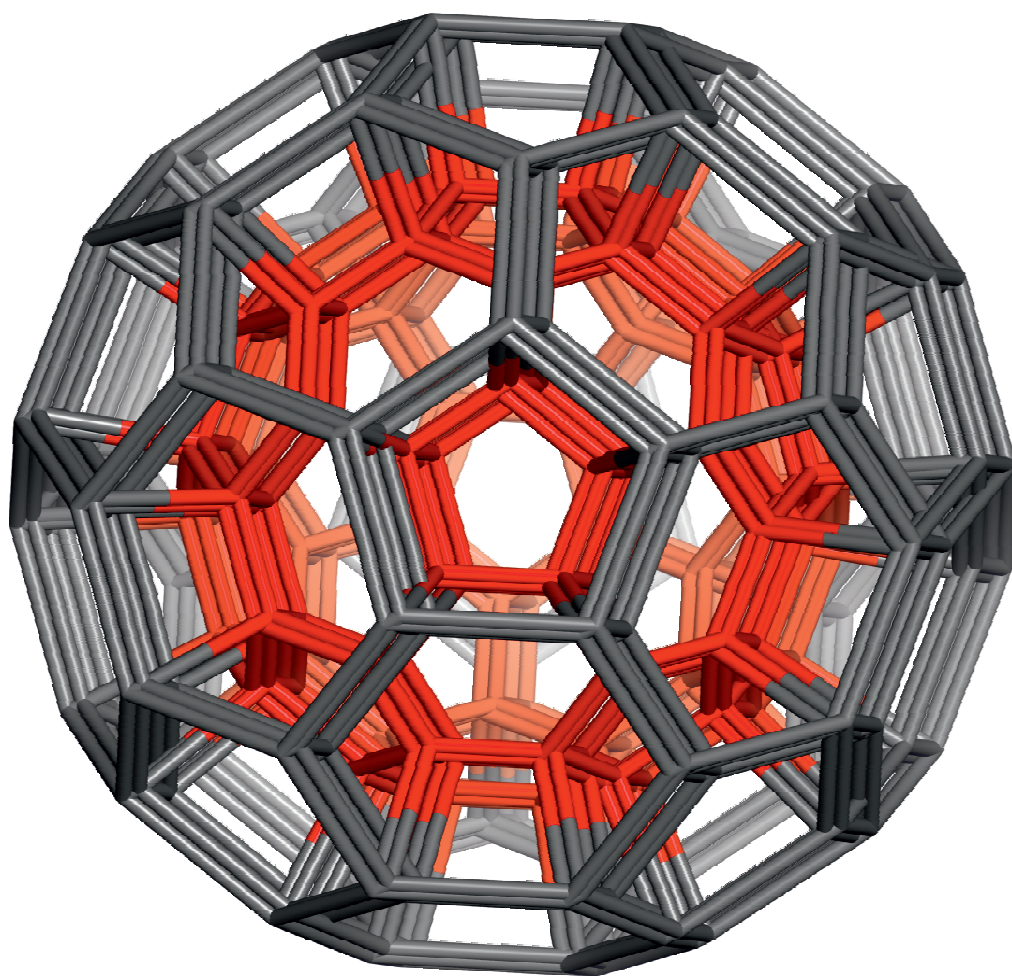




STUDIA UNIVERSITATIS
BABEŞ-BOLYAI



CHEMIA

1/2016

**STUDIA
UNIVERSITATIS BABEȘ-BOLYAI
CHEMIA**

1/2016

EDITORIAL BOARD OF STUDIA UNIVERSITATIS BABEȘ-BOLYAI CHEMIA

ONORARY EDITOR:

IONEL HAIDUC - Member of the Romanian Academy

EDITOR-IN-CHIEF:

LUMINIȚA SILAGHI-DUMITRESCU

EXECUTIVE EDITOR:

CASTELIA CRISTEA

EDITORIAL BOARD:

PAUL ȘERBAN AGACHI, Babeș-Bolyai University, Cluj-Napoca, Romania

LIVAIN BREAU, UQAM University of Quebec, Montreal, Canada

HANS JOACHIM BREUNIG, Institute of Inorganic and Physical Chemistry,
University of Bremen, Bremen, Germany

MIRCEA DIUDEA, Babes-Bolyai University, Cluj-Napoca, Romania

JEAN ESCUDIE, HFA, Paul Sabatier University, Toulouse, France

ION GROSU, Babeș-Bolyai University, Cluj-Napoca, Romania

EVAMARIE HEY-HAWKINS, University of Leipzig, Leipzig, Germany

FLORIN DAN IRIMIE, Babeș-Bolyai University, Cluj-Napoca, Romania

FERENC KILAR, University of Pecs, Pecs, Hungary

BRUCE KING, University of Georgia, Athens, Georgia, USA

ANTONIO LAGUNA, Department of Inorganic Chemistry, ICMA, University of
Zaragoza, Zaragoza, Spain

JURGEN LIEBSCHER, Humboldt University, Berlin, Germany

KIERAN MOLLOY, University of Bath, Bath, UK

IONEL CĂȚĂLIN POPESCU, Babeș-Bolyai University, Cluj-Napoca, Romania

CRISTIAN SILVESTRU, Babeș-Bolyai University, Cluj-Napoca, Romania

<http://chem.ubbcluj.ro/~studiachemia/>; studiachemia@chem.ubbcluj.ro

http://www.studia.ubbcluj.ro/serii/chemia/index_en.html

YEAR
MONTH
ISSUE

Volume 61 (LXI) 2016
MARCH
1

STUDIA UNIVERSITATIS BABEȘ-BOLYAI CHEMIA

1

*Dedicated to Professor Mircea Diudea on the Occasion
of His 65th Anniversary*

STUDIA UBB EDITORIAL OFFICE: B.P. Hasdeu no. 51, 400371 Cluj-Napoca, Romania,
Phone + 40 264 405352

CUPRINS – CONTENT – SOMMAIRE – INHALT

NAGY LEVENTE CSABA, Professor Mircea V. Diudea on His 65 th Anniversary.....	7
NAFISEH JAFARZADEH, ALI IRANMANESH, Application of Graph Theory to Biological Problems	9
OANA RAD, ROZSA TIBOR, MIHAELA DUMA, LAURIAN VLASE, ADRIAN PÎRNĂU, BRÎNDUȘA TIPERCIUC, IOANA IONUȚ, OVIDIU ONIGA, Synthesis and Antimicrobial Activity of Some 5-Amino-2-Mercapto-1,3,4-Thiadiazole Derivatives Thioeters and Schiff Bases.....	17
PAULINA VLAZAN, PAULA SFIRLOAGA, FLORINA STEFANIA RUS, Synthesis and Characterization of Lead-Free Sodium Niobate Powder	33
FÜSTÖS MELINDA-EMESE, MIRCEA V. DIUDEA, KATONA GABRIEL, Catalytic Reduction of 4-Nitrophenol Using New Cu(0)/Aromatic Core Dendrimer Complexes	43

ZOITA BERINDE, THOMAS DIPPONG, CLAUDIA BUTEAN, QSPR Study on Transition Temperature of Tetraphenylethene-Derived Columnar Liquid Crystals	51
FARZANEH FALAHATI-NEZHAD, MAHDIEH AZARI, The Inverse Sum Indeg Index of Some Nanotubes	63
LAVINIA L. PRUTEANU, SARA ERSALI, SORANA D. BOLBOACA, A QSPR Model For Steroids.....	71
FATEMEH MOOSAVI, MOHAMMAD EBRAHIM BAHROLOLOOM, RAMIN KAMJOU, Effects of Cu Doping on Nano Structure, Morphology and Photocatalytic Activity of ZnO Thin Film Synthesized by Sol- Gel Method	79
SIAMAK FIROUZIAN, MORTEZA FAGHANI, ALI REZA ASHRAFI, Approximating the Energy of Nanotubes.....	89
MIRELA SUCHEA, MARIA VAMVAKAKI, DIMITRIS LOULOUdakis, MICHAEL SIGALAS, NIKOLAOS KATSARAKIS, DIMITRA VERNARDOU, EMMANUEL KOUDOUMAS, Influence of Thickness on the Properties of TiO ₂ and Ti(Nb)O ₂ Thin Films.....	97
FATEMEH SHAHSAVARI, MARYAM EHTESHAMZADEH, PARVIN ALIZADEH ESLAMI, AHMAD IRANNEJAD, Thickness Evolution of Nickel Nano Layer on the Microstructure and Adhesion Strength of DLC Films	107
MOHAMMAD A. IRANMANESH, MAHBOUBEH SAHELI, MIRCEA V. DIUDEA, Counting Polynomials in the Crystal Network Flu (CMedDu) ...	115
NAJMEH SOLEIMANI, ESMAEEL MOHSENI, SAHAR HELALBIN, Theoretical Study of Nanostar Dendrimers	127
MARYAM VEYLAKI, MOHAMMAD JAVAD NIKMEHR, Computing the Modified Eccentric Connectivity Polynomial of Naphthylenic Lattices.....	141
LAVINIA L. PRUTEANU, LORENTZ JÄNTSCHI, MIHAELA L. UNGUREȘAN, SORANA D. BOLBOACĂ, Models of Monovalent Ions Dissolved in Water	151
M. MORADI, M. ZAHEDIFAR, T. GHORBANI, M. SAADAT, K. ROSTAMI, Optimal Conditions for Preparing CIGS Thin Film Through Two- Stepprocess of Sputtering Followed by Selenization	163
ROYA MAJIDI, ALIREZA KARAMI, Band GAP Modulation of Graphene and Graphyne Via Tetracyanoethylene Adsorption.....	177
SOHEILA ABDI, DAVOUD DORRANIAN, GHOLAM ALI NADERI, AMIRNADER EMAMI RAZAVI, Changes in Physico-Chemical Characteristics of Human Low Density Lipoprotein Nano-Particles by Electromagnetic Field Exposure	185

BOGDAN-OVIDIU ȚĂRANU, DANA VLASCICI, IULIANA SEBARCHIEVICI, EUGENIA FĂGĂDAR-COSMA, The Aggregation Behavior of an A ₃ B Free Base Porphyrin and Its Application as Chromium(III)-Selective Membrane Sensor	199
MONICA CULEA, ANDREEA MARIA IORDACHE, ELENA HORJ, CORNELIA MESAROS, RAMONA BLEIZIFFER, GC-MS Methods for Amino Acids Determination in Different Biological Extracts.....	213
MIHAELA L. UNGUREȘAN, LORENA L. PRUTEANU, LORENTZ JÄNTSCHI, SORANA D. BOLBOACĂ, Correlation Study Among Boiling Temperature and Heat of Vaporization	223
ZAHRA KHALAJ, Comparative Study of Nanocrystalline Diamond Growth Using PECVD and HFCVD Techniques	235
ALI REZA ASHRAFI, AMIR LOGHMAN, MOJGAN MOGHARRAB, On (3,6) and (4,6)–Fullerene Cayley Graphs.....	243
B. SZEFLER, M.V. DIUDEA, I.P. GRUDZINSKI, Nature of Polyethyleneimine - Glucose Oxidase Interactions	249
MODJTABA GHORBANI, MARDJAN HAKIMI-NEZHAAD, Polyhedral Graphs under Automorphism Groups.....	261
MUHAMMAD FAISAL NADEEM, SOHAIL ZAFAR, ZOHAI B ZAHID, On the Edge Version of Geometric-Arithmetic Index of Nanocones	273
SAKANDER HAYAT, HAFIZ MUHAMMAD AFZAL SIDDIQUI, On Bipartite Edge Frustration of Carbon and Boron Nanotubes	283
KHADIJEH FATHALIKHANI, ATENA PÎRVAN-MOLDOVAN, MIRCEA V. DIUDEA, Topological Indices in Hypertubes of Hypercubes.....	291
ATENA PIRVAN MOLDOVAN, SARA ERSALI, RALUCA POP, QSAR Study of Phenothiazines	305
ERRATUM, <i>STUDIA UBB CHEMIA</i> , Volume 60 (LX), 4, 2015 (p. 179).....	317
ERRATUM, <i>STUDIA UBB CHEMIA</i> , Volume 60 (LX), 2, Tom I, 2015 (p. 161-167)	319

Studia Universitatis Babes-Bolyai Chemia has been selected for coverage in Thomson Reuters products and custom information services. Beginning with V. 53 (1) 2008, this publication is indexed and abstracted in the following:

- Science Citation Index Expanded (also known as SciSearch®)
- Chemistry Citation Index®
- Journal Citation Reports/Science Edition

Professor Mircea V. Diudea on his 65th anniversary



Professor Mircea Vasile Diudea was born on November 11, 1950. He graduated the Faculty of Chemistry of the University of Cluj in 1974 and received his PhD in 1979 under the supervision of Prof. I. Bodea in the field of organic chemical synthesis. He became full professor in 1996 at the Department of Organic Chemistry of the Babes-Bolyai University from Cluj.

The research interests of Prof. Diudea include organic chemistry synthesis, chemical graph theory, QSAR/QSPR studies, carbon nanostructures, topology of crystal structures and topology of higher dimensional structures. 18 PhD thesis have been defended under his supervision.

Since 1976 when his first research paper was published in "Journal für Praktische Chemie", he has authored and co-authored more than 300 research papers, 7 books, 3 edited books, and 35 book chapters. Some of the representative book titles published at prestigious international publishers like Springer and Nova Science are: "Molecular Topology", "Nanostructures, Novel Architecture", "Periodic Nanostructures", "Nanomolecules and Nanostructures - Polynomials and Indices", and "Diamond and related nanostructures".

Many of his works were published in the journal "MATCH Communications in Mathematical and in Computer Chemistry", and in other prestigious journals like "Journal of Chemical Information and Computer Sciences", "Physical Chemistry Chemical Physics", and "Journal of Mathematical Chemistry". His work has received more than 1500 citations and his h index is 27.

Professor Diudea have organized several international conferences including "TOPMOL – 20 Years Anniversary of Molecular Topology at Cluj" in 2006, "CHEMMOD – Chemical Graph Theory and Molecular Modeling Workshop" in 2007, "Mathematical Chemistry in NANO-era symposium" in 2010, and "NanoMathChem – Nanoscience in Chemistry, Physics, Biology and Mathematics" in 2015.

Professor Diudea is an active member of the International Academy of Mathematical Chemistry, and he is the founder president of the European Society of Mathematical Chemistry.

He is member of the editorial board at several scientific international journals including "MATCH Communications in Mathematical and in Computer Chemistry", "Croatica Chemica Acta", "Studia Universitatis Babeş-Bolyai Chemia", and "Symmetry: Culture and Science". Since 2008 he is the Senior Editor of the International Journal of Chemical Modeling journal published at NOVA Publishers, New York.

Professor Diudea has participated in numerous projects and grants financed by both governmental and international organizations. He delivered 78 lectures at international conferences or at prestigious universities, as an invited lecturer, from Austria, Belgium, Croatia, England, France, Hungary, Germany, Greece, Iran, Italy, Japan, Poland, Russia, Serbia, Slovenia, Spain, Turkey, and Ukraine.

Professor Diudea has published ten volumes of poetry, in Romanian, English, Persian and Polish languages.

Nagy Levente Csaba

Cluj-Napoca, November 2015

*Dedicated to Professor Mircea Diudea
on the Occasion of His 65th Anniversary*

APPLICATION OF GRAPH THEORY TO BIOLOGICAL PROBLEMS

NAFISEH JAFARZADEH^a AND ALI IRANMANESH^{a,*}

ABSTRACT. In this paper, we investigate application of graph theory to some biological problems, specially reconstructing strings based on information about their substrings and sequence comparison by using overlap graphs and also weighted directed graph.

Keywords: *Fragment assembly, Overlap graphs, sequence comparison, Alignment-free method, Weighted directed graph.*

INTRODUCTION

Since the helical structure of DNA was proposed, many problems about this structure are posed. One of the important problems is how to read and recognize primary structure of a DNA sequence. DNA fragment assembly is a newly explored method of determining whether or not a reassembled strand of DNA, matches the original strand. One particular way to perform this method is by using concepts from graph theory. For instance see [1-4]. In order to begin the graph theoretical phase, one needs a directed graph which is built from some k -long oligonucleotides. Fragment assembly is the reconstructing of a string by using a subset of its substrings. In this method, a given piece of DNA (or rather many identical copies of it) is broken into several smaller fragments. The goal is to reconstruct the original DNA string based on the fragments. Therefore we have the following problem: Given a multiset of fragments, construct the best string that contains each

^a *Department of Mathematics, Faculty of Mathematical Sciences, Tarbiat Modares University, P.O. Box: 14115-137, Tehran, Iran*

* *Corresponding Author: Iranmanesh@modares.ac.ir*

of the strings in the multiset. A string with that property is called a superstring of multiset. Here we want to find a superstring of minimal length, called the shortest common superstring. A mathematical tool to model the problem is a graph that represents the overlap between the strings in the set F . The overlap graph of the multiset contains a node for each string in it. The solution of this problem leads to find a Hamiltonian path. Note this is an instance of the Traveling Salesman Problem, which in its general form is NP complete. Even the existence of a Hamiltonian path in a graph is an NP complete problem that there are no efficient algorithms to solve the problem. But if we can consider fragments as edges of an overlap graph, this solution leads to find an Eulerian path and as we know, solving this problem is not NP complete and there are some efficient algorithms to solve the problem. Some overlap graphs have been proposed for reconstructing DNA sequences. In this paper, by the concept of DNA graph we propose an approach of creating and analyzing a DNA graph and its role in aiding DNA fragment assembly and determining the DNA structure. Graph theory and its concepts are used for application in many fields of study, for example see [5-8]. Also it will be studied how DNA graphs and Eulerian circuits are useful to resolve some problems in DNA fragment assembly.

Biological sequence analysis and comparison is another important problem in bioinformatics which replies to the emergence and need for the analysis of different types of data generated through biological research. Molecular sequence and structure data of DNA, RNA and proteins, gene expression profiles or micro array data, metabolic pathway data are some of the major types of data being analyzed in bioinformatics. Among them, sequence data are increasing at the exponential rate due to advent of next-generation sequencing technologies. Since the origin of bioinformatics, sequence analysis has remained the major area of research with wide range of applications in database searching, genome annotation, comparative genomics, molecular phylogeny and gene prediction. The pioneering approaches for sequence analysis were based on sequence alignment, global or local, pairwise or multiple sequence alignment. Alignment-based approaches generally give excellent results when the sequences under study are closely related and can be reliably aligned, but when the sequences are divergent, a reliable alignment cannot be obtained and hence the applications of sequence alignment are limited. Another limitation of alignment-based approaches is their computational complexity when dealing with large-scale sequence data. The advent of next generation sequencing technologies has resulted in generation of voluminous sequencing data. The size of this sequence data poses challenges on alignment-based algorithms in their assembly, annotation and comparative studies. Thus, alignment-free sequence analysis approaches provide attractive

alternatives over alignment-based approaches. In this paper, we will discuss about applications of product of graphs and overlap graphs to compare DNA sequences based on an alignment-free method.

FRAGMENT ASSEMBLY

In graph theory, an n -dimensional De Bruijn graph of m symbols is a directed graph representing overlaps between sequences of symbols. It has m^n vertices, consisting of all possible length- n sequences of the given symbols; the same symbol may appear multiple times in a sequence. If we have the set of m symbols $S = \{s_1, \dots, s_m\}$ then the set of vertices is:

$$V = S^m = \{(s_1, \dots, s_1, s_1), (s_1, \dots, s_1, s_2), \dots, (s_1, \dots, s_1, s_m), (s_1, \dots, s_2, s_1), \dots, (s_m, \dots, s_m, s_m)\}$$

If one of the vertices can be expressed as another vertex by shifting all its symbols by one place to the left and adding a new symbol at the end of this vertex, then the latter has a directed edge to the former vertex. Thus the set of arcs (directed edges) is:

$$E = \{((v_1, v_2, \dots, v_n), (v_2, \dots, v_n, v_i)) : i = 1, \dots, m\}.$$

If we consider a set of 4 symbols $\{A, T, C, G\}$ we get the definition of DNA graph:

Definition 1. [9]. Let $k \geq 2$ be an integer. We say that a directed graph D with a set of vertices $V(D)$ and a set of ordered pairs of points (directed edges) $E(D)$, is a DNA graph if it is possible to assign a label $(l_1(x), \dots, l_k(x))$ of length k to each vertex x of $V(D)$ such that:

- (a) $l_i(x) \in \{A, C, T, G\}$, for every $i \in \{1, \dots, k\}$;
- (b) All labels are different, that is, $(l_1(x), \dots, l_k(x)) \neq (l_1(y), \dots, l_k(y))$ if $x \neq y$;
- (c) $(x, y) \in E(D)$ if and only if $(l_2(x), \dots, l_k(x)) = (l_1(y), \dots, l_{k-1}(y))$.

Now, we construct a DNA graph by the approach which was presented by Pevzner [2] as follows:

Each k -long oligonucleotide from the multiset becomes an arc which its initial end point is $k-1$ rightmost nucleotides of arc and its terminal end point is $k-1$ leftmost nucleotides. For example, a DNA graph with $k = 4$ is shown in Figure 1. To find the primary sequence, we need to find an Eulerian path.

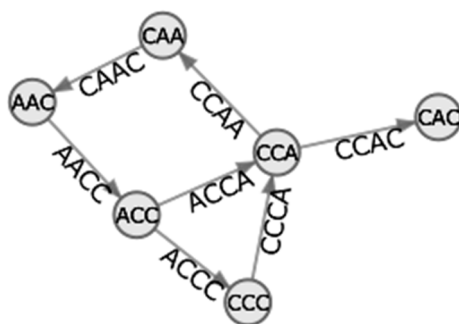


Figure 1. The DNA graph for the sequence “ACCCAACCAC”

Euler’s theorem for directed graphs gives conditions for the existence of an Eulerian path. Define for vertex v , $in(v) = |\{u: uv \in E\}|$, and $out(v) = |\{w: vw \in E\}|$.

Label the starting vertex s and the terminal vertex t . There is an Eulerian path starting at s and ending at t , if and only if

$$in(v) = out(v) \quad \forall v \neq s, t, \quad out(s) - in(s) = 1 \text{ and } out(t) - in(t) = -1$$

Since, each Eulerian path corresponds to a different DNA sequence, we can infer the sequence unambiguously if and only if the number of Eulerian paths in G is exactly one. We can reduce the problem of determining the number of Eulerian paths from s to t in G to the problem of determining the number of Eulerian cycles in the graph $G \cup ts$, which has a simple solution described below. We define an intersection graph on the cycles of $G \cup ts$ as follows. First decompose $G \cup ts$ into simple cycles: $v_{i1}, v_{i2}, \dots, v_{ik} = v_{i1}$, where no $v_i = v_j$ except for $v_{ik} = v_{i1}$. An edge can be used in at most one cycle C but a vertex can be used in arbitrarily many cycles. For these cycles, define the intersection graph G_I of the cycles C_1, C_2, \dots, C_m , where cycles correspond to vertices, and if cycles C_i and C_j have l vertices in common, we connect them by l edges in G_I . The following theorem gives the necessary and sufficient conditions for general graphs.

Theorem 1 [10]: There is a unique Eulerian cycle in G if and only if the intersection graph G_I of simple cycles from G is a tree.

Also, there exists a formula for computation of Eulerian circuits in a directed graph. Named after its inventors, de Bruijn, van Aardenne-Ehrenfest, Smith, and Tutte, [11-12], the BEST Theorem reads as follows:

Theorem 2 [13]: Given a connected directed graph G and a set of vertices $V(G) = \{v_1, \dots, v_n\}$ all of even degree, the number of Eulerian circuits $|S(G)|$ is expressed as the following, where $It_i(G)$ is the number of spanning trees rooted towards any vertex v_i in G and $d^+(v_j)$ is in-degree of v_j :

$$|S(G)| = It_i(G) \prod_{j=1}^n (d^+(v_j) - 1)!$$

There is a theorem about the number of spanning trees in a graph, showing that this number can be computed in polynomial time as the determinant of a matrix derived from the graph. This theorem is named "The matrix tree Theorem":

Theorem 3 [13]: Given a directed graph G with the set of vertices $V(G) = \{v_1, \dots, v_n\}$ and a set of spanning trees $t_i(G)$ oriented towards the vertex v_i , then $It_i(G)$ is equal to the cofactor of $L(G)$ (Laplacian matrix of G) on the i -th row and i -th column.

After creating a DNA graph for a multiset of DNA fragments, we need to examine the Eulerian path of this graph. By using the Eulerian graph theorem we make a directed Eulerian graph from DNA graph. Then we use the BEST theorem and the matrix tree theorem for counting Eulerian circuits in DNA graph. It leads us to determine primary DNA sequence.

Now, let $S = n_1 n_2 \dots n_L$ be a DNA sequence and M be a multiset of all k -long oligonucleotides of a this sequence, then we construct a DNA graph for S and call it G_s^k . The vertices of this graph will be $(K - 1)$ oligonucleotides and according to the Pevzner's approach [2], there is an Eulerian path which reveals the primary sequence S and we call P_s^k .

According to the graph theoretical method in [4], in whole genome sequencing with fragment assembly, there are two different strings to be recognized. These are the original 3'-5' string and its complement, in this method, assuming that M be a multiset of all k -long oligonucleotides of a complete DNA sequence (S), then according to above approach, G_s^k have been constructed, may be disconnected, but this graph includes two connected DNA graphs belonging to the original 3'-5' string and its complement and each graph includes an Eulerian path and these paths determine the structure of primary DNA sequence.

SEQUENCE COMPARISON

In this section we discuss about the application of graph theory to compare DNA sequences. Let us to mention some concepts in graph theory. By a *graph* we mean a set $V(G)$ of vertices, together with a set $E(G)$ of edges. A

graph is the *complete graph* K_n if any two of its distinct vertices are adjacent, and a graph is the *path* P_n if it is isomorphic to a graph on n distinct vertices v_1, v_2, \dots, v_n and $n - 1$ edges $v_i, v_{i+1}, 1 \leq i < n$.

Definition 2. [14]. The strong product $G \boxtimes H$ of graphs G and H is a graph such that

- the vertex set of $G \boxtimes H$ is the Cartesian product $V(G) \times V(H)$; and
- any two distinct vertices (u, u') and (v, v') are adjacent in $G \times H$ if and only if:
 - u is adjacent to v and $u'=v'$, or
 - $u=v$ and u' is adjacent to v' , or
 - u is adjacent to v and u' is adjacent to v'

In [5], Pesek presented a new numerical characterization of DNA sequences that is based on the modified graphical representation proposed by Hamori [15]. He used analogous embedding into the strong product of graphs, $K_4 \boxtimes P_n$, with weighted edges. Based on this representation, a novel numerical characterization is proposed which is based on the products of ten eigenvalues from the start and the end of the descending ordered list of the eigenvalues of the L/L matrices associated with DNA.

Now, we can give a new approach to sequence comparison by using pesek's approach. According to the pervious section, let $k > 1$ be an integer and $S = n_1 n_2 \dots n_L$ be a DNA sequence and M be a multiset of all k -long oligonucleotides of a this sequence; we consider $K_4 \boxtimes P_k^s$ as a new graph which just is made by multiset of all k -long oligonucleotides of a sequence and we can continue the details of pesek's method for comparing sequences.

Another approach that applies concepts of graph theory for sequence comparison is proposed by Qi et al, [16]. They constructed novel mathematical descriptors based on graph theory, for each DNA sequence, they sat up a weighted directed graph. The adjacency matrix of the directed graph will be used to induce a representative vector for DNA sequence. This new approach measures similarity based on both ordering and frequency of nucleotides so that much more information is involved.

They have shown how to construct the weighted directed multi-graph for $S = s_1 s_2 \dots s_n$, which is denoted by $G_m = (V(G_m), A(G_m))$. The vertex set $V(G_m) = \{A, C, G, T\}$. For each pair of nucleotides s_i and s_j in S with i, j , put an arc from s_i to s_j , and define a special weight of that.

Theorem 4 [16]. It is a one-to-one mapping between a DNA sequence S and its corresponding weighted directed multi-graph G_m .

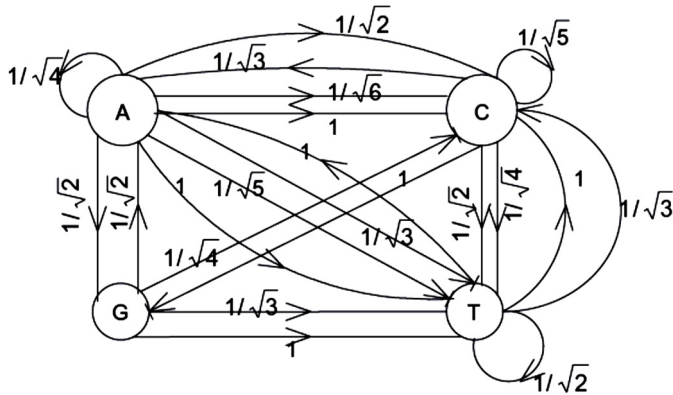


Figure 2. Directed multi-graph G_m for $S = ACGTATC$

CONCLUSIONS

Our purpose in this paper was to investigate application of some concepts in graph theory to sequencing and sequence comparison. At first, we used a multiset of fragments of a given DNA sequences and applied Pevzner's approach to achieve an overlap graphs for which the finding of superstring of minimal length is not NP-complete. Then we utilized the Eulerian path of this graph to construct a new graph by using strong product of graphs for comparing and analysing DNA sequences.

ACKNOWLEDGMENTS

This research is partially supported by Iran National Science Foundation (INSF) (Grant No. 93036169).

REFERENCES

1. R.M. Ludry, M.S. Waterman, A new algorithm for DNA sequencing assembly. *J. Comput. Biol.*, **1995**, 2, 291.
2. P.A. Pevzner, H. Tang, M.S. Waterman, A new approach to fragment assembly in DNA sequencing. *RECOMB.*, **2001**, 1, 256.
3. J. Blazewicz, M. Bryja, M. Figlerowicz, P. Gawron, M. Kasprzak, E. Kirton, D. Platt, J. Przybytek, A. Swiercz, L. Szajkowski, Whole genome assembly from 454 sequencing output via modified DNA graph concept, *Comput. Biol. Chem.*, **2009**, 33, 224.

4. N. Jafarzadeh, A. Iranmanesh, Application of DNA graphs to whole genome sequencing, *International Journal of Green Nanotechnology*, **2014**, 2, 373.
5. J. Pesek, A. Zerovnik, Numerical Characterization of Modified Hamori Curve Representation of DNA Sequences, *MATCH Commun. Math. Comput. Chem.*, **2008**, 60, 301.
6. Y. Zhang, W. Chen, New Invariant of DNA Sequences, *MATCH Commun. Math. Comput. Chem.*, **2007**, 58, 197.
7. N. Jafarzadeh, A. Iranmanesh, A Novel Graphical and Numerical Representation for Analyzing DNA Sequences Based on Codons, *MATCH Commun. Math. Comput. Chem.*, **2012**, 68, 611.
8. J. Yu, J. Wang, X. Sun, Analysis of similarities/dissimilarities of DNA sequences based on a novel graphical representation, *MATH Commun. Math. Comput. Chem.*, **2010**, 63, 493.
9. J. Blazewicz, A. Hertz, D. Kobler, On some properties of DNA graphs, *Discrete Appl Math.*, **2003**, 1, 98.
10. P.A. Pevzner, *l*-tuple DNA sequencing: a computer analysis, *J. Biota. Struct. Dyn.*, **1989**, 7, 63.
11. T. van Aardenne Ehrenfest, N.G. de Bruijn, Circuits and Trees in Oriented Linear Graphs, *Simon Stevin.*, **1951**, 28, 203.
12. W.T. Tutte, C.A.B. Smith, On Unicursal Paths in a Network of Degree 4, *Amer. Math. Monthly*, **1941**, 48, 233.
13. J. Kaptcianos, A graph theoretical approach to fragment assembly, *American Journal of Undergraduate Research*, **2008**, 7, 311.
14. W. Imrich, S. Klavžar, "Product Graphs: Structure and Recognition", John Wiley & Sons, New York, **2000**.
15. E. Hamori, Graphical representation of long DNA sequences by methods of H curves, current results and future aspects, *Biotechniques*, **1989**, 7, 710.
16. X. Qi, Q. Wu, Y. Zhang, E. Fuller, C. Zhang, A Novel Model for DNA Sequence Similarity Analysis Based on Graph Theory, *Evolutionary Bioinformatics*, **2011**, 7, 149.

*Dedicated to Professor Mircea Diudea
on the Occasion of His 65th Anniversary*

SYNTHESIS AND ANTIMICROBIAL ACTIVITY OF SOME 5-AMINO-2-MERCAPTO-1,3,4-THIADIAZOLE DERIVATIVES THIOETHERS AND SCHIFF BASES

OANA RAD^a, ROZSA TIBOR^a, MIHAELA DUMA^b,
LAURIAN VLASE^c, ADRIAN PÎRNĂU^d, BRÎNDUȘA TIPERCIUC^a,
IOANA IONUȚ^{a,*}, OVIDIU ONIGA^a

ABSTRACT. Starting from 5-amino-2-mercapto-1,3,4-thiadiazole, 23 compounds, Schiff bases and S-mercapto-substituted derivatives, were synthesized. Their structural elucidation was based on elemental analysis, mass spectrometry and proton nuclear magnetic resonance spectroscopy (¹H NMR). The screening of the antimicrobial activity of the title compounds was realized using the diffusimetric method against several strains of Gram-positive and Gram-negative bacteria and one fungal strain (*Candida albicans*). Some of the molecules showed moderate to good antibacterial activity against Gram-negative (*S. typhimurium*, *E. coli*) and better activity against Gram-positive (*B. cereus*, *L. monocytogenes*, *S. aureus*) bacterial strains. All compounds exhibited moderate to very good activity against *C. albicans*. Qualitative relationships (SAR) were also established between the chemical structures and the antimicrobial activity of these compounds.

Keywords: 1,3,4-thiadiazole, antibacterial activity, antifungal activity.

^a Iuliu Hațieganu University of Medicine and Pharmacy, Department of Pharmaceutical Chemistry, 41 Victor Babeș Street, 400012 Cluj-Napoca, Romania

^b State Veterinary Laboratory for Animal Health and Food Safety, 400572 Cluj-Napoca, Romania

^c Iuliu Hațieganu University of Medicine and Pharmacy, Faculty of Pharmacy, Department of Pharmaceutical Technology and Biopharmaceutics, 41 Victor Babeș Street, 400012 Cluj-Napoca, Romania

^d National Institute for Research and Development of Isotopic and Molecular Technologies, 1 Donath Street, Cluj-Napoca, Romania

* Corresponding Author: ionut.ioana@umfcluj.ro

INTRODUCTION

Bacterial infections have increased dramatically in recent years. Bacteria have been the cause of some of the most deadly diseases and widespread epidemics in human. The widespread use and misuse of antibiotics led to a serious public health problem: bacterial resistance to antibiotics [1].

According to WHO (World Health Organization), a great percentage of hospital-acquired infections are caused by highly resistant bacteria such as methicillin-resistant *Staphylococcus aureus* (MRSA) and vancomycin-resistant enterococci (VRE) or other so called „super bacteria” (*Clostridium difficile*, *Escherichia coli*, *Haemophilus influenzae*, *Klebsiella pneumoniae*, *Pseudomonas aeruginosa*, *Salmonella* spp., *Serratia* spp. etc.) with enhanced morbidity and mortality, being capable of surviving the effects of most, if not all, antibiotics currently in use, due to multiple mutations [2]. In addition, the theme of the World’s Health Day on the 7th of April 2011 was the antimicrobial resistance, showing that this is a major worldwide problem.

On the other hand, primary and opportunistic fungal infections continue to increase rapidly because of the increased number of immunocompromised patients [3]. The difficulties in developing safe and efficient antifungal are the easily gained resistance and the biochemical similarity of the human cell and fungi, which is also a problem for selective activity [4].

Therefore, the treatment of infectious diseases still remains an important and challenging problem due to a combination of factors including emerging infectious diseases and the dramatically increasing number of multi-drug resistant microbial pathogens [5].

This fact created in the last decades a substantial medical need for new classes of antibacterial agents. It is necessary to develop new approaches of antimicrobial resistance. In this purpose a potential method is to design novel, potent and unique molecules that can be involved in effective therapies with no cross-resistance [6].

Several five membered heteroaryl systems with three heteroatoms at symmetrical positions, such as 1,3,4-thiadiazole, have attracted continuous interest over the years due to their interesting pharmacological activities [7-9].

1,3,4-Thiadiazole is a versatile framework that acts as a “hydrogen binding domain” and as a “two- electron donor system” [10]. It is a basic pharmacophore for a wide variety of biological activities, including antibacterial properties. 1,3,4-Thiadiazole can behave as the bio-isosteric replacement of the thiazole moiety, which can be found in the structure of third and fourth generation cephalosporins. Therefore, 1,3,4-thiadiazole can be successfully used in antibiotic preparations [10,11].

The most studied regioisomeric form of the thiadiazole series, is 1,3,4-thiadiazole and its dihydro-derivatives [12,13]. These heterocyclic systems constitute the active part of several biologically active compounds (Acetazolamide, Methazolamide, Sulfamethizole [7,8], Glybuzole [14] etc.) and exhibits a wide range of therapeutic activities such as antimicrobial [15-20], diuretics [7], anti-leishmanial [21], antiulcer, anti-mycobacterial [15], anti-inflammatory [22], free radical scavenging [23], anticonvulsant [24,25], anticancer [26] and antidepressant [15].

In addition, some *N*-substituted Schiff bases bearing aryl groups or heterocyclic motifs possess excellent biological activities [27,28]. Therefore these new generations of molecules would represent a fruitful matrix for further development of better medicinal agents, being a prevalent scaffold in antimicrobials drugs discovery.

These findings prompted us to prepare and investigate potentially active new antimicrobial agents. We report herein, the synthesis of various new C-2, -5 disubstituted 1,3,4-thiadiazole derivatives and the screening of their antibacterial and antifungal activities, with the aim of having improved activity and dropped toxicity. We also discuss the structure-activity relationship, which can serve as an important tool for medicinal chemists in order to develop better agents in terms of efficacy and safety.

RESULTS AND DISCUSSION

Chemistry. The target compounds, *S*-substituted 5-amino-2-mercapto-1,3,4-thiadiazoles (**2a-f**, **3a-b**, **4a-e**) and Schiff bases (*N*-substituted 5-mercapto-1,3,4-thiadiazol-2-imines) (**5a-d**, **6a-d**, **7a,b**) were prepared following the routes shown in Schemes 1 and 2. Two of the Schiff bases obtained - **5b** [29] and **5d** [30] - have been previously reported.

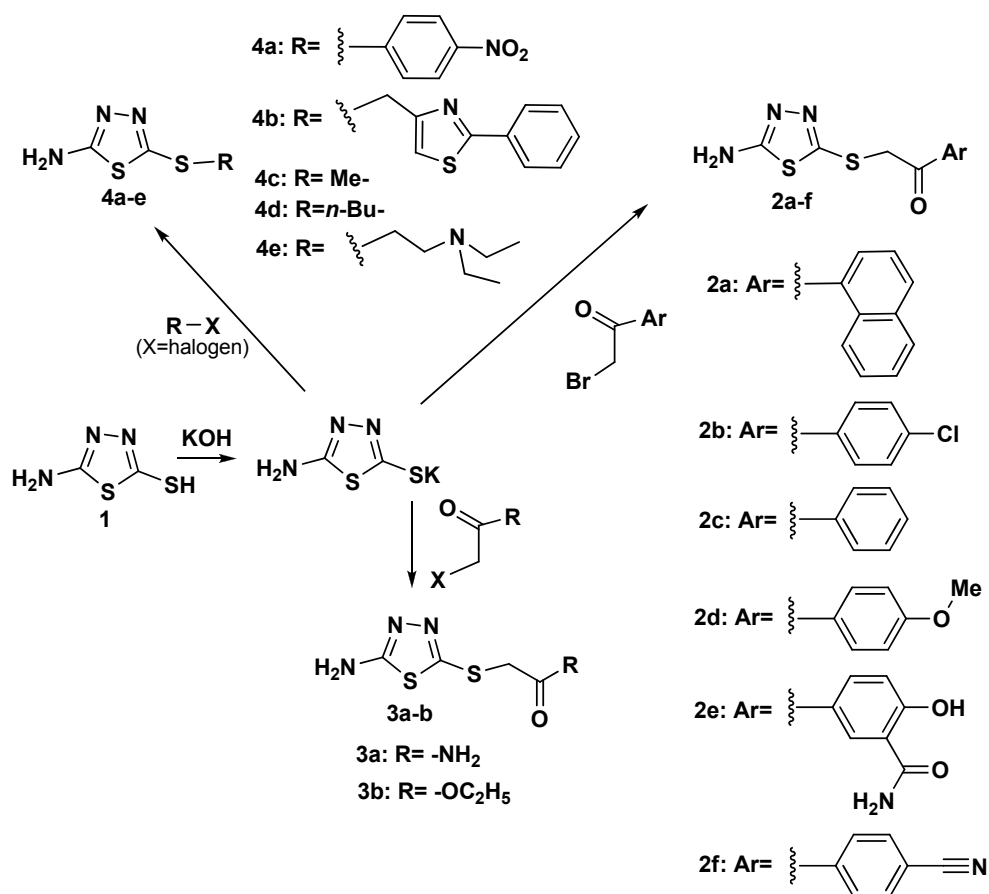
The thioethers **2a-f**, **3a-b** and **4a-e** were easily obtained via the potassium salt of the commercial 5-amino-5-mercapto-1,3,4-thiadiazole, by *S*-alkylation in aq. EtOH solutions at 0 °C.

All alkylating agents RX were commercial, except for 4- (iodomethyl)-2-phenylthiazole, whose synthesis was performed according to literature [31].

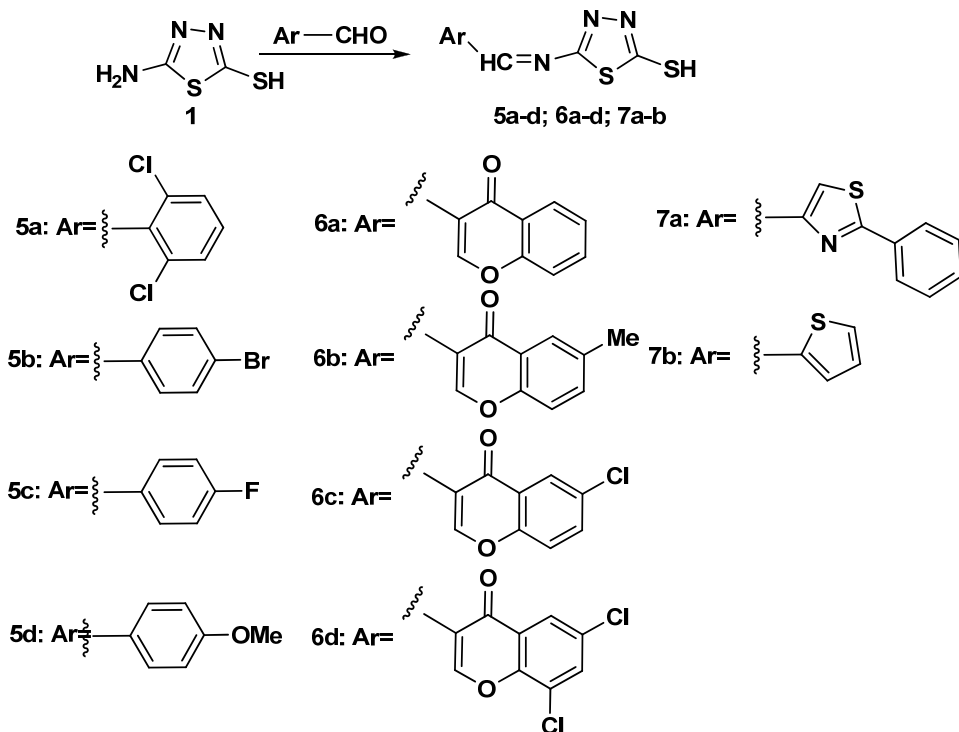
The Schiff bases **5a-d**, **6a-d** and **7a-b** were synthesized by condensation of 5-amino-2-mercapto-1,3,4-thiadiazole **1** with various aromatic aldehydes, in absolute EtOH, in the presence of AcOH as catalyst. The reactions were performed parallelly under reflux conditions, respectively using microwave irradiation. The second method presented several advantages such as: higher yields, shorter reaction durations, reduced amounts of solvents.

All aromatic aldehydes were commercial, with the exception of 2-phenylthiazole-4-carbaldehyde, which was synthesized according to literature [32].

All compounds were characterized by melting point, elemental analysis and spectroscopic data ($^1\text{H-NMR}$ and MS) which fully confirmed the proposed structures.



Scheme 1. Synthesis of S-substituted 5-amino-2-mercapto-1,3,4-thiadiazoles



Scheme 2. Synthesis of Schiff Bases

Antimicrobial activity. *In vitro* antimicrobial activity was investigated by means of agar disc diffusion method according to the National Committee for Clinical Laboratory Standards (NCCLS) guidelines. The antibacterial activity of newly synthesized compounds was evaluated against various pathogenic Gram-negative (*Salmonella typhimurium* ATCC 13311, *Escherichia coli* ATCC 25922) and Gram-positive (*Listeria monocytogenes* ATCC 35152, *Staphylococcus aureus* ATCC 25923 and *Bacillus cereus* ATCC 13061) bacterial strains. The antifungal activity of the above compounds was evaluated against a strain of *Candida albicans* ATCC 90028.

The results of antifungal and antibacterial activity of S-substituted derivatives and Schiff bases are reported in Table 1, in comparison with Ciprofloxacin and Fluconazole, as reference drugs.

Table 1. Antimicrobial activity of compounds **2** to **7**

Compound	Diameter of the inhibition zone (mm)					
	I	II	III	IV	V	VI
2a	18	14	12	12	10	22
2b	18	10	12	10	12	22
2c	18	14	10	12	12	22
2d	14	14	16	12	10	16
2e	14	10	14	12	10	18
2f	14	12	16	10	12	20
3a	12	10	10	16	12	18
3b	12	12	10	14	10	18
4a	12	12	14	10	10	18
4b	16	16	16	12	14	18
4c	14	10	14	14	10	16
4d	16	12	10	14	14	18
4e	16	10	12	12	14	16
5a	16	14	16	16	24	24
5b	18	18	18	20	22	18
5c	26	20	16	18	20	26
5d	20	20	16	18	18	26
6a	26	20	20	28	22	24
6b	20	16	22	24	26	30
6c	22	22	24	18	26	28
6d	22	18	22	26	26	18
7a	20	20	18	20	20	22
7b	22	18	16	20	22	28
C	26	12	16	26	14	-
F	-	-	-	-	-	28

- Agar diffusion technique, diameter of inhibition (mm). Solutions of compounds: 1 mg/mL (DMSO) (50 μ l/well). **Microbial strains I** = *Salmonella typhimurium* ATCC 13311; **II** = *Escherichia coli* ATCC 25922; **III** = *Bacillus cereus* ATCC 13061; **IV** = *Listeria monocytogenes* ATCC 35152; **V** = *Staphylococcus aureus* ATCC 25923; **VI** = *Candida albicans* ATCC 90028; **C**= Ciprofloxacin, **F**= Fluconazole.

All the tested thioethers showed a moderate activity against Gram-positive and Gram-negative bacterial strains, however a moderate to good antifungal activity. The most active compounds against *Salmonella typhimurium* and *Candida albicans* were those of series **2**, **2a-c** being the best. Therefore, the antifungal and the anti-*Salmonella* activity in the series of thioethers increased when the compounds were S-substituted with a 1-arylethanone group, especially in the case of unsubstituted or halogenated aryl-derivatives.

All the tested Schiff bases showed a moderate to good antibacterial activity and a good to very good antifungal activity. The antibacterial activity was significantly increased against Gram-positive bacterial strains.

In the case of compounds **5a-d**, *para*-substitution was found to be favorable for the antimicrobial activity, except for *Staphylococcus aureus*, against which the *ortho,ortho*'-disubstituted compound **5a** proved to be more active. In addition, in the series of 4-halo derivatives a higher activity against Gram-negative bacterial strains was observed for compounds substituted with the most electronegative halogen (**5c** (4-F) > **5b** (4-Br)). The best antibacterial activity against Gram-positive was detected for compounds substituted with the least electronegative halogen (**5b** (4-Br) > **5c** (4-F)).

The best antimicrobial activities in the series of Schiff bases were displayed for compounds **6a-d** possessing a 4*H*-chromen-4-one moiety. The halo-substitution in this zone (**6c-d**) generally increased the antibacterial activity, but di-halo-substitution decreased the antifungal activity. However, compound **6a** with unsubstituted chromene-4-one presented the largest diameters of the zones of inhibition against a Gram-negative (*Salmonella typhimurium*) and a Gram-positive bacteria strain (*Listeria monocytogenes*). The activity against Gram-positive bacteria (except for *Listeria monocytogenes*) was significantly increased in the case of compounds **6b-d** having a substituted chromen-4-one in their structure.

The best antifungal action was observed for the monosubstituted chromen-4-one derivatives, compound **6b** being the most active from all the synthesized molecules. Schiff bases **7a** and **7b** did not show a significant antimicrobial effect, except for **7b** (comprising a thiophene moiety in the structure), which revealed good antifungal properties.

CONCLUSIONS

In conclusion, starting from 5-amino-2-mercapto-1,3,4-thiadiazole, two series of compounds, *S*-substituted derivatives and Schiff bases, have been successfully prepared by *S*-alkylation or condensation with aromatic aldehydes respectively. The microwave irradiation method used in the synthesis of Schiff bases showed better yields than the classical procedure under reflux, as shown in Experimental part.

The antibacterial and antifungal activities were evaluated against several Gram-positive, Gram-negative bacteria and *Candida albicans*. The results indicated that some of the tested molecules show promising antibacterial and antifungal effects. The Schiff bases proved to be more active than the thioethers, representative being the chromene-4-one derivated compounds.

EXPERIMENTAL SECTION

General

Reagents and solvents were purchased from Sigma-Aldrich® and used without further purification. The melting points were measured with an Electrothermal® instrument and are uncorrected. Thin layer chromatography (TLC) used precoated Silica Gel 60F254 sheets (eluent heptane – ethylacetate 3:7 v/v, throughout). ¹H NMR Spectra were recorded at room temperature on a Bruker® Avance NMR spectrometer operating at 500 MHz. All chemical shifts (δ values) are given in parts per million (ppm) and were measured against the solvent peak. Elemental analysis was performed with a Vario El® CHNS instrument.

Chemistry

General procedure for the synthesis of thioethers (2a-f, 3a-b, 4a-e).

5-amino-2-mercapto-1,3,4-thiadiazole (**1**) (1.33 g, 10 mmol) was suspended in water (10 mL) and a solution obtained by dissolving potassium hydroxide (0.56 g, 10 mmol) in water (5 mL) was added dropwise under vigorous stirring, until complete dissolution of **1**. Ethanol (30 mL) was then added and the mixture was cooled at 0 °C. At this temperature, the corresponding alkylating agent (10 mmol), as a minimum volume of ethanol solution was added dropwise, under vigorous stirring, within one hour. After that, stirring was continued for additional 3 hours. Isolation of the final products was performed as follows:

- in the case of compounds **2a-f**, the resulted suspension was filtered off, washed with water (3 x 50 mL) to provide the crude product.
- in the case of compounds **3a-b** and **4a-e** the ethanol from the reaction mixture was evaporated in vacuum and the resulting aqueous suspension was filtered off and washed with water (3 x 50 mL) to provide the crude product.

After drying, the recrystallization from ethanol yielded the desired compounds as pure analytical samples.

2-(5-Amino-1,3,4-thiadiazol-2-ylthio)-1-(naphthalen-1-yl)ethanone

(**2a**). Synthesis was performed according to the general procedure, using 2-bromo-1-(naphthalen-1-yl)ethanone as the alkylating agent (2.48 g, 10 mmol). Yield (89%), white solid, mp 189-190 °C; ¹H NMR (DMSO-*d*₆, 500MHz, ppm) δ: 8.78 (m, 1H, ArH), 8.13-8.15 (m, 1H, ArH), 7.99-8.06 (m, 3H, ArH), 7.64-7.72 (m, 2H, ArH), 7.32 (s, 2H, -NH₂), 4.96 (s, 2H, CH₂); MS (EI, 70 eV) *m/z*: 302 (M+1). *Anal.* calcd. (%) for C₁₄H₁₁N₃O₂S: C, 55.79; H, 3.68; N, 13.94; S, 21.28. Found: C, 55.70; H, 3.74; N, 14.00; S, 21.25.

2-(5-Amino-1,3,4-thiadiazol-2-ylthio)-1-(4-chlorophenyl)ethanone

(2b). Synthesis was performed according to the general procedure, using 2-bromo-1-(4-chlorophenyl)ethanone as the alkylating agent (2.32 g, 10 mmol). Yield (87.5%), white solid, mp 192-193 °C; ¹H NMR (DMSO-*d*₆, 500MHz, ppm) δ: 8.02-8.04 (m, 2H, Ph), 7.63-7.65 (m, 2H, Ph), 7.32 (s, 2H, -NH₂), 4.80 (s, 2H, CH₂); MS (EI, 70 eV) *m/z*: 286 (M+1). *Anal.* calcd. (%) for C₁₀H₈ClN₃OS₂: C, 42.03; H, 2.82; N, 14.70; S, 21.28. Found: C, 41.95; H, 2.76; N, 14.91; S, 21.21.

2-(5-Amino-1,3,4-thiadiazol-2-ylthio)-1-phenylethanone **(2c).**

Synthesis was performed according to the general procedure, using 2-bromoacetophenone as the alkylating agent (1.98 g, 10 mmol). Yield (82%), white solid, mp 178-179 °C; ¹H NMR (DMSO-*d*₆, 500MHz, ppm) δ: 7.32 (s, 2H, -NH₂), 7.45-7.86 (m, 5H, Ph), 4.81 (s, 2H, CH₂); MS (EI, 70 eV) *m/z*: 252 (M+1). *Anal.* calcd. (%) for C₁₀H₉N₃OS₂: C, 47.79; H, 3.61; N, 16.72; S, 25.52. Found: C, 47.65; H, 3.70; N, 16.75; S, 25.55.

(5-Amino-1,3,4-thiadiazol-2-ylthio)-1-(4-ethoxyphenyl)ethanone

(2d). Synthesis was performed according to the general procedure, using 2-bromo-1-(4-methoxyphenyl)ethanone as the alkylating agent (2.28 g, 10 mmol). Yield (91%), white solid, mp 191-193 °C; ¹H NMR (DMSO-*d*₆, 500MHz, ppm) δ: 7.99-8.01 (m, 2H, Ph), 7.32 (s, 2H, -NH₂), 7.06-7.08 (m, 2H, Ph), 4.75 (s, 2H, CH₂), 3.86 (s, 3H, -CH₃); MS (EI, 70 eV) *m/z*: 282 (M+1). *Anal.* calcd. (%) for C₁₁H₁₁N₃O₂S₂: C, 46.96; H, 3.94; N, 14.93; S, 22.79. Found: C, 46.67; H, 4.06; N, 15.00; S, 22.89.

5-[2-(5-Amino-1,3,4-thiadiazol-2-ylthio)acetyl]-2-hydroxybenzamide **(2e).**

Synthesis was performed according to the general procedure, using 5'-(2-bromoacetyl)-2'-hydroxybenzamide as the alkylating agent (2.57 g, 10 mmol). Yield (95%), white solid, mp 235-257 °C; ¹H NMR (DMSO-*d*₆, 500MHz, ppm) δ: 7.49-8.01 (m, 3H, Ph), 7.34 (s, 2H, -NH₂), 7.20 (s, 2H, CONH₂), 5.85 (s, 1H, OH), 4.78 (s, 2H, CH₂); MS (EI, 70 eV) *m/z*: 311 (M+1). *Anal.* calcd. (%) for C₁₁H₁₀N₄O₃S₂: C, 42.57; H, 3.25; N, 18.05; S, 20.66. Found: C, 42.33; H, 3.30; N, 18.20; S, 20.68.

4-[2-(5-Amino-1,3,4-thiadiazol-2-ylthio)acetyl]benzotrile **(2f).**

Synthesis was performed according to the general procedure, using 4'-(2-bromoacetyl)benzo-nitrile (2.24 g, 10 mmol) as the alkylating agent. Yield (80%), white solid, mp 183 °C; ¹H NMR (DMSO-*d*₆, 500MHz, ppm) δ: 8.15-8.17 (m, 2H, Ph), 8.04-8.06 (m, 2H, Ph), 7.32 (s, 2H, -NH₂), 4.84 (s, 2H, CH₂); MS (EI, 70 eV) *m/z*: 277 (M+1). *Anal.* calcd. (%) for C₁₁H₈N₄OS₂: C, 47.81; H, 2.92; N, 20.27; S, 23.21. Found: C, 47.92; H, 2.80; N, 20.36; S, 23.11.

2-(5-Amino-1,3,4-thiadiazol-2-ylthio)acetamide (3a). Synthesis was performed according to the general procedure, using 2-chloroacetamide as the alkylating agent (0.93 g, 10 mmol), in the presence of a spatula tip of KI. Yield (84%), white solid, mp 213-215 °C; ¹H NMR (DMSO-*d*₆, 500MHz, ppm) δ: 7.34 (s, 2H, -NH₂), 7.18 (s, 2H, CONH₂), 4.82 (s, 2H, CH₂); MS (EI, 70 eV) *m/z*: 191 (M+1). *Anal.* calcd. (%) for C₄H₆N₄OS₂: C, 25.25; H, 3.18; N, 29.45; S, 33.71. Found: C, 25.12; H, 3.28; N, 29.58; S, 33.61.

Ethyl 2-(5-amino-1,3,4-thiadiazol-2-ylthio)acetate (3b). Synthesis was performed according to the general procedure, using ethyl bromoacetate as the alkylating agent (1.66 g, 10 mmol). Yield (74%), white solid, mp 83-84 °C; ¹H NMR (DMSO-*d*₆, 500MHz, ppm) δ: 7.36 (s, 2H, -NH₂), 4.74 (q, 2H, CH₂), 4.72 (s, 2H, CH₂), 1.19 (t, 3H, CH₃); MS (EI, 70 eV) *m/z*: 220 (M+1). *Anal.* calcd. (%) for C₆H₉N₃O₂S₂: C, 32.86; H, 4.14; N, 19.16; S, 29.25. Found: C, 33.04; H, 4.00; N, 20.00; S, 29.15.

5-Amino-2-(4-nitrobenzylthio)-1,3,4-thiadiazole (4a). Synthesis was performed according to the general procedure, using 4-nitrobenzyl chloride (1.71 g, 10 mmol) as the alkylating agent. Yield (82%), white solid, mp 165-166 °C; ¹H NMR (DMSO-*d*₆, 500MHz, ppm) δ: 7.75-8.30 (m, 4H, Ph), 7.28 (s, 2H, -NH₂), 4.83 (s, 2H, CH₂); MS (EI, 70 eV) *m/z*: 269 (M+1). *Anal.* calcd. (%) for C₉H₈N₄O₂S₂: C, 40.29; H, 3.01; N, 20.88; S, 23.90. Found: C, 40.40; H, 2.94; N, 20.74; S, 23.90.

5-Amino-2-[(2-phenylthiazol-4-yl)methylthio]-1,3,4-thiadiazole (4b).

Compound **1** (1.33 g, 10 mmol) was dissolved in ethanol (50 ml) and the reaction mixture was brought to reflux. Potassium carbonate was then added (1.2 eq), and an ethanolic solution of 4-(iodomethyl)-2-phenylthiazole (3 g, 10 mmol) was added dropwise during one hour, under vigorous stirring. Reflux was continued for additional 3 hours, and then the solvent was evaporated under vacuum. The obtained oily residue was extracted with CH₂Cl₂:Et₂O 1:1 (3 x 10 mL), and the solution was dried over anhydrous sodium sulfate and evaporated under vacuum. The final residue was purified by column chromatography, using silicagel G₂₅₄ and AcOEt:heptane (7:3) as eluent. Yield (76%), white solid, mp 71-73 °C; ¹H NMR (DMSO-*d*₆, 500MHz, ppm) δ: 7.92-7.94 (m, 2H, -NH₂), 7.48-7.50 (m, 5H, Ph), 5.41-5.44 (t, 1H, Thiazole-CH), 4.62-4.64 (dd, 2H, CH₂); MS (EI, 70 eV) *m/z*: 307 (M+1). *Anal.* calcd. (%) for C₁₂H₁₀N₄S₃: C, 47.03; H, 3.29; N, 18.28; S, 31.39. Found: C, 46.88; H, 3.35; N, 18.35; S, 31.44.

5-Amino-2-(methylthio)-1,3,4-thiadiazole (4c). Synthesis was performed according to the general procedure, using methyl iodide (1.42 g, 10 mmol) as the alkylating agent. Yield (79.6%), white solid, mp 179-180 °C; ¹H NMR (DMSO-*d*₆, 500MHz, ppm) δ: 7.32 (s, 2H, -NH₂), 2.60 (s, 3H, CH₃); MS (EI, 70 eV) *m/z*: 148 (M+1). *Anal.* calcd. (%) for C₃H₅N₃S₂: C, 24.47; H, 3.42; N, 28.54; S, 43.56. Found: C, 24.58; H, 3.36; N, 28.47; S, 43.58.

5-Amino-2-(butylthio)-1,3,4-thiadiazole (4d). Synthesis was performed according to the general procedure, using 1-bromobutane (1.36 g, 10 mmol) as the alkylating agent. Yield (76.7%), white solid, mp 121-122 °C; ¹H NMR (DMSO-*d*₆, 500MHz, ppm) δ: 7.34 (s, 2H, -NH₂), 2.79-2.82 (t, 2H, CH₂), 1.54-1.59 (quin, 2H, CH₂), 1.45-1.53 (sextet, 2H, CH₂), 0.89-0.92 (t, 3H, CH₃); MS (EI, 70 eV) *m/z*: 190 (M+1). *Anal.* calcd. (%) for C₆H₁₁N₃S₂: C, 38.07; H, 5.86; N, 22.20; S, 33.88. Found: C, 37.99; H, 5.78; N, 22.30; S, 33.94.

5-Amino-2-[2-(diethylamino)ethylthio]-1,3,4-thiadiazole (4e).

Synthesis was performed according to the general procedure, using 2-chloro-*N,N*-diethylethanamine (1.35 g, 10 mmol) as the alkylating agent. Yield (77%), white solid, mp 140-141 °C; ¹H NMR (DMSO-*d*₆, 500MHz, ppm) δ: 7.26 (s, 2H, -NH₂), 3.14 (t, 2H, CH₂), 2.68 (t, 2H, CH₂), 2.45-2.51 (q, 4H, CH₂), 0.92-0.95 (t, 6H, CH₃); MS (EI, 70 eV) *m/z*: 233 (M+1). *Anal.* calcd. (%) for C₈H₁₆N₄S₂: C, 41.35; H, 6.94; N, 24.11; S, 27.60. Found: C, 41.49; H, 6.86; N, 24.05; S, 27.62.

General procedure for the synthesis of Schiff bases

Technique 1 (classic):

A solution of 2-amino-5-mercapto-1,3,4-thiadiazole (0.665 g, 5 mmol) in absolute ethanol (20 mL) was warmed to reflux, when the corresponding aromatic aldehyde (5 mmol) and 3 drops of glacial acetic acid were added. The reaction mixture was stirred for 30 minutes at room temperature and then refluxed for 8 hours. The resulted solution was cooled at room temperature then evaporated to a small volume under reduced pressure. The final crystalline suspension was filtered off to provide the crude product. After drying, an additional recrystallisation from methanol:dichloromethane (9:1 v/v) yielded the desired Schiff bases as pure analytical samples.

Technique 2 (microwave):

To an ethanolic solution of 2-amino-5-mercapto-1,3,4-thiadiazole (0.266 g, 2 mmol), the corresponding aromatic aldehyde (2 mmol) and 3 drops of glacial acetic acid were added. The mixture was subjected to microwave for 20 minutes, at 100 °C and 150 W. The work-up of the reaction mixture was identical with that used in *Technique 1*.

5-(2,6-Dichlorobenzylideneamino)-1,3,4-thiadiazole-2-thiol (5a).

Synthesis was performed according to the general procedure (technique 1), using 2,6-dichlorobenzaldehyde (0.869 g, 5 mmol) as the aromatic aldehyde. Yield (70%), yellow solid, mp 280 °C; ¹H NMR (DMSO-*d*₆, 500MHz, ppm) δ: 10.00 (s, 1H, SH), 8.88 (s, 1H, OH), 7.11-7.34 (m, 3H, Ph); MS (EI, 70 eV) *m/z*: 290 (M+1). *Anal.* calcd. (%) for C₉H₅Cl₂N₃S₂: C, 37.25; H, 1.74; N, 14.48; S, 22.10. Found: C, 38.15 ; H, 1.53; N, 13.42; S, 20.52.

5-(4-Bromobenzylideneamino)-1,3,4-thiadiazole-2-thiol (5b) [29].

This compound was synthesized using the both techniques described in the general procedure: under reflux and under microwave irradiation, the last one showing better yields. 4-Bromobenzaldehyde (0.368 g, 2 mmol) was used as the aldehyde for the condensation reaction. Yield (66% - under reflux; 83% - microwave-assisted), yellow solid, mp 215 °C; ¹H NMR (DMSO-*d*₆, 500MHz, ppm) δ: 10.00 (s, 1H, SH), 8.74 (s, 1H, CH), 7.49-7.53 (m, 4H, Ph); MS (EI, 70 eV) *m/z*: 300 (M+1). *Anal. calcd.* (%) for C₉H₆BrN₃S₂: C, 36.01; H, 2.01; N, 14.00; S, 21.36. Found: C, 35.90; H, 2.10; N, 14.09; S, 21.29.

5-(4-Fluorobenzylideneamino)-1,3,4-thiadiazole-2-thiol (5c).

Synthesis was performed according to the general procedure (technique 1), using 4-fluorobenzaldehyde (0.620 g, 5 mmol) as the aromatic aldehyde. Yield (69%), yellow solid, mp 203 °C; ¹H NMR (DMSO-*d*₆, 500MHz, ppm) δ: 9.91 (s, 1H, SH), 8.92 (s, 1H, CH), 7.32-7.45 (m, 4H, Ph); MS (EI, 70 eV) *m/z*: 240 (M+1). *Anal. calcd.* (%) for C₉H₆FN₃S₂: C, 45.17; H, 2.53; N, 17.56; S, 26.80. Found: C, 45.10; H, 2.40; N, 17.65; S, 26.91.

5-(4-Methoxybenzylideneamino)-1,3,4-thiadiazole-2-thiol (5d) [30].

Synthesis was performed according to the general procedure (technique 1), using 4-methoxybenzaldehyde (0.680 g, 5 mmol) as the aromatic aldehyde. Yield (67%), yellow solid, mp 199 °C; ¹H NMR (DMSO-*d*₆, 500MHz, ppm) δ: 10.03 (s, 1H, SH), 9.00 (s, 1H, OH), 6.72-7.20 (m, 4H, Ph), 3.89 (s, 3H, CH₃); MS (EI, 70 eV) *m/z*: 252 (M+1). *Anal. calcd.* (%) for C₁₀H₉N₃O₂S₂: C, 47.79; H, 3.61; N, 16.72; S, 25.52. Found: C, 47.92; H, 3.51; N, 16.83; S, 25.44.

3-[[5-Sulfanyl-1,3,4-thiadiazol-2-yl]imino]methyl]-4H-chromen-4-one (6a). This compound was synthesized using the both techniques described in the general procedure: under reflux and under microwave irradiation, the last one showing better yields. 4-oxo-4*H*-chromene-3-carbaldehyde (0.348 g, 2 mmol) was used as the aromatic aldehyde. Yield (68% - under reflux; 86% - microwave-assisted), yellow solid, mp 230 °C; ¹H NMR (DMSO-*d*₆, 500MHz, ppm) δ: 9.98 (s, 1H, SH), 8.90 (s, 1H, CH), 8.20 (s, 1H, Chromone-CH), 7.57-8.15 (m, 4H, Chromone-CH); MS (EI, 70 eV) *m/z*: 290 (M+1). *Anal. calcd.* (%) for C₁₂H₇N₃O₂S₂: C, 49.81; H, 2.44; N, 14.52; S, 22.16. Found: C, 49.74; H, 2.50; N, 14.60; S, 22.09.

6-Methyl-3-[[5-sulfanyl-1,3,4-thiadiazol-2-yl]imino]methyl]-4H-chromen-4-one (6b). This compound was synthesized according to the general procedure in both ways: under reflux and under microwave irradiation. The aromatic aldehyde used was 6-methyl-4-oxo-4*H*-chromene-3-carbaldehyde (0.940 g, 5 mmol – under reflux 0.376 g, 2 mmol – microwave-assisted) Yield (69% - under reflux; 86% - microwave-assisted), yellow solid,

mp 260 °C; ¹H NMR (DMSO-*d*₆, 500MHz, ppm) δ: 10.09 (s, 1H, SH), 9.03 (s, 1H, CH), 8.26 (s, 1H, Chromone-CH), 7.42-7.90 (m, 3H, Chromone-CH), 2.73 (s, 3H, CH₃); MS (EI, 70 eV) *m/z*: 304 (M+1). *Anal.* calcd. (%) for C₁₃H₉N₃O₂S₂: C, 51.47; H, 2.99; N, 13.85; S, 21.14. Found: C, 51.35; H, 3.05; N, 13.98; S, 21.07.

6-Chloro-3-[[5-sulfanyl-1,3,4-thiadiazol-2-yl]imino]methyl]-4H-chromen-4-one (6c). This compound was synthesized using the both techniques described in the general procedure: under reflux and under microwave irradiation, the last one showing better yields. 6-chloro-4-oxo-4H-chromene-3-carbaldehyde (0.416 g, 2 mmol) was used as the aromatic aldehyde. Yield (65% - under reflux; 82% - microwave-assisted), yellow solid, mp 245 °C; ¹H NMR (DMSO-*d*₆, 500MHz, ppm) δ: 10.11 (s, 1H, SH), 8.97 (s, 1H, CH), 8.22 (s, 1H, Chromone-CH), 7.36-7.60 (m, 3H, Chromone-CH); MS (EI, 70 eV) *m/z*: 324 (M+1). *Anal.* calcd. (%) for C₁₂H₆ClN₃O₂S₂: C, 44.51; H, 1.87; N, 12.98; S, 19.81. Found: C, 44.70; H, 1.78; N, 12.92; S, 19.77.

6,8-Dichloro-3-[[5-sulfanyl-1,3,4-thiadiazol-2-yl]imino]methyl]-4H-chromen-4-one (6d). The synthesis was performed according to the general procedure, using the both techniques: under reflux and under microwave irradiation. 6,8-Dichloro-4-oxo-4H-chromene-3-carbaldehyde (0.484 g, 2 mmol – microwave-assisted) was used as the aromatic aldehyde. Yield (63% - under reflux; 80% - microwave assisted), yellow solid, mp 242 °C; ¹H NMR (DMSO-*d*₆, 500MHz, ppm) δ: 10.10 (s, 1H, SH), 9.05 (s, 1H, CH), 8.25 (s, 1H, Chromone-CH), 7.98 (d, 1H, Chromone-CH), 7.81 (d, 1H, Chromone-CH); MS (EI, 70 eV) *m/z*: 358 (M+1). *Anal.* calcd. (%) for C₁₂H₅Cl₂N₃O₂S₂: C, 40.23; H, 1.41; N, 11.73; S, 17.90. Found: C, 40.32; H, 1.35; N, 11.78; S, 17.82.

5-[[2-Phenyl-1,3-thiazol-4-yl]methylidene]amino]-1,3,4-thiadiazole-2-thiol (7a). Synthesis was performed according to the general procedure (technique 1), using 2-phenylthiazole-4-carbaldehyde (0.945 g, 5 mmol) as the aromatic aldehyde. Yield (70%), yellow solid, mp 244 °C; ¹H NMR (DMSO-*d*₆, 500MHz, ppm) δ: 10.04 (s, 1H, SH), 9.05 (s, 1H, CH), 7.82 (s, 1H, Thiazole-CH), 7.28-7.43 (m, 5H, Ph); MS (EI, 70 eV) *m/z*: 305 (M+1). *Anal.* calcd. (%) for C₁₂H₈N₄S₃: C, 47.35; H, 2.65; N, 18.40; S, 31.60. Found: C, 47.28; H, 2.75; N, 18.32; S, 31.65.

5-[[Thiophen-2-ylmethylidene]amino]-1,3,4-thiadiazole-2-thiol (7b). Synthesis was performed according to the general procedure (technique 1), using thiophene-2-carbaldehyde (0.560 g, 5 mmol) as the aromatic aldehyde. Yield (65%), yellow solid, mp 195 °C; ¹H NMR (DMSO-*d*₆, 500MHz, ppm) δ: 10.01 (s, 1H, SH), 9.02 (s, 1H, CH), 7.00-7.40 (m, 3H, Thiophene-CH); MS (EI, 70 eV) *m/z*: 228 (M+1). *Anal.* calcd. (%) for C₇H₅N₃S₃: C, 36.98; H, 2.22; N, 18.48; S, 42.32. Found: C, 36.85; H, 2.32; N, 18.56; S, 42.26.

Antimicrobial activity assay

For antibacterial testing, Mueller-Hinton agar medium was used. For antifungal testing Mueller-Hinton medium supplemented with 2% glucose (providing adequate growth of yeasts) and 0.5 mg/mL methylene blue (providing a better definition of the inhibition zone diameter) was used. The inoculum was prepared by suspending five representative colonies, obtained from an 18–24 h culture on non-selective nutritive agar medium, in sterile distilled water. The cell density was adjusted to the density of a 0.5 McFarland standard by measuring the absorbance in a spectrophotometer at a wavelength of 530 nm and adding sterile distilled water as required (corresponding to a population of 1.5×10^6 CFU/mL). Six-millimeter diameter wells were cut from the agar using a sterile cork-borer, and a predetermined volume of each compound solution was delivered into the wells. A sterile swab was soaked in suspension and then the Mueller-Hinton agar plates were inoculated by streaking the entire surface. After drying for 10–15 minutes, the six millimeter diameter wells were inoculated with 50 μ L from 10 mg/mL solution in dimethyl sulfoxide (DMSO) (Merck, Germany) of each compound (50 μ g/well). Ciprofloxacin (50 μ g/well) and Fluconazole (50 μ g/well) were used as standard drugs. The plates were incubated at 35°C. Zone diameters were measured to the nearest whole millimeter at a point in which there will be no visible growth after 24 – 48 h. The solvent used for the preparation of the newly synthesized compound solutions, DMSO did not show inhibition against the tested bacterial and fungal strains. Results were obtained in duplicate.

ACKNOWLEDGEMENTS

This research was financed by The Executive Agency for Higher Education Research Development and Innovation Funding – UEFISCDI, Romania, on the Contract 210/2014 – Project PN-II-PT-PCCA-2013-4-2075 and by the Iuliu Hațieganu University of Medicine and Pharmacy, Cluj-Napoca, Romania, through the internal grant no. 22714/16/06.10.2011.

REFERENCES

1. S.F. Barbuceanu, G. Saramet, G.L. Almajan, C. Draghici, F. Barbuceanu, G. Bancescu, *European Journal of Medicinal Chemistry*, **2012**, *49*, 417.
2. J. Davies, D. Davies, *Microbiology and Molecular Biology Reviews*, **2010**, *74*, 417.
3. X. Chai, J. Zhang, Y. Cao, Y. Zou, Q. Wu, D. Zhang, et al., *Bioorganic and Medicinal Chemistry Letters*, **2011**, *21*, 686.

4. C. Sheng, X. Che, W. Wang, S. Wang, Y. Cao, J. Yao, et al., *European Journal of Medicinal Chemistry*, **2011**, *46*, 1706.
5. L. Fernández, E. Breidenstein, R. Hancock, *Drug Resistance Updates*, **2011**, *14*, 1.
6. R. Moellering Jr., *International Journal of Antimicrobial Agents*, **2011**, *37*, 2.
7. U. Kalidhar, A. Kaur, *Research Journal of Pharmaceutical, Biological and Chemical Sciences*, **2011**, *2*, 1091.
8. A.K. Singh, G. Mishra, K. Jyoti, *Journal of Applied Pharmaceutical Science*, **2011**, *01*, 44.
9. N. Siddiqui, P. Ahuja, W. Ahsan, S.N. Pandeya, S. Alam, *Journal of Chemical and Pharmaceutical Research*, **2009**, *1*, 19.
10. H. Bhuvra, D. Sahua, B. Shah, D. Modi, M. Patel, *Pharmacologyonline*, **2011**, *1*, 528.
11. H. Ameen, A. Qasir, *Iraqi Journal of Pharmaceutical Sciences*, **2012**, *21*, 98.
12. N. Kushwaha, S. Kushwaha, A.K. Rai, *International Journal of ChemTech Research*, **2012**, *4*, 517.
13. G. Mishra, A. Singh, K. Jyoti, *International Journal of ChemTech Research*, **2011**, *3*, 1380.
14. A.T. El-Sayed, A.M. El-Kazak, *European Journal of Chemistry*, **2010**, *1*, 6.
15. J.K. Gupta, R. Dudhey, P.K. Sharma, *Medichemonline*, **2010**, *1*, 1.
16. S. Jalhan, A. Jindal, A. Gupta, J. Hemra, *Asian Journal of Pharmaceutical and Clinical Research*, **2012**, *5*, 199.
17. S. Jazayeri, M.H. Moshafi, L. Firoozpour, S. Emami, S. Rajabalian, M. Haddad, et al., *European Journal of Medicinal Chemistry*, **2009**, *44*, 1205.
18. V. Padmavathi, G. Sudhakar, A. Padmaja, P. Kondaiyah, A. Shazia, *European Journal of Medicinal Chemistry*, **2009**, *44*, 2106.
19. N. Siddiqui, M.S. Alam, *Biosciences Biotechnology Research Asia*, **2009**, *6*, 261.
20. A. Dhakad, M.C. Sharma, S.C. Chaturvedi, S. Sharma, *Digest Journal of Nanomaterials and Biosciences*, **2009**, *4*, 275.
21. F. Poorrajab, S.K. Ardestani, S. Emani, M. Behrouzi-Fardmoghadam, A. Shafiee, A. Foroumadi, *European Journal of Medicinal Chemistry*, **2009**, *44*, 1758.
22. A. K. Gadad, M. B. Palkar, K. Anand, M. N. Noolvi, T. S. Boreddy, J. Wagwade, *Bioorganic Medicinal Chemistry*, **2008**, *16*, 276.
23. P. Kamotra, A. Gupta, R. Gupta, *Indian Journal of Chemistry-Section B*, **2007**, *46*, 980.
24. B. Sharma, A. Verma, S. Prajapati, U.K. Sharma, *International Journal of Medicinal Chemistry*, **2013**, doi.org/10.1155/2013/348948.
25. B. Ahamad, M. Yusuf, *Indian Journal of Chemistry-Section B*, **2010**, *49*, 241.
26. K.B. Zheng, J. He, J. Zhang, *Chinese Chemistry Letters*, **2008**, *19*, 1281.
27. C.M. da Silva, D.L. da Silva, L. Modolo, R. Alves, M. de Resende, C. Martins, et al., *Journal of Advanced Research*, **2011**, *2*, 1.
28. A. Pandey, D. Dewangan, S. Verma, A. Mishra, R. Dubey, *International Journal of ChemTech Research*, **2011**, *3*, 178.
29. S.M. Alwan, *Molecules*, **2012**, *17*, 1025-1038.

30. I.K. Al-Shibani, N.K.E. Al-Yonis, A.H. Al-Dujaili, *National Journal of Chemistry*, **2006**, *21*, 94-101.
31. I. Simiti, O. Oniga, *Monatshefte fur chemie*, **1996**, *127*, 733.
32. O. Oniga, I. Grosu, S. Mager, I. Simiti, *Monatshefte fur chemie*, **1998**, *129*, 661.

*Dedicated to Professor Mircea Diudea
on the Occasion of His 65th Anniversary*

SYNTHESIS AND CHARACTERIZATION OF LEAD-FREE SODIUM NIOBATE POWDER

PAULINA VLAZAN^a, PAULA SFIRLOAGA^a, FLORINA STEFANIA RUS^{b,*}

ABSTRACT. Sodium niobate (NaNbO_3) fine powders were synthesized by hydrothermal method using ammonium niobate (V) oxalate hydrate ($\text{C}_4\text{H}_4\text{NNbO}_9 \times \text{H}_2\text{O}$), sodium hydroxide (NaOH) and sodium citrate hydrate ($\text{C}_6\text{H}_9\text{Na}_3\text{O}_9$) as precursors. The samples were characterized by X-Ray diffraction (XRD), scanning electron microscopy (SEM), AFM (Atomic Force Microscopy), UV-VIS spectroscopy and Fourier Transform Infrared Spectroscopy (FTIR).

X-ray diffraction for powder obtained by hydrothermal method revealed three phases mixture (NaNbO_3 , Nb_2O_5 , $\text{Na}_2\text{C}_2\text{O}_4$). In order to obtain a material with perovskite structure, the powder was treated for 6 h at 600°C . After calcination, the X-ray powder diffraction (XRD) patterns shown reflections of a pure cubic structure (space group $Pm-3m$) with lattice parameters ($a=b=c=3.909\text{\AA}$) comparable to those reported in the literature. The average particle sizes estimated by SEM image were 2-3 micrometers.

Keywords: *sodium niobate, hydrothermal method, X-ray diffraction, scanning electron microscopy*

INTRODUCTION

Photocatalysis is a promising technology with various applications, including water purification [1]. TiO_2 photocatalyst is the most commonly used, however, it is an effective material under UV light. Enormous efforts have been made to develop photocatalysts that have efficient photocatalytic activity in

^a *National Institute of Research-Development for Electrochemistry and Condensed Matter Timisoara, Plautius Andronescu str., 1 no., Timisoara, Romania*

^b *National Institute of Research-Development for Electrochemistry and Condensed Matter Timisoara, Dr. Aurel Paunescu Podeanu str., no. 144, 300569, Timisoara, Romania*

* *Corresponding Author: rusflorinastefania@gmail.com*

the visible range, either by modifying titanium dioxide or by developing semiconductors that show photocatalytic properties [2]. Semiconductors based on niobium oxide have received much attention in the recent years because of its photocatalytic promising characteristics, such as toxicity, chemical inertness and high stability under irradiation by the light. The most important material based on niobium oxide is probably ANbO_3 , where $A = \text{K} / \text{Na} / \text{Li}$ because it has a variety of interesting and useful properties, including the photocatalytic, piezoelectric, optical properties of ferroelectric, etc. [3]. NaNbO_3 has been prepared by various methods, such as hydrothermal synthesis [4], the sol-gel process [5], and solid-state method [6]. Among the methods of preparation, the hydrothermal synthesis, which involves the heating of Nb_2O_5 in different concentrations of KOH at $120\text{-}200^\circ\text{C}$ seems to be the most convenient and versatile. Depending on the reaction conditions, different sizes and shapes can be obtained, including micro- and nanoparticles, wires and blocks. Sodium niobate (NaNbO_3) have attracted considerable interest among scientists because of its ferroelectrics good property on high temperature, piezoelectric properties, thanks to excellent photorefractive properties and a moderate dielectric constant [7].

In general, the hydrothermal synthesis of nanocrystalline materials consists of introduction into a closed container (i.e., autoclave) of precursors and heating until the temperature and pressure generated by heating lead to the crystallization of the substances inside. Judicious control of temperature, pressure, duration of the process, the degree of filling of the autoclave, the concentration of the precursors allow to obtain nanocrystals with the size and type of crystal desired [8]. This method has many advantages, e.g., the product has a homogeneous crystallinity and it can be produced at a relatively low temperature (less than 150°C). The most important feature of the method is that it allows the reduction of the degree of particle agglomeration, small size distribution, and the control of morphology of the phase.

The crystal growth or material processing under hydrothermal conditions requires a pressure vessel capable of withstanding the high temperature and pressure and corrosive action of a solvent, as provided by the autoclave. Several Niobium combinations have been synthesized by hydrothermal method [9, 10].

The synthesis of nanotubes has become one of the most important research topics in nanotechnology and various materials have been produced in recent decades [11]. The successful titanium nanotubes synthesis is one of the examples of such intense research efforts. Kasuga et al. prepared TiO_2 nanotubes by hydrothermal method [12]. Zhang et al. reported preparation of potassium hexatitanate ($\text{K}_2\text{Ti}_6\text{O}_{13}$) using microwave activation [13]; this way is very attractive because of its short response time and low power consumption compared to conventional methods.

Ghamsari et al. reported the synthesis of potassium titanate by mixed method, sol-gel and hydrothermal [14]. Subohi et al. synthesized bismuth titanate with urea through combustion method; the product shows ferroelectric and dielectric properties [15].

RESULTS AND DISCUSSION

In our study we obtained sodium niobate (NaNbO_3) fine powders by hydrothermal method at 220°C and post annealing at 600°C in order to get a unique phase. Precursors used in this synthesis were ammonium niobate (V) oxalate hydrate ($\text{C}_4\text{H}_4\text{NNbO}_9 \cdot x\text{H}_2\text{O}$), sodium hydroxide (NaOH) and sodium citrate hydrate ($\text{C}_6\text{H}_9\text{Na}_3\text{O}_9$).

Structure of the sample phases were investigated by X-ray diffraction (XRD) using PANalytical X'Pert PRO MPD diffractometer with $\text{Cu K}\alpha$ radiation, $\lambda = 1.5406 \text{ \AA}$, 2θ -step of 0.016° from 15° to 80° . In the prelevated samples, three mixed phases were observed: NaNbO_3 , Nb_2O_5 , and $\text{Na}_2\text{C}_2\text{O}_4$. (Figure 1 a). In order to obtain a material with perovskite structure, the powder was annealed for 6 h at 600°C . After calcination, the X-ray powder diffraction (XRD) patterns shown reflections of a pure cubic structure (space group $Pm-3m$) with lattice parameters $a=b=c=3.909\text{\AA}$. Table 1 lists the extracted parameters of this structure.

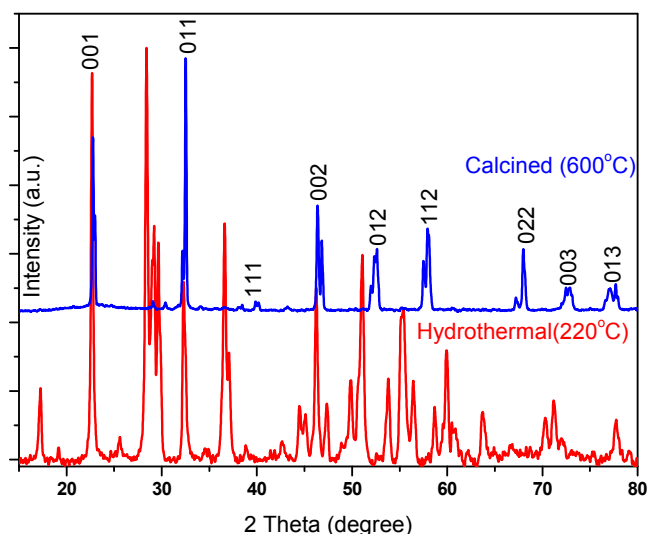


Figure 1 a). X-ray diffraction of NaNbO_3 obtained by hydrothermal method at 220°C and after thermal treatment at 600°C

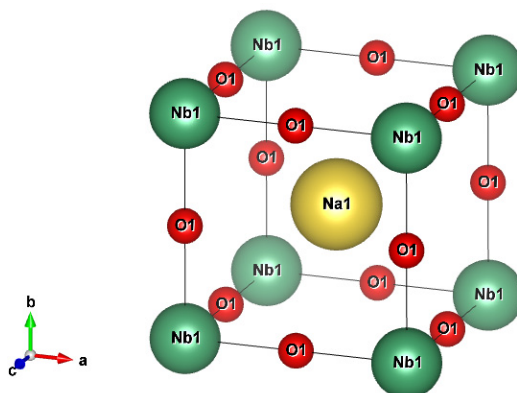


Figure 1 b). The structure of NaNbO_3 obtained by a hydrothermal method after thermal treatment

Table 1. The structure parameters of NaNbO_3 obtained by a hydrothermal method

Formula sum	$\text{Na}_{1.00}\text{Nb}_{1.00}\text{O}_{3.00}$
Formula mass/ g/mol	163.8944
Density (calculated)/ g/cm ³	4.5569
Weight fraction/ %	100.000000
Space group (No.)	$P m -3 m (221)$
Lattice parameters	
a/ Å	3.909(2)
b/ Å	3.909(2)
c/ Å	3.909(2)
V/ 10 ⁶ pm ³	59.71494

In order to study the size and shape of particles we used SEM technique. Figure 2 shows the micrograph of NaNbO_3 powder obtained by hydrothermal method at 220°C.

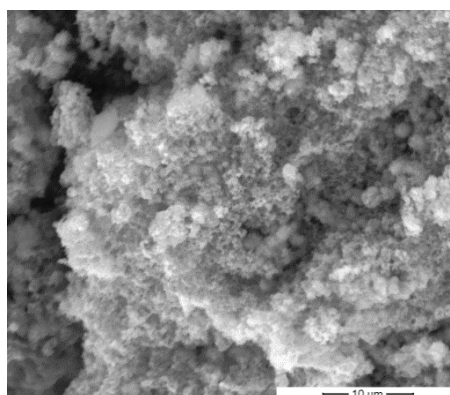


Figure 2. SEM images of mixed phases of NaNbO_3 powder obtained by hydrothermal method at 220°C

SEM images of the single phase of NaNbO_3 powder, as obtained after annealing treatment at 600°C , are illustrated in Figure 3. The average size of particles with a cubic shape was estimated around 2-3 micrometers. The EDX signal of this single phase is shown in Figure 4. The presence of all elements: Na, Nb and Oxygen have been confirmed.

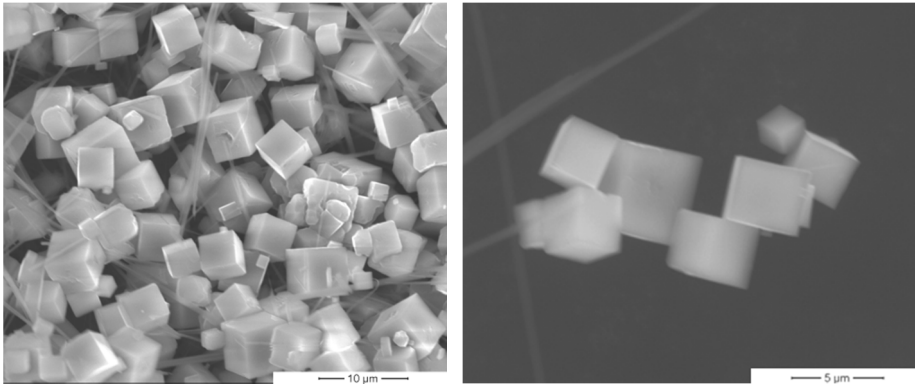


Figure 3. SEM images of single phase of NaNbO_3 powder as obtained and thermal treatment at 600°C

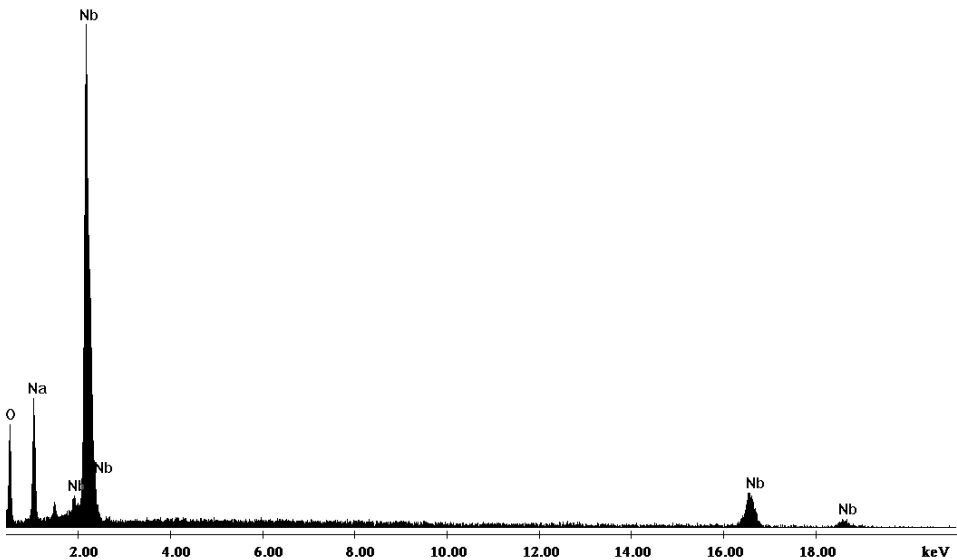


Figure 4. EDX images of single phase of NaNbO_3 powder as obtained after the thermal treatment at 600°C

The topography of NaNbO_3 was observed by Atomic force microscopy (Nanosurf® EasyScan 2 - Figure 5).

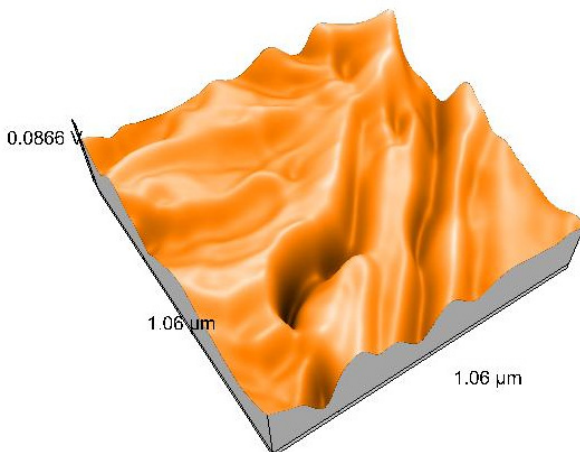


Figure 5. 3D topography of NaNbO_3 powder

The optical band gaps UV-VIS spectrometer was used in order to get the optical properties of NaNbO_3 powder. The pure NaNbO_3 sample shows only one intense absorption with steep edges in the UV region (Figure 6). The absorption and transmission spectra were recorded by LAMBDA 950 UV/Vis/NIR spectrophotometer.

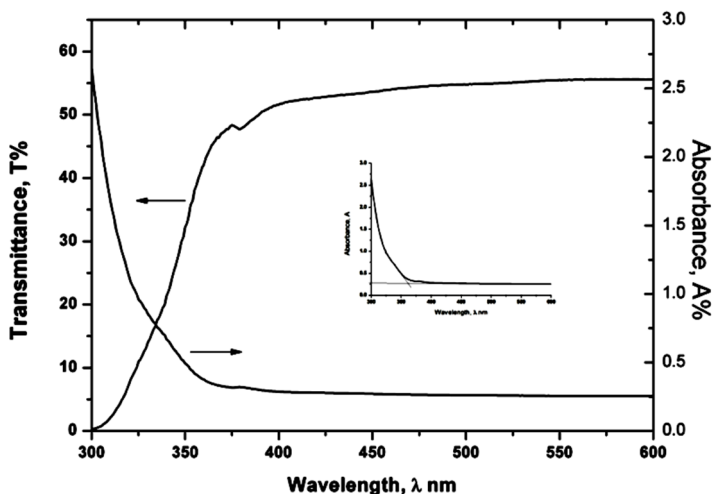


Figure 6. The absorption and transmission spectra of NaNbO_3 , inset is represented the estimate band gap of NaNbO_3 .

The band gap of NaNbO_3 is evaluated around 3.45 eV (inset of Figure 6), compared with those reported in literature [1].

IR spectrum was recorded on an FTIR spectrometer Shimadzu Prestige in the mid-IR range of 500-4000 wavenumbers operated in the transmittance mode, the KBr pellet technique.

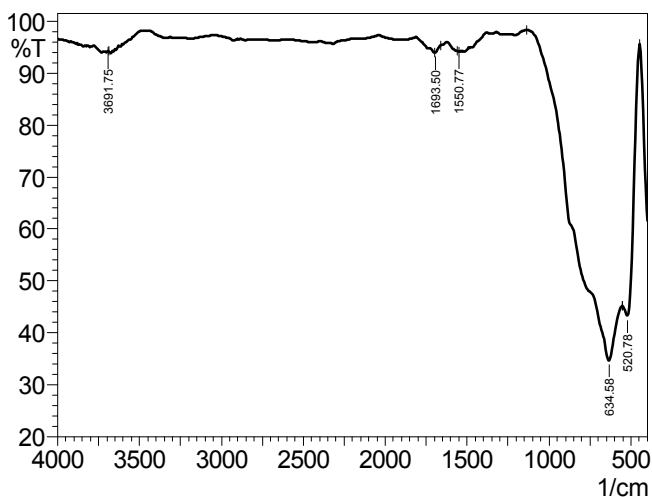


Figure 7. FT-IR spectra of the obtained NaNbO_3 powder after thermal treatment

Figure 7 shows the FT-IR spectrum of the obtained NaNbO_3 powder. The sharp peaks at 634 cm^{-1} and 520 cm^{-1} correspond to the vibrations of the Na-Niobate framework including Nb-O stretching, Nb-O-Nb bending and lattice vibrations. The spectrum also shows important signals such as: 3691 cm^{-1} (O-H stretching), 1693 cm^{-1} (C=O stretching vibrations), 1550 cm^{-1} [16]. The bands located at 1693 cm^{-1} and 1550 cm^{-1} can be assigned to the antisymmetric stretching and symmetric vibrations of carbon-oxygen bonds from COO- groups of the residual citric acid [17].

CONCLUSIONS

In this paper, we presented the synthesis of sodium niobate powder through hydrothermal method using $(\text{C}_4\text{H}_4\text{NNbO}_9 \times \text{H}_2\text{O})$, sodium hydroxide (NaOH) and sodium citrate hydrate $(\text{C}_6\text{H}_9\text{Na}_3\text{O}_9)$ as precursors. The particle size of sodium niobate was 2-3 micrometers with an estimated bandgap of 3.45 eV. The formation of NaNbO_3 phase is further confirmed by FT-IR analysis.

EXPERIMENTAL SECTION

Sodium niobate (NaNbO_3) powder was synthesized by the hydrothermal method, followed by annealing at 600°C to achieve a perovskite phase structure. The precursors used for synthesis were $\text{C}_4\text{H}_4\text{NNbO}_9 \cdot \text{H}_2\text{O}$ (ammonium niobate (V) oxalate hydrate), $\text{C}_6\text{H}_5\text{O}_7\text{Na}_3 \cdot 2 \text{H}_2\text{O}$ (sodium citrate) and NaOH (sodium hydroxide) 7M solution.

Niobate and citrate salts were dissolved in distilled water in a determined molar ratios and then were precipitated with 7M NaOH solution under strong stirring to obtain a homogeneous suspension. The suspension was introduced into the autoclave by teflon with steel jacketed to ensure a good seal. The autoclave was held at 220°C for 10 hours. After autoclaving, particle separation was made by decantation and filtration. The precipitate was washed on the filter paper with distilled water and ethyl alcohol before being dried in an oven at 80°C for 2 hours. Powder characterization was made by: X-ray diffraction (XRD), scanning electron microscopy (SEM). The mixture of phases of the primary powder was heated at 600°C for 6 hours. After calcination, the resulted single phase was characterized by XRD, SEM / EDAX, AFM, UV-VIS and FTIR.

Structure of the phases were investigated by X-ray diffraction (XRD) using PANalytical X'Pert PRO MPD diffractometer with $\text{Cu K}\alpha$ radiation, $\lambda = 1.5406 \text{ \AA}$, 2θ -step of 0.016° from 15° to 80° .

The morphology and quantitative analysis of the powders were investigated by SEM / EDAX using an *Inspect S* PANalytical SEM / EDX.

The topography of NaNbO_3 was studied by Atomic force microscopy type Nanosurf® EasyScan 2.

The absorption and transmission spectra was recorded with a LAMBDA 950 UV/Vis/NIR spectrophotometer.

IR spectra were recorded on an FTIR spectrometer Shimadzu Prestige in the mid-IR range of 500-4000 wavenumbers operated in the transmittance mode, the KBr pellet technique.

ACKNOWLEDGMENTS

Partnerships Program - Applied Research Collaborative Projects (PCCA) – 177/2014.

The authors would like to thank Mihaela Bîrdeanu for AFM pictures

REFERENCES

1. P. Li, H. Abe and J. Ye, *International Journal of Photoenergy*, **2014**, 2014, 1.
2. M.R. Hoffmann, S.T. Martin, W. Choi, D.W. Bahnemann, *Chemical Review* **1995**, 95, 69.
3. Y. Saito, H. Takao, T. Tani, T. Nonoyama, K. Takatori, T. Homma, T. Nagaya, M. Nakamura. *Nature*, **2004**, 432, 84.
4. H. Hayashi, Y. Hakuta, Y. Kurata, *Journal of Materials Chemistry*, **2004**, 14, 2046.
5. M.M. Amimi, M.D. Sacks, *Journal of the American Ceramic Society*, **1991**, 74, 53.
6. S. Yamazoe, T. Kawawaki, K. Shibata, K. Kato, T. Wada, *Chemistry of Materials*, **2011**, 23, 4498.
7. E. Ringgaard, T. Wurlitzer, *Journal of the European Ceramic Society*, **2005**, 25, 2701.
8. N. Drnovšek, N. Daneu, A. Rečnik, M. Mazaj, J. Kovač, S. Novaka, *Surface and Coatings Technology Journal*, **2009**, 203, 1462.
9. Y. Min, F.-J. Zhang, W. Zhao, F.C. Zheng, Y.C. Chen, Y.G. Zhang, *Chemical Engineering Journal*, **2012**, 209, 215.
10. G.K. Zhang, J.L. Yang, S.M. Zhang, Q. Xiong, B.B. Huang, J.T. Wang, W.Q. Gong, *Journal of Hazardous Materials*, **2009**, 172, 986.
11. Chung-Kung Lee, Kuen-Song Lin, Chian-Fu Wu, Meng-Du Lyu, Chao-Chun Lo, *Journal of Hazardous Materials*, **2008**, 150, 494.
12. T. Kasuga, M. Hiramatsu, A. Hoson, T. Sekino, K. Niihara, *Advanced Materials*, **1999**, 11, 1307.
13. J.Zhang, Y.Wang, J. Yang, J. Chen, Z. Zhang, *Materials Letters*, **2006**, 60, 3015.
14. M. Sasani Ghamsari, S. Rahim, S. Radiman, J. Hasani, *Materials Letters*, **2012**, 85, 81.
15. O. Subohi, G.S. Kumar, M.M. Malik, R. Kurchania, *Optik*, **2014**, 125, 820.
16. T.V. Mathew, S. Kuriakose, *Journal of Advanced Ceramics*, **2013**, 2, 11.
17. S. Coste, A. Lecomte, P. Thomas, T. Merle-Mejean, J.C. Champarnaud-Mesjard, *Journal of Sol-Gel Science and Technology*, **2007**, 41, 79.

*Dedicated to Professor Mircea Diudea
on the Occasion of His 65th Anniversary*

CATALYTIC REDUCTION OF 4-NITROPHENOL USING NEW Cu(0)/AROMATIC CORE DENDRIMER COMPLEXES

FÜSTÖS MELINDA-EMESE^a, MIRCEA V. DIUDEA^a,
KATONA GABRIEL^{a,*}

ABSTRACT. Dendrimers are macromolecules with well-defined shape and size, being typically symmetric around the core. A new class of aromatic core 0 generation dendrimers and their Cu(0) complexes were synthesized.

The obtained adducts were tested as catalysts for reduction of 4-nitrophenol. Higher catalytic activity was observed in each case compared to Cu(0) prepared in situ.

Keywords: dendrimer complexes, aromatic core, catalyst, Cu(0), *p*-nitrophenol

INTRODUCTION

Dendrimers chemistry began in 1978 with the synthesis of highly branched macromolecules [1] followed by the synthesis of the first PAMAM dendrimer reported in 1985 by Tomalia's group [2]. Due to their symmetrical shape and controlled size, dendrimers are excellent candidates for dendrimer-based nanocatalysts by binding metal nanoparticles, which leads to mono or bimetallic complexes. It has been reported that bimetallic Cu(II) and Pd(II) complexes with nitrile group derivatized dendrimers show high catalytic activity in case of oxidation reactions [3]; poly(amidoamine) and polypropylene imine (PPI) dendrimer–Pd complexes proved to be suitable for selective hydrogenation [3]. Metal nanocatalysts are also widely used in different oxidation [4], reduction [5] or dehydrogenation reactions [6].

^a Babeş-Bolyai University, Faculty of Chemistry and Chemical Engineering, Arany János Street 11, 400028, Cluj-Napoca, Romania

* Corresponding Author: gabik@chem.ubbcluj.ro

Phenols and nitrophenol derivatives represent an important class of organic pollutants found mostly in industrial wastewater among dyes. It is well-known that a high number of aromatic contaminants have proven to be carcinogenic and mutagenic in nature [7]. PNP (*p*-nitrophenol) is a frequent byproduct from the pesticides production. Also, it results from pharmaceutical and petrochemical industries. The processes focused on nitrophenol degradation include catalysis among chemical- and photochemical oxidation or biological degradation, respectively [8].

Catalytic reduction of *p*-nitrophenol to *p*-aminophenol (PAP) using NaBH_4 as reducing agent in presence of $\text{Cu}(0)$ nanoparticles became a model reaction due to the low cost of the catalyst [9]. Literature data reveals also the use of Pt, Au [10], Pd [11] and Ag [12] noble metal nanoparticles in the catalytic reduction process. In order to improve the catalytic activity thus to decrease the reaction time required for the transformation of the PNP, the copper nanoparticles are deposited on different surfaces like porous silicon powder [13], silicon nanowires [14] or mesoporous silica [15] and used in heterogeneous catalysis.

Herein is presented an alternative method for homogenous catalysis using new aromatic core zero generation dendrimers as support for the metallic copper nanoparticles.

RESULTS AND DISCUSSION

For the catalytic activity test of the obtained *2a-Cu*, *2b-Cu*, *2c-Cu*, *2d-Cu* complexes, two aqueous solutions: 1.2 mM PNP and 15 mM NaBH_4 were prepared. As a reference, the absorbance spectra of the *p*-nitrophenol was recorded. This revealed a maximum at 318 nm. When PNP was mixed with the reducing agent (NaBH_4), the absorbance maximum was red shifted to 401 nm (Figure 1). PAP reveals an absorbance maximum at 300 nm.

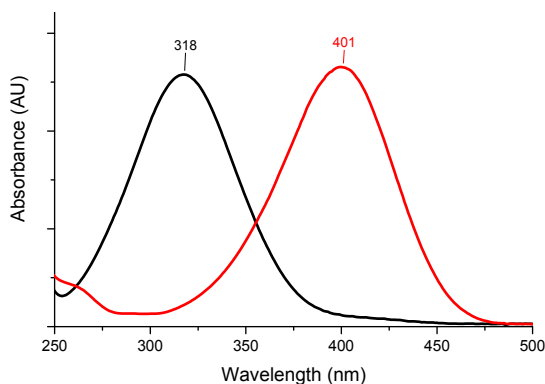


Figure 1. Absorbance spectra of PNP (black trace), PNP+ NaBH_4 (red trace)

In order to calculate the molar extinction coefficient (ϵ) by Lambert-Beer law ($A = \epsilon \cdot c \cdot l$), the absorbance at 401 nm of known PNP concentration solutions was measured. In all cases, the samples contain 1 mL 15 mM NaBH₄. The final volume of each sample was 2.7 mL, the cuvette diameter was 1 cm. Figure 2 presents the obtained standard calibration curve. The value of the molar extinction coefficient was determined from the fitted linear equation as being 17.214 L·mmol⁻¹·cm⁻¹. The appearance of the prepared catalysts is shown in Figure 3.

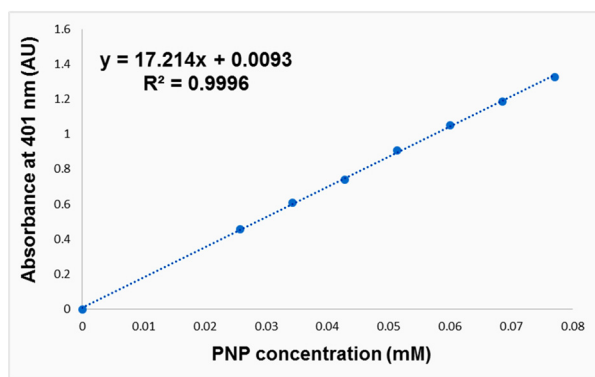


Figure 2. Determination of the molar extinction coefficient

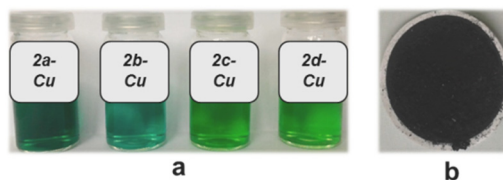


Figure 3. Appearance of the prepared catalysts

When catalyst is added to the PNP+NaBH₄ mixture, the reduction of the nitro compound is produced. To each sample containing 180 μ L 1.2 mM PNP + 1 mL 15 mM NaBH₄ and 1.62 mL DI H₂O, 30 μ L of catalyst (2a-Cu, 2b-Cu, 2c-Cu, and 2d-Cu) was added. As a reference, Cu(0) was used (1 mg). The kinetic data acquisition was performed for 500 s in each case and spectra were recorded at 0.5 s intervals at room temperature under continuous stirring (480 rpm) at two fixed wavelengths 300 and 401 nm, for monitoring the PNP consumption (401 nm) and the PAP formation (300 nm), respectively.

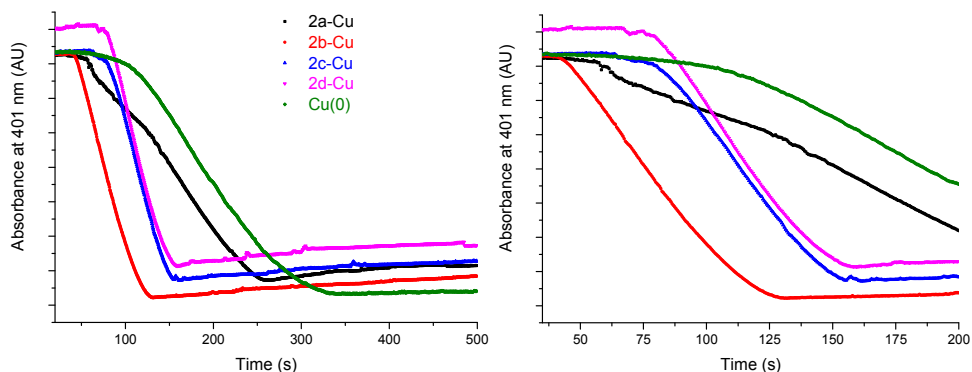


Figure 4. Monitoring the catalytic reaction in time

Experimental data show that each catalyst (*2a-Cu*, *2b-Cu*, *2c-Cu*, *2d-Cu*) shows a higher activity compared to the reference *Cu(0)*. Within this, the hydrogenation reaction was the fastest when *2b-Cu* catalyst was used (Figure 4). As can be seen in Figure 5, the characteristic peak for PNP (black trace) disappeared (by the catalyst addition to the PNP+NaBH₄ mixture) after 65 s and the peak for PAP appeared at 300 nm wavelength (red trace) proving the transformation of the nitro compound.

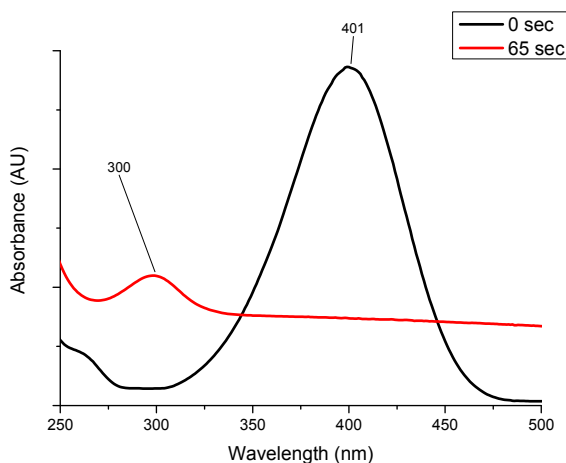


Figure 5. Reaction monitoring using *2b-Cu* catalyst

The reaction rate was assumed to be independent of the NaBH₄ concentration in all cases, therefore pseudo first order kinetic equation was applied when *2b-Cu* was used as catalyst (Figure 6).

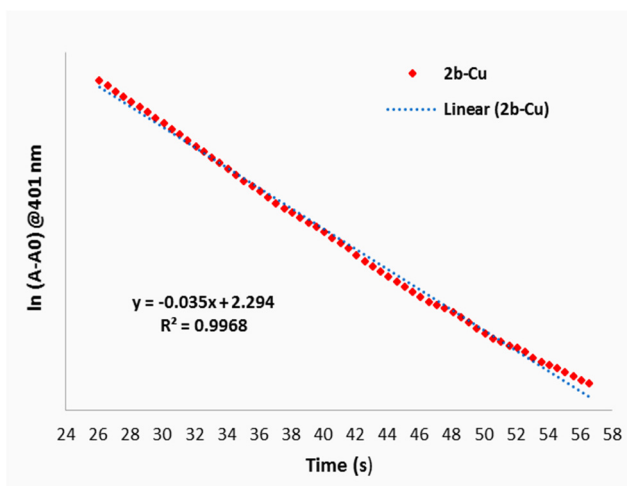


Figure 6. Pseudo first order kinetic plot of PNP reduction catalyzed by *2b-Cu*

CONCLUSIONS

The use of Cu(0)/dendrimer complexes as catalysts in the homogenous chemical reduction of PNP represents a good alternative to the heterogeneously catalyzed reduction. The reaction time highly decreased in comparison with Cu(0) nanoparticles prepared in situ used as heterogeneous catalyst.

EXPERIMENTAL SECTION

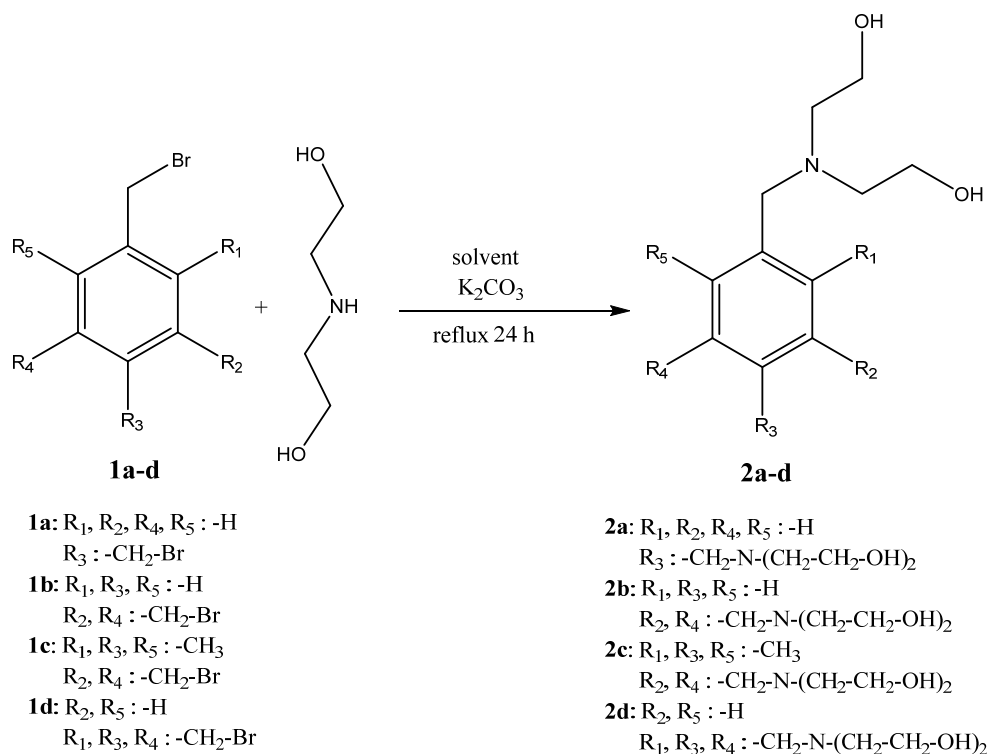
Materials and methods

1,4-bis(bromomethyl)benzene, copper(II) chloride dihydrate, 1,3,5-tris(bromomethyl)benzene, 1,3,5-tris(bromomethyl)-2,4,6-trimethylbenzene, anhydrous potassium carbonate, 1,2,4,5-tetrakis(bromomethyl)benzene, 4-nitrophenol and diethanolamine were purchased from Sigma-Aldrich. The solvents were supplied from Merck. All reagents were used as received without further purification.

Thin layer chromatography (TLC) monitoring was carried out using Merck Kieselgel 60 F 254 sheets. Spots were visualized under UV light at 254 nm. UV-Visible absorbance spectra were recorded on Agilent 8453 spectrophotometer. Mass spectra of the dendrimers were recorded on Agilent /Technologies 6320 spectrometer at room temperature while their ^1H and ^{13}C NMR spectra were recorded on Bruker spectrometers operating at 400 and 100 MHz respectively at 600 and 150 MHz.

Synthesis of dendrimers

In the first step, the dendrimers were prepared according to the procedure previously described by [16]. For the preparation of a novel zero generation dendrimer (compound **2d**), a tetrasubstituted benzene core, namely 1,2,4,5-tetrakis(bromomethyl)benzene was used. The synthesis was carried out under similar conditions using a mixture of solvents instead of MeCN (dioxane:acetonitrile 2:1). The general procedure is presented in Scheme 1.



Scheme 1. General procedure for the synthesis of dendrimers

Preparation of catalysts

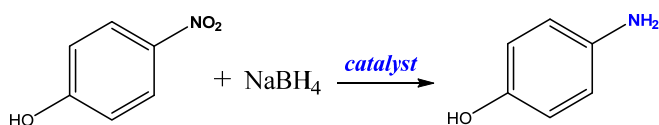
A solution of 5 % $CuCl_2 \cdot 2H_2O$ in methanol was prepared. In a 10 mL round bottom flask to 5 mL of copper salt solution 0.18 mmol dendrimer **2a-d** dissolved in 1 mL MeOH was added dropwise under continuous stirring. The resulted mixture was refluxed for 24 h, let to reach room temperature, filtered and washed with MeOH (5 mL). To the filtrate 1.85 mmol $NaBH_4$ was added

portionwise under strong stirring for the reduction of the Cu^{2+} to metallic copper. The resulted suspension was filtrated on PTFE membrane filter (0.22 μm pore diameter) under vacuum in order to remove the formed solid Cu(0) nanoparticles which were not encapsulated into the dendrimer's cavity. The precipitate was washed with MeOH (5 mL). The resulted filtrate (Figure 3a) was used as catalyst (noted further as *2a-Cu*, *2b-Cu*, *2c-Cu*, *2d-Cu*) and its activity was tested within the chosen model hydrogenation reaction⁹ (Scheme 2).

As the reference, Cu(0) was prepared as follows: in an Erlenmeyer flask, at 5 mL of the prepared copper(II) chloride dihydrate methanolic solution, 70 mg NaBH_4 was added portionwise under rigorous stirring. The resulted solid metallic copper nanoparticles (Figure 3b) were filtered off on PTFE membrane filter (0.22 μm pore diameter) and dried in air.

Catalytic activity testing

For the catalytic activity testing of the dendrimer-Cu(0) complexes the reaction presented in Scheme 2 was followed.



Scheme 2. Reduction of *p*-nitrophenol

The reaction was monitored spectrophotometrically. The yellow colored *p*-nitrophenol aqueous solution turned into colorless and contained black solid particles. This proved, that upon the catalysis Cu(0) nanoparticles bounded into the dendrimers were released.

ACKNOWLEDGMENTS

This research was realized having financial support from Romanian UEFISCDI grant no. PN-II-ID-PCE-2011-3-0346.

REFERENCES

1. E. Buhleier, W. Wehner, F. Vögtle, *Synthesis*, **1978**, 2, 155.
2. D.A. Tomalia, H. Baker, J. Dewald, M. Hall, G. Kallos, S. Martin, J. Roeck, J. Ryder, P. Smith, *Polymer Journal*, **1985**, 17, 117.

3. E.A. Karakhanov, A.L. Maximov, V.A. Skorkin, A.V. Zolotukhina, A.S. Smerdov, A. Yu. Tereshchenko, *Pure and Applied Chemistry*, **2009**, 81(11), 2013.
4. H. Lang, S. Maldonado, K.J. Stevenson, B.D. Chandler, *Journal of the American Chemical Society*, **2004**, 126, 12949.
5. Z.D. Pozun, S.E. Rodenbusch, E. Keller, K. Tran, W. Tang, K.J. Stevenson, G. Henkelman, *The Journal of Physical Chemistry C*, **2013**, 117, 7598.
6. J.F. Sonnenberg, R.H. Morris, *ACS Catalysis*, **2013**, 3, 1092.
7. H. Hu, J.H. Xin, H. Hu, X. Wang, D. Miao, Y. Liu, *Journal of Materials Chemistry A*, **2015**, 3, 11157.
8. T. Vincent, E. Guibal, *Langmuir*, **2003**, 19, 8475.
9. S. Gu, S. Wunder, Y. Lu, M. Ballauff, R. Fenger, K. Rademann, B. Jaquet, A. Zaccone, *The Journal of Physical Chemistry C*, **2014**, 118, 18616.
10. S. Wunder, F. Polzer, Y. Lu, Y. Mei, M. Ballauff, *The Journal of Physical Chemistry C*, **2010**, 114(19), 8814.
11. B. Baruah, G.J. Gabriel, M.J. Akbashev, M.E. Booher, *Langmuir*, **2013**, 29, 4225.
12. J.A. Johnson, J.J. Makis, K.A. Marvin, S.E. Rodenbusch, K.J. Stevenson, *The Journal of Physical Chemistry C*, **2013**, 117, 22644.
13. M.Y.A. Halim, W.L. Tan, N.H.H. Abu Bakar, M. Abu Bakar, *Materials*, **2014**, 7, 7737.
14. S. Amdouni, Y. Coffinier, S. Szunerits, M.A. Zaibi, M. Queslati, R. Boukherroub, *Semiconductor and Science Technology*, **2016**, 31, 014011.
15. B.K. Ghosh, S. Hazra, B. Naik, N.N. Ghosh, *Powder Technology*, **2015**, 269, 371.
16. M.E. Füstös, T.A. Sipos, M.V. Diudea, G. Katona, *Croatica Chemica Acta*, **2015**, 88(2), 129.

*Dedicated to Professor Mircea Diudea
on the Occasion of His 65th Anniversary*

QSPR STUDY ON TRANSITION TEMPERATURE OF TETRAPHENYLETHENE-DERIVED COLUMNAR LIQUID CRYSTALS

ZOITA BERINDE^{a,*}, THOMAS DIPPONG^a, CLAUDIA BUTEAN^a

ABSTRACT. The paper presents a study regarding the correlation of the transition temperature for nine derivatives of the tetraphenylethene, a class of columnar liquid crystals, with 35 molecular descriptors (22 topological indices and 13 Van der Waals parameters), calculated for these compounds. Their transition temperature was modelled in mono- and multivariate linear regression equations. In linear, simple correlations, 19 out of the 22 topological indices and 3 out of the 13 Van der Waals parameters show a correlation coefficient higher than 0,8; in multivariate linear correlations the results are even better, with correlation coefficients larger than 0,9.

Keywords: *correlation, columnar crystals, topological indices*

INTRODUCTION

Derivatives of the tetraphenylethene are chemical compounds whose molecules have structural characteristics and features that include them in the columnar liquid crystals [1]. The transition temperature is an important physical property of liquid crystals in general and of thermotropic liquid crystals in particular, the derivatives of tetraphenylethene belonging to the latter category. Study of liquid crystals begun back in 1888, when Reinitzer [2] and Lehman [3] discovered that the cholesteryl benzoate presents, between solid and liquid phases, several intermediary stable phases, which are: anisotropic, just like

^a *Technical University of Cluj-Napoca, Faculty of Sciences North University Center at Baia Mare, Department of Chemistry and Biology, 76 Victoriei Street, 430122 Baia Mare, Romania*

* *Corresponding Author: zoita_berinde@yahoo.com*

the solid crystals, and fluid, just like liquids. These intermediary stable phases have been called the "liquid crystal state". The liquid crystals, are, therefore, condensed fluid states with spontaneous anisotropy, also called mesophases while the molecules they discovered have been called mesogenic [4,5].

The number of studies and publications dealing with the mesogens and mesophases had continuously increased, especially after 1964, when Ferguson [6] draws the attention upon the practical applications of liquid crystals: in the fabrication of alphanumeric and analog displays, for the conversion of pictures to matrix type screens for showing the pictures [7,8], in the skin thermography and diagnosis, as solvents in UV, VIZ, RMN, RES spectroscopy, giving information about the bond length of the dissolved molecules [9,10] and many other uses.

By studying the relationship between the chemical structure and mesophases, Vorländer found that liquid crystal phases often occur within compounds with elongated and relatively rigid molecules, along their longitudinal axis [11], such as the tetraphenylethenes. Taking into account only the symmetry of their structure, Friedel [12,13] classified the liquid crystals into three important categories: nematic liquid crystals, cholesteric liquid crystals and smectic liquid crystals. By the shape of molecules, the liquid crystals can be divided into: calamitic liquid crystals (with fusiform molecules) and discotic liquid crystals (with disc-shaped molecules), as discovered by Chandrasekhar [14]. According to Friedel și Lawrance [15,16], liquid crystals may be: thermotropic (formed by temperature alteration) and lyotropic (formed by the alteration of their concentration in a solution). Thermotropic liquid crystals are important in fundamental research and technological applications while lyotropic crystals play an important role in biological systems [17]. The tetraphenylethene derivatives are thermotropic liquid crystals and belong to the disc-shaped molecules, for which the mesophase is characterized by the superposition of the discs in columns, wherefrom the name of columnar liquid crystals [18].

The temperature at which the transition, from the crystal state to the mesophase, is produced is often called melting point, and that of the transition, from the mesophase to the isotropic liquid, is called clarification point or clarification temperature [19]. The transition temperature is that at which the number of ordered subsystems equal the number of disordered ones.

This aim of present QSPR study is to find the best regression equations for predicting the transition temperature of columnar liquid crystals of the tetraphenylethene derivatives. In this respect, we calculated and tested 35 molecular descriptors: 22 topological indices and, respectively, 13 Van der Waals parameters. Next, the used descriptors were defined, the work methods described and the results discussed; at the end, conclusions were drawn.

Topological molecular descriptors

Wiener (W) and Polarity (P) indices:

The Wiener index (W) can be defined as the half-sum of the entries d_{ij} in the distance matrix associated to the molecular graph [20]:

$$W = \frac{1}{2} \cdot \sum_{i=1}^n \sum_{j=1}^n d_{ij} \quad (1)$$

The polarity index (P) has also been defined by Wiener in the same pioneering paper [20] and is obtained by summing up the number of atom pairs, separated by three edges, in a molecule:

$$P = \frac{1}{2} \cdot \sum_i d_{3,i} \quad (2)$$

Gordon-Scantlebury Index (N₂):

This index counts the number of two-edges paths P_2 in a molecular graph [21]:

$$N_2 = \sum_i (P_2)_i \quad (3)$$

Zagreb (M₁ and M₂) Indices:

Gutman and collabs. [22,23] proposed two indices based on the vertex degrees δ_i, δ_j :

$$M_1 = \sum_{i=1}^n (\delta_i)^2 \quad (4)$$

$$M_2 = \sum_{(i,j) \in E(G)} (\delta_i \cdot \delta_j) \quad (5)$$

Connectivity indices:

The original connectivity index was proposed by Randić [24] as:

$${}^1\chi = \sum_{i,j} (\delta_i \cdot \delta_j)^{-\frac{1}{2}} \quad (6)$$

Balaban [25] extended the above definition by changing the vertex degree with the distance sum D_i, D_j :

$$J = \frac{q}{\mu+1} \cdot \sum (D_i \cdot D_j) \quad (7)$$

where q represents the number of edges, and μ is the cyclomatic number ($\mu=q-n+1$, and n = no. atoms). By multiplying the local invariants (D_i) by the covalent radii, Mulliken's electronegativities and by Van der Waals radii, some extended indices J^{rc} , J^{el} , J^{Rw} are obtained.

Kier and Hall Indices

Kier and Hall [26] further generalized the *Randić*-type index:

$${}^m \chi = \sum_r (\delta_1 \cdot \delta_2 \cdot \dots \cdot \delta_{m+1})^{-\frac{1}{2}} \quad (8)$$

where r represents all the possible m length ways in the molecular graph.

In the following, we used, for the Kier-Hall versions only sequences containing at most 3 bonds, as shown below:

$${}^2 \chi = \sum_{r=2} (\delta_i \cdot \delta_j \cdot \delta_k)^{-\frac{1}{2}} \quad (9)$$

$${}^3 \chi = \sum_{r=3} (\delta_i \cdot \delta_j \cdot \delta_k \cdot \delta_l)^{-\frac{1}{2}} \quad (10)$$

$${}^2 J_p = \frac{q}{\mu+1} \sum_{r=2} (d_i \cdot d_j \cdot d_k)^{-\frac{1}{2}} \quad (11)$$

$${}^3 J_p = \frac{q}{\mu+1} \sum_{r=3} (d_i \cdot d_j \cdot d_k \cdot d_l)^{-\frac{1}{2}} \quad (12)$$

The D index (average square distance) was also calculated:

$$D = \left(\sum_i \sum_j d_{ij}^2 \right)^{\frac{1}{2}} \quad (13)$$

Based on these data, the indices $\chi^{D^{el}}$, JD^{el} were calculated for Mulliken's electronegativities, the indices $\chi^{D^{rc}}$ și JD^{rc} for the covalent radii, and, respectively, the indices $\chi^{D^{Rw}}$, JD^{Rw} for van der Waals radii.

Van der Waals parameters

The volume and surface of the molecules may be computed based on the 3D cartesian coordinates and they bring information regarding the dimension and shape of three-dimensional molecules. The most frequently used Van der Waals parameters are van der Waals radius (R^w), van der Waals volume (V^w) and van der Waals surface (S^w). The 2 latter parameters are obtained using the Monte Carlo method [27,28], but can also be calculated analytically [29]. The atoms are considered to be spherical, incompressible, with a radius equal to Van der Waals radius [30] while the molecules are assimilated to spheres having the same radii as Van der Waals radii of the constitutive atoms.

The distance at which the antagonist attraction and rejection forces are balanced is called *van der Waals (R^w) radius*. The steric effects are usually ascribed to the repulsive forces that occur when direct, non-bound atoms get close to a shorter distance than the sum of the Van der Waals radii (R^w), which leads to the appearance of a compression.

The *Van der Waals Molecular Volume* (V^W) represents the volume sum of the spheres of constitutive atoms of the considered molecule. The van der Waals molecular volume (V^W) is a useful parameter in the studies regarding the packing density of organic compounds in crystal structures and in many other studies that describe the molecule structure [30]. The *van der Waals surface* (S^W), represents the molecular surface related to a Van der Waals volume (V^W).

Sometimes it is helpful to analyse the ratio V^W/S^W , which has the measurement units of a length; also, the parameters of the ellipsoid about which the molecule is circumscribed. The semi-axes of such an ellipsoid defined within the approximation of hard spheres, characterize the globularity of the molecule:

$$GL1 = V^{SF} / V^W \quad (14)$$

$$GL2 = V^{SF} / V^{EL} \quad (15)$$

The ellipsoid and the three parameters that describe it (i.e., its semi-axes, E_x , E_y , E_z) represent indices of the molecular shape and can be used in QSAR studies [30].

Two other parameters, that define the molecular geometry can be calculated: (i) the ellipsoidal globularity degree (GL_{EL}), as the ratio of the volume of the ellipsoid (V^{EL}) that circumscribes about the molecule to the volume of the sphere (V^{SF}) with the same radius as the longest semi-axis of the ellipsoid (relation 16); and (ii) the degree of volume globularity ($GLOB$), as the ratio of the Van der Waals volume (V^W) to the sphere volume (V^{SF}) (relation 17).

$$GL_{EL} = V^{EL} / V^{SF} \quad (16)$$

$$GLOB = V^W / V^{SF} \quad (17)$$

RESULTS AND DISCUSSION

The values of Pearson's correlation coefficient R , resulted from the linear correlation tests, between the transition temperature T_z and each of the 35 molecular descriptors are shown in Table 1. The positive value of the correlation coefficient R , in all cases, shows that the transition temperature increases when the value of the molecular descriptor increases.

In case of topological indices, most of them are correlated to the transition temperature, having the correlation coefficient R about 0.82 (excepting only Balaban's index 2J , with $R=0.5189$, Wiener's index, where $R=0.7392$ and Balaban's 3J with $R=0.7148$ – not included in Table 1). The best correlation, $R = 0.8712$, was found in case of Balaban's index, weighted by the Mulliken electronegativities, symbolized by J^{el} .

The values of the correlation coefficient $R > 0,8$ in case of the Van der Waals molecular volume (V^W) and Van der Waals surface (S^W), proves the existence of a correlation between the transition temperature and these parameters, correlation that is improved when using the ratio V^W/S^W . The bigger the volume of the molecule is, the higher its transition temperature. It is interesting that amongst the three semi-axes of the ellipsoid circumscribed about the molecular aggregate, only the semi-axis E_Y has a correlation coefficient $> R=0.7609$, which shoes a significant relationship with the transition temperature.

The best statistical parameters were obtained in the case of the transition temperature modelling by a simple linear equation using the ratio of Van der Waals volume to the corresponding surface (relation 18). It should be noted that using this ratio we get an improvement of the quality of regression using the Van der Waals volume (0.8261) or surface (0.8258) as independent variables. The best thre monovariate linear equations that model the transition temperature are as follows:

Table 1. Statistics of the monovariate regression equations

X	Statistics			X	Statistics		
	R	F	s		R	F	s
V^W	0.826	15.044	25.6	χ^{el}	0.826	15.143	25.6
S^W	0.825	15.018	25.6	χ^{Rw}	0.836	16.332	24.9
E_Y	0.760	9.630	29.5	$\chi^{D^{rc}}$	0.844	17.477	24.3
V^W/S^W	0.885	25.421	21.1	$\chi^{D^{el}}$	0.836	16.255	24.9
N_2	0.849	18.189	24.0	$\chi^{D^{Rw}}$	0.832	15.811	25.2
P	0.864	20.792	22.8	J^{rc}	0.850	18.319	23.9
M_1	0.843	17.300	24.4	J^{el}	0.871	22.064	22.3
M_2	0.852	18.600	23.8	J^{Rw}	0.852	18.625	23.8
$^1\chi$	0.835	16.119	25.0	JD^{rc}	0.830	15.543	25.3
$^2\chi$	0.840	16.781	24.7	JD^{el}	0.853	18.856	23.7
$^3\chi$	0.832	15.811	25.2	JD^{Rw}	0.861	20.115	23.1
χ^{rc}	0.837	16.445	24.8	X = Independent variable			

$$T_z = -4424.59 + 5576.456 V^W/S^W \quad (18)$$

$$R = 0.885 \quad s = 21.1 \quad F = 25.422$$

$$T_z = 462.232 - 3011.261 J^{el} \quad (19)$$

$$R = 0.871 \quad s = 22.3 \quad F = 22.064$$

$$T_z = 456.366 + 869.326 JD^{Rw} \quad (20)$$

$$R = 0.861 \quad s = 23.144 \quad F = 20.116$$

In general, an improvement of the correlation coefficient may be found as the number of predictor variables increases. However, if the number of predictor variables is larger than the number of observations, chance correlations may occur. In our study, we considered two, three and four predictor variables. When the two predictor variables are topological indices, the correlation coefficient does not exceed 0.9:

$$\begin{aligned} T_z &= 351.214 + 2815.676 \cdot J - 2730.661 \cdot J^{el} \\ R &= 0.891 \quad s = 22.3 \quad F = 11.55 \end{aligned} \quad (21)$$

In case of Van der Waals parameters, in several combinations, the correlation coefficient exceeds 0.92. From a statistical point of view, the best bi-variable regression equation is:

$$\begin{aligned} T_z &= -7997.780 + 9897.055 \cdot V^W/S^W + 0.009 \cdot V^{EL} \\ R &= 0.950 \quad s = 15.4 \quad F = 27.55 \end{aligned} \quad (22)$$

This correlation coefficient is slightly improved when three predictor variables are used, especially those belonging to the category of Van der Waals parameters:

$$\begin{aligned} T_z &= -9303.279 + 1139.967V^W/S^W + 0.007V^{EL} + 5.811E_Y \\ R &= 0.954 \quad s = 16.07 \quad F = 17.068 \end{aligned} \quad (23)$$

When we use the predictor variables from the topological indices category, the highest correlation coefficient is 0.9474, lower than in the previous case, but higher than in the case of topological indices bi-variable correlation:

$$\begin{aligned} T_z &= 1444.9 + 11.3 \cdot \chi + 7291.9 \cdot J^{rc} - 98426.5 \cdot J^{el} \\ R &= 0.947 \quad s = 17.24 \quad F = 14.615 \end{aligned} \quad (24)$$

Adding another predictor variable, from both the Van der Waals parameter category and the topological indices category, leads to a very slight increase of the correlation coefficient value:

$$\begin{aligned} T_z &= 1054.997 + 18600.248 \cdot J - 12.971N_2 - 25482.873 \cdot J^{el} + 19.128 P \\ R &= 0.958 \quad s = 17.23 \quad F = 11.221 \end{aligned} \quad (25)$$

$$\begin{aligned} T_z &= -10615.02 + 12848.2V^W/S^W + 6.39 \cdot E_Y + 0.011V^{EL} + 837.8 GLOB \\ R &= 0.960 \quad s = 16.89 \quad F = 11.72 \end{aligned} \quad (26)$$

The correlation coefficient R increases when using more independent variables but the system could become over-estimated. In such situations, Topliss and Costello [31] recommend the use of two independent variables for a small number of values for the dependent variable, e.g., T_z . In order to exclude the chance correlation, in the case of equations 25 and 26 (with four variables), we applied the “random test” which assumes the random mixture of the values of T_z and then the computation of the corresponding correlation coefficients, which are given in Table 1a.

Table 1a. Random mixed Y values

1	2	3	4	5	6	7	8	9	(25)	(26)
37	29	139	40	34	47	126	55	101	0.665	0.806
55	29	101	37	34	40	126	139	47	0.415	0.787
40	29	37	139	55	126	101	34	47	0.652	0.503
40	34	37	47	126	55	29	139	101	0.598	0.869
55	47	29	40	126	34	101	37	139	0.559	0.724
29	40	55	101	47	126	34	37	139	0.578	0.449
37	34	29	101	139	40	126	47	55	0.617	0.591
40	34	37	139	47	55	101	126	29	0.571	0.648
126	55	34	139	40	37	29	101	47	0.520	0.675

In our study, we determined a number of linear regression relations: among these, the best statistics is provided by equation (22), with: $R = 0.950$; $s = 15.4$; $F = 27.55$. This equation shows the lowest standard error of estimate, s , that is a strong requirement for a statistical model.

CONCLUSIONS

The results herein reported show that, a part of the tested Van der Waals parameters and all topological descriptors considered, are correlated with the transition temperature of the derivatives of tetra-phenylethene of the columnar liquid crystals.

The statistical quality of the simple or multiple regression models, recommends the used descriptors (Van der Waals- type descriptors and topological indices, respectively) to predict the transition temperature of columnar liquid crystals.

Including the descriptors concerning the molecular flexibility, electronegativities of the constitutive atoms or the atom size, by covalent radii or Van der Waals radii, led to the improvement of statistical parameters of the models.

EXPERIMENTAL SECTION

In our study we had in mind four main directions:

1. Drawing, by means of the Hyperchem software, of the 9 structures (S1-S9), standing for the tetraphenylethene derivatives which belong to the category of columnar liquid crystals. Figure 1 illustrates the general structure of this category of liquid crystals, detailed in Table 2.

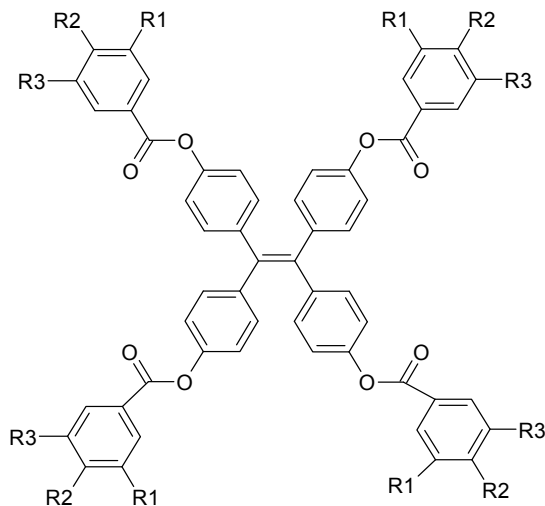


Figure 1. General structure of columnar crystals

Table 2. R1, R2 and R3 radicals for 9 compounds (S1-S9)

Compound	R1	R2	R3	T_z ($^{\circ}\text{C}$)
S1	H	$\text{OC}_{10}\text{H}_{21}$	H	139
S2	$\text{OC}_{10}\text{H}_{21}$	$\text{OC}_{10}\text{H}_{21}$	H	101
S3	OC_5H_{11}	OC_5H_{11}	OC_5H_{11}	126
S4	OC_6H_{11}	OC_6H_{13}	OC_6H_{13}	55
S5	OC_7H_{15}	OC_7H_{15}	OC_7H_{15}	37
S6	OC_8H_{17}	OC_8H_{17}	OC_8H_{17}	47
S7	OC_9H_{19}	OC_9H_{19}	OC_9H_{19}	40
S8	$\text{OC}_{10}\text{H}_{21}$	$\text{OC}_{10}\text{H}_{21}$	$\text{OC}_{10}\text{H}_{21}$	29
S9	$\text{OC}_{12}\text{H}_{25}$	$\text{OC}_{12}\text{H}_{25}$	$\text{OC}_{12}\text{H}_{25}$	34

The transition temperatures T_z ($^{\circ}\text{C}$) of the 9 tetraphenylethene derivatives, were taken from Schultz's work 2001 [32].

2. The values of the calculated 35 molecular descriptors (22 topological indices and 13 Van der Waals parameters), for each of the considered 9 structures are given in Tables 3, 3a and 3b and Tables 4 and 4a.

Table 3. Topological indices

Sample	W	N2	P	M1	M2	$^1\chi$	$^2\chi$	$^3\chi$
S1	95417	130	152	510	573	48.100	36.412	21.967
S2	220861	178	208	694	769	69.895	52.183	32.952
S3	145589	166	204	638	725	61.690	46.886	28.612
S4	183473	178	216	686	773	67.690	51.129	31.612
S5	227209	190	228	734	821	73.690	55.371	34.612
S6	277205	202	240	782	869	79.690	59.614	37.612
S7	333869	214	252	830	917	85.690	63.856	40.612
S8	397609	226	264	878	965	91.690	68.099	43.612
S9	547949	250	288	974	1061	103.690	76.584	49.612

Table 3a. Topological indices (continuation)

Sample	χ^{rc}	χ^{el}	χ^{Rw}	χD^{rc}	χD^{el}	χD^{Rw}
S1	64.720	2.234	26.959	16.619	-45.866	-21.141
S2	93.442	4.849	39.902	23.546	-65.046	-29.992
S3	83.203	3.704	35.199	21.513	-57.985	-26.491
S4	90.995	4.456	38.728	23.305	-63.233	-28.961
S5	98.787	5.208	42.257	25.097	-68.481	-31.432
S6	106.58	5.960	45.787	26.889	-73.729	-33.902
S7	114.372	6.712	49.316	28.681	-78.978	-36.373
S8	122.164	7.464	52.846	30.474	-84.226	-38.844
S9	137.748	8.967	59.905	34.058	-94.722	-43.785

Table 3b. Topological indices (continuation)

Sample	2J	3J	J^{rc}	J^{el}	J^{Rw}	JD^{rc}	JD^{el}	JD^{Rw}
S1	0.027	0.0007	1.149	0.104	0.517	0.278	-0.766	-0.353
S2	0.024	0.0005	1.339	0.120	0.603	0.325	-0.893	-0.410
S3	0.031	0.0007	1.457	0.128	0.655	0.359	-0.969	-0.442
S4	0.029	0.0006	1.481	0.131	0.666	0.364	-0.986	-0.451
S5	0.027	0.0006	1.504	0.134	0.676	0.368	-1.001	-0.458
S6	0.026	0.0005	1.525	0.136	0.686	0.372	-1.016	-0.466
S7	0.024	0.0005	1.545	0.138	0.695	0.376	-1.029	-0.472
S8	0.023	0.0004	1.563	0.140	0.703	0.380	-1.042	-0.479
S9	0.021	0.0003	1.595	0.144	0.718	0.386	-1.064	-0.490

Table 4. Van der Waals Parameters

Sample	V ^W	S ^W	V ^{SF}	S ^{SF}	V ^{EL}	E _x
S1	1414.894	1732.120	63806.6	7721.965	6816.521	24.789
S2	2115.972	2623.446	70800.47	8276.401	11355.38	25.663
S3	1807.141	2222.947	30794.91	4751.201	5956.107	19.444
S4	2006.938	2481.165	37366.59	5405.133	6803.804	20.740
S5	2209.620	2743.427	43134.60	5947.959	7859.230	21.756
S6	2411.699	3003.459	51191.36	6667.278	11290.38	23.034
S7	2613.578	3260.065	59358.21	7358.760	13228.16	24.199
S8	2806.754	3521.798	70808.77	8277.049	14656.55	25.665
S9	3216.908	4036.716	92594.17	9897.828	15677.04	28.065

Table 4a. Van der Waals Parameters (continuation)

Sample	E _γ	E _z	GLOB	GL1	GL2	GL _{EL}	V ^W /S ^W
S1	15.140	4.336	0.099	45.096	4.458	4.818	0.817
S2	20.729	5.096	0.094	33.460	3.155	5.367	0.807
S3	16.834	4.344	0.125	17.041	2.137	3.296	0.813
S4	17.856	4.386	0.117	18.619	2.178	3.390	0.809
S5	19.554	4.411	0.111	19.521	2.168	3.557	0.805
S6	20.063	5.833	0.105	21.226	2.22	4.682	0.803
S7	21.467	6.079	0.099	22.711	2.257	5.061	0.802
S8	22.341	6.102	0.093	25.228	2.35	5.222	0.797
S9	24.597	5.422	0.085	28.784	2.452	4.873	0.797

3. Correlation analysis was performed by Pearson's linear correlation. The results are listed in Tables 1 and 1a and equations (18) to (26), as above discussed.

REFERENCES

1. A. Shuly, S. Diele, S. Laschat, "Novel columnar tetraphenylethenes", Technische Universität Braunschweig, **1998**.
2. S. Laschat, *Beilstein J Org Chem*, **2009**, *5*, 48.
3. I. Sage, *Liquid Crystals*, **2011**, *38*, 1551.
4. A. Dequidt, P. Oswald, *The European Physical Journal E*, **2007**, *24*, 157.
5. Y. Chen, F. Peng, T. Yamaguchi, X. Song, S-T. Wu, *Crystals*, **2013**, *3*, 483.

6. Patent US 3114836 A, **1963**, Inventor: Ferguson James.
7. G. Singh, G.V. Prakash, A. Choudhary, *Physica B*, **2010**, 405, 2118.
8. I. Abdulhalim, R. Moses, R. Sharon, *Acta Physica Polonica A*, **2007**, **112**, 715.
9. B. Svensson, A. Marini, H. Zimmermann, A. Maliniak, *J. Phys. Chem. B*, **2011**, 115 (23), 7561.
10. E. Westphal, M. Prehm, I.H. Bechtold, C. Tschierske, H. Gallardo *J. Mater. Chem. C*, **2013**, 1, 8011.
11. S. Yilmaz, H. Melik, F. Angay, M. Emek, A. Yildirim, *Journal of Modern Physics*, **2011**, 2, 248.
12. S. Chandrasekhar, "Liquid Crystals", Cambridge University Press, **1992**.
13. D. Demus, J.W.G. Goodby, G.W. Gray, H.W. Spiess, "Handbook of Liquid Crystals", Wiley-VCH, **1998**.
14. S. Chandrasekhar, B.K. Sadashiva, K.A. Suresh, *Pramana*, **1977**, 9, 471-480
15. D. Jurašin, M. Vinceković, A. Pustak, I. Šmit, M. Bujan, *Soft Matter*, **2013**, 9, 3349.
16. M.R. Alcantara, E.G. Fernandes, *J. Phys.*, **2002**, 2, 32.
17. I. Dumitrașcu, D.O. Dorohoi, „Proprietăți optice ale mediilor cu ordonare parțială. Aplicații”, Editura Tehnopres, Iași, **2009**.
18. H. Bock, *Columnar Liquid Crystals*, **2001**, 355.
19. Britannica Concise Encyclopedia, Encyclopædia Britannica Inc., **2006**.
20. H. Wiener, *J. Amer. Chem. Soc.*, **1947**, 69, 17.
21. M. Gordon, G.R. Scantlebury, *Trans. Faraday Soc.*, **1964**, 60, 604.
22. I. Gutman, N. Trinajstić, *Chem. Phys. Lett.*, **1972**, 17, 535.
22. I. Gutman, I. Rusčić, N. Trinajstić, C.F. Wilcox, Jr., *J. Chem. Phys.*, **1975**, 62, 3339.
23. M. Randić, *J. Amer. Chem. Soc.*, **1975**, 97, 6609.
25. A.T. Balaban, L.V. Quintas, *MATCH Commun. Math. Comput. Chem.*, **1983**, 14, 213.
26. L.B. Kier, L.H. Hall, "Molecular Connectivity in Chemistry and Drug Research", Acad. Press, **1976**.
27. A. Tkatchenko, M. Scheffler, *Physical Review Letters*, **2009**, 102, 073005.
28. A. Schultz S. Laschat, S. Diele, M. Nimtz, *European Journal of Organic Chemistry*, **2003**, 15, 2829.
29. A. Schultz, S. Diele, S. Laschat, M. Nimtz, *Advanced Functional Materials*, **2001**, 11 (6), 441.
30. D. Ciubotariu, M. Medeleanu, V. Vlaia, T. Olariu, C. Ciubotariu, D. Dragoș, C. Seiman, *Molecules*, **2004**, 9, 1053.
31. J.G. Topliss, R.J. Costello, *J. Med. Chem.*, **1972**, 1066.
32. A. Schultz, S. Diele, S. Laschat, M. Nimtz, *Adv. Funct. Mater.*, **2001**, 11 (6), 441.

***Dedicated to Professor Mircea Diudea
on the Occasion of His 65th Anniversary***

THE INVERSE SUM INDEG INDEX OF SOME NANOTUBES

FARZANEH FALAHATI-NEZHAD^a, MAHDIEH AZARI^b

ABSTRACT. Discrete Adriatic indices have been defined by Vukičević and Gašperov (2010), as a way of generalizing well-known molecular descriptors defined as the sum of individual bond contributions. One of these indices is the inverse sum indeg index which is a significant predictor of total surface area of octane isomers. In this paper, exact formulas for computing the inverse sum indeg index of some nanotubes are presented.

Keywords: *ISI index, Nanotube.*

INTRODUCTION

A *molecular descriptor* (also known as *topological index*, *measure* or *graph invariant*) is any function on a graph that does not depend on a labeling of its vertices. In organic chemistry, topological indices have been found use in chemical documentation, isomer discrimination, structure-property relationships (SPR), structure-activity relationships (SAR), and pharmaceutical drug design [1,2]. Some of the most famous molecular descriptors are *bond-additive*, *i.e.*, they can be presented as the sum of edge contributions. *Discrete Adriatic indices* were defined by Vukičević and Gašperov [3] as a way of generalizing well-known bond-additive molecular descriptors. One hundred forty eight discrete Adriatic indices have been defined [3] and QSAR and QSPR studies of them have been performed [3] on the benchmark sets [4] proposed by the International Academy of Mathematical Chemistry [5]. Twenty

^a *Department of Mathematics, Safadasht Branch, Islamic Azad University, Tehran, Iran, falahatinejad@safaiu.ac.ir*

^b *Department of Mathematics, Kazerun Branch, Islamic Azad University, P.O. Box: 73135-168, Kazerun, Iran, azari@kau.ac.ir*

of these indices have shown good predictive properties. One of these twenty indices is the *inverse sum indeg index* that was selected in [3] as a significant predictor of total surface area for octane isomers. The inverse sum indeg index $ISI(G)$ of a simple graph G is defined as

$$ISI(G) = \sum_{uv \in E(G)} \frac{1}{\frac{1}{d_u} + \frac{1}{d_v}} = \sum_{uv \in E(G)} \frac{d_u d_v}{d_u + d_v},$$

where $E(G)$ is the edge set of G ; and d_u and d_v are the degrees of the vertices u and v in G , respectively. For more information on ISI index see [6].

A nanostructure is an object of intermediate size between molecular and microscopic structures. It is a product derived through engineering at molecular scale. The most important class of these new materials is that of carbon nanotubes. Carbon nanotubes (CNTs) are allotropes of carbon with molecular structure and tubular shape, having diameters ranging from a few nanometers and lengths up to several millimeters. Nanotubes are categorized as single-walled (SWNTs) and multi-walled (MWNTs) nanotubes. In 1991, Iijima [7] discovered carbon nanotubes as multi-walled structures. In this paper, we present exact formulas for computing the inverse sum indeg index of some well-known nanotubes such as $TUAC_6$, $TUZC_6$, $TUC_4C_8(R)$, $TUC_4C_8(S)$, $TUHC_5C_7$, $TUSC_5C_7$, $TUHAC_5C_7$, and $TUHAC_5C_6C_7$. For more information on computing topological indices of nanostructures see [8-19]. The symbols, nomenclature and some of the following figures were taken from refs. [9,10] by permission of Professor Diudea.

RESULTS AND DISCUSSION

In this section, we compute ISI index of $TUAC_6$, $TUZC_6$, $TUC_4C_8(R)$, $TUC_4C_8(S)$, $TUHC_5C_7$, $TUSC_5C_7$, $TUHAC_5C_7$, and $TUHAC_5C_6C_7$ nanotubes.

Let G be one of the above-mentioned nanotubes. It is easy to see that, the degree of each vertex in G is either 2 or 3. So, we can partition the edge set of G into the three sets as follows:

$$\begin{aligned} E_1(G) &= \{uv \in E(G) : d_u = d_v = 2\}; \\ E_2(G) &= \{uv \in E(G) : d_u = 2, d_v = 3\}; \\ E_3(G) &= \{uv \in E(G) : d_u = d_v = 3\}. \end{aligned}$$

Now, the ISI index of the nanotube G can be computed from the following formula:

$$\begin{aligned}
 |SI(G)| &= \frac{2 \times 2}{2+2} |E_1(G)| + \frac{2 \times 3}{2+3} |E_2(G)| + \frac{3 \times 3}{3+3} |E_3(G)| \\
 &= |E_1(G)| + \frac{6}{5} |E_2(G)| + \frac{3}{2} |E_3(G)|.
 \end{aligned} \tag{1}$$

Consequently, for computing the ISI index of the nanotube G , it is enough to find the cardinality of the sets $E_1(G)$, $E_2(G)$, and $E_3(G)$.

Polyhex nanotubes

A polyhex net is a trivalent covering made entirely by hexagons C_6 . Two classes of polyhex nanotubes are armchair and zig-zag polyhex nanotubes.

TUAC₆ nanotubes

Let $G=TUAC_6(p,q)$ be an armchair polyhex nanotube, where p is the number of hexagons in each row and q is the number of rows in the molecular graph of G (see Fig. 1).

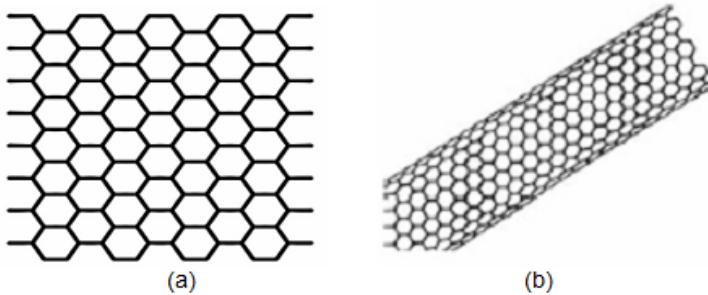


Figure 1. (a) The 2-dimensional lattice of $TUAC_6(4,8)$ nanotube, (b) $TUAC_6$ nanotube.

It is easy to see that, $|E_1(G)| = 2p$, $|E_2(G)| = 4p$, and $|E_3(G)| = 6pq - 8p$. Now using Eq. (1), we easily arrive at:

Theorem 1. The ISI index of $G=TUAC_6(p,q)$ nanotube is given by:

$$|SI(G)| = 9pq - \frac{26}{5}p.$$

TUZC₆ nanotubes

Let $G=TUZC_6(p,q)$ be a zigzag polyhex nanotube, where p is the number of hexagons in each row and q is the number of zigzag lines in the molecular graph of G (see Fig. 2).

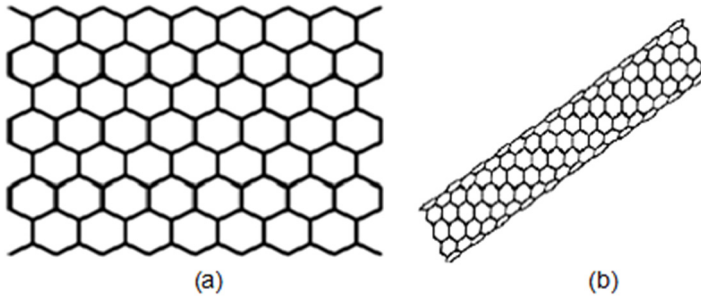


Figure 2. (a) The 2-dimensional lattice of $TUZC_6(8,8)$ nanotube, (b) $TUZC_6$ nanotube.

It is easy to see that, $|E_1(G)| = 0$, $|E_2(G)| = 4p$, and $|E_3(G)| = 3pq - 5p$. Now using Eq. (1), we easily arrive at:

Theorem 2. The ISI index of $G=TUZC_6(p,q)$ nanotube is given by:

$$ISI(G) = \frac{9}{2}pq - \frac{27}{10}p.$$

TUC₄C₈ nanotubes

A C_4C_8 net is a trivalent decoration constructed from alternating squares C_4 and octagons C_8 . Two classes of these nanotubes are $TUC_4C_8(R)$ nanotubes and $TUC_4C_8(S)$ nanotubes.

TUC₄C₈(R) nanotubes

Let $G=TUC_4C_8(R)$ (see Fig. 3). We denote the number of squares in each row of by p and the number of squares in each column by q .

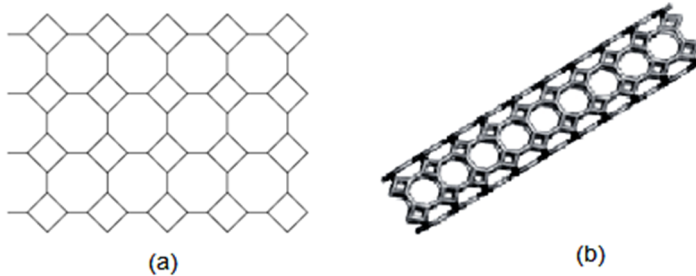


Figure 3. (a) The 2-dimensional lattice of $TUC_4C_8(R)$ nanotube with $p=5$ and $q=4$, (b) $TUC_4C_8(R)$ nanotube.

It is easy to see that, $|E_1(G)| = 0$, $|E_2(G)| = 4p$, and $|E_3(G)| = 6pq - 5p$. Now using Eq. (1), we easily arrive at:

Theorem 3. The ISI index of $G=TUC_4C_8(R)$ nanotube is given by:

$$ISI(G) = 9pq - \frac{27}{10}p.$$

TUC₄C₈(S) nanotubes

Let $G=TUC_4C_8(S)$ (see Fig. 4). We denote the number of squares in each row of by p and the number of rows by q .

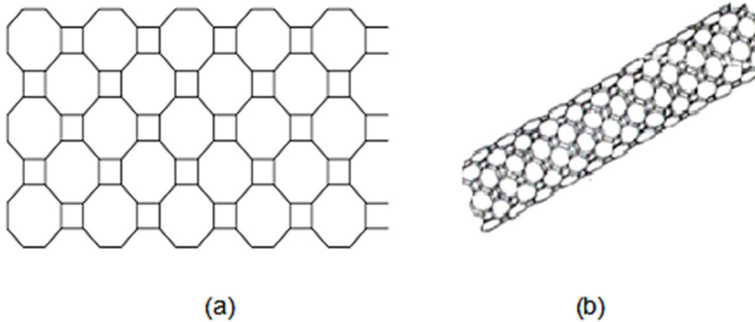


Figure 4. (a) The 2-dimensional lattice of $TUC_4C_8(S)$ nanotube with $p=5$ and $q=6$, (b) $TUC_4C_8(S)$ nanotube.

It is easy to see that, $|E_1(G)| = 2p$, $|E_2(G)| = 4p$, and $|E_3(G)| = 6pq - 8p$. Now using Eq. (1), we easily arrive at:

Theorem 4. The ISI index of $G=TUC_4C_8(S)$ nanotube is given by:

$$ISI(G) = 9pq - \frac{26}{5}p.$$

TUC₅C₇ nanotubes

A C_5C_7 net is a trivalent decoration constructed from alternating pentagons C_5 and heptagons C_7 . Three members of these nanotubes are $TUHC_5C_7$ nanotubes, $TUSC_5C_7$ nanotubes, and $TUHAC_5C_7$ nanotubes.

TUHC₅C₇ nanotubes

Let $G=TUHC_5C_7(p,q)$ (see Fig. 5). We denote the number of pentagons in each row by p . In this nanotube, the four first rows of vertices and edges are repeated, alternatively. We denote the number of this repetition by q .

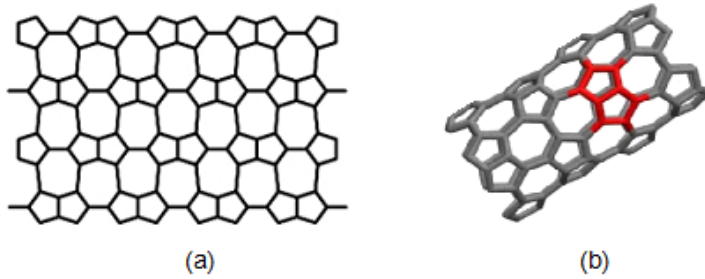


Figure 5. (a) The 2-dimensional lattice of $TUHC_5C_7(8,2)$ nanotube, (b) $TUHC_5C_7$ nanotube.

It is easy to see that, $|E_1(G)| = 0$, $|E_2(G)| = 4p$, and $|E_3(G)| = 12pq - 5p$. Now using Eq. (1), we easily arrive at:

Theorem 5. The ISI index of $G=TUHC_5C_7(p,q)$ nanotube is given by:

$$ISI(G) = 18pq - \frac{27}{10}p.$$

TUSC₅C₇ nanotubes

Let $G=TUSC_5C_7(p,q)$ (see Fig. 6). We denote the number of pentagons in each row by p . In this nanotube, the two first rows of vertices and edges are repeated, alternatively. We denote the number of this repetition by q .

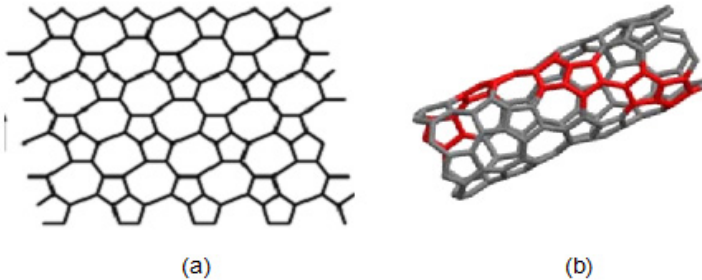


Figure 6. (a) The 2-dimensional lattice of $TUSC_5C_7(4,4)$ nanotube, (b) $TUSC_5C_7$ nanotube.

It is easy to see that, $|E_1(G)| = p$, $|E_2(G)| = 6p$, and $|E_3(G)| = 12pq - 12p$. Now using Eq. (1), we easily arrive at:

Theorem 6. The ISI index of $G=TUSC_5C_7(p,q)$ nanotube is given by:

$$ISI(G) = 18pq - \frac{49}{5}p.$$

TUHAC₅C₇ nanotubes

Let $G=TUHAC_5C_7(p,q)$ (see Fig. 7). We denote the number of heptagons in each row by p . In this nanotube, the three first rows of vertices and edges are repeated, alternatively. We denote the number of this repetition by q .

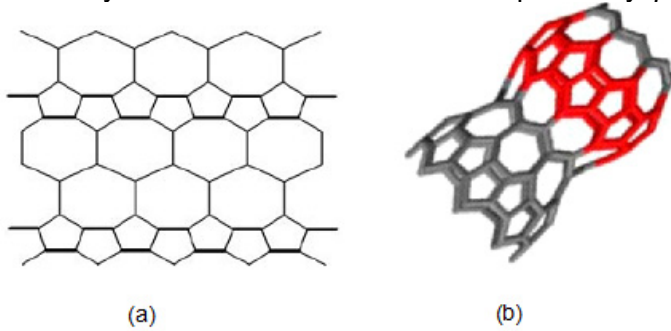


Figure 7. (a) The 2-dimensional lattice of $TUHAC_5C_7(4,2)$ nanotube, (b) $TUHAC_5C_7$ nanotube.

It is easy to see that, $|E_1(G)| = 0$, $|E_2(G)| = 4p$, and $|E_3(G)| = 12pq - 5p$. Now using Eq. (1), we easily arrive at:

Theorem 7. The ISI index of $G=TUHAC_5C_7(p,q)$ nanotube is given by:

$$ISI(G) = 18pq - \frac{27}{10}p.$$

TUHAC₅C₆C₇ nanotube

A $C_5C_6C_7$ net is a trivalent decoration constructed from alternating pentagons C_5 , hexagons C_6 , and heptagons C_7 . Let $G=TUHAC_5C_6C_7(p,q)$ (see Fig. 8). We denote the number of pentagons in each row by p . In this nanotube, the three first rows of vertices and edges are repeated, alternatively. We denote the number of this repetition by q .

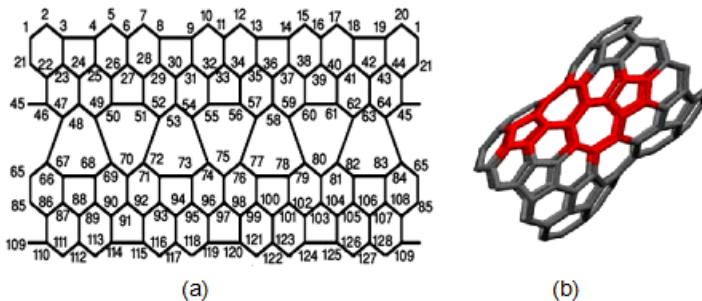


Figure 8. (a) The 2-dimensional lattice of $TUHAC_5C_6C_7(4,2)$ nanotube, (b) $TUHAC_5C_6C_7$ nanotube.

It is easy to see that, $|E_1(G)| = 0$, $|E_2(G)| = 8p$, and $|E_3(G)| = 24pq - 10p$. Now using Eq. (1), we easily arrive at:

Theorem 8. The ISI index of $G=TUHAC_5C_6C_7(p,q)$ nanotube is given by:

$$ISI(G) = 36pq - \frac{27}{5}p.$$

REFERENCES

1. I. Gutman, O.E. Polansky, "Mathematical Concepts in Organic Chemistry", Springer, Berlin, **1986**.
2. M.V. Diudea (Ed.), "QSPR/QSAR Studies by Molecular Descriptors", NOVA, New York, **2001**.
3. D. Vukičević, M. Gašperov, *Croat. Chem. Acta*, **2010**, 83(3), 243.
4. <http://www.molecularDescriptors.eu/dataset/dataset.htm>
5. <http://www.iamc-online.org/>
6. J. Sedlar, D. Stevanović, A. Vasilyev, *Discrete Appl. Math.*, **2015**, 184, 202.
7. S. Iijima, *Nature*, **1991**, 354, 56.
8. M.V. Diudea, *MATCH Commun. Math. Comput. Chem.*, **1995**, 32, 71.
9. M.V. Diudea, *Studia Univ. Babeş-Bolyai Chem.*, **2003**, 48(2), 17.
10. M.V. Diudea, C.L. Nagy, "Periodic Nanostructures", Springer, Dordrecht, Netherlands, **2007**.
11. H. Shababi, A.R. Ashrafi, I. Gutman, *Studia Univ. Babeş-Bolyai Chem.*, **2010**, 55(4), 107.
12. M. Azari, A. Iranmanesh, *Studia Univ. Babeş-Bolyai Chem.*, **2011**, 56(3), 59.
13. Y. Alizadeh, M. Azari, T. Došlić, *J. Comput. Theor. Nanosci.*, **2013**, 10(6), 1297.
14. M. Azari, A. Iranmanesh, I. Gutman, *MATCH Commun. Math. Comput. Chem.*, **2013**, 70, 921.
15. M. Azari, A. Iranmanesh, *MATCH Commun. Math. Comput. Chem.*, **2014**, 71, 373.
16. A. Iranmanesh, M. Azari, *Curr. Org. Chem.*, **2015**, 19(3), 219.
17. A. Iranmanesh, M. Azari, "The first and second Zagreb indices of several interesting classes of chemical graphs and nanostructures", in: M.V. Putz, O. Ori (Eds.), *Exotic Properties of Carbon Nanomatter*, Springer Netherlands, Dordrecht, **2015**, 8, 153.
18. M. Azari, F. Falahati-Nezhad, *J. Comput. Theor. Nanosci.* (to appear).
19. M. Azari, A. Iranmanesh, M.V. Diudea, *Studia Univ. Babeş-Bolyai Chem.* (to appear).

***Dedicated to Professor Mircea Diudea
on the Occasion of His 65th Anniversary***

A QSPR MODEL FOR STEROIDS

LAVINIA L. PRUTEANU^{a,*}, SARA ERSALI^a, SORANA D. BOLBOACA^b

ABSTRACT. A QSPR (Quantitative Structure-Property Relationship) model was derived for a set of forty 7 beta-hydroxysteroid compounds selected from PubChem database in order to assess the link between structural features and lipophilicity expressed as logP. After optimization and topological indices data collecting, the cluster of molecules was superposed onto a representative hypermolecule. Based on each molecule atoms positions, a binary vector and its weighted by mass fragments was computed for each molecule in the set. A model relating the structure with logP was identified based on the contributions of statistically significant positions of each molecule superposed on the hypermolecule and based on structural descriptors. The obtained model was validated in leave-one-out analysis as well as on training versus test analysis.

Keywords: 7 beta-Hydroxysteroid, QSPR (Quantitative Structure-Property Relationships), logP, hypermolecule

INTRODUCTION

The interest for production of steroidal drugs began in 1952 when Murray and Peterson used *Rhizopus* species and patented the process of 11 alfa-hydroxylation of progesterone [1]. Since then, numerous studies based on transformation of steroids have been developed in order to find new drugs and also hormones derived from steroids, hydroxylation being one of the most widely applied transformations [2-4]. The 7 beta-hydroxysteroid derivatives are steroid compounds having one hydrogen atom replaced by a hydroxyl group at the carbon atom in position 7. For this study, forty molecules of this group have

^a Babeş-Bolyai University, Faculty of Chemistry and Chemical Engineering, 11 Arany Janos str., RO-400028, Cluj-Napoca, Romania

^b Iuliu Hațieganu University of Medicine and Pharmacy, Department of Medical Informatics and Biostatistics, 6 Louis Pasteur str., RO-400349, Cluj-Napoca, Romania

* Corresponding Author: pruteanulavinia@gmail.com

been downloaded from the PubChem database, namely those molecules with a high structural similarity. One of the predictive methods used for modeling different properties is represented by Quantitative Structure Property Relationships (QSPR).

There are some more elaborated methods for prediction of molecular properties, such as Comparative Molecular Field Analysis (CoMFA) [5, 6], CODESSA (Comprehensive Descriptors for Structural and Statistical Analysis), Hologram QSAR [7], PDTA (Photodynamic Therapy Activity) [7], along with the traditional QSPR procedures using simple or multiple linear regression analysis (MLRA) [8-11].

In this study, the concept of reunion, of molecular structural features of the studied set, as a hypermolecule [12], was used to investigate the relation between structural features of a sample 7 beta-Hydroxysteroid and its lipophilicity.

RESULTS AND DISCUSSION

A significant regression model with estimation abilities was obtained with seven variables identified as significant positions (Eq. 1 is represented in Table 1).

$$\log P = 36.2431 + 0.0180 \cdot CjDi - 1.6780 \cdot AD - 0.0353 \cdot DI + 0.0228 \cdot CjDe - 0.0605 \cdot P18 - 0.0542 \cdot P33 - 0.0495 \cdot P35 \quad (1)$$

$$R^2 = 0.9610, R^2_{adj} = 0.9525, Q^2 = 0.9413; s = 0.4808, n = 40$$

$$F\text{-statistics (p-value)} = 113 (1.02 \cdot 10^{-20})$$

where R^2 = determination coefficient, R^2_{adj} = adjusted determination coefficient; Q^2 = determination coefficient in leave-one-out analysis; s = standard error of estimate; n = sample size; F -statistics = Fisher statistics, p -value = probability to obtain the model by chance.

Table 1. Significant positions and their regression coefficients

Variable	Coefficients	Standard Error	t Stat (p-value)
Intercept	36.2431	4.4755	8.10 (3.01 · 10 ⁻⁹)
CjDi	0.0180	0.0020	8.82 (4.41 · 10 ⁻¹⁰)
AD	-1.6780	0.2383	-7.04 (5.53 · 10 ⁻⁸)
DI	-0.0353	0.0060	-5.85 (1.69 · 10 ⁻⁶)
CjDe	0.0228	0.0043	5.35 (7.12 · 10 ⁻⁶)
P18	-0.0605	0.0197	-3.07 (4.37 · 10 ⁻³)
P33	-0.0542	0.0157	-3.44 (1.63 · 10 ⁻³)
P35	-0.0495	0.0137	-3.61 (1.04 · 10 ⁻³)

CjDi = Cluj distance; AD = Adjacency;
 DI = Distance; CjDe = Cluj detour;
 P18 = Position 18; P33 = Position 33; P35 = Position 35

The model was selected as the best alternative, being the one with high explanatory power at the smallest number of predictors. The model was obtained by applying successively the forward stepwise method for the set of descriptors given in Tables 3 and 4. Having a insignificant contribution to the model able to explain the logP values, the following descriptors were excluded from the model (in this order: CON, p28, p36, p37 at 5% risk being in error; p43, p40 at 1% risk being in error followed by a procedure of backward stepwise which removed the rest of the non-explanatory variables: CFDi, CFDe, p17, p26, p34, p50, D3D and DE).

The obtained model seems to have the errors between the predicted and the observed values homogenously distributed between observations, as the goodness-of-fit plot reveals (Figure 1).

The explanatory power of the model was analyzed with leave-one-out strategy, when the obtained explanatory power was 0.9413 (see Eq.1).

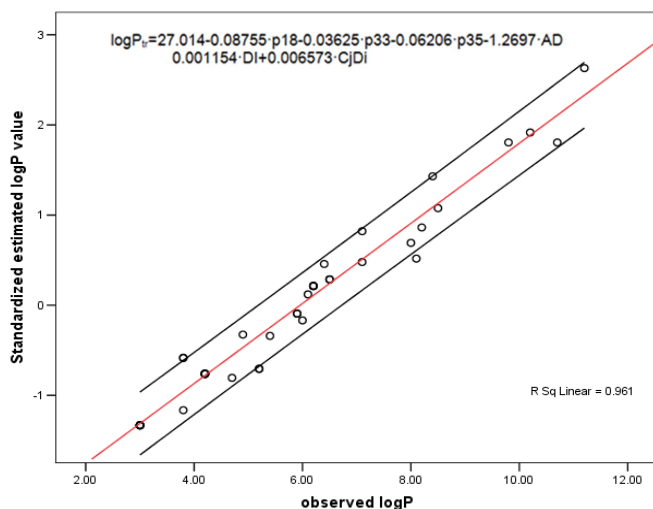


Figure 1. Goodness-of-fit of estimation model (the red line is the model fit and the black line is associated 95% confidence interval)

A training vs. test analysis was conducted on the selected pool of descriptors, when the set of 40 molecules were split in 24 molecules as the training set and 16 of them were used for the test of the model obtained. Following molecules were randomly selected to belong to the training set: 57396177, 49823443, 16082386, 16758147, 22216291, 9922115, 70688976, 70682680, 22213946, 11647965, 57390981, 12358742, 313039, 76325907, 57401396, 76327928, 76322252, 16759984, 24982302, 52947587, 12760132, 76336739, 76310266, and 70697302. The regression equation obtained with these molecules was used to predict the logP values for the rest of the molecules

(test set). The equation is:

$$\begin{aligned} \log P_{tr} = & 27.014 - 0.08755 \cdot p18 - 0.03625 \cdot p33 - 0.06206 \cdot p35 - 1.2697 \cdot \\ & AD - 0.001154 \cdot DI + 0.006573 \cdot CjDi \end{aligned} \quad (2)$$

$r^2_{tr} = 0.9337$, $F_{tr} = 40$ (probability of wrong model $p_F < 5 \cdot 10^{-9}$)
 $r^2_{ts} = 0.8730$, $F_{ts} = 9$ (probability of wrong model $p_F < 2.6 \cdot 10^{-3}$)

where tr = training set; ts = test set

As the training vs. test analysis shown, it is a little drop in the explanatory power when the model is not fed with the whole pool of molecules, and this fact can be explained by the large number of descriptors used to construct de structure-property relationship (in this case, a number of 7 variables were used, with an average of 5.7 molecules per descriptor for the whole pool of molecules and 5.0 molecules if we count the intercept too and a number of 3.42 molecules per descriptor for the training set and 3.0 molecules if we count the intercept too). Therefore, it is expected for a model having a small ratio between the number of molecules and the number of descriptors to produce such drop in the explanatory power when the input data are reduced in size.

CONCLUSIONS

The analysis drawn with the hypermolecule constructed from superposition of the molecules from the dataset shows a series of advantages, such as the natural reconstruction of the expected profile of action, as well as a series of disadvantages, such as the dropping of the explanatory power for the analysis conducted with a test set. Based on the selected model, which includes a series of positions in the hypermolecule, one can say that the positions 18, 33 and 35 are the ones which decreases the most (all these positions have a negative effect on the logP value, coefficients of it being negative) the value of logP.

MATERIALS AND METHODS

The set of forty 7 β -hydroxysteroid derivatives was downloaded from PubChem database [13] and were used as input data in this analysis. The name, PubChem identification numbers along with the value of logP are given in Table 2.

The molecules geometry was optimized in HyperChem program at semi-empirical PM3 level of theory. The resulted log-files with the data collection were extracted using the utility program JSChem [14].

Table 2. The forty derivatives of 7 β -Hydroxysteroids

No.	ID	logP									
1	12760132	10.2	11	76310266	8.2	21	57390981	5.2	31	76322257	10.7
2	70682679	7.1	12	56663807	6.4	22	16758147	8.5	32	76325907	3.8
3	70682680	6.5	13	56847117	6.2	23	22213946	6.2	33	76327928	3.8
4	70688976	6.2	14	70686910	6	24	16759984	5.9	34	76333144	4.2
5	70693211	6.2	15	70691082	7.1	25	16758161	4.2	35	371617	6.1
6	70697302	6.5	16	11647965	8.4	26	76336739	11.2	36	313039	8
7	12836861	4.7	17	52947587	4.9	27	57396177	3	37	9922115	4.2
8	24867469	4.2	18	24982302	3.8	28	57399636	3	38	9924252	5.4
9	16082386	8.1	19	49823443	5.9	29	57401396	3	39	11551321	3
10	12358742	5.2	20	22216291	3	30	76322252	9.8	40	11957457	4.2

A series of topological descriptors [15] were calculated by TopoCluj program [16] on the matrices: adjacency (AD), connectivity (CON), distance (DI), D3D - 3D (three-dimensional) distance, detour (DE), Cluj distance (CjDi), Cluj detour (CjDe), Cluj indices (on distance CFDi and on detour CFDe), the results being given in Table 3.

All the molecular structures were superposed to draw a hypermolecule by using Nano Studio program [17]. The resulted hypermolecule mimics the configuration or shape of the biological receptor to which the ligands have to bind [18].

Table 3. Calculated topological indices for the 7 beta-Hydroxysteroids in Table 2

Mol.	AD	CON	DI	D3D	DE	CjDi	CjDe	CFDi	CFDe
1	35	35	2522	4138.48	7313	4573.5	1750.5	5062	1809
2	34	34	2670	3980.77	6965	4467	1923.5	4918	1966.5
3	33	33	2369	3510.96	6451	4047	1665	4487	1706.5
4	33	33	2342	3522.35	6424	4019.5	1638	4460	1679.5
5	33	33	2342	3355.66	6424	4019.5	1638	4460	1679.5
6	33	33	2369	3520.97	6451	4047	1665	4487	1706.5
7	25	25	926	1354.38	3297	1729.5	546.5	1983	572.5
8	24	24	802	1163.2	2969	1504.5	463	1739	486.5
9	33	33	2335	3350.73	6511	4029	1648.5	4550.5	1693
10	26	26	1052	1868.14	3627	1956.5	632	2229	660.5
11	35	35	2237	3659.41	8399	4455.5	1302	5281	1361
12	33	33	2345	3436.73	6348	3996	1647.5	4362	1687.5
13	33	33	2342	3309.13	6424	4019.5	1638	4460	1679.5
14	32	32	2098	3117.36	5967	3657.5	1436.5	4086	1476.5
15	34	34	2560	3759.51	6855	4349.5	1813.5	4808	1856.5
16	36	36	2435	3417.31	8962	4849.5	1424.5	5718	1485
17	24	24	796	1153.47	2949	1490.5	461	1732	488
18	27	27	1149	1681.56	3971	2130	715.5	2485	747.5
19	23	23	699	988.57	2662	1310	402	1516	421.5
20	25	25	887	1279.08	3279	1655	535.5	1966	562.5
21	26	26	1052	1530.66	3627	1956.5	632	2229	660.5
22	36	36	2436	3497	9036	4811.5	1459.5	5703.5	1521.5
23	33	33	2342	3355.66	6424	4019.5	1638	4460	1679.5
24	23	23	699	1023	2662	1310	402	1516	421.5
25	24	24	802	1158.41	2969	1504.5	463	1739	486.5

Mol.	AD	CON	DI	D3D	DE	CjDi	CjDe	CFDi	CFDe
26	35	35	2944	4219.49	7659	5068.5	2080.5	5527	2130
27	25	25	887	1279.08	3279	1655	535.5	1966	562.5
28	25	25	887	1279.08	3279	1655	535.5	1966	562.5
29	25	25	887	1279.08	3279	1655	535.5	1966	562.5
30	34	36	2668	3785.72	7103	4609	1864.5	5048.5	1911.5
31	34	34	2668	3828.26	7103	4609	1864.5	5048.5	1911.5
32	27	27	1172	1646	3967	2178	728	2483	763
33	27	27	1172	1654.23	3967	2177.5	728	2482.5	762.5
34	24	24	802	1169.48	2969	1504.5	463	1739	486.5
35	24	24	732	1086.05	2660	1437	483.5	1707.5	501.5
36	32	32	2276	3204.88	6075	3832	1619	4173	1656.5
37	24	24	802	1169.48	2969	1504.5	463	1739	486.5
38	28	30	1412	2008.12	4395	2535	914	2829	944.5
39	25	25	887	1279.08	3279	1655	535.5	1966	562.5
40	24	24	802	1169.48	2969	1504.5	463	1739	486.5

The hypermolecule description was made by means of mass fragments with respect to the logP as the modelled property in order to identify a model able to both estimate and predict the logP on a series of 7 β -hydroxysteroid derivatives. This has been demonstrated as an efficient and helpful method in prediction of molecular property and/or bioactivities [11, 18, 19].

Superposition of the forty ligands over the hypermolecule (Figure 2) resulted in a binary vector, of value 1 for those positions with existing atoms and value 0 otherwise.

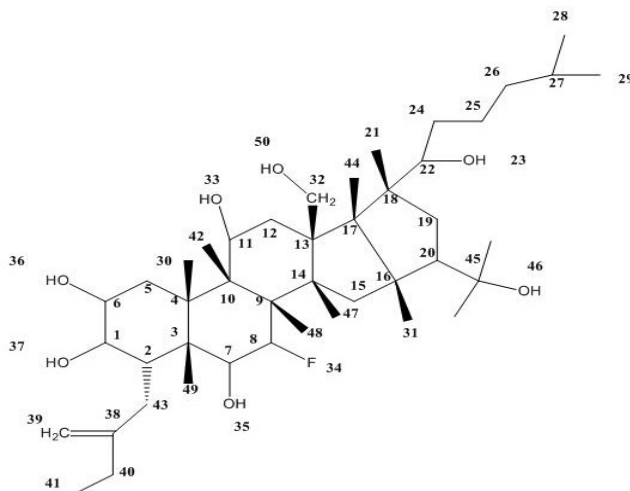


Figure 2. Representation in ChemBioDraw of the hypermolecule comprising all common and different structural features of each molecule and its atoms positions

Next, the value 1 was replaced by the corresponding mass fragment weight. After a primary correlation, only statistically significant positions were retained (Table 4).

A QSPR MODEL FOR STEROIDS

Table 4. Statistically significant positions, calculated with the mass fragment weight

Mol.	p17	p18	p26	p28	p33	p34	p35	p36	p37	p40	p43	p50
1	12.011	12.011	12.011	0	0	0	0	0	17.007	0	12.011	0
2	12.011	12.011	12.011	12.011	0	0	17.007	0	17.007	0	0	0
3	12.011	12.011	12.011	12.011	0	0	17.007	0	17.007	0	0	0
4	12.011	12.011	12.011	0	0	0	17.007	0	17.007	0	0	0
5	12.011	12.011	12.011	0	0	0	17.007	0	17.007	0	0	0
6	12.011	12.011	12.011	12.011	0	0	17.007	0	17.007	0	0	0
7	12.011	17.007	0	0	0	0	0	0	17.007	0	0	0
8	12.011	17.007	0	0	0	0	0	0	17.007	0	0	0
9	12.011	12.011	12.011	0	0	19	17.007	0	17.007	0	0	0
10	12.011	12.011	0	0	0	0	0	0	17.007	0	0	0
11	12.011	12.011	0	0	0	0	0	0	17.007	0	12.011	0
12	12.011	12.011	12.011	0	0	0	0	0	17.007	0	0	0
13	12.011	12.011	12.011	0	0	0	17.007	0	17.007	0	0	0
14	12.011	12.011	12.011	0	0	0	17.007	0	17.007	0	0	0
15	12.011	12.011	12.011	12.011	0	0	17.007	0	17.007	0	0	0
16	12.011	12.011	0	0	0	0	0	0	17.007	0	12.011	0
17	12.011	0	0	0	0	0	0	17.007	17.007	0	0	0
18	12.011	12.011	0	0	17.007	0	0	0	17.007	0	0	0
19	12.011	0	0	0	0	0	0	0	17.007	0	0	0
20	12.011	17.007	0	0	17.007	0	0	0	17.007	0	0	0
21	12.011	12.011	0	0	0	0	0	0	17.007	0	0	0
22	12.011	12.011	0	0	0	0	17.007	0	0	0	0	0
23	12.011	12.011	12.011	0	0	0	17.007	0	17.007	0	0	0
24	12.011	0	0	0	0	0	0	0	17.007	0	0	0
25	12.011	17.007	0	0	0	0	0	0	17.007	0	0	0
26	12.011	12.011	12.011	0	0	0	0	0	17.007	12.011	12.011	0
27	12.011	17.007	0	0	17.007	0	0	0	17.007	0	0	0
28	12.011	17.007	12.011	0	17.007	0	0	0	17.007	0	0	0
29	12.011	17.007	0	0	17.007	0	0	0	17.007	0	0	0
30	12.011	12.011	12.011	0	0	0	0	0	17.007	0	12.011	0
31	12.011	12.011	12.011	0	0	0	0	0	17.007	12.011	12.011	0
32	12.011	12.011	0	0	0	0	0	0	17.007	0	0	17.007
33	12.011	12.011	0	0	0	0	0	0	17.007	0	0	17.007
34	12.011	17.007	0	0	0	0	0	0	17.007	0	0	0
35	0	0	0	0	0	0	17.007	17.007	17.007	0	0	0
36	12.011	12.011	12.011	17.007	0	0	0	0	17.007	0	0	0
37	12.011	17.007	0	0	0	0	0	0	17.007	0	0	0
38	12.011	12.011	0	0	0	0	0	0	17.007	0	0	0
39	12.011	17.007	0	0	17.007	0	0	0	17.007	0	0	0
40	12.011	17.007	0	0	0	0	0	0	17.007	0	0	0

LogP property was modeled using mass fragments for weighting the superposition vectors. The model was validated by the leave-one-out and training vs. test procedures [20,21].

The whole sample was randomly split [22] in training and test sets, with ~2/3 of compounds in training set. The compounds in the training set was used to identify the model while the compounds in test set was used to validate this model.

ACKNOWLEDGMENTS

This paper is a result of a doctoral research being financially supported by the Sectoral Operational Programme for Human Resources Development 2007-2013. co-financed by the European Social Fund under the project POSDRU/187/1.5/S/155383 - "Doctoral and postdoctoral programs for scientific research support".

REFERENCES

1. D.H. Peterson, H.C. Murray, *Journal of the American Chemical Society*, **1952**, *74*, 5933.
2. S.B. Mahato, S. Garai, *Steroids*, **1997**, *62(4)*, 332.
3. A. Malaviya, J. Gomes, *Bioresource Technology*, **2008**, *99*, 6725.
4. H. Pellissier, M. Santelli, *Organic Preparations and Procedure International*, **2001**, *33(1)*, 1.
5. H. Hong, H. Fang, Q. Xie, R. Perkins, D.M. Sheehan, W. Tong, *SAR QSAR Environmental Research*, **2003**, *14(5-6)*, 373.
6. T.G. Gantchev, H. Ali, J.E. Van Lier, *Journal of Medicinal Chemistry*, **1994**, *37*, 4164.
7. W. Tong, D.R. Lowis, R. Perkins, Y. Chen, W.J. Welsh, D.W. Goddette, T.W. Heritage, D.M. Sheehan, *Journal of Chemical Information and Computer Sciences*, **1998**, *38(4)*, 669.
8. N. Frimayanti, M.L. Yam, H.B. Lee, R. Othman, S.M. Zain, N.A. Rahman, *International Journal of Molecular Sciences*, **2011**, *12*, 8626.
9. A. Golbraikh, A. Tropsha, *Journal of Computer-Aided Molecular Design*, **2002**, *5*, 231.
10. S.D. Bolboacă, L. Jäntschi, *BIOMATH. International Conference on Mathematical Methods and Models in Biosciences*, **2013**, *2(1)*, 1309089
11. M. Goodarzi, B. Dejaegher, Y.V. Heyden, *Journal of AOAC International*, **2012**, *95(3)*, 636.
12. A.M. Harsa, T.E. Harsa, S.D. Bolboacă, M.V. Diudea, *Current Computer-Aided Drug Design*, **2014**, *10(2)*, 115.
13. PubChem [online] Available from: <https://pubchem.ncbi.nlm.nih.gov/compound/439865>.
14. C.L. Nagy, M.V. Diudea, JSCHEM 1.0. Babeş-Bolyai University, Cluj, **2004**.
15. M.V. Diudea, I. Gutman, L. Jäntschi, *Molecular Topology*, NOVA: New York, **2002**.
16. O. Ursu, M.V. Diudea, TOPOCLUJ software program, Babeş-Bolyai University, Cluj, **2005**.
17. C.L. Nagy, M.V. Diudea, Nano Studio. 1.0., Babeş-Bolyai University, Cluj, **2009**.
18. A.M. Harsa, T.E. Harsa, M.V. Diudea, *Journal of Enzyme Inhibition and Medicinal Chemistry*, **2011**, *26(4)*, 1.
19. T.E. Harşa, A.M. Harşa, M.V. Diudea, B. Szeffler, *Revue Roumaine de Chimie*, **2015**, *60(7-8)*, 727.
20. S.D. Bolboacă, L. Jäntschi, M.V. Diudea, *Current Computer-Aided Drug Design*, **2013**, *9(2)*, 195.
21. S.D. Bolboacă, L. Jäntschi, *Environmental Chemistry Letters*, **2008**, *6*, 175.
22. S.D. Bolboacă, *Applied Medical Informatics*, **2010**, *28(2)*, 9.

*Dedicated to Professor Mircea Diudea
on the Occasion of His 65th Anniversary*

EFFECTS OF Cu DOPING ON NANO STRUCTURE, MORPHOLOGY AND PHOTOCATALYTIC ACTIVITY OF ZnO THIN FILM SYNTHESIZED BY SOL-GEL METHOD

**FATEMEH MOOSAVI^a, MOHAMMAD EBRAHIM BAHROLOLOOM^{a,*},
RAMIN KAMJOU^b**

ABSTRACT. Zinc oxide has been investigated due to its large band gap and several applications in science and industry. However, doping extrinsic impurities would change the resistivity of ZnO films which enhance their properties. In the present study, nano-structured ZnO and Cu-doped ZnO photocatalysts were successfully prepared on glass substrates by sol-gel dip-coatig method. Various techniques such as X-ray diffraction (XRD), scanning electron microscopy (SEM), field emission scanning electron microscopy (FESEM) and UV-VIS absorption spectroscopy were used to investigate the effect of the Cu-doped on ZnO thin film. The results showed that the doping greatly changed the microstructure, morphology and optical properties of ZnO, which may contribute to the enhancement of photocatalytic activity. The photocatalytic activity of the prepared pure ZnO and Cu-doped ZnO photocatalyst was investigated by the degradation of Methylene Blue solution. The results indicated that Cu-doped ZnO had a higher photocatalytic activity and Cu dopant greatly increased the photocatalytic activity of ZnO. Using C# programming language, we developed a software for more analyzing results.

Keyword: *Cu-doped ZnO, Thin film, Sol-Gel, Photocatalyst.*

^a *Department of Materials Science and Engineering, Shiraz University, Shiraz, Iran*

^b *Young Researchers and Elite Club, Shiraz Branch, Islamic Azad University, Shiraz, Iran*

* *Corresponding Author: bahrolom@shirazu.ac.ir*

INTRODUCTION

As a very low cost and environmental friendly material, zinc oxide is an n-type semiconductor that has a wide band gap (3.3 eV) and exciton binding energy (60 meV) [1]. It is one of the most important metal oxide semiconductors that found applications in many fields such as transparent conducting oxide (TCO) [2], photocatalyst [3], piezoelectric anogenerators [4], solar cells [5], gas sensors [6], UV detectors [7], optoelectronic devices [8], and so on. Also TiO₂ is a very good photocatalyst but, in some cases, ZnO presents higher advantages [9], because of the mobility and separation of its photo induced electrons and holes and non-expensive, high yield production [10]. Owing to aforementioned applications of ZnO, various methods such as chemical vapor deposition (CVD) [11], sputtering [12], metal organic chemical vapor deposition (MOCVD) [13], pulsed laser deposition [14] and sol-gel have been used to prepare ZnO thin films. Among these methods, sol-gel technique is very popular, since it is non-expensive and reliable technique, that needs simple equipment [15]. In this work we report the influence of Cu doping on the microstructure, morphology, optical properties and photocatalytic activity of ZnO thin films prepared by sol-gel method. Also pristine ZnO thin films were produced and their properties compared with Cu doped samples.

RESULTS AND DISCUSSION

Structural and Morphological Characterization

Figure 1 (a & b) shows the XRD patterns of un-doped and Cu-doped thin films. From this figure, three main diffraction peaks of (111), (002) and (101) planes can be seen, indicating the films have a polycrystalline hexagonal wurtzite structure (JCPDS card no. 36-1451) while the diffraction peaks of copper oxides (CuO or Cu₂O) were not detected. Moreover, Figure 1 indicates that Cu doping shifts the XRD peaks to higher angles. The average crystallite size was estimated by using of Scherrer equation [16]:

$$d = \frac{k\lambda}{\beta \cos\theta} \quad (1)$$

where k is a constant (0.9) and d, λ , θ and β are the average crystallite size (nm), wavelength of X ray radiation (0.1546 nm), Bragg's angle of diffraction and full-width at half maximum intensity of the peaks, respectively. According to calculations, Cu doping decreased the average crystallite size from 21.245 nm to 17.514 nm.

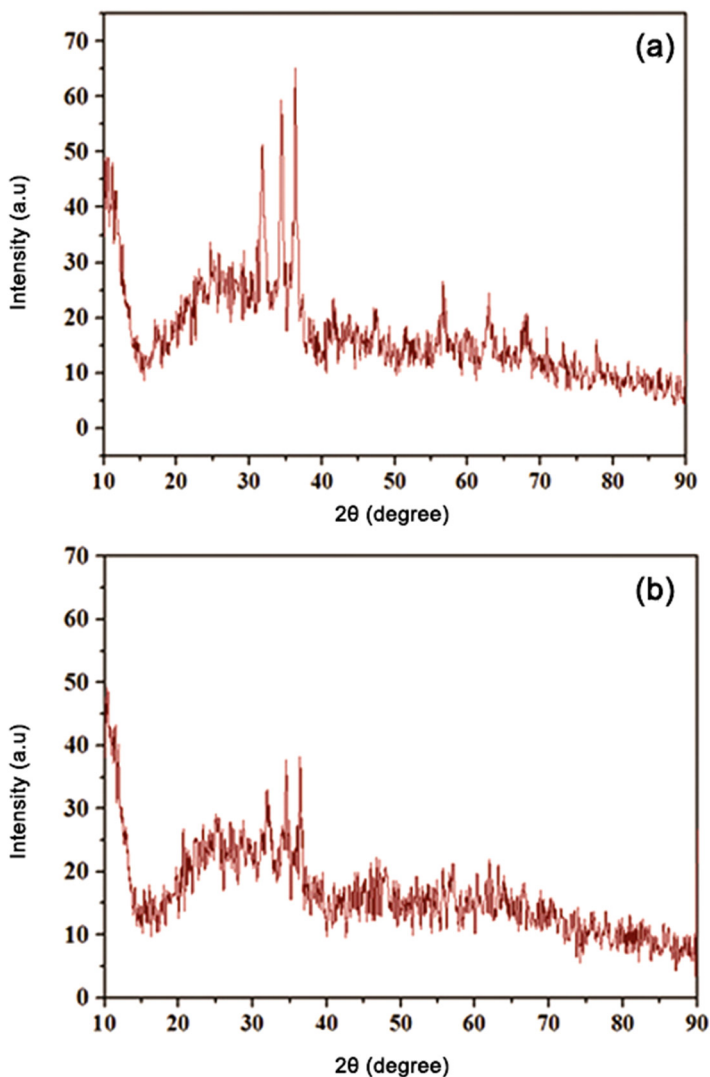


Figure 1. XRD patterns of: (a) ZnO thin film, (b) Cu-doped ZnO thin film.

The surface morphology of pristine ZnO and Cu doped ZnO thin film is shown in Figure 2. The ZnO thin film shows a wrinkle morphology, with an approximate width of 0.5-1 μm , whereas the Cu-doped ZnO film has a spherical morphology, where diameter of the spheres is about 0.5-1 μm .

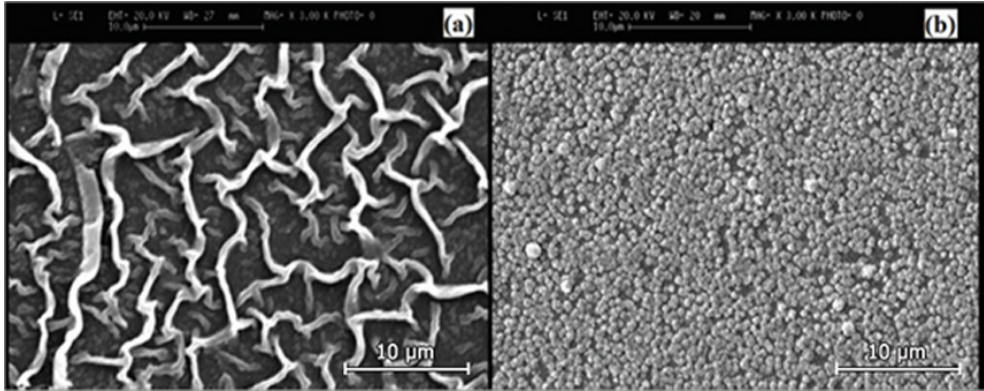


Figure 2. SEM micrographs of (a) pristine ZnO thin film and (b) Cu-doped ZnO thin film.

Cross-section FE-SEM micrographs of pristine and Cu-doped ZnO thin films is shown in Figure 3. It is obvious that thickness of ZnO thin film increased by Cu doping. It is well-known that in dip coating process, thickness of films is controlled by the viscosity of the liquid, the solid content and the withdrawal speed [17]. Since the total dissolved solids in the solution of Cu doped ZnO is larger than in that of pristine ZnO, the thickness of doped ZnO thin film is expected to be higher, while the viscosity of the liquid increased.

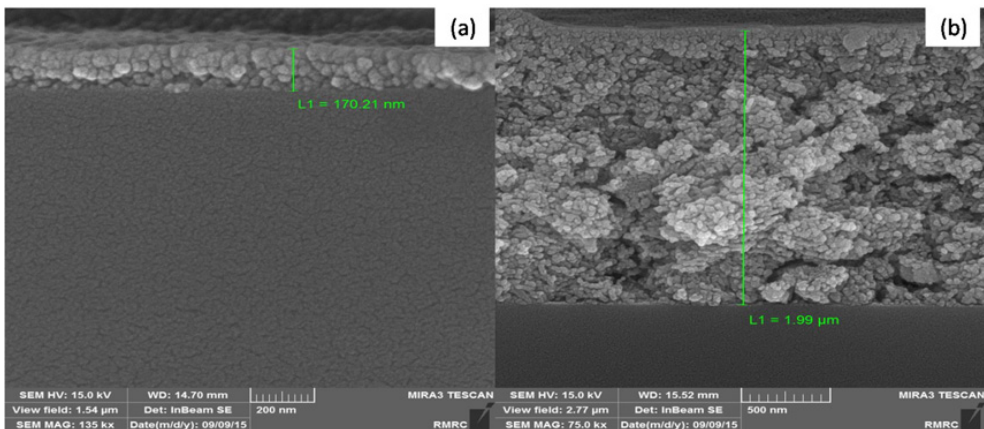


Figure 3. FESEM micrographs of (a) pristine ZnO thin film and (b) Cu-doped ZnO thin film.

Figure 4 shows the optical absorbance spectra of pristine and Cu doped ZnO thin films deposited on glass substrates. It seems that band gap energy of ZnO thin film decreased by Cu doping. According to [18] by increasing in thickness of sample, UV absorbance will increase. Therefore, as shown in Figure 4, the absorption edge of ZnO thin films has moved toward longer wavelength by Cu doping.

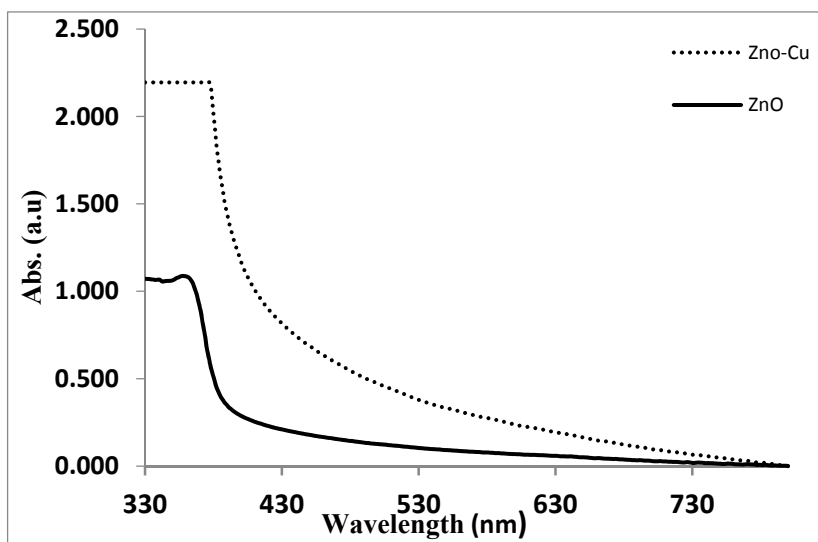
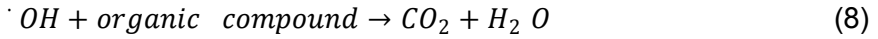


Figure 4. Absorbance spectra of non-doped and Cu-doped ZnO thin films.

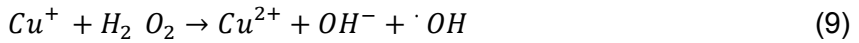
Photocatalytic Activity

The photocatalytic activity of pristine and Cu doped ZnO thin films were measured by degradation of methylene blue (MB) in an aqueous solution. Curves of degradation of methylene blue (%) versus time, for pristine and Cu doped ZnO are shown in Figure 5. According to the photocatalytic activity principles, when photons with energy equal or greater than ZnO band gap hit on the surface, the valence band electrons are excited and go to the conduction band therefore a hole is created in the valence band. The mechanism of photocatalytic activity of ZnO thin films is presented as follows [3]:





It is seen that the catalytic efficiency of the thin films increases with Cu doping. In the case of Cu-doped ZnO thin film, Cu can improve the photocatalytic activity of ZnO thin film by the following mechanism [19]:



Also the surface to volume ratio of Cu-doped ZnO thin film is higher in comparison with pristine ZnO thin film. This is an advantage that may improve the photocatalytic activity of Cu-doped ZnO thin films [20].

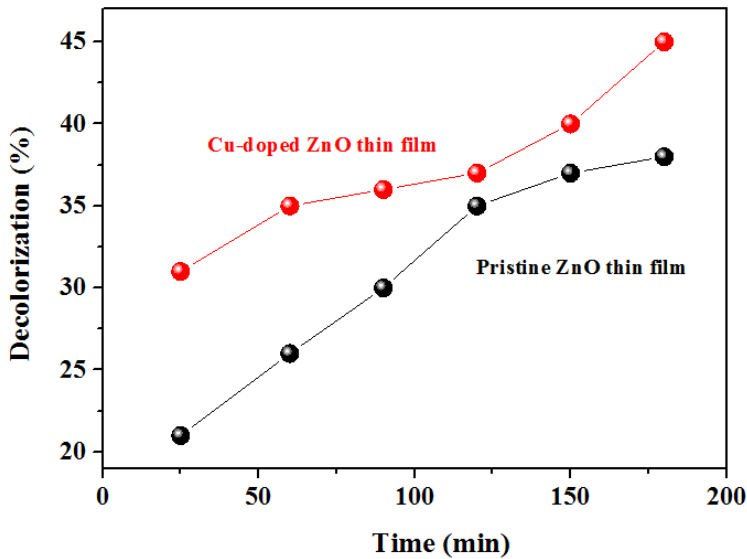


Figure 5. Time dependence of the decolouring efficiency of MB solution by doped and undoped ZnO thin films.

CONCLUSIONS

Pristine ZnO and Cu doped ZnO thin films were prepared by sol-gel followed by dip coating techniques. The thin films (doped and undoped) were characterized by XRD, SEM, FESEM and UV-VIS spectroscopy. The results showed that thin films had ZnO crystallite with a hexagonal wurtzite structure. It was observed that the surface morphology of ZnO thin film transformed from wrinkle morphology to spherical morphology by Cu doping. Furthermore Cu doping increased the thickness of thin film and the absorption edge was shifted to longer wavelengths. The photocatalytic activity of Cu doped ZnO thin film was greater than the activity achieved by pristine ZnO thin films under UV-light illumination.

EXPERIMENTAL SECTION

ZnO and Cu-doped ZnO thin films were synthesized by the sol-gel dip coating on the glass slides. To prepare a solution for coating, 0.3M zinc acetate dehydrate was dissolved in 10 ml iso-propanol containing monoethanolamine (as a stabilizer). The mole ratio of Zn^{2+} to MEA was kept 1:1. The required amounts of copper acetate was dissolved into the above solution to obtain a mole ratio of Cu^{2+} to Zn^{2+} =0.1. Then the mixed solution was stirred at 70°C for 1 h to accelerate the hydrolysis reaction. Final solution was clear and homogeneous which after being aged for 24h was used as the coating solution. Thin films were deposited by dip coating method on glass substrates (10mm × 15mm × 1.5mm) at room temperature. After each successive coating, the layers were dried for 10 min in an oven at 80 °C to remove the solvent. The coating and drying process were repeated ten times. Then the gel films were calcined at 400 °C for 60 min and finally the thin films cooled to room temperature to obtain the pristine ZnO and Cu-doped ZnO thin films.

The crystal structure of the un-doped and Cu-doped ZnO thin films was identified by using of an X-ray diffractometer (XRD, D-8 Advanced). Surface morphology of the thin films was determined by scanning electron microscopy (SEM, S-360 Cambridge). UV-VIS spectrophotometer (UV-4802UNCO) was used for the measurement of UV-Vis absorbance spectra of thin films.

The photocatalytic activity of thin films was quantified by means of the degradation of methylene blue (MB) in an aqueous solution. 5 mL of MB solution at an initial concentration of 10 mg/lit (10 ppm) was put in a glass container. Then the thin films were submersed in the glass container and this disposition was exposed to UV radiation. The light source of illumination was two

parallel UV lamp in a dark space. After irradiating for 0.5, 1, 1.5, 2, 2.5 and 3 h, the concentration of residual MB was determined in the same UV-VIS spectrophotometer used for measuring the optical transmission spectra of the thin films.

Developing Software

To make better use of this research, a software was developed (in C# language programming) by “Visual Studio 2012”, and the results were categorized by this software, named "ZnO Master". Physical properties, optical properties, etc. of ZnO, and the Method of doping ZnO are categorized in this software (Figure 6).

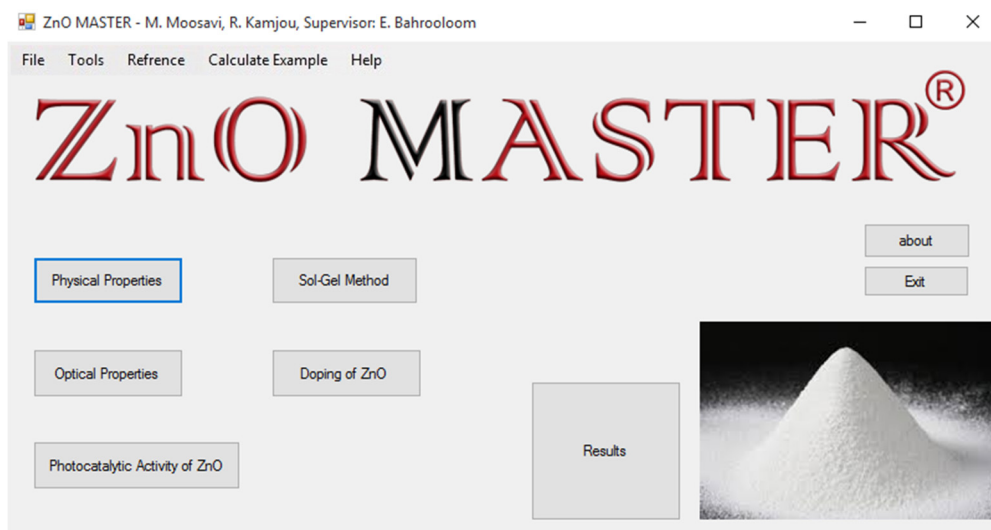


Figure 6. ZnO Master software environment.

ACKNOWLEDGMENTS

The authors would like to thank Prof. Sirus Javadpour and Eng. Ali Mirzaei for some advice and comments on this paper.

REFERENCES

1. P. Jongnavakit, P. Amornpitoksuk, S. Suwanboon, T. Ratana, *Thin Solid Films*, **2012**, 520, 5561.
2. N.V. Kaneva, D.T. Dimitrov, C.D. Dushkin, *Applied Surface Science*, **2011**, 257, 8113.
3. P. Jongnavakit, P. Amornpitoksuk, S. Suwanboon, N. Ndiege, *Applied Surface Scienc*, **2012**, 258, 8192.
4. W. Zhong Lin and J. Song, *Science*, **2006**, 312, 242.
5. O. Kluth, G. Schöpe, J. Hüpkes, C. Agashe, J. Müller, B. Rech, *Thin solid films*, **2003**, 442, 80.
6. N.J. Dayan, S.R. Sainkar, R.N. Karekar, R.C. Aiyer, *Thin Solid Films*, **1998**, 325, 254.
7. S. Safa, R. Sarraf-Mamoory, R. Azimirad, *Physica E: Low-dimensional Systems and Nanostructures*, **2014**, 57, 155.
8. V.L. Colvin, M.C. Schlamp, A.P. Alivisatos, *Nature*, **1994**, 370, 354.
9. D. Wang and G.P. Bierwagen, *Progress in Organic Coatings*, **2009**, 64, 327.
10. S. Sakthivel, B. Neppolian, M.V. Shankar, B. Arabindoo, M. Palanichamy, V. Murugesan, *Solar Energy Materials and Solar Cells*, **2003**, 77, 65.
11. K. Haga, M. Kamidaira, Y. Kashiwaba, T. Sekiguchi, H. Watanabe, *Journal of Crystal Growth*, **2000**, 214, 77.
12. V. Tvarozek, I. Novotny, P. Sutta, S. Flickyngerova, K. Schterevea, E. Vavrinsky, *Thin Solid Films*, **2007**, 515, 8756.
13. Y. Chen, N.T. Tuan, Y. Segawa, H. Ko, S. Hong, T. Yao, *Applied Physics Letters*, **2001**, 78, 1469.
14. X.M. Fan, J.S. Lian, Z.X. Guo, H.J. Lu, *Applied Surface Science*, **2005**, 239, 176.
15. B. Pal and M. Sharon, *Materials Chemistry and Physics*, **2002**, 76, 82.
16. K. Thongsuriwong, P. Amornpitoksuk, S. Suwanboon, *Advanced Powder Technology*, **2013**, 24, 275.
17. S.M. Attia, *Journal of Materials Science and Technology*, **2002**, 18, 211.
18. M. Öztas and M. Bedir, *Thin Solid Films*, **2008**, 516, 1703.
19. H.W.P. Carvalho, A.P.L. Batista, P. Hammer, T.C. Ramalho, *Journal of Hazardous Materials*, **2010**, 184, 273.
20. J. Lv, W. Gong, K. Huang, J. Zhu, F. Meng, X. Song, Zh. Sun, *Superlattices and Microstructures*, **2011**, 50, 98.

*Dedicated to Professor Mircea Diudea
on the Occasion of His 65th Anniversary*

APPROXIMATING THE ENERGY OF NANOTUBES

SIAMAK FIROUZIAN^{a,*}, MORTEZA FAGHANI^a AND
ALI REZA ASHRAFI^{b,c}

ABSTRACT. The eigenvalues of a graph are the eigenvalues of its adjacency matrix and the energy of a molecular graph is defined as the sum of absolute values of its eigenvalues. In this paper, some classical methods are used to evaluate the energy of nanotubes.

Keywords: *Eigenvalue, energy, nanotube.*

INTRODUCTION

A molecular graph $G(M)$ is called the pair $(V(M), E(M))$ of the sets $V(M)$ and $E(M)$ of atoms and chemical bonds of the molecule M . Throughout this paper we consider only simple molecular graphs, without multiple bonds and loops [1]. Suppose $V(M) = \{v_1, v_2, \dots, v_n\}$. Then the adjacency matrix $A(M) = [a_{ij}]$ is an $n \times n$ $\{0, 1\}$ -matrix in which for all integers i and j , $1 \leq i, j \leq n$, $a_{ij} = 1$ if and only if there is a chemical bond between v_i and v_j . The spectrum of a molecular graph $G(M)$ (simply denoted by M) is a multiset containing all numbers which are eigenvalues of $A(G)$, together with their multiplicities. Here, a multiset is a generalization of the concept of a set in which multiple instances of elements are allowed [2,3].

A molecular graph M is called bipartite if its vertex set can be partitioned into two disjoint sets R and S such that every edge connects a vertex in R and a vertex in S . The energy of a molecular graph, $\tilde{E}(M)$, is defined as the sum of

^a *Department of Mathematics, Payame Noor University, PO Box 19395-3697, Tehran, IRAN*

^b *Department of Mathematics, Faculty of Mathematical Sciences, University of Kashan, Kashan 87317-51167, I. R. Iran*

^c *Department of Nanocomputing, Institute of Nanoscience and Nanotechnology, University of Kashan, Kashan 87317-51167, I. R. Iran*

* *Corresponding Author: siamfirouzian@pnu.ac.ir*

absolute values of eigenvalues of M . In chemistry, the energy of a conjugated hydrocarbon is computed by the Hückel theory. Ivan Gutman [4,5] proved that if the molecular graph is bipartite then the two different concepts for energy will coincide. In [6], the dependence of energy on the size of the molecule and the number of Kekulé structures are studied in details, and in [7], the connection between the energy and the total electron energy of a class of organic molecules together with some basic mathematical properties of graph energy are presented.

Gutman et al. [8] proved that if F is a fullerene or nanotube with n carbon atoms, then $1.34n \leq \bar{E}(F) \leq 1.73n$; in [9] an infinite sequence of fullerene containing $10n$ vertices is considered. They proved that all terms of this sequence have a centrosymmetric adjacency matrix and by properties of centrosymmetric matrices and Key–Fan theorem, a better lower bound to the energy of the fullerene may be obtained for $n \in \{10 \times 2 \times 5, 10 \times 2 \times 7, 10 \times 2 \times 11, 10 \times 2 \times 13\}$. In [10], the centrosymmetry of another infinite series of fullerene graphs is proved and its upper bound is given.

John and Sachs [11] developed an elementary method to factor the characteristic polynomial of (3,6)–fullerene into smaller polynomials, all of the same size and in [12] the authors applied this result to compute the energy of a nanotorus and that of a (3, 6)–fullerene. In [13], some numerical methods are given in view of estimating the energy of nanohorns. In this paper, we continue [13] to approximate the energies of some nanotubes.

MAIN RESULTS

The Mathematical Nanoscience is a new branch of science that considers mathematical properties of nano-objects. The symmetry and topology are two important subjects in mathematics used for study of these new materials. For more information in this topic, we refer to innovating works of Diudea [14–18]. This section is concerned with the use of numerical techniques in the study of energy of the molecular graph of nanotubes. An approximation for the energy of the molecular graphs of a class of nanotubes (Figure 1) is presented. In Table 1, we search for the best of such a function to fit data listed in this table. Our main method applies a combination of two computer packages TopoCluj [19] and DataFit [20].

Suppose we have a data set $A = \{(x_1, y_1), \dots, (x_n, y_n)\} \subseteq \mathbb{C} \times \mathbb{C}$, where \mathbb{C} denotes the set of all complex numbers. This data set is usually based on an experiment or a measurement. It is easy to see that it is possible to find a sequence $\{\alpha_t\}_{t \geq n}$ such that $\alpha_t(x_i) = y_i$, for each i and t with $1 \leq i \leq n$ and $t \geq n$.

However, the function that fits data set A is not unique. By this reason finding a curve β with a given property to fit data set A is an important question in numerical analysis. In an exact phrase, the curve fitting is a curve that has the best fit to a series of data points and allows other constrains.

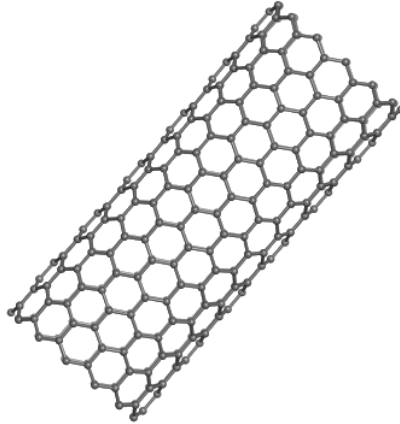


Figure 1. The Molecular Graph of a Nanotube.

Let $C: y = f(x)$ is a curve. We say that a point (a,b) belongs to this curve, if $b = f(a)$. This curve is called linear if for points (x_1,y_1) and (x_2,y_2) on C , we have $y_1 + y_2 = f(x_1 + x_2)$. For evaluating the energy of a sequence of nanotubes, we are interested in curve fitting by elementary functions containing polynomials, exponential and logarithmic functions.

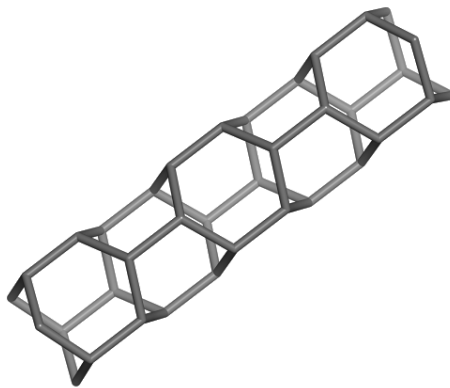


Figure 2. The Molecular Graph of $E[6]$.

In what follows, the eigenvalues of a sequence $\{E[n]\}_{n \geq 1}$ of zig-zag nanotubes with exactly $6n + 12$ vertices is considered (Figure 2). We have to note that the molecular graph of the open nanotubes is bipartite. A well-known result in algebraic graph theory states that the eigenvalues of every bipartite graph are symmetric about zero. Thus, the Energy of $E[n]$ is two times the summation of positive eigenvalues.

Recall that since the molecular graph of a nanotube is bipartite its graph and Hückel energies are the same. In Table 1, the positive eigenvalues of $E[n]$, $1 \leq n \leq 7$, together with their graph energies are given.

Table 1. The Positive Eigenvalues of $E[n]$, $1 \leq n \leq 7$.

Nano-tubes	Positive Eigenvalues	Energy
E[1]	2.7616, 2.1249, 1.8019, 1.8019, 1.3633, 1.2470, 1.2470, 0.4450, 0.4450	26.4752
E[2]	2.8512, 2.4329, 1.8794, 1.8794, 1.8372, 1.5321, 1.5321, 1.2555, 1.0000, 1.0000, 0.3473, 0.3473	35.7888
E[3]	2.8986, 2.6067, 2.1636, 1.9190, 1.9190, 1.6825, 1.6825, 1.6453, 1.3097, 1.3097, 1.1898, 0.8308, 0.8308, 0.2846, 0.2846	45.1144
E[4]	2.9265, 2.7123, 2.3770, 1.9565, 1.9419, 1.9419, 1.7709, 1.7709, 1.5120, 1.4971, 1.4970, 1.1466, 1.1361, 1.1361, 0.7092, 0.7092, 0.2411, 0.2411	54.4468
E[5]	2.9443, 2.9443, 2.5204, 2.1823, 1.9563, 1.9563, 1.8271, 1.8271, 1.7976, 1.6180, 1.6180, 1.4159, 1.3383, 1.3383, 1.1167, 1.0000, 1.0000, 0.6180, 0.6180, 0.2091, 0.2091	63.7832
E[6]	2.9564, 2.8276, 2.6203, 2.3458, 2.0215, 1.9659, 1.9659, 1.8650, 1.8649, 1.7004, 1.7004, 1.6740, 1.4780, 1.4780, 1.3443, 1.2053, 1.2053, 1.0951, 0.8915, 0.8915, 0.5473, 0.5473, 0.1845, 0.1845	73.1214
E[7]	2.9649, 2.8610, 2.6924, 2.4663, 2.1934, 1.9727, 1.9727, 1.8916, 1.8909, 1.8899, 1.7589, 1.7589, 1.5783, 1.5775, 1.5772, 1.3546, 1.3546, 1.2897, 1.0939, 1.0939, 1.0790, 0.8034, 0.8034, 0.4910, 0.4910, 0.1652, 0.1652	82.4630

Suppose $\lambda_1 \leq \lambda_2 \leq \dots \leq \lambda_{6n+12}$ are eigenvalues of the molecular graph of $E[n]$. From our calculations given in Table 1, we can suggest the following observations:

1. If $n > m$ then $\lambda_{6n+12}(E[n]) > \lambda_{6m+12}(E[m])$. As a consequence, $\lim_{n \rightarrow \infty} \lambda_{6n+12}(E[n]) = 3$.
2. There is no zero eigenvalue, but $\lim_{n \rightarrow \infty} \lambda_{3n+6}(E[n]) = 0$.
3. The function $a + b \times \ln(x) + c \times \exp(-x)$ is the best approximation model for energy.

Next we consider another sequence $\{F[n]\}_{n \geq 1}$, of armchair nanotubes (Figure 3), with exactly $6n + 6$ vertices. In Table 2, the positive eigenvalues of $F[n]$, $1 \leq n \leq 8$, and their energies are listed.

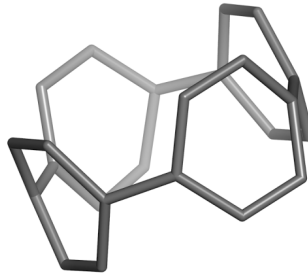


Figure 3. The Molecular Graph of $F[3]$.

Table 2. The Positive Eigenvalues of $F[n]$, $1 \leq n \leq 8$.

Nano-tubes	Positive Eigenvalues	Energy
F[1]	2.4142, 1.7321, 1.7321, 1, 1, 0.4142	16.5852
F[2]	2/4142, 2/101, 2/101, 1/2593, 1/2593, 1, 1, 1, 0.4142	25.098
F[3]	2.4142, 2.2361, 2.2361, 1.7321, 1.7321, 1, 1, 1, 1, 1, 0.4142	33.5296
F[4]	2.4142, 2.2996, 2.2996, 1.9683, 1.9683, 1.4581, 1.4581, 1, 1, 1, 1, 1, 0.8437, 0.4142	41.9356
F[5]	2.4142, 2.3344, 2.3344, 2.1010, 2.1010, 1.7320, 1.7320, 1.2593, 1.2593, 1, 1, 1, 1, 1, 1, 0.7420, 0.7420, 0.4142	50.3316
F[6]	2.4142, 2.3555, 2.3555, 2.1825, 2.1825, 1.9051, 1.9051, 1.5397, 1.5397, 1.1120, 1.1120, 1, 1, 1, 1, 1, 1, 1, 0.6721, 0.6721, 0.4142	58.7244
F[7]	2.4142, 2.3692, 2.3692, 2.2361, 2.2361, 2.0205, 2.0205, 1.7320, 1.7320, 1.3848, 1.3848, 1, 1, 1, 1, 1, 1, 1, 1, 1, 0.6220, 0.6220, 0.4142	67.1152
F[8]	2.4142, 2.3786, 2.3786, 2.2730, 2.2730, 2.1010, 2.1010, 1.8685, 1.8685, 1.5839, 1.5839, 1.2593, 1.2593, 1, 1, 1, 1, 1, 1, 1, 1, 1, 0.9129, 0.9129, 0.5849, 0.5849, 0.4142	75.5052

We now assume that $\sigma_1 \leq \sigma_2 \leq \dots \leq \sigma_{6n+12}$ are eigenvalues of the molecular graph of $F[n]$. From our calculations given Table 2, we can draw the following observations:

1. The maximum eigenvalue of $F[n]$, $n \geq 1$, is $\sqrt{2} + 1$. This eigenvalue is simple.
2. The minimum positive eigenvalues of $F[n]$, $n \geq 1$, is $\sqrt{2} - 1$. This eigenvalue is simple.

3. If $n > m$ then $\sigma_{6n+5}(F[n]) > \sigma_{6m+5}(F[m])$. As a consequence, $\lim_{n \rightarrow \infty} \sigma_{6n+5}(F[n]) = 1 + \sqrt{2}$.
4. If n is even then the multiplicity of 1 is $n + 1$ and for odd n , the multiplicity is $2n$.
5. The function $a + b \times \ln(x) + c \times \exp(-x)$ is the best approximation model for energy.

CONCLUSION

In this paper the power of numerical methods for investigation of energy of armchair and zig-zag nanotubes are investigated. Some results obtained by our numerical investigation can be proved in general, but evaluation of energy for nanotubes of arbitrary length and diameter is an open question for future study.

ACKNOWLEDGMENTS

The first author is partially supported by the Payame Noor University.

REFERENCES

1. N. Trinajstić, "Chemical Graph Theory", CRC Press, Boca Raton, FL, **1992**.
2. N. Biggs, "Algebraic Graph Theory", Second ed., Cambridge University Press, Cambridge, **1993**.
3. D. Cvetković, M. Doob, H. Sachs, "Spectra of Graphs—Theory and Application", third ed., Johann Ambrosius Barth Verlag, Heidelberg, Leipzig, **1995**.
4. I. Gutman, *Theoret. Chim. Acta (Berlin)*, **1977**, 45, 79.
5. I. Gutman, *Ber. Math.-Statist. Sect. Forschungszentrum Graz.*, **1978**, 103, 1.
6. I. Gutman, *Topics Curr. Chem.*, **1992**, 162, 29.
7. I. Gutman, The energy of a graph: old and new results, In: "Algebraic Combinatorics and Applications", A. Betten, A. Kohnert, R. Laue, A. Wassermann (Eds.), Springer-Verlag, Berlin, **2001**, pp. 196–211.
8. I. Gutman, S. Zare Firoozabadi, J.A. de la Peña and J. Rada, *MATCH Commun. Math. Comput. Chem.*, **2007**, 57, 435.
9. G.Y. Katona, M. Faghani and A.R. Ashrafi, *Discuss. Math. Graph Theory*, **2014**, 34, 751.

10. M. Ghorbani, M. Faghani, A.R. Ashrafi, S. Heidari-Rad and A. Graovac, *MATCH Commun. Math. Comput. Chem.*, **2014**, 71, 341.
11. P.E. John and H. Sachs, *Discrete Math.*, **2009**, 309, 2663.
12. S. Madani and A.R. Ashrafi, *Appl. Math. Letters*, **2012**, 25, 2365.
13. A.R. Ashrafi, F. Nassaj, M. Faghani and P.V. Khadikar, *Studia Universitatis Babes-Bolyai Chemia*, **2012**, 57, 137.
14. M.V. Diudea, *Bull. Chem. Soc. Jpn.*, **2002**, 75, 487.
15. M.V. Diudea and P.E. John, *MATCH Commun. Math. Comput. Chem.*, **2001**, 44, 103.
16. M.V. Diudea, B. Parv and E.C. Kirby, *MATCH Commun. Math. Comput. Chem.*, **2003**, 47, 53.
17. M.V. Diudea and E.C. Kirby, *Fullerene Sci. Technol.*, **2001**, 9, 445.
18. A. Parvan-Moldovan and M.V. Diudea, *Iranian J. Math. Chem.*, **2015**, 6, 163.
19. M.D. Diudea, O. Ursu and L.Cs. Nagy, TOPOCLUJ, Babes-Bolyai University, Cluj, **2002**.
20. P. Young, "Everything you wanted to know about data analysis and fitting but were afraid to ask", Springer Briefs in Physics, DOI 10.1007/978-3-319-19051-8_1.

*Dedicated to Professor Mircea Diudea
on the Occasion of His 65th Anniversary*

INFLUENCE OF THICKNESS ON THE PROPERTIES OF TiO₂ AND Ti(Nb)O₂ THIN FILMS

MIRELA SUCHEA^{a,b,c,*}, MARIA VAMVAKAKI^d,
DIMITRIS LOULOUidakis^a, MICHAEL SIGALAS^e,
NIKOLAOS KATSARAKIS^{a,b}, DIMITRA VERNARDOU^{a,b},
EMMANUEL KOUDOUMAS^{a,b}

ABSTRACT. Pure and Nb doped titanium dioxide films were grown by magnetron sputtering, for integration in hybrid polymer-semiconductor solar cells. The effect of the thickness of the films on their physical properties was investigated, emphasis given on the optical transparency, the surface morphology, the wettability and the conductivity. Particular surface parameters were determined and their variation with film thickness was investigated. Finally, a hydrophobic to hydrophilic transition under UV irradiation was studied.

Keywords: metal oxides, titanium dioxide, thin films, thickness, solar cells applications.

INTRODUCTION

Titanium dioxide (TiO₂) is a wide energy gap semiconductor, with its conduction band minima composing of the Ti 3d band and its valence maxima composed primarily of the O 2p states. As a result of oxygen deficiency and the occupied defect states, TiO_x (x < 2) is an n-type semiconductor, typically

^a Center of Materials Technology and Photonics, School of Engineering Technological Educational Institute of Crete, 71004 Heraklion, Greece

^b Electrical Engineering Department, School of Engineering Technological Educational Institute of Crete, 71004 Heraklion, Greece

^c "Al.I. Cuza" University of Iasi, 11 Bulevard Carol I, Iasi, 700506, Romania, Romania

^d Department of Materials Science and Technology, University of Crete, 70013 Heraklion, Greece

^e Department of Materials Science, University of Patras, 26504 Rio, Patras, Greece

* Corresponding Author: mirasucnea@staff.teicrete.gr

used as an electron transporting material in dye sensitized solar cells, [1, 2]. However, the traditional preparation methods of nano-crystalline TiO_2 are not compatible with processing of polymer solar cells. Moreover, high temperatures (450°C) required to obtain crystalline TiO_2 cannot be used for both polymers and plastic substrate processing, in the corresponding flexible version. Finally, mesoporous TiO_2 films obtained from the TiCl_4 precursor [3] have a large roughness and are not effective as an electrode interlayer. As a result, most TiO_2 films used for polymer solar cells are in amorphous phase, made as an example by a sol-gel process.

In such a case, the solution precursor is typically prepared using titanium isopropoxide, along with various solvent additives. After spin coating, TiO_2 films are formed upon hydrolysis at a temperature of about 150°C . Using such amorphous TiO_2 films, both conventional and inverted polymer solar cells have been fabricated and studied. In conventional cells, the incorporation of TiO_2 as an electron transporting layer resulted in enhanced short circuit currents and fill factors, when compared with those in devices using aluminum electrodes only. Using PCDTBT:PC71BM as the active medium, the optimum devices presented a power conversion efficiency of 6.1% [4], the enhancement of the power conversion efficiency attributed to the improved electrical coupling with PC71BM and the enhanced light harvesting due to optical interference with the TiO_2 film, acting as an optical spacer [5]. In bulk heterojunction solar cells, an active layer as thin as 60–80 nm is usually a good strategy, for polymers with low hole mobility and high absorption coefficient, since the optical field distribution in the absorber is sensitive to its distance from the back electrode, making the I–V characteristics highly dependent on the spacer thickness [6]. When TiO_2 was used as the bottom electrode interlayer, with PEDOT: PSS/gold as the top electrode, the power conversion efficiency of the resulting inverted P3HT:PC71BM cells was about 3% [7, 8]. TiO_2 has also been used as an n-type material for the interconnecting charge recombination layer for solution processed tandem polymer solar cells. With P3HT:ICBA and PDTS-BTD:PC71BM as the two absorbing layers, a power conversion efficiency of 7% [9] was reported.

Organic–inorganic photovoltaic cells based on conjugated polymers and inorganic semiconductors have attracted a great interest as an alternative type of polymer solar cells, as a trial in developing low-cost, large-area, flexible photovoltaic devices, due to the advantage of high electron mobility and excellent chemical and physical stabilities of the inorganic semiconductors [10–14]. In this type of device, an electron-donor material (p-type conjugated polymers, such as poly(3-hexylthiophene) (P3HT)) and an electron-acceptor material (n-type inorganic nanocrystals, such as CdSe, TiO_2 , ZnO and CdS) are used as the active layer, which can form polymer-nanoparticle bulk heterojunctions [15–23]. Broad visible-infrared absorption, higher charge carrier mobility, and suitable electronic energy levels of both the donor and the acceptor

materials are important parameters for high-efficiency polymer solar cells. To balance exciton dissociation and charge transport, an ideal configuration of polymer-inorganic photovoltaic cell should be a columnar segregated donor/acceptor structure, with the size of each donor or acceptor section within the exciton diffusion length, perpendicular to the device electrodes, to provide unconstrained way for charge carrier transport. Nanostructured TiO₂ thin films and nanostructures with large surface-to-volume ratio in highly ordered arrays or less ordered structures could be involved to facilitate separation of the photo-excited charges and provide excellent electron percolation pathways for fabricating high performance organic-inorganic photovoltaic cells.

TiO₂ films are promising photoanode structures for the polymer-inorganic photovoltaic cells if provided: (a) an effective method for their transfer onto conductive transparent layers, that can ensure perfect electrical contact; (b) a spectral response broader than their limited UV absorption (<387 nm); (c) appropriate wettability of their surface, that could be tuned, so that high-quality polymer-TiO₂ interfaces can be obtained, since TiO₂ is hydrophilic, while polymers are hydrophobic. The present study is focused on the effect of thickness on the physical properties of pure and Nb doped TiO₂ thin films, grown by magnetron sputtering.

RESULTS AND DISCUSSION

TiO₂ and Ti(Nb)O₂ thin films with thickness in the range 50 to 1000nm were grown onto Corning 1737F glass substrates, in an 100% argon atmosphere and deposition parameters: total pressure (8×10^{-3} mbar), substrate temperature 27°C (RT) and plasma current $I=0.45$ A. The films were characterised and their properties were analysed, so that these can be optimized for energy applications.

XRD characterization of all deposited films showed that these were amorphous, a result in agreement with previous studies on TiO₂ based thin films, deposited at room temperature (RT) [24,25]. Electrical measurements performed before and after UV irradiation, using the two-point method on films with ohmic contacts, showed that pure, as well as the Nb doped TiO₂ films were insulators. The films were found to be highly transparent in the visible wavelength region, with an average transmittance of 70-80% in both pure and doped case, the respective transmission being slightly higher for Nb doped films, as shown in Figure 1a. It is interesting to note that the transmittance in the visible does not seem to be strongly affected by the thickness, at least for the range of thicknesses studied. This can be seen in the Figure 1b for TiO₂ films with thickness from 50 to 1000nm. AFM images of the surfaces of the TiO₂ and

Ti(Nb)O₂ thin films with different thickness are shown in Figure 2. The images revealed a clear tendency for an increasing of the lateral grain size with increasing the thickness, from 12 to about 40 nm for TiO₂ films and 10 to 30 nm for Ti(Nb)O₂ films respectively. Larger thickness leads to the appearance of grain agglomerations on the film surface, with dimensions in the range of 100-200 nm. An example is shown in figure (2d) for the 1 μ m thick TiO₂ thin film, where RMS is about 10.53 nm, while z range is 63.19nm. In contrast, RMS of thinner films was quite smaller, being in the range of about 0.20 nm to 0.75 nm, the maximum height of the respective features on the surface being about 5 nm.

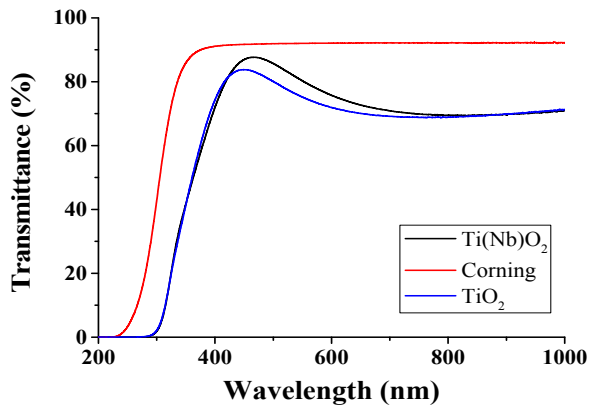


Figure 1a. UV-VIS transmission spectra of 100 nm TiO₂ and Ti(Nb)O₂ thin films

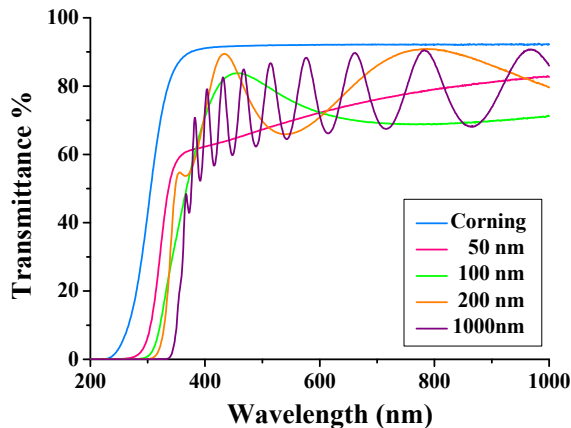


Figure 1b. UV-VIS transmission spectra of TiO₂ thin films with different thickness.

INFLUENCE OF THICKNESS ON THE PROPERTIES OF TiO₂ AND Ti(Nb)O₂ THIN FILMS

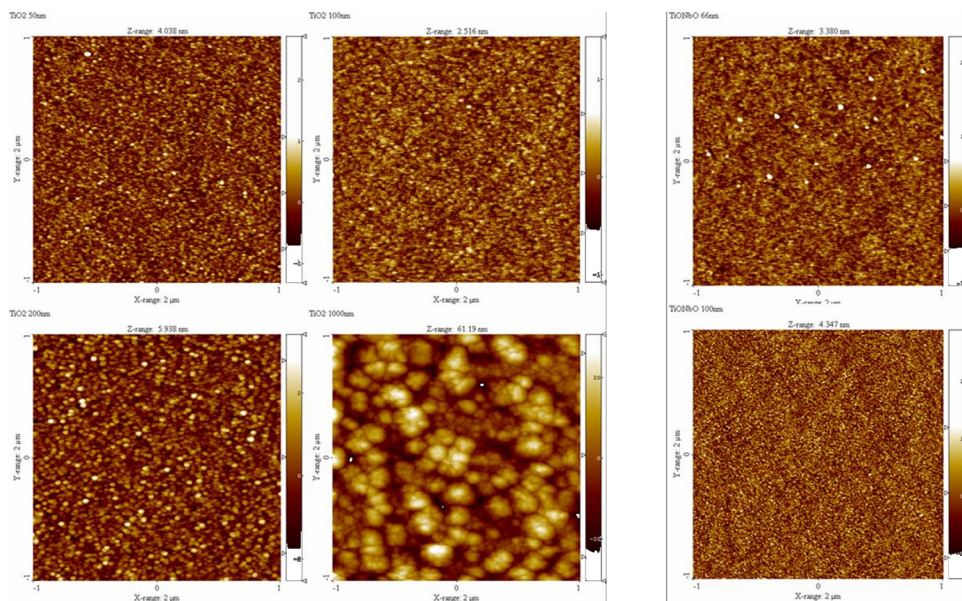


Figure 2. AFM images of TiO₂ films with different thickness (a: 50nm, b: 100nm, c: 200nm and d: 1 μ m) and (Nb)O₂ films (e: 66nm, f: 100nm). Scan size 2x2 μ m.

For more accurate description of the surface morphology, surface bearing index (S_{bi}), surface fractal dimension (SFD), skewness (SSK) and real surface ratio (SR) were also estimated. With increasing thickness, S_{bi} values were found to be almost constant, having values between 0.56 and 0.6 for pure TiO₂ and 0.6 to 0.64 for Nb doped films, while SR was increased from about 0.15% to over 6% in both cases. It is worth to mention that for similar thickness, Nb doped films showed overall larger SR and S_{bi} values. SFD and SSK were also found to increase with increasing thickness. Larger SFD values can be associated with higher compactness of the surface, while larger skewness reflects hill over valley domination. These variations are correlated with the film formation. In the case of thinner films, the growth time is shorter and the resulted surface exhibits a more homogeneous distribution of small grains, resulting in low RMS values. At the same time, SSK, SFD and SR values are small due to the large concentrations of valley like boundaries. For longer deposition periods, small grains aggregation leads to the formation of larger grains with a subsequent increase in the measured lateral grain size, leading to an overall “bulkier”, rougher film, with larger active surface. Nb doping of thin films seems to induce a slight decrease of the lateral surface grains size, resulting lower roughness, but also improved homogeneity and higher SSK, SFD and SR values with respect to those of the pure TiO₂ films.

The TiO₂ thin films were found to exhibit an amphiphilic behavior, since the surface was formed by both hydrophilic and hydrophobic domains. Those domains are generated mainly by the molecules adsorbed on the surface, this phenomenon occurring because the crystalline lattice tends to extend, in order to achieve similar vicinity for the surface atoms as for those of the bulk material and because the surface atoms are bond deficient. Due to this property, reversible transitions from hydrophobic to hydrophilic surface behavior can be achieved. Surface amphiphilicity is determined by the growth conditions.

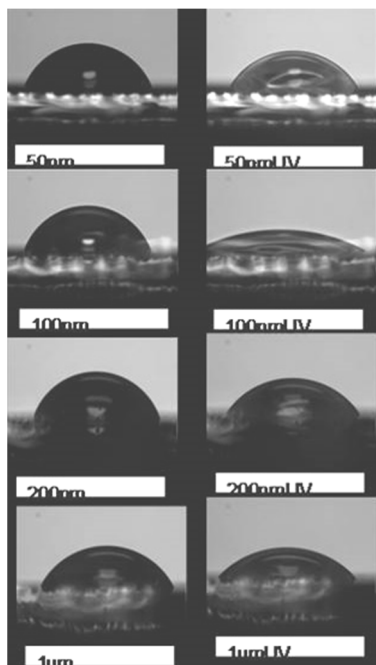


Figure 3a. Photos of water droplets on the surface of the TiO₂ films

The sessile drop geometry was then employed to determine the contact angle of water on the TiO₂ film surfaces. The method is based on the principle that the profile of a sessile drop of one fluid is governed by a balance between the surface/interfacial tensions. The advantage of this method for the determination of the contact angles is the fact that one uses the whole drop profile and not just the contact points with the substrate surface, since then, the actual value of the contact angle is extracted from the data and is not affected by possible impurities at the drop edges at the surface. Each drop (10 μL) of distilled, deionised Millipore water (18.2 MΩ) was formed from a capillary tip, and was detached gently upon the substrate of interest. The atmosphere around the droplet was kept rich in water vapours, in order to achieve minimum evaporation. The contact angle was then calculated by integration of the best-fit differential

equations that characterize the droplet shape. Moreover, in order to check the contact angle after the photo-reduction of the surface, the samples were directly irradiated in air by the UV light of a mercury pencil lamp at a distance of approximately 5 cm for 10 min, so that a steady state can be obtained. As found out, the contact angle depends on the film thickness, the respective dependence shown in Figure 3, which presents both photos of the water droplets on the surface of the films and the variation of the calculated contact angles with thickness before and after the UV irradiation. As can be seen, the contact angles are reduced after the UV irradiation, indicating a hydrophobic to

hydrophilic transition. Moreover, this transition was found to be more effective in the pure TiO₂ films and the films with larger thickness. Due to the fact that all experiments were performed in similar conditions, we can assume that the observed differences are due to the film surface. Then, we tried to correlate the observed changes with surface parameters calculated from AFM surface scans for the films. Figure 4 shows the variation of the contact angle after UV exposure with S_{bi} . As can be seen, increasing of S_{bi} results in a more hydrophilic behaviour.

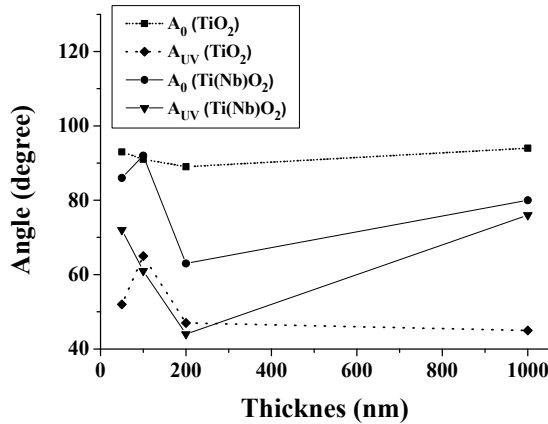


Figure 3b. Variation on contact angle as a function of thickness before (A_0) and after (A_{UV}) UV irradiation.

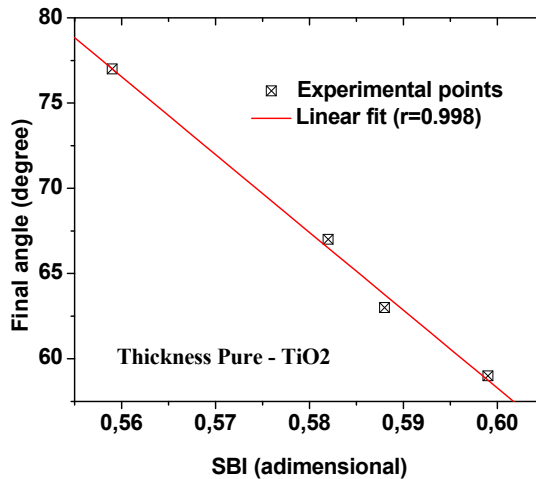


Figure 4. Contact angle variation with the S_{bi} after UV exposure.

S_{bi} is related to the material available for initial load support and it is defined as the ratio of the RMS deviation over the surface height at 5% bearing area.

$$S_{bi} = \frac{RMS}{Z_{0.05}} = \frac{1}{h_{0.05}}$$

where $h_{0.05}$ is the normalized surface height at 5% bearing area. A larger surface bearing index indicates a good bearing property. For a Gaussian height distribution, S_{bi} approaches 0.608 for increasing number of pixels.

The contact angle for water droplets deposited on clean films is linearly varying with the surface bearing index. The clean surface is obtained by irradiating the thin film with UV light.

Finally, the SR effect on the contact angle values before and after UV exposure is shown in figure 5. As can be seen, very small and very large values of SR result in small contact angles.

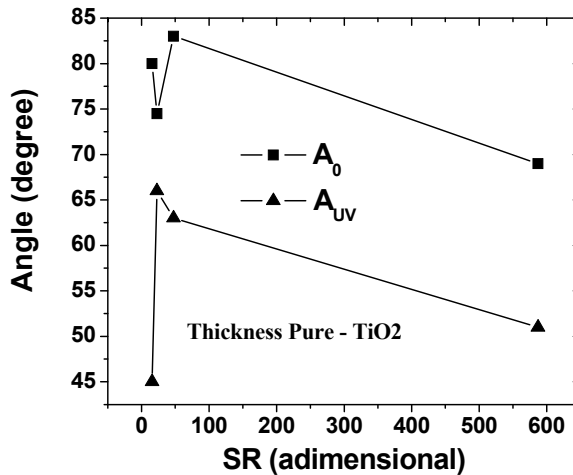


Figure 5. SR effect on the contact angle before and after UV exposure.

CONCLUSIONS

Pure and Nb doped titanium dioxide films were grown by magnetron sputtering for integration in hybrid polymer-semiconductor solar cells and the effect of film thickness on the physical properties of the films was investigated. As found out, under the used experimental conditions, the films are amorphous, highly transparent and of low conductivity. Moreover, thinner films exhibit a more homogeneous distribution of small grains, while, small grains aggregation

leads to “bulkier”, rougher films with larger active surface. Nb doping was found to induce a slight decrease of the lateral surface grains size, resulting lower roughness, but also improved homogeneity. Finally, the films surface was found to present a reversible transition from hydrophobic to hydrophilic, the overall behavior correlating the surface parameters.

EXPERIMENTAL SECTION

The deposition of the TiO₂ and Ti(Nb)O₂ films was carried out in an magnetron sputtering system using pure ceramic targets, total pressure 8×10^{-3} mbar, substrate temperature 27 °C (RT) and plasma current 0.45A. The thickness was measured using an in-situ thickness monitor and verified using a profilometer. AFM measurements were performed in air at RT using a Digital Instrument AFM with Nanoscope III controller in tapping mode. Ultra-sharp silicon cantilevers (NSC15 series, 125 mm long, spring constant ~ 40 N/m, resonant frequency ~ 200 -400 kHz) were used. The images were collected at 512×512 pixels per image at a scan rate of 1 Hz. In the present study the RMS (which is considered to be an index for the roughness), S_{bi} (surface bearing index) and SR (the ratio between real of the film surface and geometric scan surface) grain radius and features dimensions were evaluated using the Scanning Probe Image Processor, SPIP image processing software on the captured images. In order to study the crystal structure of the deposited films, X-ray diffraction (XRD) measurements were performed using a Discovery 8 diffractometer with CuK α X-rays. The optical transmittance was measured using a Shimadzu ultraviolet visible spectrophotometer (UV-Vis). Contact angle measurements were performed on as-deposited and during/ after 10 min UV exposure. Electrical measurements were performed using the two points method on films with Ohmic contacts, before and after UV exposure.

ACKNOWLEDGMENTS

This project is implemented through the Operational Program "Education and Lifelong Learning" action Archimedes III and is co-financed by the European Union (European Social Fund) and Greek national funds (National Strategic Reference Framework 2007 - 2013).

REFERENCES

1. B. Oregan and M. Gratzel, *Nature*, **1991**, 353, 737.
2. U. Bach, D. Lupo, P. Comte, J.E. Moser, F. Weissortel, J. Salbeck, H. Spreitzer and M. Gratzel, *Nature*, **1998**, 395, 583.

3. B.C. O'Regan, J.R. Durrant, P.M. Sommeling and N.J. Bakker, *J. Phys. Chem. C*, **2007**, *111*, 14001.
4. S.H. Park, A. Roy, S. Beaupre, S. Cho, N. Coates, J.S. Moon, D. Moses, M. Leclerc, K. Lee and A.J. Heeger, *Nat. Photonics*, **2009**, *3*, 297.
5. J.Y. Kim, S.H. Kim, H.H. Lee, K. Lee, W.L. Ma, X. Gong and A.J. Heeger, *Adv. Mater.*, **2006**, *18*, 572.
6. A. Roy, S.H. Park, S. Cowan, M.H. Tong, S.N. Cho, K. Lee and A.J. Heeger, *Appl. Phys. Lett.*, **2009**, *95*, 013302.
7. C. Waldauf, M. Morana, P. Denk, P. Schilinsky, K. Coakley, S.A. Choulis and C.J. Brabec, *Appl. Phys. Lett.*, **2006**, *89*, 233517.
8. T. Kuwabara, T. Nakayama, K. Uozumi, T. Yamaguchi and K. Takahashi, *Sol. Energy Mater. Sol. Cells*, **2008**, *92*, 1476.
9. J. Yang, R. Zhu, Z.R. Hong, Y.J. He, A. Kumar, Y.F. Li and Y. Yang, *Adv. Mater.*, **2011**, *23*, 3465.
10. L. Shen, G.H. Zhu, W.B. Guo, C. Tao, X.D. Zhang, C.X. Liu, W.Y. Chen, S.P. Ruan, *Appl. Phys. Lett.*, **2008**, *93*, 073307.
11. S. Tepavcevic, S.B. Darling, N.M. Dimitrijevic, T. Rajh, S.J. Sibener, *Small*, **2009**, *5*, 1776.
12. K.J. Jiang, K. Manseki, Y.H. Yu, N. Masaki, K. Suzuki, Y.L. Song, S. Yanagida, *Adv. Funct. Mater.*, **2009**, *19*, 2481.
13. Muktha, D. Mahanta, S. Patil, G. Madras, *J. Solid State Chem.*, **2007**, *180*, 2986.
14. M. Mall, P. Kumar, S. Chand, L. Kumar, *Chem. Phys. Lett.*, **2010**, *495*, 236.
15. R. Po, M. Maggini, N. Camaioni, *J. Phys. Chem. C.*, **2010**, *114*, 695.
16. N. Lu, S. Chen, H.T. Wang, X. Quan, H.M. Zhao, *J. Solid State Chem.*, **2008**, *181*, 2852.
17. K. Palaniappan, J.W. Murphy, N. Khanam, J. Horvath, H. Alshareef, M. Quevedo-Lopez, M.C. Biewer, S.Y. Park, M.J. Kim, B.E. Gnade, M.C. Stefan, *Macromolecules*, **2009**, *42*, 3845.
18. X.X. Jiang, F. Chen, H. Xu, L.G. Yang, W.M. Qiu, M.M. Shi, M. Wang, *Sol. Energy Mater. Sol. Cells*, **2014**, *94*, 338.
19. J.A. Labastide, M. Baghgar, I. Dujovnet, Y. Yang, A.D. Dinsmore, B.G. Sumpter, D. Venkataraman, M.D. Barnes, *J. Phys. Chem. Lett.*, **2011**, *2*, 3085.
20. M. Krunks, A. Katerski, T. Dedova, I.O. Acik, A. Mere, *Sol. Energy Mater. Sol. Cells*, **2008**, *92*, 1016.
21. J.S. Kim, Y. Park, D.Y. Lee, J.H. Lee, J.H. Park, J.K. Kim, K. Cho, *Adv. Funct. Mater.*, **2015**, *20*, 18.
22. Y.Y. Lin, T.H. Chu, C.W. Chen, W.F. Su, *Appl. Phys. Lett.*, **2008**, *92*, 0533121.
23. G.K. Mor, S. Kim, M. Paulose, O.K. Karghese, K. Shankar, J. Bsaham, C.A. Grimes, *Nano Lett.*, **2009**, *9*, 4250.
24. E.V. Buta, P. Pascariu, F. Prihor, L. Vlad, V. Pohoatã, R. Apetrei, D. Luca, A. Nastuță, I. Alupoaei, D. Mardare, *Scientific Annals of "Alexandru Ioan Cuza din Iași" University*, **2008**, Tomul I, 4.
25. D. Wicaksana, A. Kobayashi, A. Kinbara, *J. Vac. Sci. Technol. A*, **1992**, *10*, 1479.

*Dedicated to Professor Mircea Diudea
on the Occasion of His 65th Anniversary*

THICKNESS EVOLUTION OF NICKEL NANO LAYER ON THE MICROSTRUCTURE AND ADHESION STRENGTH OF DLC FILMS

FATEMEH SHAHSAVARI^{a,*}, MARYAM EHTESHAMZADEH^b,
PARVIN ALIZADEH ESLAMI^c, AHMAD IRANNEJAD^b

ABSTRACT. Diamond-like carbon (DLC) films are metastable amorphous hydrogenated or non-hydrogenated forms of carbon, with excellent properties that make them reliable to use in various fields of science and technology. However, poor adhesion of DLC films to the substrate limits their performance. Using an interlayer is one of the methods to reduce the stress in films and improve the adhesion. In this study, different thickness of the nickel nano layers was deposited on the silicon substrates as an interlayer for the growth of DLC films. The Ni nano layers with the thickness of 10, 20, 40 and 80 nanometers were deposited on the substrates by DC magnetron sputtering while DLC films were synthesized by plasma enhancement chemical vapor deposition (PECVD) system with a mixture of argon and methane gases as the precursors. Morphology and the surface roughness of Ni interlayers were investigated by atomic force microscopy (AFM) which showed low surface roughness changing with thickness of interlayer. For the characterization of DLC films, Raman spectroscopy was used; it proved high degree of diamond-like character for the films grown on 10 nanometers nickel interlayer, as given by the ratio of I_D to I_G . FE-SEM (Field emission scanning electron microscopy) cross-section images of DLC films showed increasing of the thickness of DLC films by increasing of nickel nano layer thickness. The adhesion strength also was investigated by the nanoscratch test.

Keywords: *Nickel Nano Layer, Diamond-Like Carbon film, Adhesion Strength, Raman Spectroscopy*

^a Young Researchers Society, Mineral Industries Research Center, Shahid Bahonar University of Kerman, Kerman, Iran

^b Department of Materials Engineering, Shahid Bahonar University of Kerman, Kerman, Iran, P.O. Box 76169-133

^c Department of Chemistry, Tabriz Branch, Islamic Azad University, Tabriz, Iran

* Corresponding Author: shahsavari.fa@gmail.com

INTRODUCTION

Diamond like carbon (DLC) is a metastable form of amorphous carbon containing a mixture of tetragonal sp^3 and planar sp^2 carbon-carbon bonds [1]. The ratio of sp^3 to sp^2 bonds present in DLC films, largely affects their overall properties [1, 2]. DLC coatings have excellent properties like high hardness, high band gap, low friction coefficient, chemical inertness, wear resistance and biocompatibility [2-4]. Poor adhesion of DLC films to the substrate is the main limitation for their wide applications which is due to the presence of high internal compressive stress in the film and high diffusion of carbon into the substrate [3, 5]. Using a metal interlayer such as Cr, Ti, Al and Ni between the DLC and Si substrate is a one of the strategies to overcome this limitation [5-9].

In this work, the nickel nano interlayer was selected as an interlayer between DLC film and silicon substrate and various thicknesses of the Ni thin films were sputtered on the substrates. Plasma enhancement chemical vapor deposition (PECVD) technique [10] was applied for synthesis of DLC films. The results illustrate that the thickness of Ni nano layer is very effective in the microstructure and adhesion strength of DLC films.

RESULTS AND DISCUSSION

After the deposition of Ni layer, atomic force microscopy (AFM) was adopted to investigate the surface morphology and surface roughness of the layer. The AFM images of Ni layers are shown in Figure 1; they were named S_1 , S_2 , S_3 and S_4 according to their Ni layer thickness (10nm, 20nm, 40nm and 80nm, respectively).

Surface roughness of the substrate is one of the important parameters which could be characterized by atomic force microscopy in terms of RMS roughness [11]. In this study, the WSxM 5.0 software was used to measure the roughness and make the histogram of distribution of nano metal particle sizes. The results of RMS are shown in Figure 1, for each sample; one can see the increase of roughness by increasing the thickness of Ni nano layer. The histogram of distribution of Ni nano particle sizes on the surface (shown in Figure 2) indicates a homogenous distribution for all the samples.

Figure 3 presents the cross-sectional FE-SEM images of DLC films deposited on Ni nano layer and Si without an interlayer. In the absence of Ni, a very thin layer, with thickness of about 14nm was formed (Figure 3(a)). The Ni layer promotes the thickness of DLC film from 114nm to 728 nm, function of the Ni layer thickness (Figures 3 (b to e)); this fact proves the catalytic activity of Ni in adsorption and surface diffusion of carbon atoms to precipitate and form the DLC film [5, 12].

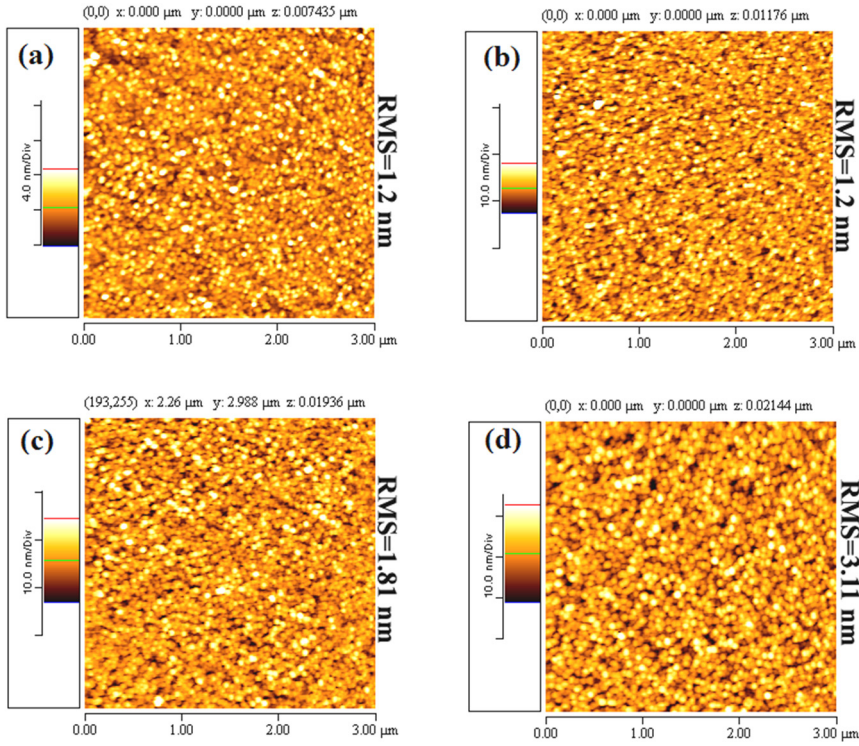


Figure 1. AFM images of a $3 \times 3 \mu\text{m}^2$ area of surface (a) S₁, (b) S₂, (c) S₃ and (d) S₄. The RMS surface roughness of each sample was inserted in right of each image.

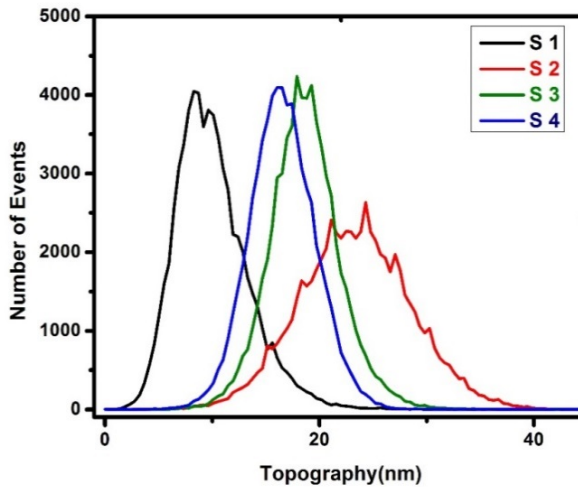


Figure 2. Size distribution of nickel nano particles on the surface of silicon substrate.

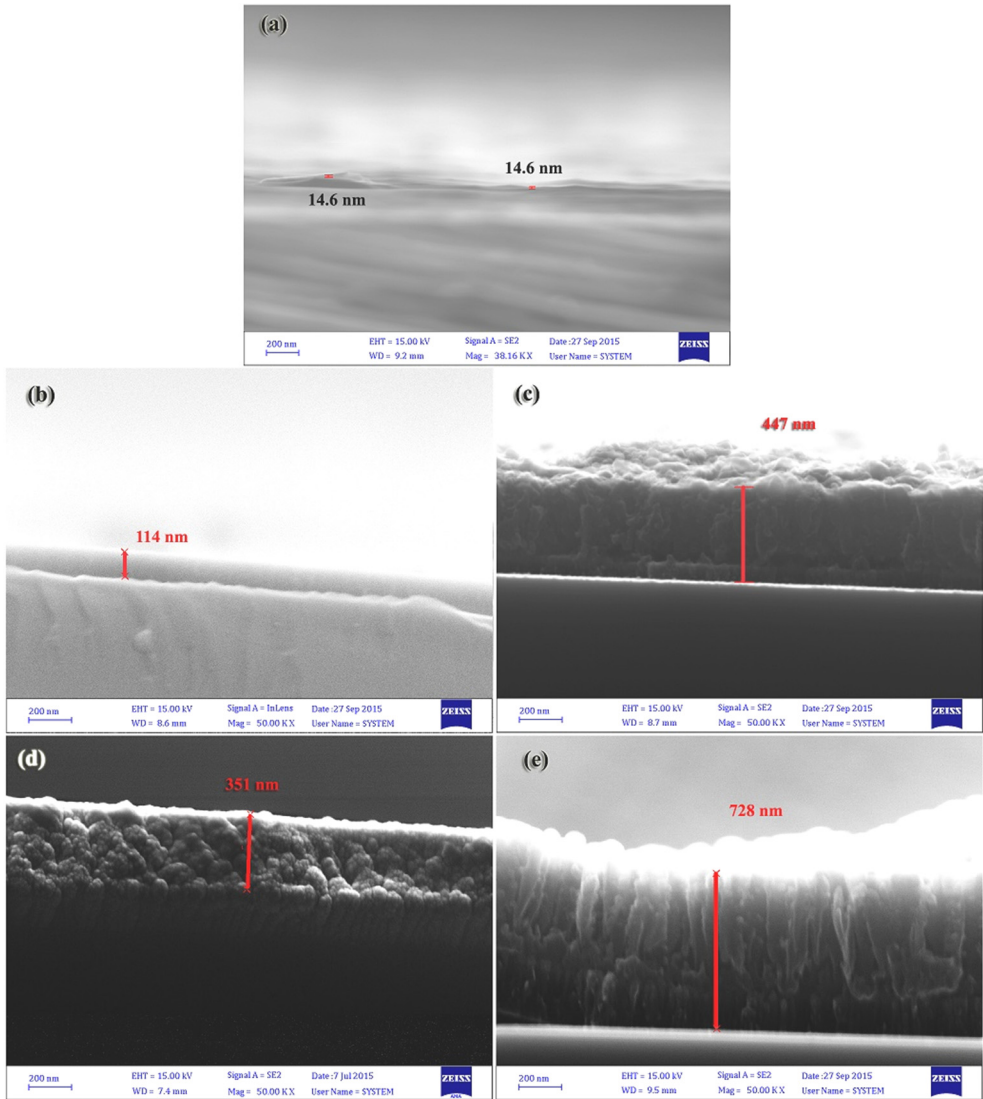


Figure 3. FE-SEM morphology of DLC films grown on the substrate (a) without interlayer, and with interlayer thickness of (b) 10nm, (c) 20nm, (d) 40nm and (e) 80 nm.

Raman Spectroscopy is a non-destructive and important technique for determining the bonding types in DLC film [13, 14]. Usually, amorphous carbon thin films exhibit two main Raman bands (D and G) in the wavenumber region of 1000–1800 cm^{-1} . The Position and the relative intensity of G and D are important factors in the properties of DLC [8, 15]. Figure 4 and Table 1 show the Raman spectra and their results, respectively.

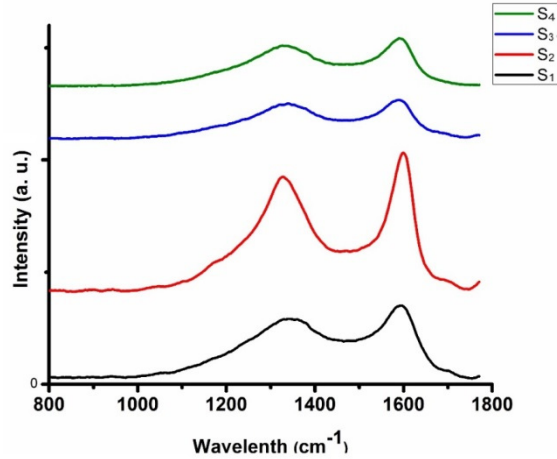


Figure 4. Raman spectra of DLC films grown on S₁, S₂, S₃ and S₄.

As can be seen from Table 1, the intensity ratio of the D to G bands (I_D to I_G) changes with the thickness of interlayer. The lowest value of I_D/I_G is for sample S₁ which had the lowest thickness of Ni layer. The ratio of I_D/I_G is correlated to the sp^2/sp^3 ratio in the DLC films, and a lower intensity ratio (I_D/I_G) can be interpreted as corresponding to higher sp^3 content [16]. The Raman spectra also show the G peak positions shifted upwards in all the samples. This is indicative of lower amount of internal compressive stress [17]. Thus, the results obtained from shifting of G peak position and I_D/I_G ratio value exhibit an enhancement in diamond-like character which S₁ sample has the highest degree of diamond-like character (sp^3 bonding) and lowest value of sp^2 carbon clustering.

Table 1. Raman spectra data of DLC films deposited at different thicknesses of Ni nanolayers

	<i>D band Position (cm⁻¹)</i>	<i>G band Position (cm⁻¹)</i>	I_D/I_G
S ₁	1345	1592	0.84
S ₂	1329	1597	0.85
S ₃	1337	1587	0.92
S ₄	1332	1591	0.87

Mechanical properties of the films were studied using the nano scratch test [18, 19]. The AFM surface morphology of the scratch track on the DLC film of S₁ and S₂ can be seen in Figure 5. The surface roughness of S₁ is lower than that of S₂ and a narrower scratch track and lower residual wear depth

were formed indicating better mechanical properties. The friction coefficients of DLC films obtained from nanoscratch test were also illustrated (Figure 5,c) which demonstrate a lower value for the film grown on 10 nanometers Ni interlayer (S_1).

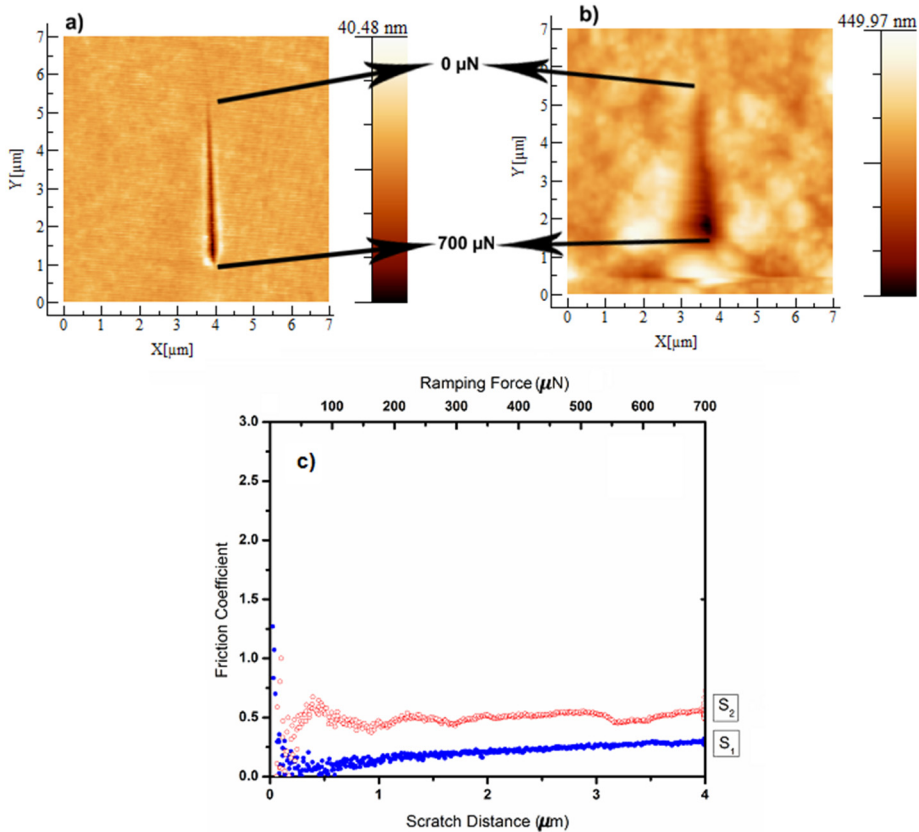


Figure 5. AFM images of the nano scratch test on a) S_1 and b) S_2 ; c) Changing of friction coefficient during ramping force and scratch distance for S_1 and S_2 .

CONCLUSIONS

Different thicknesses of nickel nano layers, from 10 to 80 nanometers, were used for the growth of DLC films on silicon substrates. The morphology study of Ni nano layer showed a low surface roughness with homogeneous size distribution of Ni particles, which increased with the thickness of Ni layer. The FE-SEM images represented thicker DLC films formed with increasing

the thickness of Ni nano layer. Raman study revealed minor changes in the value of I_D/I_G ratio of DLC films; the ratio had the lowest value for S_1 , indicating lower sp^2 fraction and better mechanical properties than other samples. Nanoscratch test confirmed the Raman results and showed better adhesion of DLC film on 10 nanometers Ni layer, which also had a lower surface roughness and friction coefficient.

EXPERIMENTAL SECTION

Silicon (p-type (400)) wafers were used as the substrate for deposition of the DLC films and were cleaned ultrasonically in ethanol, acetone and deionized water, each of them for 15 minutes, to rinse the contamination from substrates. Nickel nano layer was deposited on substrates by DC sputtering magnetron (Pishtaz Engineering Co. High Vacuum Technology Center (ACECR-Sharif University. Branch-Iran)) at 10^{-5} Torr base pressure in thickness of 10, 20, 40 and 80 nanometers. For the growth of DLC films, DC-plasma enhanced chemical vapor deposition (DC-PECVD) chamber [10] was exhausted to 10^{-5} Torr. At first, methane was introduced to the chamber for 30 minutes with a flow rate of 20 sccm. Then a mixture of methane and argon (25 vol. % CH_4) was inserted to the system with a total flow of 40 sccm. The growth temperature was $300^\circ C$ and duration of growth was 60 minutes.

The topographical and surface roughness of the Ni nano layers were studied by atomic force microscopy (AFM, XE-NSOM, in contact mode). The morphology and thicknesses of DLC films were studied using Zeiss Sigma VP field emission scanning electron microscopes (FE-SEM). Raman spectroscopy (Nd:YAG laser with wavelength of 532 nm) was used to measure the atomic bonds of DLC films. The nanoscratch tests (A Hysitron Inc. TriboScope[®] Nanomechanical Test Instrument) were performed to measure the DLC film's adhesion to the substrate. Each scratch test was performed by moving the probe (Berkovich indenter) laterally in a distance of 4 μm while concurrently ramping the normal force from 0 to 700 μN [20].

ACKNOWLEDGMENTS

Authors would like to acknowledge Dr. Zahra Khalaj and Professor Mircea V. Diudea for their valuable assistance and support in this work.

REFERENCES

1. J. Robertson, *Materials Science and Engineering: R: Reports*, **2002**, 37, 129.
2. A.E. Christophe Donnet, "Tribology of Diamond-Like Carbon Films: Fundamentals and Applications", Springer US, Cambridge, UK, **2008**, 664.
3. J. Robertson, *Super Hard Materials Journal*, **2014**, 3, 101.
4. A.H. Lettington, *Carbon*, **1998**, 36, 555.
5. R.K.S. Gayathri, T.R. Ravindran, S. Tripura Sundari, S. Dash, A.K. Tyagi, Baldev Raj, M. Sridharan, *Materials Res. Bull.*, **2012**, 47, 843.
6. Z. Khalaj, M. Ghoranneviss, E. Vaghri, A. Saghaleini and M.V. Diudea, *Acta Chim. Slov.*, **2012**, 59, 338.
7. Y.-S.W. Chehung Wei, Fong-Cheng Tai, *Diamond and Relat. Materials*, **2009**, 18, 407.
8. Y.S.P. Youngsook Jeon, Hyung Jin Kim and Byungyou Hong, *J. Korean Phys. Soc.*, **2007**, 51, 1124.
9. J.-Y.Y. Chehung Wei, *Diamond & Relat. Materials*, **2007**, 16, 1325.
10. Z. Khalaj, Ghoranneviss, M., Vaghri, E., Ponta O., *J. Carbon Materials: Chem. & Phys.*, **2013**, 6, 29.
11. J.-F. Y. Chehung Wei, Fong-Cheng Tai, *Diamond and Relat. Materials*, **2011**, 20, 839.
12. H.L.D.S. Dandy, "Diamond Chemical Vapor Deposition: Nucleation and Early Growth Stages", Elsevier, Burlington, **1996**, p. 206.
13. J.R.A. Ferrari, *Phys. Rev. B*, **2001**, 64, 075414.
14. J.C.P. Yang, Y. Leng, H. Sun, N. Huang, P. Chu, *Surface and Coatings Technol.*, **2004**, 186, 125.
15. P.K. Ali Modabberasl, M. Ranjbar, H. Salamati, R. Ashiri, *Carbon*, **2015**, 94, 485.
16. F.M. Mansoureh Ebrahimi, M. R. Naimi-Jamal, *Diamond and Related Materials*, **2015**, 52, 32.
17. B.C.M. Lubwama, K.V. Rajani, C.S. Wong, J.B. Kirabira, A. Sebbit, K.A. McDonnell, D. Dowling, K. Sayers, *Surface & Coatings Technology*, **2013**, 232, 521.
18. B.S.D. Bootkul, N. Saenphinit, C. Aramwit, S. Intarasiri, *Applied Surface Science*, **2014**, 310, 284.
19. Z.L.P.C.Q. Guo, D. Fan, J. Gong, C. Sun, *Diamond and Related Materials*, **2015**, 60, 66.
20. H.T.A. Molazemhosseini, M.R. Naimi-Jamal, A. Khavandi, *Polymer Testing*, **2013**, 32, 525.

*Dedicated to Professor Mircea Diudea
on the Occasion of His 65th Anniversary*

COUNTING POLYNOMIALS IN THE CRYSTAL NETWORK FLU (CMedDu)

MOHAMMAD A. IRANMANESH^{a,*}, MAHBOUBEH SAHELI^a,
MIRCEA V. DIUDEA^b

ABSTRACT. The crystal network named *flu*, belonging to the symmetry group *Fm-3m*, can be designed by map operations Medial and Dual, applied subsequently on the Cube. The topology of the network was characterized by Omega, Cluj and related polynomials.

Keywords: *Crystal like network, Omega polynomial, Cluj polynomial, Map operation*

INTRODUCTION

Design of polyhedral units, forming crystal-like lattices, is of interest in crystallography as many metallic oxides or more complex salts have found applications in chemical catalysis. Various applied mathematical studies have been performed, in an effort to give new, more appropriate characterization of the world of crystals. Recent articles in crystallography promoted the idea of topological description and classification of crystal structures. They present data describing real but also hypothetical lattices designed by computer.

Some basic map operations like Leapfrog **Le**, Quadrupling **Q** and Capra **Ca**, associated or not with the more simple Medial **Med** and/or Dual **Du** operations, are most often used to transform small polyhedral objects into more complex units. These transforms preserve the symmetry of the parent

^a Department of Mathematics, Yazd University, 89175-741, Yazd, Iran

^b Faculty of Chemistry and Chemical Engineering, "Babes-Bolyai" University, 400028 Cluj, Romania

* Corresponding Author: Iranmanesh@yazduni.ac.ir

object/net. The article is devoted to the study of a new crystal like network, by using some topological descriptions in terms of Omega, Cluj and related counting polynomials.

The network in Figure 1 is known as *flu/fluorite*; *sqc169*; *CMedDu* (Diudea's name), a 2-nodal net, with the point symbol for net: $(4^{12}.6^{12}.8^4)(4^6)_2$; 4,8-c net with stoichiometry (4-c)2(8-c) and belonging to the group *Fm-3m*. It was drawn by using operations on maps: Medial **Med** and Dual **Du**, applied subsequently on the Cube **C**.

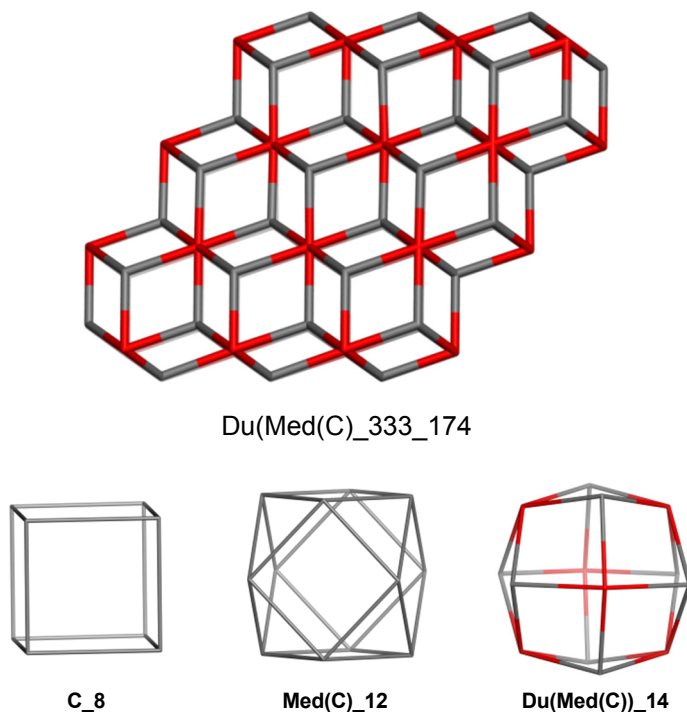


Figure 1. The network flu/CMedDu and its “history” originating in the Cube C

A map M is a discretized representation of a (closed) surface. In the following, we denote in a map: v – the number of vertices, e - the number of edges, f – the number of faces and d – the vertex degree; a subscript “0” will mark the corresponding parameters in the parent map. The number of vertices and edges in this structure are equal to $v = 3k^3 + 10k^2 + k$ and $e = 8k^3 + 20k^2 - 4k$, respectively.

Dual of a map, $Du(M)$, is achieved by locating a point in the center of each face, next two such points are joined if their corresponding faces share a common edge. It is the *Dual* $Du(M)$. The vertices of $Du(M)$ represent faces of M and vice-versa [1]. The parent and transformed map are related by the parameters: $Du(M)$; $v = f_0$; $e = e_0$; $f = v_0$. Dual of the dual returns the original map: $Du(Du(M)) = M$.

Medial of a map, $Med(M)$, can be performed if put new vertices in the middle of each of the original edges [1]. Join two vertices if the edges span an angle (and are consecutive within a rotation path around their common vertex in M). Medial is a 4-valent graph and $Med(M) = Med(Du(M))$. The transformed map parameters are: $Med(M)$; $v = e_0$; $e = 2e_0$; $f = f_0 + v_0$.

The medial operation rotates parent s -gonal faces by π/s . Points in the medial transformed map represent original edges; this property can be used in topological analysis of edges in the parent polyhedron. Similarly, the points in the dual map give information on the topology of parent faces.

A finite sequence of some graph-theoretical categories/properties, such as the distance degree sequence or the sequence of numbers of k -independent edge sets, can be described by so-called counting polynomials [2]:

$$P(G, x) = \sum_k p(G, k) \cdot x^k \quad (1)$$

where $p(G, k)$ is the frequency of occurrence of the property partitions of G , of length k , and x is simply a parameter to hold k .

OMEGA POLYNOMIAL

Let G be a connected graph with the vertex set $V = V(G)$ and edge set $E = E(G)$, without loops. Two edges $e = ab$ and $f = xy$ of G are called *co-distant* (briefly: e *co* f) if for $k = 0, 1, 2, \dots$ there exist the relations: $d(a, x) = d(b, y) = k$ and $d(a, y) = d(b, x) = k+1$ or vice versa. For some edges of a connected graph G there are the following relations satisfied:

$$e \text{ co } f \quad (2)$$

$$e \text{ co } f \Leftrightarrow f \text{ co } e \quad (3)$$

$$e \text{ co } f \ \& \ f \text{ co } g \Rightarrow e \text{ co } g \quad (4)$$

though, the relation (4) is not always valid.

Let $C(e) := \{ e' \in E(G) ; e' \text{ co } e \}$ denote the set of all edges of G which are codistant to the edge e . If all the elements of $C(e)$ satisfy the relations (2)-(4) then $C(e)$ is called an *orthogonal cut* "oc" of the graph G . The graph G is called *co-graph* if and only if the edge set $E(G)$ is the union of disjoint orthogonal cuts: $C_1 \cup C_2 \cup \dots \cup C_k = E(G)$ and $C_i \cap C_j = \emptyset$ for $i \neq j$, $i, j = 1, 2, \dots, k$.

We say that edges e and f of a plane graph G are in relation *opposite*, e *op* f , if they are opposite edges of an inner face of G . Note that the relation *co* is defined in the whole graph while *op* is defined only in faces. Using the relation *op* we can partition the edge set of G into opposite edge strips, *ops*. An *ops* is a quasi-orthogonal cut *qoc*, since *ops* is not transitive.

Let G be a connected graph and S_1, S_2, \dots, S_k be the *ops* strips of G . Then the *ops* strips form a partition of $E(G)$. The length of *ops* is taken as maximum. It depends on the size of the maximum fold face/ring F_{\max}/R_{\max} considered, so that any result on omega polynomial will have this specification.

Denote by $m(G, s)$ the number of *ops* of length s and define the Omega polynomial as [3-9]:

$$\Omega(G, x) = \sum_s m(G, s) \cdot x^s \tag{5}$$

Its first derivative (in $x=1$) equals the number of edges in the graph:

$$\Omega'(G, 1) = \sum_s m(G, s) \cdot s = e = |E(G)| \tag{6}$$

on Omega polynomial, the Cluj-Ilmenau index, $CI=CI(G)$, was defined:

$$CI(G) = \{[\Omega'(G, 1)]^2 - [\Omega'(G, 1) + \Omega''(G, 1)]\} \tag{7}$$

Omega polynomial and Cluj-Ilmenau index of crystal network *flu* with some examples are presented in Table 1.

Table 1. Omega polynomial and CI index in crystal network *flu*.

Formulas			
$\Omega(G, x) = \sum_{i=1}^{k-1} 4x^{4k+2+(2k+2)(i-1)} + (2k+2)x^{2k^2+4k}$			
$CI(G) = \frac{1}{3}(192k^6 + 920k^5 + 832k^4 - 696k^3 + 56k^2 - 8k)$			
$ R(4) = 6k^3 + 10k^2 - 5k + 1$			
Examples			
k	$\Omega(G, x)$	$CI(G)$	$ R(4) $
1	$4x^6$	432	12
2	$4x^{10}+6x^{16}$	16560	79
3	$4x^{14}+4x^{22}+8x^{30}$	137536	238
4	$4x^{18}+4x^{28}+4x^{38}+10x^{48}$	632608	525
5	$4x^{22}+4x^{34}+4x^{46}+4x^{58}+12x^{70}$	2103120	976

CLUJ POLYNOMIAL

Cluj matrices and indices have been proposed by Diudea on the ground of fragments/subgraphs [10-12] $CJ_{i,j,p}$ that collects vertices v lying closer to i than to j , the endpoints of a path $p(i,j)$. Such fragments represent vertex proximities of i against any vertex j , joined by the path p , with the distances measured in the subgraph $D_{(G-p)}$, as shown in relation:

$$CJ_{i,j,p} = \left\{ v \mid v \in V(G); D_{(G-p)}(i,v) < D_{(G-p)}(j,v) \right\} \quad (8)$$

In graphs containing rings, more than one path could join the pair (i,j) , thus resulting more than one fragment related to i (with respect to j and a given path p); the entries in the Cluj matrix are taken, by definition, as the maximum cardinality among all such fragments:

$$[UCJ]_{ij} = \max_p \left| CJ_{i,j,p} \right| \quad (9)$$

Cluj polynomials are developed on the non-symmetric matrices $UCJDI$ calculated on path $UCJDI_p$ or on edges $UCJDI_e$.

The general form of Cluj polynomial is [13-16]:

$$CJ(x) = \sum_k m(k) \cdot x^k \quad (10)$$

They count the vertex proximity of the vertex i with respect to any vertex j in G , joined to i by an edge (the Cluj-edge polynomials $CJDI_e(x)$) or by a path (the Cluj-path polynomials $CJDI_p(x)$). In (10), the coefficients $m(k)$ can be calculated from the entries of $UCJDI$ matrices by the **TOPOCLUJ** software program [17]. The summation runs over all $k = |\{p\}|$ in G .

In bipartite graphs, the coefficients of cluj polynomial can be calculated by an orthogonal edge-cut procedure [18-20]. For this, a theoretical background is needed.

For any edge $e=(u,v)$ of a connected graph G , let n_{uv} denote the set of vertices lying closer to u than to v : $n_{uv} = \{w \in V(G) \mid d(w,u) < d(w,v)\}$. It follows that $n_{uv} = \{w \in V(G) \mid d(w,v) = d(w,u) + 1\}$. The sets (and subgraphs) induced by these vertices, n_{uv} and n_{vu} , are called *semicubes* of G ; the *semicubes* are called *opposite semicubes* and are disjoint [4,21,22].

A graph G is bipartite if and only if, for any edge of G , the opposite *semicubes* define a partition of G : $n_{uv} + n_{vu} = v = |V(G)|$. These *semicubes* are just the vertex proximities (see above) of (the endpoints of) edge $e=(u,v)$, which CJ_e polynomial counts. In partial cubes, the *semicubes* can be estimated by an orthogonal edge-cutting procedure.

To any orthogonal cut c_k , two numbers are associated: first one represents the *number of edges* e_k intersected (or the cutting cardinality $|c_k|$) while the second is v_k or the number of points lying to the left hand with respect to c_k . Because in bipartite graphs the opposite semicubes define a partition of vertices, it is easily to identify the two semicubes: $n_{uv} = v_k$ and $n_{vu} = v - v_k$ or vice-versa.

By this cutting procedure, four polynomials can be count, they differing only in the mathematical operation used to re-compose the local contributions to the global graph property [19]:

(1) **Summation**; the polynomial is called *Cluj-Sum* and is symbolized *CJS* [13-15,23]

$$CJS(x) = \sum_e (x^{v_k} + x^{v-v_k}) \quad (11)$$

(2) **Pair-wise summation**; the polynomial is called PI_v (vertex-Padmakar-Ivan) [24-28]

$$PI_v(x) = \sum_e x^{v_k + (v-v_k)} \quad (12)$$

(3) **Pair-wise product**; the polynomial is called *Cluj-Product* (and symbolized *CJP*) [10-12,16,18,19] or also Szeged (and symbolized *SZ*) [26-30]

$$CJP(x) = SZ(x) = \sum_e x^{v_k(v-v_k)} \quad (13)$$

(4) **Single edge pair-wise product**; the polynomial is called *Wiener* and symbolized W [19]

$$W(x) = \sum_k x^{v_k(v-v_k)} \quad (14)$$

The first derivative (in $x=1$) of a counting polynomial provides single numbers, often called topological indices. The coefficients of polynomial terms are calculated (except $W(x)$ as the product of three numbers: $\text{sym}(G) \times \text{freq}(c_k) \times e_k$).

One can see that the first derivative (in $x=1$) of the first two polynomials gives one and the same value, however, their second derivative is different and the following relations hold in any graph [16,19]

$$CJS'(1) = PI_v'(1); CJS''(1) \neq PI_v''(1) \quad (15)$$

In bipartite graphs, the first derivative (in $x=1$) of $PI_v(x)$ takes the maximal value:

$$PI'_v(1) = e \cdot v = |E(G)| \cdot |V(G)| \quad (16)$$

Keeping in mind the definition of the corresponding index, one can see that [31]

$$PI_v(G) = PI'_v(1) = \sum_{e=uv} n_{u,v} + n_{v,u} = |V| \cdot |E| - \sum_{e=uv} m_{u,v} \quad (17)$$

where $n_{u,v}$, $n_{v,u}$ count the non-equidistant vertices with respect to the endpoints of the edge $e=(u,v)$ while $m_{u,v}$ is the number of equidistant vertices vs. u and v . However, it is known that, in bipartite graphs, there are no equidistant vertices, so that the last term in (17) is missing. The value of $PI_v(G)$ is thus maximal in bipartite graphs, among all graphs on the same number of vertices; the result of (14) can be used as a criterion for the “biparity” of a graph [14].

The third polynomial, $CJP(x)$, uses the pair-wise product; it is precisely the (vertex) Szeged polynomial $SZ_v(x)$, defined by Ashrafi *et al* [26-28]. This comes out from the relations between the basic Cluj (Diudea [11,12]) and Szeged (Gutman [30]) indices:

$$CJP'(1) = CJDI(G) = SZ(G) = SZ'_v(1) \quad (18)$$

All the three above polynomials (and their derived indices) do not count the equidistant vertices, an idea introduced in Chemical Graph Theory by Gutman [30]. We call these: *polynomials of vertex proximity*.

The last polynomial, $W(x)$, we call Wiener, because it is calculated as Wiener performed the index $W(G)$ in tree graphs: multiply the number of vertices lying to the left and to the right of each edge (actually read orthogonal cut c_k):

$$W(G) = W'(1) = \sum_k v_k \cdot (v - v_k) \quad (19)$$

where v_k and $v-v_k$ are the disjoint semicubes forming a partition with respect to each edge in c_k taken as a “single edge” (as in trees). In partial cubes, the exponents of $W(x)$ are identical to those in $CJP(x)$ and $SZ(x)$ while the coefficients are those in the above polynomials, divided by e_k . When subscript letter is missing, $SZ(x)$ is $SZ_v(x)$.

Numerical calculation were done by our original software programs **TOPOCLUJ** [17]. In this article all above formulas also examples are presented for flu structure in Tables 2-6.

Table 2. Cluj and related polynomial in crystal network *flu*.

	PI_v, PI'_v and PI''_v
1	$PI_v(G) = (8k^3 + 20k^2 - 4k)x^{3k^3+10k^2+k}$
2	$PI'_v(1) = 24k^6 + 140k^5 + 196k^4 - 20k^3 - 4k^2$
3	$PI''_v(1) = 72k^9 + 660k^8 + 2012k^7 + 2016k^6 - 156k^5$ $- 256k^4 + 16k^3 + 4k^2$

Cluj polynomial

4	$Cluj(G, x) = \sum_{i=1}^{\lfloor \frac{k}{2} \rfloor} (8k^2 + 16k)x^{(3k^3+7k^2-3k)-(3k^2+7k)(i-1)}$ $+ \sum_{i=1}^{\lfloor \frac{k}{2} \rfloor} (8k^2 + 16k)x^{(-6k^2-19k-7)+(3k^2+7k)(i-1)}$ $+ \sum_{i=1}^{k-1} [(16k + 8) + (8k + 8)(i - 1)]x^{(3k^3+10k^2-4k-2)-(8k+5)(i-1)-(3k+3)\frac{(i-1)(i-2)}{2}}$ $+ \sum_{i=1}^{k-1} [(16k + 8) + (8k + 8)(i - 1)]x^{(5k+2)+(8k+5)(i-1)+(3k+3)\frac{(i-1)(i-2)}{2}}$ $+ [(3 - (-1)^k)(4k^2 + 8k)]x^{2\frac{3}{2}k^3+5k^2+\frac{1}{2}k}$
5	$Cluj'(1) = 24k^6 + 140k^5 + 196k^4 - 20k^3 - 4k^2$
6	$Cluj''(1) = \frac{1}{15}(720k^9 + 6402k^8 + 18786k^7 + 16426k^6$ $- 6848k^5 - 5082k^4 - 46k^3 - 106k^2 - 12k)$

Wiener

$$7 \quad W(G) = \frac{1}{30}(216k^7 + 1677k^6 + 3336k^5 + 790k^4 - 76k^3 - 67k^2 + 4k)$$

Szeged

$$8 \quad CJP(x) = SZ(x) = \sum_{i=1}^{\lfloor \frac{k}{2} \rfloor} (8k^2 + 16k) x^{(k^2(3k^2+10k+4-3ki-7i)(-3+3ki+7i))}$$

$$+ \sum_{i=1}^{k-1} [(16k+8) + (8k+8)(i-1)] x^{\frac{(6k^3+20k^2+2k-7ki-i-3ki^2-3i^2)(7k+1+3ki+3i)}{4}}$$

$$+ [(3-(-1)^k)(2k^2+4k)] x^{\frac{(\frac{3}{2}k^3+5k^2+\frac{1}{2}k)^2}{2}}$$

$$9 \quad Sz(G) = \frac{1}{15}(180k^9 + 1749k^8 + 5697k^7 + 6907k^6 + 2254k^5 + 621k^4 + 143k^3 + 83k^2 + 6k)$$

$PI_e, PI_e'(1)$ and $PI_e''(1)$

$$10 \quad PI_e(G, x) = \sum_{i=1}^{k-1} [(16k+8) + (8k+8)(i-1)] x^{(8k^3+20k^2-8k-2)-(2k+2)(i-1)}$$

$$+ (4k^3 + 12k^2 + 8k) x^{8k^3+18k^2-8k}$$

$$11 \quad PI_e'(1) = \frac{1}{3}(192k^6 + 920k^5 + 832k^4 - 696k^3 + 56k^2 - 8k)$$

$$12 \quad PI_e''(1) = \frac{1}{3}(1536k^9 + 10880k^8 + 22152k^7 + 2568k^6 - 20264k^5 + 4832k^4 + 240k^3 + 80k^2 + 24k)$$

Table 3. Examples, PI_v , PI'_v , PI''_v , number of vertices and edges in crystal network flu .

k	PI_v Polynomial	PI'_v	PI''_v	v	e
1	$24x^{14}$	336	4368	14	24
2	$136x^{66}$	8976	583440	66	136
3	$384x^{174}$	66816	11559168	174	384
4	$816x^{356}$	290496	103126080	356	816
5	$180x^{630}$	932400	586479700	630	1480

Table 4. Cluj and related polynomials in crystal network flu .

k	Cluj polynomial	$CJ'(1)$	$CJ''(1)$
1	$48x^7$	336	2016
2	$40x^{54} + 64x^{46} + 64x^{33} + 64x^{20} + 40x^{12}$	8976	344144
3	$56x^{157} + 120x^{135} + 88x^{128} + 240x^{87} + 88x^{46} + 120x^{39} + 56x^{17}$	66816	7143792
4	$72x^{334} + 112x^{297} + 192x^{292} + 152x^{245} + 192x^{216} + 192x^{178} + 192x^{140} + 152x^{111} + 192x^{64} + 112x^{59} + 72x^{22}$	290496	65003856
5	$88x^{603} + 136x^{558} + 280x^{535} + 184x^{495} + 280x^{425} + 232x^{414} + 560x^{315} + 232x^{216} + 280x^{205} + 184x^{135} + 280x^{95} + 136x^{72} + 88x^{27}$	932400	373783936

Table 5. Examples; cluj polynomial in crystal network flu .

k	Szeged polynomial	Szeged index	Wiener index
1	$24x^{49}$	1176	196
2	$64x^{920} + 40x^{648} + 32x^{1089}$	119648	8450
3	$120x^{5265} + 56x^{2669} + 88x^{5888} + 120x^{7569}$	2207688	85564
4	$192x^{18688} + 192x^{30240} + 72x^{7348} + 112x^{17523} + 152x^{27195} + 96x^{31684}$	19061112	467344
5	$280x^{50825} + 280x^{87125} + 88x^{16281} + 136x^{40176} + 184x^{66825} + 232x^{89424} + 280x^{99225}$	106347832	1799524

Table 6. Examples; PI_e , $PI_e'(1)$ and $PI_e''(1)$ in crystal network flu.

k	PI_e	$PI_e'(1)$	$PI_e''(1)$
1	$24x^{18}$	432	7344
2	$40x^{126}+96x^{120}$	15560	2000880
3	$536x^{370}+88x^{362}+240x^{354}$	137536	49136576
4	$72x^{798}+112x^{788}+152x^{778}+480x^{768}$	632608	489881696
5	$88x^{1458}+136x^{1446}+184x^{1434}+232x^{1422}+840x^{1410}$	2103120	2986825680

CONCLUSIONS

In this paper we presented the Omega and Cluj polynomials in crystal-like network *flu*. Definitions and relations with other polynomials and topological indices were given. Analytical formulas as well as examples were tabulated.

REFERENCES

1. T. Pisanski and M. Randić, *MAA Notes*, **2000**, 53, 174.
2. I. Gutman, S.J. Cyvin and V. Ivanov–Petrović, *Z. Naturforsch.*, **1998**, 53, 699.
3. M.V. Diudea, *Carpath. J. Math.*, **2006**, 22, 43.
4. M.V. Diudea, S. Cigher and P.E. John, *MATCH Commun. Math. Comput. Chem.*, **2008**, 60, 237.
5. M. Saheli, M.A. Iranmanesh and M.V. Diudea, *Studia Univ. Babes-Bolyai Chemia*, **2014**, 2, 79.
6. M. Saheli, A.R. Ashrafi and M.V. Diudea, *Studia Univ. Babes-Bolyai Chemia*, **2010**, 4, 233.
7. M. Saheli and M.V. Diudea, *Studia Univ. Babes-Bolyai Chemia*, **2010**, 4, 215.
8. M. Saheli, M. Ghorbani, M.L. Pop and M.V. Diudea, *Studia Univ. Babes-Bolyai Chemia*, **2010**, 4, 241.
9. M. Saheli, O. Pop, L. Pop and M.V. Diudea, *Studia Univ. Babes-Bolyai Chemia*, **2010**, 4, 215.
10. M.V. Diudea, *MATCH Commun. Math. Comput. Chem.*, **1997**, 35, 169.
11. M.V. Diudea, *J. Chem. Inf. Comput. Sci.*, **1997**, 37, 300.
12. M.V. Diudea, *Croat. Chem. Acta*, **1999**, 72, 835.

13. M.V. Diudea, *J. Math. Chem.*, **2009**, 45, 295.
14. M.V. Diudea, A.E. Vizitiu and D. Janežič, *J. Chem. Inf. Model.*, **2007**, 47, 864.
15. M.V. Diudea, A. Ilić, M. Ghorbani and A.R. Ashrafi, *Croat. Chem. Acta*, **2010**, 83, 283.
16. M.V. Diudea, N. Dorosti and A. Iranmanesh, *Carpath. J. Math.*, **2010**, 4, 247.
17. O. Ursu, M.V. Diudea, **TOPOCLUJ** software program, *Babes-Bolyai University*, **2005**.
18. M.V. Diudea, *Novel Molecular Structure Descriptors-Theory and Applications I*, **2010**, 191.
19. M.V. Diudea, *Novel Molecular Structure Descriptors-Theory and Applications II*, **2010**, 57.
20. I. Gutman and S. Klavžar, *J. Chem. Inf. Comput.*, **1995**, 35, 1011.
21. M.V. Diudea, S. Cigher and P.E. John, *MATCH Commun. Math. Comput. Chem.*, **2008**, 60, 237.
22. M.V. Diudea and S. Klavžar, *Acta. Chem. Sloven.*, **2010**, 57, 565.
23. A.E. Vizitiu and M.V. Diudea, *Studia Univ. Babes-Bolyai Chemia*, **2009**, 54, 173.
24. P.V. Khadikar, *Nat. Acad. Sci. Lett.*, **2000**, 23, 113.
25. M.H. Khalifeh, H. Yousefi-Azari and A.R. Ashrafi, *Discrete Appl. Math.*, **2008**, 156, 1780.
26. M.H. Khalifeh, H. Yousefi-Azari and A.R. Ashrafi, *Linear Algebra Appl.*, **2008**, 429, 2702.
27. A.R. Ashrafi, M. Ghorbani and M. Jalali, *J. Theor. Comput. Chem.*, **2008**, 7, 221.
28. T. Mansour and M. Schork, *Discr. Appl. Math.*, **2009**, 157, 1600.
29. M.V. Diudea, *Croat. Chem. Acta*, **1999**, 72, 835.
30. I. Gutman, *Graph Theory Notes*, **1994**, 27, 9.
31. A. Ilić, *Appl. Math. Lett.*, **2010**, 23, 1213.

*Dedicated to Professor Mircea Diudea
on the Occasion of His 65th Anniversary*

THEORETICAL STUDY OF NANOSTAR DENDRIMERS

NAJMEH SOLEIMANI^{a,*}, ESMAEEL MOHSENI^b, SAHAR HELALBIN^b

ABSTRACT. In this paper, we give some theoretical results about nanostar dendrimers by topological indices. Formulas for computing topological indices based on distance and degree in a graph such as eccentric connectivity, total eccentricity, fourth version of atom-bond connectivity and fifth version of geometric-arithmetic indices of two types of nanostar dendrimers are presented.

Keywords: *Dendrimers, Eccentric, Vertex-degree, Connectivity indices.*

INTRODUCTION

Dendrimers are large and complex molecules with well tailored chemical structures. There are numerous topological descriptors that have found applications in theoretical chemistry, particularly in QSPR/QSAR research [1]. Among them, topological indices have a prominent place. In some research papers [2-9], the authors have computed some topological indices of nanostar dendrimers, nanostructures and other graphs.

In this paper, we discuss four topological descriptors, namely ξ^c , θ , ABC_4 and GA_5 indices for two types of nanostar dendrimers. The article is organized as follows: within the second part of this work, we give the necessary definitions. Section 3 contains our main results. Conclusions and references will close this article.

^a Young Researchers and Elite Club, Qaemshahr Branch, Islamic Azad University, Qaemshahr, Iran

^b Salehan Institute of Higher Education, Qaemshahr, Iran

* Corresponding Author: soleimani.najmeh@gmail.com

DEFINITIONS

Now, we introduce some notations and terminology which is needed for the rest of the paper. A molecular graph is a simple graph such that its vertices correspond to the atoms and the edges to the bonds of a molecule. Let $G = (V, E)$ be a simple molecular graph without directed and multiple edges and without loops, the vertex and edge sets of it are represented by $V = V(G)$ and $E = E(G)$, respectively. The degree (i.e., the number of first neighbors) of a vertex $u \in V(G)$ is denoted by $deg_G(u)$. The edge connecting the vertices u and v is denoted by uv . The distance between u and v in $V(G)$, $d(u, v)$, is the length of a shortest u - v path in G . For a vertex u of $V(G)$ its eccentricity $\varepsilon_G(u)$ is the largest distance between u and any other vertex v of G , $\varepsilon_G(u) = \max\{d(u, v) | v \in V(G)\}$. The maximum and minimum eccentricity over all vertices of G are called the diameter and radius of G and denoted by $d(G)$, $r(G)$ respectively. In 2011, Doslić et al. [10], have proposed the eccentric connectivity polynomial. This polynomial is defined as follows:

$$\xi^c(G, x) = \sum_{u \in V(G)} deg_G(u) x^{\varepsilon_G(u)},$$

where x is a dummy variable. A topological index is a real number derived from molecular graphs of chemical compounds. The oldest topological index is the Wiener index, introduced by Harold Wiener [11]. The eccentric-connectivity index of the molecular graph G , $\xi^c(G)$, was proposed by Sharma et al. [12]. It is easy to see that the eccentric-connectivity index of a graph can be obtained from the corresponding polynomials by evaluating its first derivative, at $x = 1$. The eccentric and total connectivity indices of G are defined as follows:

$$\xi^c(G) = \sum_{u \in V(G)} deg_G(u) \varepsilon_G(u), \quad \theta(G) = \sum_{u \in V(G)} \varepsilon_G(u).$$

We encourage readers to references [13–15] to study some properties of eccentric-connectivity index of some nanostructures.

Among topological connectivity indices, the atom-bond connectivity (ABC) index and geometric-arithmetic (GA) index are of great importance. For other studies on these topological indices, we suggest refs. [16,17]. In 2010, Ghorbani et al. [18] introduced a new version of atom-bond connectivity (ABC_4) index. It is defined as follows:

$$ABC_4(G) = \sum_{uv \in E(G)} \sqrt{\frac{S_u + S_v - 2}{S_u S_v}},$$

where S_u is the sum of degrees of all vertices adjacent to vertex u . In other words, $S_u = \sum_{v \in N_G(u)} deg_G(v)$ and $N_G(u) = \{v \in V(G) | uv \in E(G)\}$.

Recently a fifth version of geometric-arithmetic (GA_5) index is proposed by Graovac et al. [19] in 2011, as follows:

$$GA_5(G) = \sum_{uv \in E(G)} \frac{2\sqrt{S_u S_v}}{S_u + S_v}.$$

RESULTS AND DISCUSSION

The main aim of this section is to compute the eccentric-connectivity polynomial, eccentric-connectivity, total eccentricity, fourth version of atom-bond connectivity and fifth version of geometric-arithmetic indices of the molecular graph of two types of nanostar dendrimers (see Figure 1). In this paper, $D_1[n]$ and $D_2[n]$ denotes the n^{th} growth of nanostar dendrimer for every infinite integer n . For background materials, see *references* [20, 21].

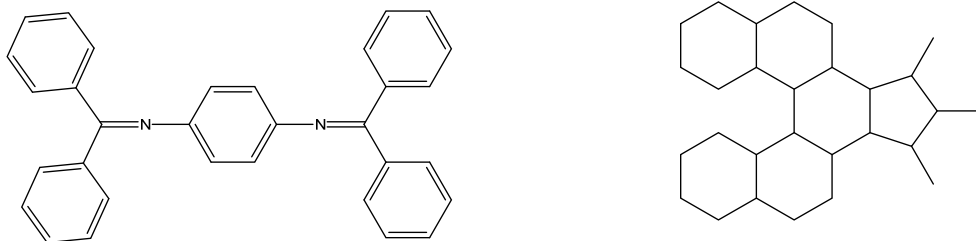


Figure 1. First generation of diphenylazomethine dendrimer (left) and Wang's Helicene-based dendrimers (right).

Calculation of polynomials and topological Indices

Before we proceed to our main results, we explain the examples which will be further used.

Example 1. Let us consider the first kind of nanostar dendrimer, of which grown 1 – 3 steps are denoted by $D_1[n]$ for $n = 1, 2, 3$.

Obviously, for $n = 1$, $|V| = 34$ and $|E| = 38$. The eccentric-connectivity polynomial is equal to:

$$\xi^c(D_1[1], x) = 8x^{15} + 16x^{14} + 16x^{13} + 12x^{12} + 6x^{11} + 4x^{10} + 6x^9 + 8x^8.$$

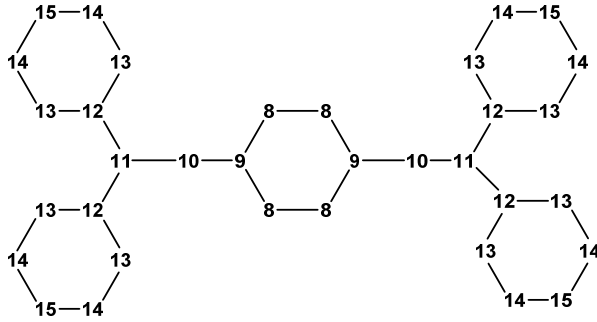


Figure 2. The molecular graph of $D_1[n]$ for $n = 1$.

For $n = 2$, $|V| = 90$ and $|E| = 102$. The eccentric-connectivity polynomial is equal to:

$$\xi^c(D_1[2], x) = 16x^{27} + 32x^{26} + 32x^{25} + 24x^{24} + 12x^{23} + 8x^{22} + 12x^{21} + 16x^{20} + 16x^{19} + 12x^{18} + 6x^{17} + 4x^{16} + 6x^{15} + 8x^{14}.$$

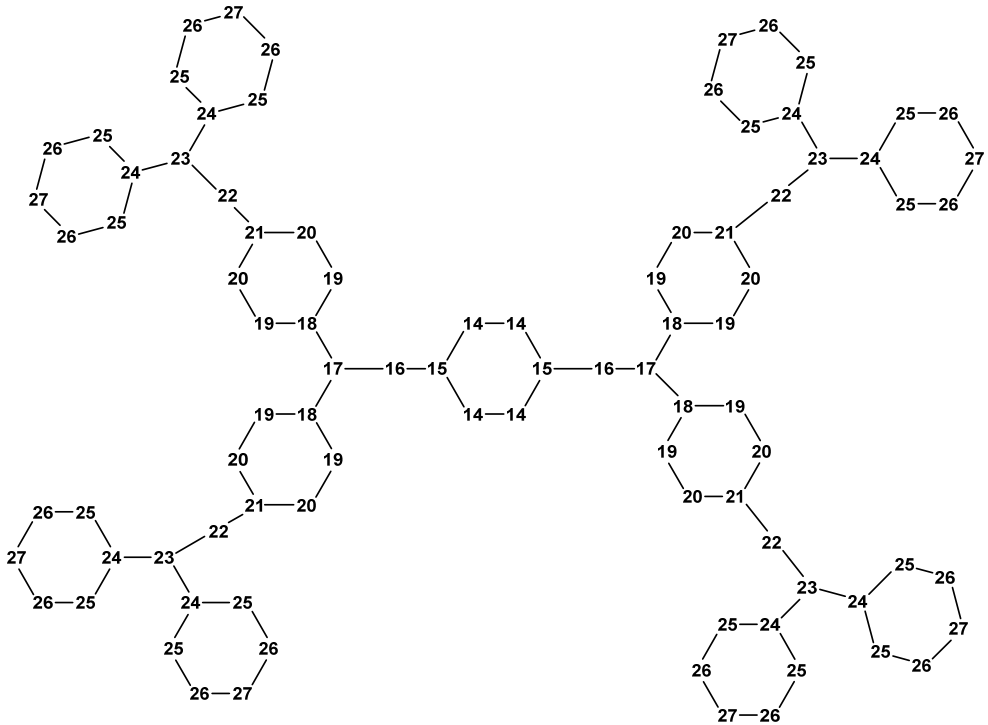


Figure 3. The molecular graph of $D_1[n]$ for $n = 2$.

Also, for $n = 3$, $|V| = 202$ and $|E| = 230$. The eccentric-connectivity polynomial is equal to:

$$\begin{aligned} \xi^c(D_1[3], x) = & 32x^{39} + 64x^{38} + 64x^{37} + 48x^{36} + 24x^{35} + 16x^{34} + 24x^{33} + 32x^{32} \\ & + 32x^{31} + 24x^{30} + 12x^{29} + 8x^{28} + 12x^{27} + 16x^{26} + 16x^{25} + 12x^{24} \\ & + 6x^{23} + 4x^{22} + 6x^{21} + 8x^{20}. \end{aligned}$$

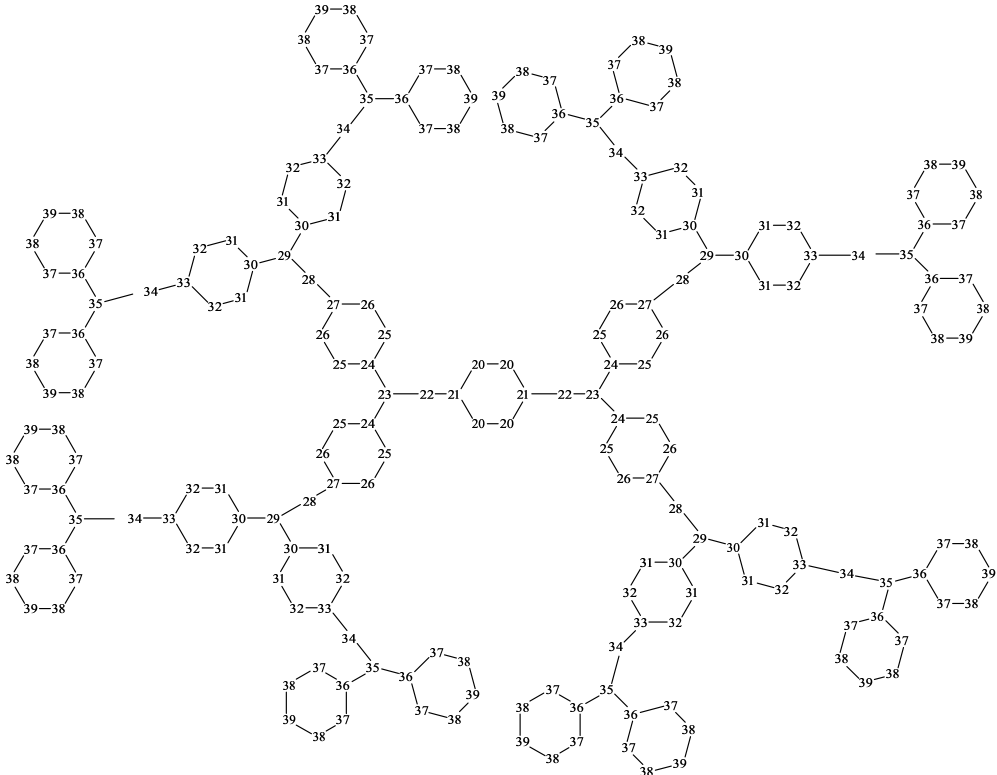


Figure 4. The molecular graph of $D_1[n]$ for $n = 3$.

Using calculations given above, it is possible to evaluate the eccentric-connectivity polynomial of this class of nanostar dendrimers.

Theorem 2. The eccentric-connectivity polynomial of the nanostar dendrimer $D_1[n]$ for $n \geq 1$ is given by the formula:

$$\begin{aligned} \xi^c(D_1[n], x) = & 2^{n+2} x^{12n+3} + 2^{n+3} x^{12n+2} + \sum_{k=1}^n 2^k (8x^{6(n+k)+1} + 6x^{6(n+k)} \\ & + 3x^{6(n+k)-1} + 2x^{6(n+k)-2} + 3x^{6(n+k)-3} + 4x^{6(n+k)-4}). \end{aligned}$$

Proof. To prove the theorem, we apply induction on n . By considering the general form of this graph, $|V(D_1[n])| = 28 \times 2^n - 22$ and $|E(D_1[n])| = 32 \times 2^n - 26$. We compute maximum vertex eccentric connectivity and minimum vertex eccentric connectivity for nanostar dendrimer graph $D_1[n]$. For $u \in V(D_1[n])$, we have $d(D_1[n]) = 12n + 3$ and $r(D_1[n]) = 6n + 2$. The degrees, frequencies and eccentricities of these vertices are listed in Table 1.

Table 1. The representatives of vertices of $D_1[n]$ with their degree, eccentricity and frequency of occurrence, for $1 \leq k \leq n$.

Vertex type	Degree	Eccentricity	Frequency
1	2	$12n + 3$	2^{n+1}
2	2	$12n + 2$	2^{n+2}
3	2	$6n + 6k + 1$	2^{k+2}
4	3	$6n + 6k$	2^{k+1}
5	3	$6n + 6k - 1$	2^k
6	2	$6n + 6k - 2$	2^k
7	3	$6n + 6k - 3$	2^k
8	2	$6n + 6k - 4$	2^{k+1}

By using data in Table 1 and definition of eccentric-connectivity polynomial calculation may be achieved.

From Theorem 2, it is possible to calculate the eccentric-connectivity index of these nanostar dendrimers. We have:

Theorem 3. The eccentric-connectivity index of $D_1[n]$ for $n \geq 1$ is computed as follows:

$$\xi^c(D_1[n]) = 2^n(768n - 332) - 312n + 360.$$

Proof. From the definition, we have $\xi^c(D_1[n]) = \frac{\partial(\xi^c(D_1[n],x))}{\partial x} \Big|_{x=1}$.

Thus:

$$\begin{aligned} \xi^c(D_1[n]) &= 2^{n+2}(12n + 3) + 2^{n+3}(12n + 2) \\ &+ \sum_{k=1}^n 2^k \left((8(6(n+k) + 1)) + 6(6(n+k)) + (3(6(n+k) - 1)) \right. \\ &\left. + (2(6(n+k) - 2)) + (3(6(n+k) - 3)) + (4(6(n+k) - 4)) \right) \\ &= 2^n(768n - 332) - 312n + 360. \end{aligned}$$

Theorem 4. The total eccentricity index of $D_1[n]$ for $n \geq 1$ is computed as follows:

$$\theta(D_1[n]) = 2^n(336n - 138) - 132n + 152.$$

Proof. The total eccentricity index of a graph is the sum of eccentricities of all the vertices. Therefore by the calculations given in Table 1, the theorem is proved.

Theorem 5. The fourth atom-bond connectivity index of $D_1[n]$ for $n \geq 1$ is computed as follows:

$$ABC_4(D_1[n]) = \frac{4355257157954373 \times 2^{n+2}}{1125899906842624} + \frac{4625405229014641 \times 2^n}{2251799813685248} - \frac{3896323959238067}{281474976710656}.$$

Proof. Let $D_1[n]$ be the graph of first kind of nanostar dendrimer. We compute the edge partition of $D_1[n]$ based on the degree sum of neighbors of end vertices of each edge (Table 2).

Table 2. The edge partition of $D_1[n]$ based on the degree sum of neighbors of the end vertices of each edge.

(S_u, S_v) $uv \in E(D_1[n])$	No. edges	(S_u, S_v) $uv \in E(D_1[n])$	No. edges
(4,4)	2^{n+2}	(8,6)	$2^{n+1} - 2$
(5,4)	2^{n+2}	(6,6)	$2^{n+1} - 2$
(7,5)	$2^{n+3} - 8$	(6,5)	$2^{n+2} - 4$
(7,8)	$2^{n+2} - 4$	(5,5)	$2^{n+2} - 6$

Now, we use this partition to compute ABC_4 index of $D_1[n]$.

$$\begin{aligned} ABC_4(D_1[n]) &= \sum_{uv \in E(D_1[n])} \sqrt{\frac{S_u + S_v - 2}{S_u S_v}} \\ &= 2^{n+2} \sqrt{\frac{4+4-2}{4 \times 4}} + 2^{n+2} \sqrt{\frac{5+4-2}{5 \times 4}} + (2^{n+3} - 8) \sqrt{\frac{7+5-2}{7 \times 5}} \\ &\quad + (2^{n+2} - 4) \sqrt{\frac{7+8-2}{7 \times 8}} \\ &\quad + (2^{n+1} - 2) \sqrt{\frac{8+6-2}{8 \times 6}} + (2^{n+1} - 2) \sqrt{\frac{6+6-2}{6 \times 6}} + (2^{n+2} - 4) \sqrt{\frac{6+5-2}{6 \times 5}} \\ &\quad + (2^{n+2} - 6) \sqrt{\frac{5+5-2}{5 \times 5}}. \end{aligned}$$

After an easy simplification, we get

$$\begin{aligned}
 ABC_4(D_1[n]) &= 2^{n+2} \left(\frac{\sqrt{35} + \sqrt{30} + 4\sqrt{2}}{10} + \frac{14\sqrt{6} + 16\sqrt{14} + \sqrt{728}}{56} \right) + 2^n \left(\frac{3 + \sqrt{10}}{3} \right) \\
 &\quad - \left(\frac{6 + 2\sqrt{10}}{6} + \frac{4\sqrt{30} + 24\sqrt{2}}{10} + \frac{\sqrt{728} + 16\sqrt{14}}{14} \right) \\
 &= \frac{4355257157954373 \times 2^{n+2}}{1125899906842624} + \frac{4625405229014641 \times 2^n}{2251799813685248} \\
 &\quad - \frac{3896323959238067}{281474976710656},
 \end{aligned}$$

which proves the theorem.

Theorem 6. The fifth geometric-arithmetic index of $D_1[n]$ for $n \geq 1$ is computed as follows:

$$GA_5(D_1[n]) = \frac{2238947875180617 \times 2^{n+2}}{281474976710656} - \frac{3636956611970403}{140737488355328}.$$

Proof. By using definition of GA_5 index and Table 2, one can see that:

$$\begin{aligned}
 GA_5(D_1[n]) &= \sum_{uv \in E(D_1[n])} \frac{2\sqrt{S_u S_v}}{S_u + S_v} \\
 &= 2^{n+2} \frac{2\sqrt{4 \times 4}}{4+4} + 2^{n+2} \frac{2\sqrt{5 \times 4}}{5+4} + (2^{n+3} - 8) \frac{2\sqrt{7 \times 5}}{7+5} + (2^{n+2} - 4) \frac{2\sqrt{7 \times 8}}{7+8} \\
 &\quad + (2^{n+1} - 2) \frac{2\sqrt{8 \times 6}}{8+6} + (2^{n+1} - 2) \frac{2\sqrt{6 \times 6}}{6+6} + (2^{n+2} - 4) \frac{2\sqrt{6 \times 5}}{6+5} + (2^{n+2} - 6) \frac{2\sqrt{5 \times 5}}{5+5}.
 \end{aligned}$$

After a bit calculation, we get

$$\begin{aligned}
 GA_5(D_1[n]) &= 2^{n+2} \left(\frac{4\sqrt{5} + 3\sqrt{35}}{9} + \frac{75 + 8\sqrt{14}}{30} + \frac{22\sqrt{3} + 14\sqrt{30}}{77} \right) \\
 &\quad - \left(\frac{120 + 20\sqrt{35} + 16\sqrt{14}}{15} + \frac{88\sqrt{3} + 56\sqrt{30}}{77} \right) \\
 &= \frac{2238947875180617 \times 2^{n+2}}{281474976710656} - \frac{3636956611970403}{140737488355328},
 \end{aligned}$$

that proves our theorem.

Example 7. We consider now the second kind of nanostar dendrimer, with the grown 1 – 3 steps denoted by $D_2[n]$ for $n = 1, 2, 3$.

Obviously, for $n = 1$, $|V| = 28$ and $|E| = 33$. The eccentric-connectivity polynomial is equal to:

$$\xi^c(D_2[1], x) = 7x^9 + 21x^8 + 20x^7 + 12x^6 + 6x^5.$$

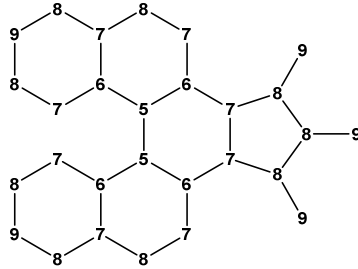


Figure 5. The molecular graph of $D_2[n]$ for $n = 1$.

For $n = 2$, $|V| = 82$ and $|E| = 99$. The eccentric-connectivity polynomial is equal to:

$$\xi^c(D_2[2], x) = 8x^{27} + 16x^{26} + 20x^{25} + 20x^{24} + 20x^{23} + 12x^{22} + 16x^{21} + 12x^{20} + 6x^{19} + 9x^{18} + 21x^{17} + 20x^{16} + 12x^{15} + 6x^{14}.$$

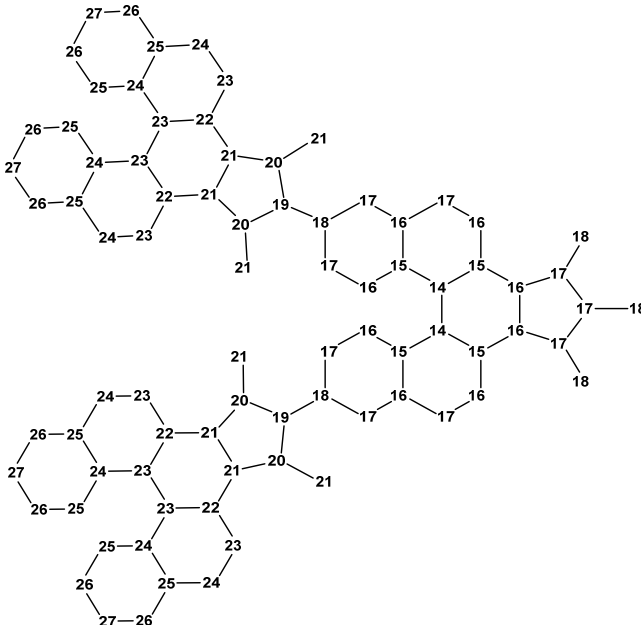


Figure 6. The molecular graph of $D_2[n]$ for $n = 2$.

Also, for $n = 3$, $|V| = 190$ and $|E| = 231$. The eccentric-connectivity polynomial is equal to:

$$\begin{aligned} \xi^c(D_2[3], x) = & 16x^{45} + 32x^{44} + 40x^{43} + 40x^{42} + 40x^{41} + 24x^{40} + 32x^{39} \\ & + 24x^{38} + 12x^{37} + 12x^{36} + 16x^{35} + 20x^{34} + 20x^{33} + 20x^{32} \\ & + 12x^{31} + 16x^{30} + 12x^{29} + 6x^{28} + 9x^{27} + 21x^{26} + 20x^{25} \\ & + 12x^{24} + 6x^{23}. \end{aligned}$$

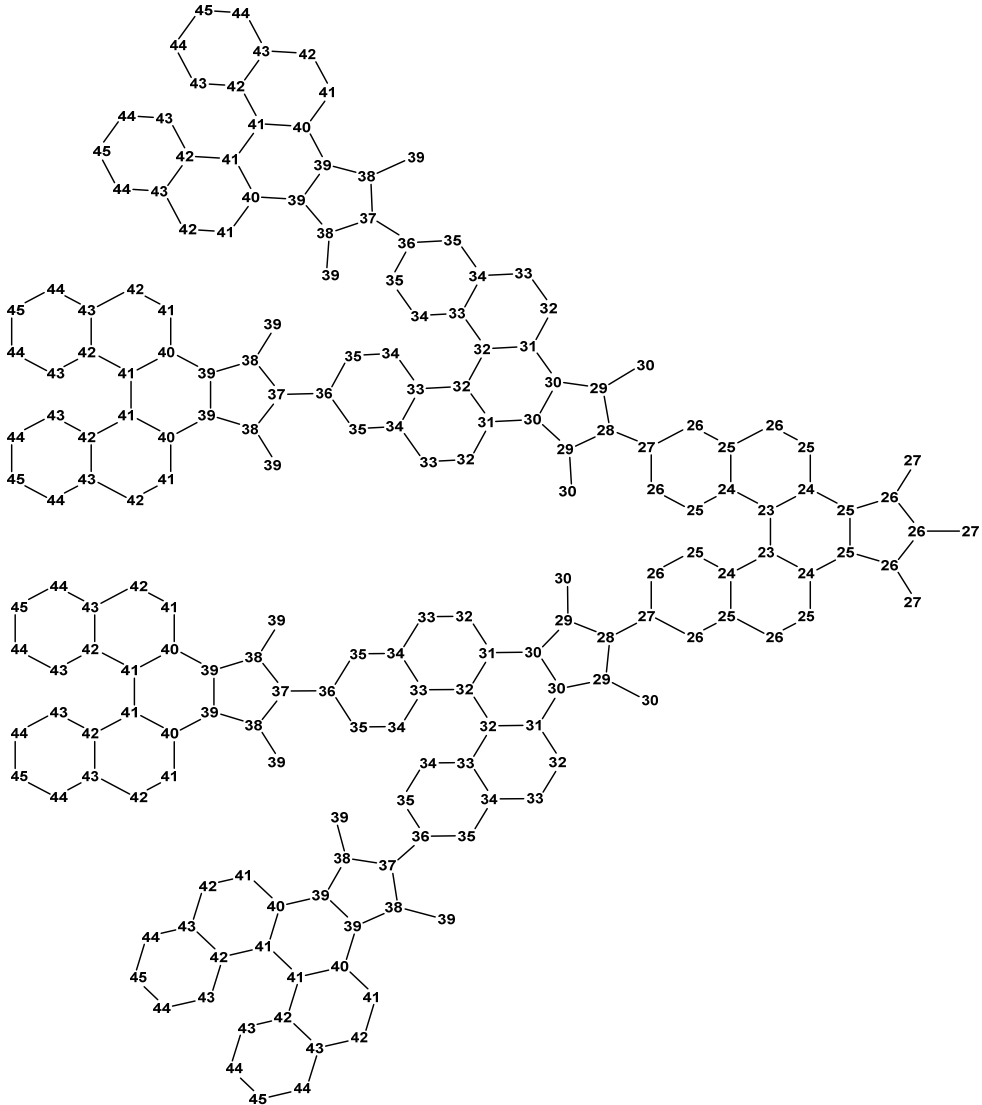


Figure 7. The molecular graph of $D_2[n]$ for $n = 3$.

Similar to the proof of Theorem 2, we can prove the following theorem:

Theorem 8. The eccentric-connectivity polynomial of the nanostar dendrimer $D_2[n]$ for $n \geq 3$ is computed as follows:

$$\begin{aligned} \xi^c(D_2[n], x) &= 2^{n+1} x^{18n-9} + 9x^{9n} + 21x^{9n-1} + 20x^{9n-2} + 12x^{9n-3} + 6x^{9n-4} \\ &+ \sum_{k=1}^{n-1} 2^k (8x^{9(n+k)-1} + 10x^{9(n+k)-2} + 10x^{9(n+k)-3} + 10x^{9(n+k)-4} \\ &+ 6x^{9(n+k)-5} + 8x^{9(n+k)-6} + 6x^{9(n+k)-7} + 3x^{9(n+k)-8}) \\ &+ \sum_{k=1}^{n-2} 2^k (6x^{9(n+k)}) \end{aligned}$$

Proof. Using a simple calculation, one can show that $|V(D_2[n])| = 27 \times 2^n - 26$ and $|E(D_2[n])| = 33 \times 2^n - 33$. For $u \in V(D_2[n])$, we have $d(D_2[n]) = 18n - 9$ and $r(D_2[n]) = 9n - 4$. By considering the general form of this second nanostar dendrimer, we can fill the Table 3. By using data in this table the proof is straightforward.

Table 3. The representatives of vertices of $D_2[n]$ with their degree, eccentricity and frequency of occurrence, for $1 \leq k \leq n - 1$ and $n \geq 3$.

Vertex type	Degree	Eccentricity	Frequency
1	2	$18n - 9$	2^n
2	3	$9n$	2
3	1	$9n$	3
4	3	$9n - 1$	3
5	2	$9n - 1$	6
6	3	$9n - 2$	4
7	2	$9n - 2$	4
8	3	$9n - 3$	4
9	3	$9n - 4$	2
10	2	$9n + 9k - 1$	2^{k+2}
11	3	$9n + 9k - 2$	2^{k+1}
12	2	$9n + 9k - 2$	2^{k+1}
13	3	$9n + 9k - 3$	2^{k+1}
14	2	$9n + 9k - 3$	2^{k+1}
15	3	$9n + 9k - 4$	2^{k+1}
16	2	$9n + 9k - 4$	2^{k+1}
17	3	$9n + 9k - 5$	2^{k+1}

Vertex type	Degree	Eccentricity	Frequency
18	3	$9n + 9k - 6$	2^{k+1}
19	1	$9n + 9k - 6$	2^{k+1}
20	3	$9n + 9k - 7$	2^{k+1}
21	3	$9n + 9k - 8$	2^k
22	3	$\sum_{k=1}^{n-2} 9n + 9k$	$\sum_{k=1}^{n-2} 2^{k+1}$

By Table 3 and some simple calculations by MATLAB, we can prove the following theorem:

Theorem 9. The eccentric-connectivity index and total eccentricity index of $D_2[n]$ for $n \geq 1$ are computed as follows:

$$\begin{aligned} \xi^c(D_2[n]) &= 2^n(1188n - 1439) - 594n + 1569, \\ \theta(D_2[n]) &= 2^n(486n - 582) - 234n + 633. \end{aligned}$$

Theorem 10. The fourth atom-bond connectivity index and fifth geometric-arithmetic index of $D_2[n]$ for $n \geq 1$ are computed as:

$$\begin{aligned} GA_5(D_2[n]) &= \frac{286724064989901 \times 2^n}{8796093022208} - \frac{2298465931078229}{70368744177664}, \\ ABC_4(D_2[n]) &= \frac{2\sqrt{2}(3 \times 2^n - 4)}{5} + \frac{1072236973249725 \times 2^n}{70368744177664} - \frac{251086321269759}{17592186044416}. \end{aligned}$$

Proof. These results are proven like Theorem 5 and Theorem 6 therefore, we omit the proofs.

Table 4. The edge partition of $D_2[n]$ based on the degree sum of neighbors of the end vertices of each edge.

(S_u, S_v) $uv \in E(D_2[n])$	No. edges	(S_u, S_v) $uv \in E(D_2[n])$	No. edges
(3,7)	$2^{n+1} - 1$	(5,5)	$3 \times 2^n - 4$
(7,7)	2	(5,7)	$4(2^n - 1)$
(7,9)	$5(2^n) - 8$	(4,5)	2^{n+1}
(9,9)	$2^{n+1} - 2$	(4,4)	2^n
(9,8)	$6(2^n - 1)$	(7,8)	$2^{n+1} - 2$
(8,5)	$4(2^n - 1)$	(6,7)	$4(2^{n-1} - 1)$

CONCLUSIONS

Among topological descriptors, topological indices are very important and they play a prominent role in Mathematical Chemistry. In this paper, we studied the nanostar dendrimers. As main results, we derived exact formulas for the eccentric-connectivity index, total eccentricity index, fourth version of atom-bond connectivity index and fifth version of geometric-arithmetic index of two types of nanostar dendrimers.

REFERENCES

1. R. Todeschini, V. Consonni, Handbook of Molecular Descriptors, Weinheim, Wiley-VCH, **2000**.
2. N.E. Arif, R. Hasni, S. Alikhani, *Journal of Applied Sciences*, **2012**, 12, 2279.
3. A.R. Ashrafi, M. Mirzagar, *Indian Journal of Chemistry*, **2008**, 47A, 538.
4. M.R. Farahani, W. Gao, R. Kanna M.R., *Indian Journal of Fundamental and Applied Life Sciences*, **2015**, 5 (S4), 766.
5. N. Soleimani, M.J. Nikmehr, H.A. Tavallaee, *Studia UBB. Chemia*, **2014**, 59(4), 139.
6. N. Soleimani, M.J. Nikmehr, H.A. Tavallaee, *Journal of the National Science Foundation of Sri Lanka*, **2015**, 43(2), 127.
7. M.J. Nikmehr, M. Veylaki, N. Soleimani, *Optoelectron. Adv. Mater.-Rapid Comm.*, **2015**, 9(9), 1147.
8. M.J. Nikmehr, N. Soleimani, H.A. Tavallaee, *Proceedings of the Institute of Applied Mathematics*, **2015**, 4(1), 20.
9. M.J. Nikmehr, L. Heidarzadeh, N. Soleimani, *Studia Scientiarum Mathematicarum Hungarica*, **2014**, 51, 133.
10. T. Doslić, M. Ghorbani, M.A. Hosseinzadeh, *Utilitas Mathematica*, **2011**, 84, 297.
11. H. Wiener, *J. Am. Chem. Soc.*, **1947**, 69, 17.
12. V. Sharma, R. Goswami, A.K. Madan, *J. Chem. Inf. Comput. Sci.*, **1997**, 37, 273.
13. A.R. Ashrafi, M. Saheli, M. Ghorbani, *Journal of Computational and Applied Mathematics*, **2011**, 235(16), 4561.
14. N. De, S.M.A. Nayeem, A. Pal, *Ann. Pure Appl. Math.*, **2014**, 7(1), 59.
15. N. De, A. Pal, S.M.A. Nayeem, *Malaya J. Mat.*, **2015**, 3(4), 523.
16. E. Estrada, L. Torres, L. Rodriguez, I. Gutman, *Indian Journal of Chemistry*, **1998**, 37, 849.
17. D. Vukičević, B. Furtula, *Journal of Mathematical Chemistry*, **2009**, 46, 1369.
18. M. Ghorbani, H. Hosseinzadeh, *Optoelectron. Adv. Mater. - Rapid Comm.*, **2010**, 4, 1419.

19. A. Graovac, M. Ghorbani, M.A. Hosseinzadeh, *J. Math. Nanosci.*, **2011**, 1, 33.
20. H. Shabani, A.R. Ashrafi, I. Gutman, *Studia UBB. Chemia*, **2010**, 4, 107.
21. M. Higuchi, S. Shiki, K. Ariga, K. Yamamoto, *J. Am. Chem. Soc.*, **2001**, 123 (19), 4414.

*Dedicated to Professor Mircea Diudea
on the Occasion of His 65th Anniversary*

COMPUTING THE MODIFIED ECCENTRIC CONNECTIVITY POLYNOMIAL OF NAPHTHYLENIC LATTICES

MARYAM VEYLAKI^{a,*} AND MOHAMMAD JAVAD NIKMEHR^b

ABSTRACT. Let $G = (V, E)$ be a graph, where G is a non-empty set of vertices $V(G)$ and $E(G)$ is a set of edges. In such chemical graphs the vertices of the graph corresponds to the atoms of the molecule, and the edges represent the chemical bonds. The aim of this paper is to compute the modified eccentric connectivity polynomial for the naphthylenic molecular graph.

Keywords: *modified eccentric connectivity polynomial, molecular graph, naphthylenic lattice*

INTRODUCTION

Molecular descriptors, especially topological indices, play an important role in the research of chemical compounds. A topological index is a numeric quantity derived from the structure of a graph which is invariant under automorphisms of the graph under consideration.

There are known many topological indices that have found some usage in QSPR/QSAR investigation. All graphs in this paper are finite and simple. A simple graph $G = (V, E)$ is a finite nonempty set $V(G)$ of objects called vertices together with a set $E(G)$ of unordered pairs of distinct vertices of G called edges. In chemical graphs, the vertices of a graph correspond to the atoms of a molecule, and the edges represent chemical bonds. A distance-

^a *Young Researchers and Elite Club, Sari Branch, Islamic Azad University, Sari, Iran*

^b *Faculty of Mathematics, K.N. Toosi University of Technology, P.O. Box 16315-1618, Tehran, Iran*

* *Corresponding Author: veylaki@yahoo.com*

based topological index for a graph G is a topological index related to the distance function $d(-, -): V(G) \times V(G) \rightarrow \mathbb{R}$ in which $d(u, v)$ is defined as the length of a minimal path connecting u and v . The eccentricity of a vertex u in $V(G)$, denoted $ecc(u)$, is defined as $ecc(u) = \text{Max}\{d(u, v) \mid v \in V(G)\}$ [1 – 5].

The eccentric connectivity index of the molecular graph, $ecc(G)$, was proposed by Sharma, Goswami and Madan [6]. It is defined as $\xi^c(G) = \sum_{u \in V(G)} \text{deg}(u) ecc(u)$, where $\text{deg}(u)$ denotes the degree of vertex u in G .

The modified eccentric connectivity polynomial was proposed by Ashrafi [7] and it is defined as $\Lambda(G, x) = \sum_{u \in V(G)} n_G(u) x^{ecc(u)}$, where $n_G(u)$ is the sum of the degrees of neighborhoods of a vertex u . As a result, MEC index is the first derivative of this polynomial in $x = 1$.

The aim of this paper is to compute modified eccentric connectivity (MEC) polynomial for an infinite family of naphthylenic graphs. We encourage the reader to consult the papers [7-12] for more details about some properties of this topological index of some nanostructures.

RESULTS AND DISCUSSION

Following Diudea [13,14], we propose now the naphthylenic net, with the sequence: $C_6, C_6, C_4, C_6, C_6 \dots C_6, C_6, C_4, C_6, C_6$, and repeat unit C_6, C_6, C_4 . The naphthylenic patterns, $NP[n, n]$ was designed as in Figure 1.

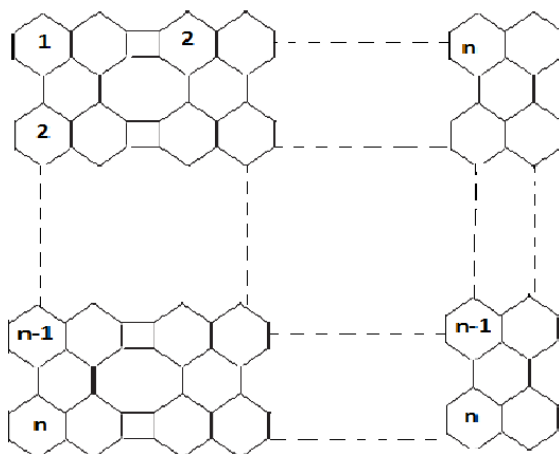


Figure 1. The 2D lattice of $NP[n, n]$

MODIFIED ECCENTRIC CONNECTIVITY POLYNOMIAL OF NAPHTHYLENIC LATTICES

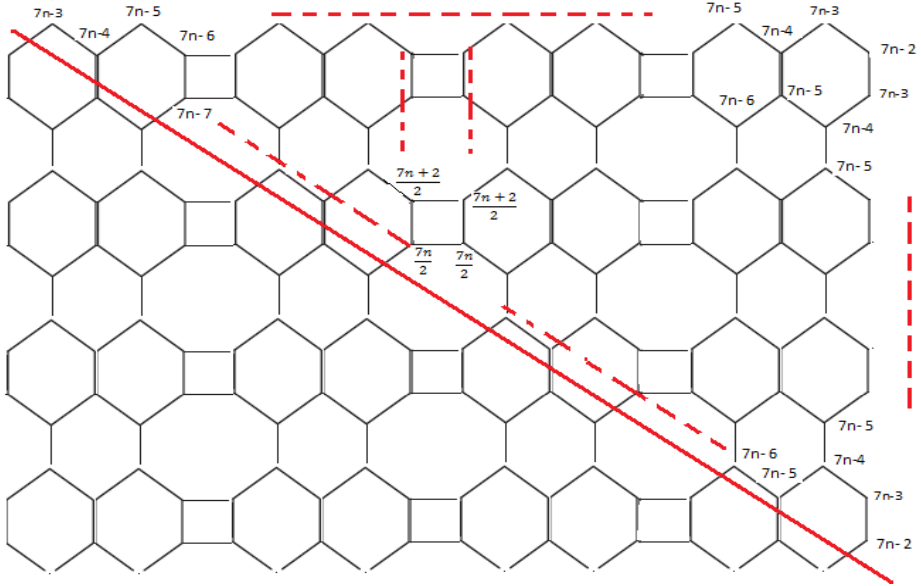


Figure 2. The maximum and minimum eccentricity of $NP[2k, 2k]$

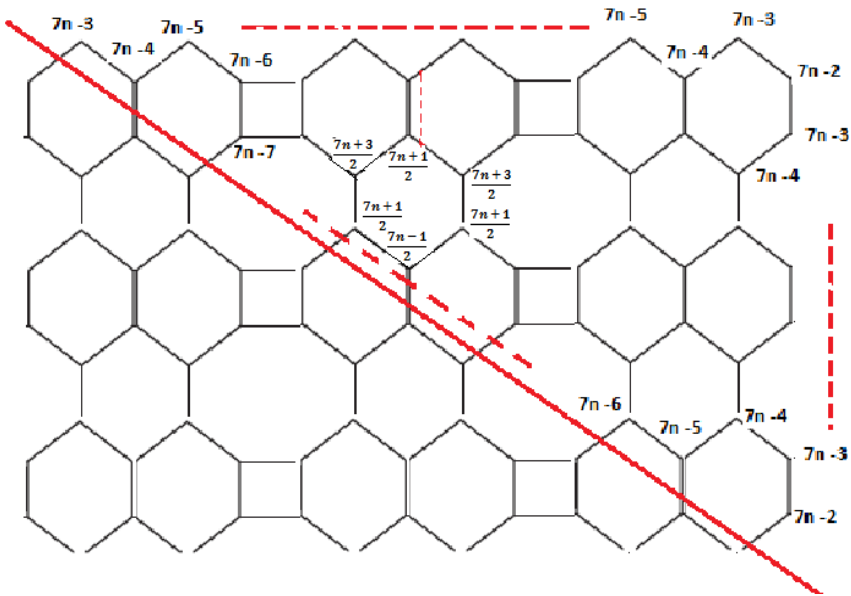


Figure 3. The maximum and minimum eccentricity of $NP[2k + 1, 2k + 1]$

In the following lemma, the maximum and minimum eccentric connectivity of $NP[n, n]$ is computed.

Lemma 1. For any vertex u in $V(NP[n, n])$, we have:

$$\begin{aligned} \text{Max} (ecc(u)) &= 7n - 2, \\ \text{Min} (ecc(u)) &= \begin{cases} \frac{7n}{2} & \text{if } 2|n, \\ \frac{7n-1}{2} & \text{if } 2 \nmid n. \end{cases} \end{aligned}$$

Proof. Suppose u is a vertex of $NP[n, n]$, then from Figures 2 and 3, one can see that for each vertex v , the longest path with maximum length is $7n - 2$, and the shortest paths with maximum length, when n is even or odd, are $\frac{7n}{2}$ and $\frac{7n-1}{2}$, respectively. Thus the proof is completed.

In the following theorem we compute the modified eccentric connectivity polynomial for $NP(n, n)$.

Theorem 2. The modified eccentric connectivity polynomial of $NP(n, n)$ is computed as:

$$\begin{aligned} \Lambda(NP(n, n), x) &= 8x^{7n-2} + 20x^{7n-3} + 40x^{7n-4} + 56x^{7n-5} + 78x^{7n-6} \\ &\quad + 192x^{7n-7} + \begin{cases} A & 2|n \quad n \geq 6 \\ B & 2 \nmid n, \quad n \geq 7 \end{cases} \end{aligned}$$

A and B are as follows, respectively.

$$\begin{aligned} A &= 2(5n + 70)x^{7n-8} + 2(12n + 32)x^{7n-9} + 2(17n + 16)x^{7n-10} \\ &\quad + 18 \sum_{k=0}^{n-2} (2k + 2)x^{\frac{7n}{2}+k} + 36 \sum_{k=n-1}^{\frac{7n-22}{2}} (n - 1)x^{\frac{7n}{2}+k} \\ &\quad + 32 \sum_{k=0}^{\frac{n-4}{2}} x^{\frac{9n-2}{2}+5k} + 24 \sum_{k=0}^{\frac{n-6}{2}} x^{\frac{9n}{2}+5k} + 28 \sum_{k=0}^{\frac{n-6}{2}} x^{\frac{9n+2}{2}+5k} \\ &\quad + 24 \sum_{k=0}^{\frac{n-6}{2}} x^{\frac{9n+4}{2}+5k} + 32 \sum_{k=0}^{\frac{n-6}{2}} x^{\frac{9n+6}{2}+5k}, \end{aligned}$$

$$\begin{aligned}
 B = & 220x^{7n-8} + 2(5n + 85)x^{7n-9} + 2(13n + 29)x^{7n-10} + 2(17n + 5)x^{7n-11} \\
 & + 18 \sum_{k=0}^{\frac{n-2}{2}} (2k + 1)x^{\frac{7n-1}{2}+k} + 36 \sum_{k=n-1}^{3n-7} (n - 1)x^{\frac{7n-1}{2}+k} \\
 & + 28 \sum_{k=0}^{\frac{n-5}{2}} x^{\frac{9n-3}{2}+5k} + 24 \sum_{k=0}^{\frac{n-5}{2}} x^{\frac{9n-1}{2}+5k} + 32 \sum_{k=0}^{\frac{n-5}{2}} x^{\frac{9n+1}{2}+5k} \\
 & + 32 \sum_{k=0}^{\frac{n-7}{2}} x^{\frac{9n+3}{2}+5k} + 24 \sum_{k=0}^{\frac{n-7}{2}} x^{\frac{9n+5}{2}+5k} - 14x^{\frac{9n-3}{2}}.
 \end{aligned}$$

Proof. Considering Figures 2 and 3, it can be seen that there are several types of vertices. By computing the eccentricity of these vertices we have the results in Tables 1 and 2.

Table 1. Types of vertices of $NP(2k, 2k)$

Number	ECC	$N_G(u)$
2	$7n - 2$	4
4	$7n - 3$	5
2	$7n - 4$	8
2	$7n - 4$	7
2	$7n - 4$	5
2	$7n - 5$	9
2	$7n - 5$	8
2	$7n - 5$	6
2	$7n - 5$	5
4	$7n - 6$	9
4	$7n - 6$	8
2	$7n - 6$	5
6	$7n - 7$	9
4	$7n - 7$	8
2	$7n - 7$	5
8	$7n - 8$	9
2	$7n - 8$	8
2	$7n - 8$	6
$n - 6$	$7n - 8$	5
10	$7n - 9$	9

Number	ECC	$N_G(u)$
$n - 6$	$7n - 9$	8
2	$7n - 9$	7
$n - 6$	$7n - 9$	5
$n + 4$	$7n - 10$	9
$n - 4$	$7n - 10$	8
2	$7n - 10$	6
$2(n - 1)$	$7n - 11$	9
2	$7n - 11$	8
000
$2(n - 1)$	$(7n + 2(n - 2))/2$	9
$2(n - 2)$	$(7n + 2(n - 3))/2$	9
000
6	$(7n + 4)/2$	9
4	$(7n + 2)/2$	9
2	$7n/2$	9

Table 2. Types of vertices of $NP(2k + 1, 2k + 1)$

Number	ECC	$N_G(u)$
2	$7n - 2$	4
4	$7n - 3$	5
2	$7n - 4$	8
2	$7n - 4$	7
2	$7n - 4$	5
2	$7n - 5$	9
2	$7n - 5$	8
2	$7n - 5$	6
2	$7n - 5$	5
4	$7n - 6$	9
4	$7n - 6$	8
2	$7n - 6$	5
6	$7n - 7$	9
4	$7n - 7$	8
2	$7n - 7$	5
8	$7n - 8$	9
2	$7n - 8$	8
2	$7n - 8$	6

Number	ECC	$N_G(u)$
2	$7n - 8$	5
10	$7n - 9$	9
2	$7n - 9$	8
2	$7n - 9$	7
$n - 7$	$7n - 9$	5
12	$7n - 10$	9
$n - 7$	$7n - 10$	8
2	$7n - 10$	6
$n - 7$	$7n - 10$	5
$n + 5$	$7n - 11$	9
$n - 7$	$7n - 11$	8
$2(n - 1)$	$7n - 12$	9
2	$7n - 12$	8
000
$2n - 3$	$(7n - 1 + 2(n - 2))/2$	9
$2n - 5$	$(7n - 1 + 2(n - 3))/2$	9
000
5	$7n + 3/2$	9
3	$7n + 1/2$	9
1	$7n - 1/2$	9

This implies that:

$$\begin{aligned}
 \Lambda(NP(2k, 2k), x) &= 2(2 \times 4x^{7n-2} + 4 \times 5x^{7n-3} + (2 \times 8 + 2 \times 7 + 2 \times 5)x^{7n-4} \\
 &+ (2 \times 9 + 2 \times 8 + 2 \times 6 + 2 \times 5)x^{7n-5} \\
 &+ (4 \times 9 + 4 \times 8 + 2 \times 5)x^{7n-6} + (6 \times 9 + 4 \times 8 + 2 \times 5)x^{7n-7} \\
 &+ (8 \times 9 + 2 \times 8 + 2 \times 6 + 5(n - 6))x^{7n-8} \\
 &+ (10 \times 9 + 8(n - 6) + 2 \times 7 + 5(n - 6))x^{7n-9} \\
 &+ (9(n + 4) + 8(n - 4) + 6 \times 2)x^{7n-10} \\
 &+ (18(n - 1) + 2 \times 8)x^{7n-11} + \dots \\
 &+ \left(2 \times 9x^{\frac{7n}{2}} + 4 \times 9x^{\frac{7n+2}{2}} + \dots + 2(n - 1) \times 9x^{\frac{7n}{2}+(n-2)} \right),
 \end{aligned}$$

Therefore,

$$\begin{aligned}
 \Lambda (NP(2k, 2k), x) &= 16x^{7n-2} + 40x^{7n-3} + 80x^{7n-4} + 112x^{7n-5} + 156x^{7n-6} \\
 &+ 192x^{7n-7} + 2(5n + 70)x^{7n-8} + 2(12n + 32)x^{7n-9} \\
 &+ 2(17n + 16)x^{7n-10} \\
 &+ 18 \sum_{k=0}^{n-2} (2k + 2)x^{\frac{7n}{2}+k} + 36 \sum_{k=n-1}^{\frac{7n-22}{2}} (n - 1)x^{\frac{7n}{2}+k} + 32 \sum_{k=0}^{\frac{n-4}{2}} x^{\frac{9n-2}{2}+5k} \\
 &+ 24 \sum_{k=0}^{\frac{n-6}{2}} x^{\frac{9n}{2}+5k} + 28 \sum_{k=0}^{\frac{n-6}{2}} x^{\frac{9n+2}{2}+5k} \\
 &+ 24 \sum_{k=0}^{\frac{n-6}{2}} x^{\frac{9n+4}{2}+5k} + 32 \sum_{k=0}^{\frac{n-6}{2}} x^{\frac{9n+6}{2}+5k}.
 \end{aligned}$$

and for $n = 2k + 1$ we have:

$$\begin{aligned}
 \Lambda (NP(2k + 1, 2k + 1), x) &= 2(2 \times 4x^{7n-2} + 2 \times 5x^{7n-3} + (2 \times 8 + 2 \times 7 + 2 \times 5)x^{7n-4} \\
 &+ (2 \times 9 + 2 \times 8 + 2 \times 6 + 2 \times 5)x^{7n-5} \\
 &+ (4 \times 9 + 4 \times 8 + 4 \times 5)x^{7n-6} + (6 \times 9 + 4 \times 8 + 2 \times 5)x^{7n-7} \\
 &+ (8 \times 9 + 2 \times 8 + 2 \times 6 + 2 \times 5)x^{7n-8} \\
 &+ (10 \times 9 + 2 \times 8 + 2 \times 7 + 5(n - 7))x^{7n-9} \\
 &+ (12 \times 9 + 8(n - 7) + 2 \times 6 + 5(n - 7))x^{7n-10} \\
 &+ (9(n + 5) + 8(n - 5))x^{7n-11} + (18(n - 1) + 2 \times 8)x^{7n-12} + \dots) \\
 &+ \left(1 \times 9x^{\frac{7n-1}{2}} + 3 \times 9x^{\frac{7n+1}{2}} + \dots + (2n - 3) \times 9x^{\frac{7n-1}{2}+(n-2)} \right).
 \end{aligned}$$

Therefore,

$$\begin{aligned} \Lambda(NP(2k+1, 2k+1), x) &= 16x^{7n-2} + 40x^{7n-3} + 80x^{7n-4} + 112x^{7n-5} + 156x^{7n-6} \\ &+ 192x^{7n-7} + 220x^{7n-8} + 2(5n+85)x^{7n-9} + 2(13n+29)x^{7n-10} \\ &+ 2(17n+5)x^{7n-11} \\ &+ 18 \sum_{k=0}^{\frac{n-2}{2}} (2k+1)x^{\frac{7n-1}{2}+k} + 36 \sum_{k=n-1}^{3n-7} (n-1)x^{\frac{7n-1}{2}+k} \\ &+ 28 \sum_{k=0}^{\frac{\frac{n-5}{2}}{2}} x^{\frac{9n-3}{2}+5k} + 24 \sum_{k=0}^{\frac{\frac{n-5}{2}}{2}} x^{\frac{9n-1}{2}+5k} + 32 \sum_{k=0}^{\frac{\frac{n-5}{2}}{2}} x^{\frac{9n+1}{2}+5k} \\ &+ 32 \sum_{k=0}^{\frac{\frac{n-7}{2}}{2}} x^{\frac{9n+3}{2}+5k} + 24 \sum_{k=0}^{\frac{\frac{n-7}{2}}{2}} x^{\frac{9n+5}{2}+5k} - 14x^{\frac{9n-3}{2}}. \end{aligned}$$

Some exceptional cases are given in Table 3.

Table 3. Some exceptional cases of $NP(n, n)$

Naphtylenic graph	MEC polynomial, $2 \leq n \leq 5$
$NP(2,2)$	$16x^{12} + 40x^{11} + 80x^{10} + 60x^9 + 68x^8 + 36x^7$
$NP(3,3)$	$16x^{26} + 40x^{25} + 80x^{24} + 112x^{23} + 104x^{22} + 104x^{21}$ $+ 132x^{20} + 136x^{19} + 132x^{18} + 140x^{17}$ $+ 108x^{16} + 72x^{15} + 36x^{14}.$
$NP(4,4)$	$16x^{26} + 40x^{25} + 80x^{24} + 112x^{23} + 104x^{22} + 104x^{21}$ $+ 132x^{20} + 136x^{19} + 132x^{18} + 140x^{17}$ $+ 108x^{16} + 72x^{15} + 36x^{14}$
$NP(5,5)$	$16x^{33} + 40x^{32} + 80x^{31} + 112x^{30} + 156x^{29} + 172x^{28}$ $+ 176x^{27} + 172x^{26} + 168x^{25} + 176x^{24}$ $+ 176x^{23} + 168x^{22} + 158x^{21} + 126x^{20}$ $+ 90x^{19} + 54x^{18} + 18x^{17}$

REFERENCES

1. A. Dobrynin, A. Kochetova, *J. Chem. Inf. Comput. Sci.*, **1994**, *34*, 1082.
2. I. Gutman. *J. Chem. Inf. Comput. Sci.*, **1994**, *34*, 1087.
3. I. Gutman, O.E. Polansky, *Mathematical Concepts in Organic Chemistry*, Springer-Verlag: New York, **1986**.
4. M.A. Johnson, G.M. Maggiora, *Concepts and Applications of Molecular Similarity*, Wiley Interscience: New York, **1990**.
5. B. Zhou, Z. Du, *MATCH Commun. Math. Comput. Chem.*, **2010**, *63*(1), 101.
6. V. Sharma, R. Goswami, A.K. Madan, *J. Chem. Inf. Comput. Sci.*, **1997**, *37*, 273.
7. A.R. Ashrafi, M. Ghorbani, *Electronic Mater. Lett.*, **2010**, *6* (2), 87.
8. J. Asadpour, R. Mojarad, B. Danseshian, *Studia Univ. Babes-Bolyai Chemia*, **2014**, *4*, 157.
9. A.R. Ashrafi, M. Ghorbani, M. Jalali, *Ind. J. Chem.*, **2008**, *47A*, 535.
10. M. Ghorbani, A. R. Ashrafi, *J. Comput. Theor. Nanosci.*, **2006**, *3*, 803.
11. A.R. Ashrafi, M. Jalali, M. Ghorbani, M.V. Diudea, *MATCH Commun. Math. Comput. Chem.*, **2008**, *60*(3), 905.
12. M. Ghorbani, M. Jalali, *Digest J. Nanomater. Biostruct.*, **2008**, *3* (4), 269.
13. M.V. Diudea, *Nanotubes Carbon Nanostruct.*, **2002**, *10*(4), 273.
14. M.V. Diudea, *Studia Univ. Babes-Bolyai Chemia*, **2003**, *48* (2), 17.

*Dedicated to Professor Mircea Diudea
on the Occasion of His 65th Anniversary*

MODELS OF MONOVALENT IONS DISSOLVED IN WATER

LAVINIA L. PRUTEANU^{a,b}, LORENTZ JÄNTSCHI^{a,b,*},
MIHAELA L. UNGUREȘAN^b, SORANA D. BOLBOACĂ^c

ABSTRACT. A computational study on water-ions clusters for six ions (NH_4^+ , F^- , Cl^- , Li^+ , Na^+ , and K^+) is described. Restricted Hartree-Fock method with 6-31G* basis set was used to optimize the investigated water ion-clusters. Stable ion-water clusters proved to form with four ($\text{NH}_4^+ \cdot 4\text{H}_2\text{O}$ and $\text{Li}^+ \cdot 4\text{H}_2\text{O}$), five ($\text{Cl}^- \cdot 5\text{H}_2\text{O}$ and $\text{Na}^+ \cdot 5\text{H}_2\text{O}$) and respectively six water molecules ($\text{F}^- \cdot 6\text{H}_2\text{O}$ and $\text{K}^+ \cdot 6\text{H}_2\text{O}$). The arrangement of water molecules around the investigated ions proved not be symmetrical. Furthermore, the investigation of the stability of dodecahedral cages constructed with the investigated ions showed a stable symmetry for $\text{O}_{12}\text{N}_8\text{H}_{50}$, $\text{O}_{12}\text{Li}_8\text{H}_{18}$, and $\text{O}_{15}\text{K}_5\text{H}_{29}$.

Keywords: *ion-water cluster; monovalent ion; stabilization*

INTRODUCTION

Structure of the water is a subject of theoretical physics [1], and differs significantly from gaseous state and solid state (ice) to liquid state (where the lack of geometrical symmetry makes more difficult the analysis) [2]. Eighteen crystalline phases (where the oxygen atoms are in fixed positions relative to each other but the hydrogen atoms may or may not be disordered but obeying the “ice rules”) and three amorphous (non-crystalline) phases are known to date [3, 4].

^a Babeș-Bolyai University, Institute for Doctoral Studies, 1 Kogălniceanu Str., RO-400084, Cluj-Napoca, Romania

^b Technical University of Cluj-Napoca, Department of Physics and Chemistry, 103-105 Muncii Blvd., RO-400641, Cluj-Napoca, Romania

^c Iuliu Hațieganu University of Medicine and Pharmacy, Department of Medical Informatics and Biostatistics, 6 Louis Pasteur Str., RO-400349, Cluj-Napoca, Romania

* Corresponding Author: lori@chimie.utcluj.ro

The crystalline phases formed by two “close-packed” structures have been identified: hexagonal (at upper temperatures) [5] and cubic (at lower temperatures) [6-8]. The distances between atoms in ice proved to be either 100pm ($d(\text{O}-\text{H})$) or 175pm ($d(\text{O}\dots\text{H})$) [9]. The $d(\text{O}-\text{H})$ length of water was determined experimentally [10] and furthermore calculate at different levels of theory (Table 1 [10]), showing that the top 3 closest values are given by the following methods: M06-2X/6-31G*, HF/3-21G* and MP3/6-31G*.

Water clusters, hydrogen bounded assembly [11] (the smallest water cluster being the water dimer $(\text{H}_2\text{O})_2$), are important components of the atmospheric chemistry [12]. Different water clusters, such as $(\text{H}_2\text{O})_6$ (function of the method, different temperature transition and density were reported [13]), dodecahedral $(\text{H}_2\text{O})_{20}$ [14], edge-sharing pentagonal prisms, fused cubes, and face-sharing pentagonal prisms [15], etc. were identified and investigated.

Table 1. $d(\text{O}-\text{H})$ length in water: experimental vs. calculated [10]

Method	$d(\text{O}-\text{H})$ pm
Experimental	95.78
MP4/6-31G*	97.03
MP3/6-31G*	96.68
MP2/6-31G*	96.89
M06-2X/6-31G*	96.56
HF/6-31G*	94.73
HF/3-21G*	96.65
HF/STO-3G	98.92

Properties of Ion-water clusters $X[\text{H}_2\text{O}]_n$ (where X is the ion) have also been investigated. The importance of $(\text{H}_2\text{O})_{20}$ surrounding monovalent cations has been demonstrated by infrared photo-dissociation spectroscopy and blackbody infrared radiative dissociation [16]. Global minima were identified for $\text{Na}^+(\text{H}_2\text{O})_{20}$, $\text{Cl}^-(\text{H}_2\text{O})_{17}$, and $\text{Na}^+(\text{H}_2\text{O})_{100}$ using PBHaT algorithm (a hybrid algorithm able to sample efficiently the partition function from the global minima to the liquid state) [17].

The aim of our research was to investigate the bond angles and distances in ion-water clusters on stable states, defined as the equilibrium state for which adding water molecules change neither the distances in ion-water cluster nor angles between atoms in the cluster, for NH_4^+ , F^- , Cl^- , Li^+ , Na^+ , and K^+ . Further, by using the dodecahedron arrangement of water and ammonia molecules, possible stable states of water and ammonia mixtures were explored.

RESULTS AND DISCUSSION

Stable ion-water clusters have been proved to form with four ($\text{NH}_4^+ \cdot 4\text{H}_2\text{O}$ and $\text{Li}^+ \cdot 4\text{H}_2\text{O}$), five ($\text{Cl}^- \cdot 5\text{H}_2\text{O}$ and $\text{Na}^+ \cdot 5\text{H}_2\text{O}$) and six water molecules ($\text{F}^- \cdot 6\text{H}_2\text{O}$ and $\text{K}^+ \cdot 6\text{H}_2\text{O}$), respectively. The stable ion-water clusters are presented in **Figure 1**. Note that these structures are without constrains since the *in silico* modelling was conducted in water.

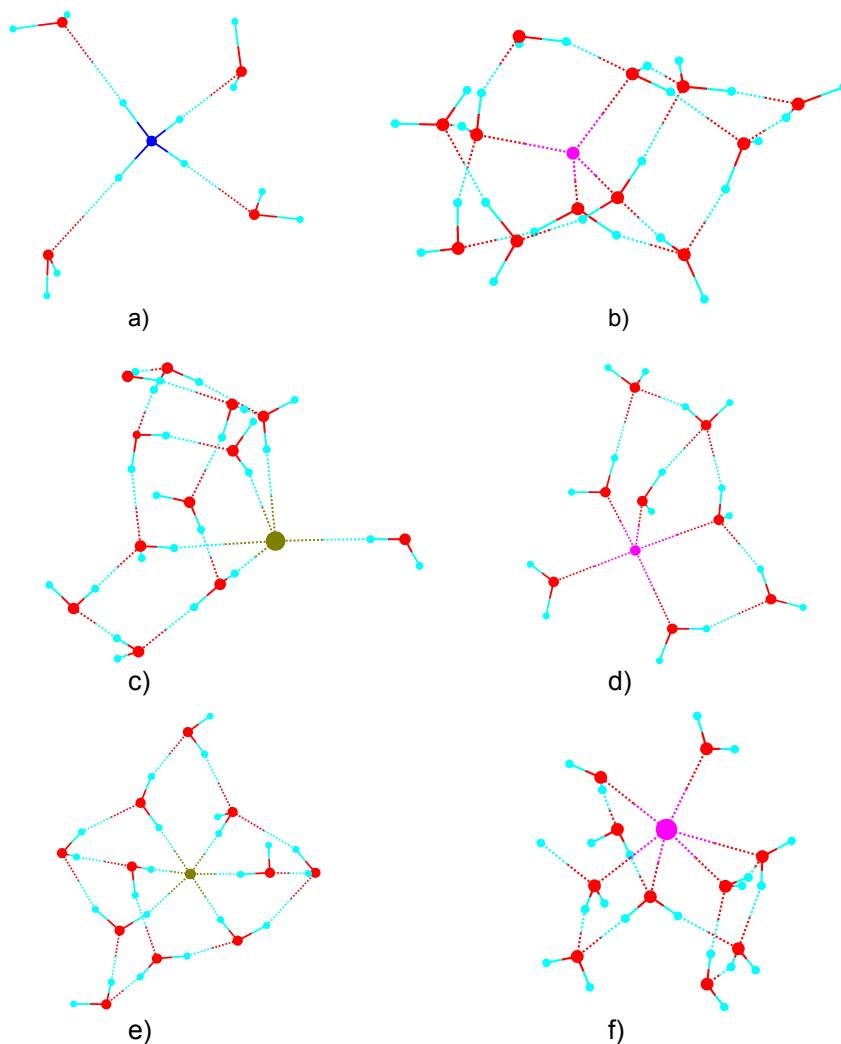


Figure 1. Ion-water clusters: a) $\text{NH}_4^+ \cdot 4\text{H}_2\text{O}$ cluster, b) $\text{Li}^+ \cdot 4\text{H}_2\text{O}$ cluster, c) $\text{Cl}^- \cdot 5\text{H}_2\text{O}$ cluster, d) $\text{Na}^+ \cdot 5\text{H}_2\text{O}$ cluster, e) $\text{F}^- \cdot 6\text{H}_2\text{O}$ cluster, f) $\text{K}^+ \cdot 6\text{H}_2\text{O}$ cluster

The first solved ion ($\text{NH}_4^+ \cdot 4\text{H}_2\text{O}$) was selected as a reference for reproducibility of the calculation and for the validation of the chosen method of analysis. The obtained results are in agreement with the known data [18-21]. Since different ion-water clusters were investigated, the lengths of the bonds as well as the angles between bonds are different from one cluster to another (see **Tables 2** and **3**).

The analysis of the other ion-water clusters showed that the arrangement of water molecule around investigated ions is not symmetrical even if sometimes (e.g. **Fig. 1a**) the symmetry is mimed. Additional more water, added on the direction of some cluster bonds led to clusters of water molecules highly unsymmetrical.

One can be said that the expected molecular arrangement symmetry broken when higher energy orbitals become available in the studied ion. Actually, it is hard to believe that, in diluted solutions, the arrangement of water molecules will follow the expected symmetry of the fundamental state of the *in vitro* ion. By using the calculated bond angles (see, e.g., **Table 2**, for fluoride ion), a deviation from the ideal symmetrical of square bi-pyramidal arrangement can be recorded (the standard deviation between expected (90° and 180°) and obtained angles is about 9°).

Table 2. Bond lengths and bond angles in $\text{Cl}^- \cdot 5\text{H}_2\text{O}$ cluster and in $\text{F}^- \cdot 6\text{H}_2\text{O}$ cluster

Distance		Angle			
d(Atom...Atom)	pm	(Atom...Atom) _{d(Atom...Atom)}	($^\circ$)	(Atom...Atom) _{d(Atom...Atom)}	($^\circ$)
Cl$^-$·5H$_2$O cluster					
d(H...Cl)	265	(H...Cl) ₂₈₁ —(H...Cl) ₃₀₇	67	(H...Cl) ₂₇₄ —(H...Cl) ₂₈₁	96
d(H...Cl)	274	(H...Cl) ₂₇₄ —(H...Cl) ₃₀₇	76	(H...Cl) ₂₆₅ —(H...Cl) ₂₇₄	101
d(H...Cl)	281	(H...Cl) ₂₈₁ —(H...Cl) ₂₈₄	82	(H...Cl) ₂₆₅ —(H...Cl) ₂₈₄	129
d(H...Cl)	284	(H...Cl) ₂₇₄ —(H...Cl) ₂₈₄	82	(H...Cl) ₂₈₄ —(H...Cl) ₃₀₇	140
d(H...Cl)	307	(H...Cl) ₂₆₅ —(H...Cl) ₃₀₇	89	(H...Cl) ₂₆₅ —(H...Cl) ₂₈₁	146
F$^-$·6H$_2$O cluster					
d(H...F)	179	(H...F) ₁₇₉ —(H...F) ₁₈₄	77	(H...F) ₁₈₄ —(H...F) ₁₈₅	89
d(H...F)	182	(H...F) ₁₈₄ —(H...F) ₁₈₇	85	(H...F) ₁₇₉ —(H...F) ₁₈₅	90
d(H...F)	183	(H...F) ₁₈₂ —(H...F) ₁₈₃	85	(H...F) ₁₈₃ —(H...F) ₁₈₇	93
d(H...F)	184	(H...F) ₁₇₉ —(H...F) ₁₈₃	86	(H...F) ₁₈₂ —(H...F) ₁₈₇	109
d(H...F)	185	(H...F) ₁₈₅ —(H...F) ₁₈₇	87	(H...F) ₁₇₉ —(H...F) ₁₈₇	162
d(H...F)	187	(H...F) ₁₈₃ —(H...F) ₁₈₄	88	(H...F) ₁₈₂ —(H...F) ₁₈₄	165
		(H...F) ₁₇₉ —(H...F) ₁₈₂	89	(H...F) ₁₈₃ —(H...F) ₁₈₅	177

In case of anions (Cl^- and F^-), bridges are created between water molecules and the ions by means of “hydrogen bonds” HB. This fact is explained by the presence of a rich electron region surrounding the anions.

Thus, the distances and the angles of the arrangements are given relative to hydrogen atoms involved in HB (see **Table 2** for Cl^- and F^-). The $\text{H}\dots\text{Cl}^-$ distances in $\text{Cl}^- \cdot 5\text{H}_2\text{O}$ cluster are close to the values of $\text{H}\dots\text{Cl}^-$ distance in the normal clathrate [22].

In case of chlorine ion, the symmetry is totally broken, maybe due to the effect of chlorine d-type orbitals (see Table 2). Other important remark is in regard of the number of water molecules surrounding the anion. Since the bonds are created via hydrogen atoms, it is expected that the electronegativity to play an important role in the ability of HB creation. Indeed, if fluorine was able to attract in the first layer 6 hydrogen atoms of water molecules, chlorine, with less electronegativity, is able to form only 5 HB with the water molecules. By recalculating the standard deviation between the obtained and expected angles (in five- and six-fold regular faces: $6 \times 90^\circ$, $3 \times 120^\circ$, $1 \times 180^\circ$) the standard deviation becomes about twice (16°) compared to the fluoride ion-water cluster.

For the fluoride ion solved in water, the arrangement of water molecules in the first layer surrounding F^- ion is, based on the angles, close to a square bi-pyramidal arrangement (see **Table 2**). In an ideal arrangement (when the hydrogen atoms are attracted with equal strengths, such in liquid HF), it is expected that the preferred arrangement to be a symmetrical square bi-pyramidal one. However, because of the difference in electronegativity between oxygen and fluorine, an unsymmetrical square bi-pyramidal arrangement of hydrogen atoms surrounding fluorine ion is observed.

For cations, the situation is reversed and the bridge between water molecules and the cation is created through oxygen atoms. Due to this fact, the ion electronegativity is expected to work in a reversed way, compared to the case of anions (6 for F^- , 5 for Cl^-). Indeed, lithium ion coordinates 4 oxygen atoms in the first layer surrounding it, sodium coordinates 5 while potassium coordinates 6 (**Table 3**).

Table 3. Bond lengths and bond angles in cations-water clusters:
 $\text{NH}_4^+ \cdot 4\text{H}_2\text{O}$, $\text{Li}^+ \cdot 4\text{H}_2\text{O}$, $\text{Na}^+ \cdot 5\text{H}_2\text{O}$, $\text{K}^+ \cdot 6\text{H}_2\text{O}$

Distance		Angles			
$d(\text{Atom}\dots\text{Atom})$ pm	$(\text{Atom}\dots\text{Atom})_{d(\text{Atom}\dots\text{Atom})}$	$d(\text{Atom}\dots\text{Atom})_{d(\text{Atom}\dots\text{Atom})}$	$(^\circ)$	$(\text{Atom}\dots\text{Atom})_{d(\text{Atom}\dots\text{Atom})}$	$(^\circ)$
$\text{NH}_4^+ \cdot 4\text{H}_2\text{O}$ cluster					
$d(\text{O}-\text{H})$	95	$(\text{H}-\text{O})_{95}-(\text{O}-\text{H})_{95}$		105	
$d(\text{N}-\text{H})$	101	$(\text{H}-\text{N})_{101}-(\text{N}-\text{H})_{101}$		109	
$d(\text{O}\dots\text{H})$	208	$(\text{H}-\text{O})_{95}-(\text{O}\dots\text{H})_{208}$		113	
$\text{Li}^+ \cdot 4\text{H}_2\text{O}$ cluster					
$d(\text{Li}\dots\text{O})$	193	$(\text{Li}\dots\text{O})_{193}-(\text{Li}\dots\text{O})_{196}$	99	$(\text{Li}\dots\text{O})_{193}-(\text{Li}\dots\text{O})_{200}$	111
$d(\text{Li}\dots\text{O})$	194	$(\text{Li}\dots\text{O})_{194}-(\text{Li}\dots\text{O})_{200}$	104	$(\text{Li}\dots\text{O})_{194}-(\text{Li}\dots\text{O})_{196}$	116
$d(\text{Li}\dots\text{O})$	196	$(\text{Li}\dots\text{O})_{196}-(\text{Li}\dots\text{O})_{200}$	110	$(\text{Li}\dots\text{O})_{193}-(\text{Li}\dots\text{O})_{194}$	117
$d(\text{Li}\dots\text{O})$	200				

Distance		Angles			
d(Atom...Atom) pm	(Atom...Atom) _{d(Atom...Atom)}	(°)	(Atom...Atom) _{d(Atom...Atom)}	(°)	
Na⁺·5H₂O cluster					
d(Na...O)	231	(Na...O) ₂₃₄ —(Na...O) ₂₃₉	84	(Na...O) ₂₃₄ —(Na...O) ₂₃₅	97
d(Na...O)	234	(Na...O) ₂₃₆ —(Na...O) ₂₃₉	85	(Na...O) ₂₃₁ —(Na...O) ₂₃₄	100
d(Na...O)	235	(Na...O) ₂₃₁ —(Na...O) ₂₃₉	88	(Na...O) ₂₃₄ —(Na...O) ₂₃₆	123
d(Na...O)	236	(Na...O) ₂₃₁ —(Na...O) ₂₃₅	93	(Na...O) ₂₃₁ —(Na...O) ₂₃₆	135
d(Na...O)	239	(Na...O) ₂₃₅ —(Na...O) ₂₃₆	94	(Na...O) ₂₃₁ —(Na...O) ₂₃₅	178
K⁺·6H₂O cluster					
d(O...K)	278	(O...K) ₂₈₅ —(O...K) ₂₉₃	58.1	(O...K) ₂₇₈ —(O...K) ₂₈₄	94.4
d(O...K)	279	(O...K) ₂₈₁ —(O...K) ₂₈₅	79.0	(O...K) ₂₈₁ —(O...K) ₂₉₃	100.5
d(O...K)	281	(O...K) ₂₈₄ —(O...K) ₂₉₃	79.1	(O...K) ₂₇₉ —(O...K) ₂₈₄	121.6
d(O...K)	284	(O...K) ₂₇₈ —(O...K) ₂₈₁	80.8	(O...K) ₂₈₄ —(O...K) ₂₈₅	127.8
d(O...K)	285	(O...K) ₂₈₁ —(O...K) ₂₈₄	81.3	(O...K) ₂₇₈ —(O...K) ₂₈₅	128.8
d(O...K)	293	(O...K) ₂₇₉ —(O...K) ₂₉₃	86.2	(O...K) ₂₇₉ —(O...K) ₂₈₁	157.1
		(O...K) ₂₇₉ —(O...K) ₂₈₅	86.3	(O...K) ₂₇₈ —(O...K) ₂₉₃	173.0
		(O...K) ₂₇₈ —(O...K) ₂₇₉	92.5		

In the terms of the deviation from the ideal platonic arrangements (with 4, 5 and 6 water molecules placed in the first layer surrounding the ions) the standard deviations for the case of cations is almost 7° for Li⁺, 9° for Na⁺ and 22° for K⁺ (again, the presence of the d-type orbitals disturbed significant the symmetry).

The mean of bond lengths proved significantly different among the investigated ion-water clusters (ANOVA test: p-value = 2.71·10⁻¹⁰). The post-hoc Bonferroni test identified significant differences in regards of bond lengths for the following pairs of clusters (the differences were considered significant according to the adjusted significance level of 0.3333%):

- The mean of bond lengths in NH₄⁺·4H₂O cluster was significantly smaller compared to the one observed in Cl⁻·5H₂O cluster (p=1.07·10⁻⁸), Na⁺·5H₂O cluster (8.74·10⁻⁶), and respectively K⁺·6H₂O cluster (5.00·10⁻⁹).
- The mean of bond lengths in Li⁺·4H₂O cluster was significantly smaller compared to the one in Cl⁻·5H₂O cluster (p=2.34·10⁻⁵), and K⁺·6H₂O cluster (1.60·10⁻⁵)
- The mean of bond lengths in Cl⁻·5H₂O cluster was significantly higher compared to the one in F⁻·6H₂O cluster (p=5.06·10⁻⁷)
- The mean of bond lengths on F⁻·6H₂O cluster was significantly smaller compared to the one observed on K⁺·6H₂O cluster (p=1.80·10⁻⁷)

The analysis of the angles listed in Table 2 and 3 led to the following conclusions:

- The smallest angle between bonds is observed on a cluster with 6 water molecules, $K^+ \cdot 6H_2O$ cluster (angle=58.1°). The minimum value of the bond angles varied from 58.1° ($K^+ \cdot 6H_2O$ cluster) to 105° ($NH_4^+ \cdot 4H_2O$ cluster). The maximum value of the angle is of 178° and is found in $Na^+ \cdot 5H_2O$ cluster. The range defined as the difference between maximum and minimum increased as the number of water molecules increased (is equal 8° for $NH_4^+ \cdot 4H_2O$ cluster and 114.9° for $K^+ \cdot 6H_2O$ cluster), as expected.
- No significant differences were found when the bond angles inside a cluster were investigated (Friedman ANOVA statistic=4.27 p=0.5119).

The bonds and angles, as obtained in the actual simulation study, seem to be natural formation of bonds in the water environment. The obtained results could be used to explain the solvation effects. Burnham et al. [17] reported temperature-dependent solvation of Na^+ , Cl^- , and H^+ ions in water clusters and identified the global minimum for $Na^+(H_2O)_{20}$ and $Cl^-(H_2O)_{17}$. Burnham et al. [17] tried to identify the optimal size of the water cluster surrounding the ions. Cui et al. [23] proved, by a computational study (B3LYP and BP86 methods with 6-311++G** basis set), that the symmetry of materials $HB(N_5)_3X$ ($X = Li, Na, K, \text{ and } Rb$) is related to local minima on the potential energy surface.

Nevertheless, our study was focused on the arrangement of water molecules in the first layer around the ions. Our results correspond to 'infinite dilution', e.g. no other ions are in the vicinity. It is expected that bonds lengths and angles between bonds to change when other ions (of the same type) exists in the vicinity, while it is also expected that the symmetry to be preserved.

Dodecahedral cages were constructed following the methods described in the literature [23] for each of the investigated cation (NH_4^+ , Li^+ , Na^+ , and K^+) and the obtained structures are presented in Figure 2.

The symmetry of the structures was stabilized in all four cases, as can be observed from Figure 2. The structure of $O_{14}Na_6H_{22}$ is similar to that of $Na^+(H_2O)_{20}$ complex described by Burnham et al. [17]. A special case was observed in ammonia cluster ($O_{12}N_8H_{50}$) for which six O—H stabilized inside the cluster and six O—H stabilized outside, in the stable symmetrical structure (**Fig. 2**). This behavior is in some way expected since it is known that monovalent ions do not affect the water hydrogen-bonding network while a multivalent ion does affect it [24].

The formation and/or stability of the dodecahedral clusters by hydration were further investigated in case of ammonia. Several arrangements for $O_xN_{20-x}H_{50}$ (**Fig. 3**) were investigated and the results are listed in **Table 4**.

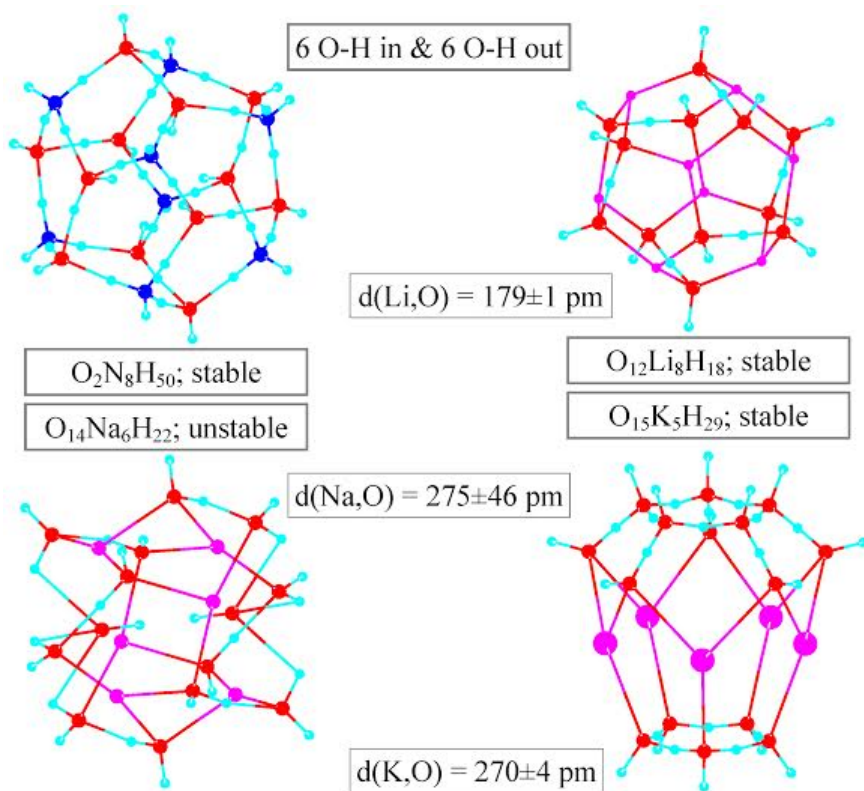


Figure 2. Dodecahedral clusters of NH^+ , Li^+ , Na^+ , and K^+ cations

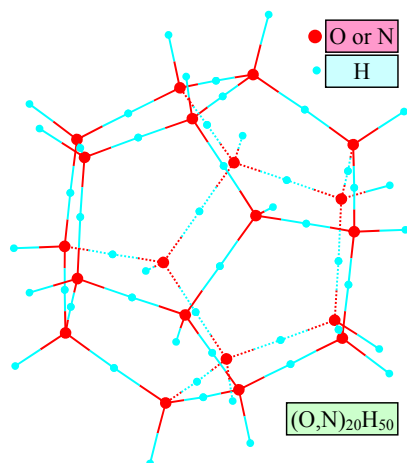


Figure 3. General pattern for $\text{O}_x\text{N}_{20-x}\text{H}_{50}$

Table 4. Arrangements for $O_xN_{20-x}H_{50}$

No.	Cluster	H ₂ O	NH ₃	H ₃ O ⁺	HO ⁻	[⁺ / ⁻]/H ₂ O	Reaction of formation	N/(N+O) %
0	O ₀ N ₂₀	0	20	10	0	+(10)/(0+10)	20NH ₃ + 10H ₂ O → O ₀ N ₂₀ H ₅₀ + 10H ₃ O ⁺	18/28=100
1	O ₂ N ₁₈	2	18	8	0	+(8)/(2+8)	18NH ₃ + 10H ₂ O → O ₂ N ₁₈ H ₅₀ + 8H ₃ O ⁺	18/28=64.3
2	O ₄ N ₁₆	4	16	6	0	+(6)/(6+4)	16NH ₃ + 10H ₂ O → O ₄ N ₁₆ H ₅₀ + 6H ₃ O ⁺	16/26=61.5
3	O ₅ N ₁₅	5	15	5	0	+(5)/(5+5)	15NH ₃ + 10H ₂ O → O ₅ N ₁₅ H ₅₀ + 5H ₃ O ⁺	15/25=60.0
4	O ₆ N ₁₄	6	14	4	0	+(4)/(4+6)	14NH ₃ + 10H ₂ O → O ₆ N ₁₄ H ₅₀ + 4H ₃ O ⁺	14/24=58.3
5	O ₈ N ₁₂	8	12	2	0	+(2)/(2+8)	12NH ₃ + 10H ₂ O → O ₈ N ₁₂ H ₅₀ + 2H ₃ O ⁺	12/22=54.5
6	O ₁₀ N ₁₀	10	10	0	0	(0)/(0+10)	10NH ₃ + 10H ₂ O → O ₁₀ N ₁₀ H ₅₀	10/20=50.0
7	O ₁₂ N ₈	12	8	0	2	-(2)/(2+12)	8NH ₃ + 14H ₂ O → O ₁₂ N ₈ H ₅₀ + 2HO ⁻	8/22=36.4
8	O ₁₄ N ₆	14	6	0	4	-(4)/(4+14)	6NH ₃ + 18H ₂ O → O ₁₄ N ₆ H ₅₀ + 4HO ⁻	6/24=25.0
9	O ₁₅ N ₅	15	5	0	5	-(5)/(5+15)	5NH ₃ + 20H ₂ O → O ₁₅ N ₅ H ₅₀ + 5HO ⁻	5/25=20.0
10	O ₁₆ N ₄	16	4	0	6	-(6)/(6+16)	4NH ₃ + 22H ₂ O → O ₁₆ N ₄ H ₅₀ + 6HO ⁻	4/26=15.4
11	O ₁₈ N ₂	18	2	0	8	-(8)/(8+18)	2NH ₃ + 26H ₂ O → O ₁₈ N ₂ H ₅₀ + 8HO ⁻	2/28=7.1
12	O ₂₀ N ₀	20	0	0	10	-(10)/(10+20)	0NH ₃ + 30H ₂ O → O ₂₀ N ₀ H ₅₀ + 10HO ⁻	0/30=0.00

Not all random arrangements of ammonia and water molecules may preserve a certain level of symmetry (see Figure 3). Six different patterns of alternating water and ammonia, and therefore eleven different arrangements of placing water and ammonia in these patterns (see Table 4) can be observed, at a choice level of symmetry (associated with a supplementary stabilization of the aggregate). Several calculations were done for different arrangements for $O_xN_{20-x}H_{50}$ and the obtained results are listed in Table 4, as follows: the ratio H₂O/NH₃ per cluster, the number of hydronium (H₃O⁺ column) and hydroxide (HO⁻ column) ions created (released) due to the formation of the cluster, the ratio of the released charge per total number of involved water molecules ([⁺/⁻]/H₂O column), the reaction leading to the formation of the cluster (column 'Reaction of formation' which is also a checking key for the previous calculations) as well as the ratio O/N (nitrogen/oxygen) atoms corresponding to the arrangement of water and ammonia.

The bond angles in the studied ion-water clusters were successfully obtained; the clustering with a certain number of water molecules could explain the dissolution of investigated ions in water. 'Certain number' of molecules also named 'magic number clusters' were investigated on Li_nNa_{8-n}, Na_nK_{8-n}, and K_nLi_{8-n} [25], (C₅H₅N)_n (H₂O)_m (n=1~2, m=1~4) [26], methyl tert-butyl ether (MTBE)-water clusters [27], H⁺(NH₃)(pyridine) (H₂O)_n, H⁺(NH₃)(pyridine)₂(H₂O)_n (n= 18, 20, and 27) [28], H⁺(NH₃)₅(H₂O)₂₀ (tetrahedral ammonium core encapsulated in a dodecahedral (H₂O)₂₀ structure, found in clathrates) [29].

A series of important results regarding the symmetry broken at solvation, due to high energy orbitals in some monovalent ions, were obtained in this study. Distribution of clusters in different solutions of water and ammonia, at different concentrations and temperatures, can be further conducted starting with these results.

CONCLUSIONS

Our study has shown that there is a significant difference among the congeneric ions in the tendency of clustering with water; at infinite dilution, and in the absence of other ions, the arrangements show, in general, a broken symmetry. In the presence of other ions (in concentrated solutions) dodecahedral clusters containing 8 atoms of lithium (Li) and four atoms of potassium (K) are symmetric and stable while dodecahedral clusters containing 6 atoms of sodium are unstable while the symmetry is broken.

MATERIALS AND METHODS

In-silico computational study was conducted for six ions: NH_4^+ , F^- , Cl^- , Li^+ , Na^+ , and K^+ . The geometry optimization of water ion-clusters was performed using restricted Hartree-Fock (RHF) method (proposed in [30-34]) with 6-31G* basis set (spin-valence basis set, proposed by Ditchfield et al. [35], Hehre et al. [36], and Hariharan and Pople [37]) in water (SM8 solvation model [38-40]). To obtain the stable ion-water cluster, the molecules of water were progressively added and the geometry was optimized to identify those ion-water clusters that are stable. The step-by-step procedure applied to obtain the most stable $\text{X}(\text{H}_2\text{O})_n$ ion-clusters was as follows:

- Step 1: a number of water molecules were placed in the vicinity of the investigated ion
- Step 2: geometry optimization was conducted
- Step 3: other water molecules were added in the empty spaces in the vicinity of the investigated ion
- Step 2 and 3 were repeated till no changes were observed in the arrangement of the water molecules surrounding the investigated ion in the first layer

The above-described steps were applied for each investigated ion. Geometry optimization and calculations were performed by Spartan software (v. 10). For each ion-water cluster, distance between atoms (expressed in pm) and the bond angles were collected.

The investigation of cations as components of a dodecahedral arrangement of water was conducted by building dodecahedron cages by NH^+ , Li^+ , Na^+ , and K^+ following the steps presented by Twarock et al. [41].

The mean of bond lengths were compared by ANOVA test at a significance level of 0.33% (adjusted $\alpha=0.05$ by the number of comparisons being considered – in our case the number of investigated ions; $\alpha^*=0.05/[6*(6-1)/2]$) followed by Bonferroni test whenever significant differences were observed. Friedman ANOVA test was applied to find the differences between angles in the investigated ion-water clusters. Statistical analysis was done by Statistica software (v. 8.).

ACKNOWLEDGMENTS

This paper is dedicated to Prof. Mircea V. Diudea with the occasion of his 65th birthday.

REFERENCES

1. K.T. Wikfeldt, *Structure, Dynamics and Thermodynamics of Liquid Water: Insights from Molecular Simulations*, Thesis for the Degree of Doctor of Philosophy in Theoretical Physics, Department of Physics, Stockholm University, Stockholm, **2011**.
2. J. Siepman, F. Siepman, *International Journal of Pharmaceutics*, **2013**, 453, 12.
3. T. Bartels-Rausch, V. Bergeron, J.H.E. Cartwright, R. Escibano, J.L. Finney, H. Grothe, P.J. Gutierrez, J. Haapala, W.F. Kuhs, J.B.C. Pettersson, S.D. Price, C.I. Sainz-Daz, D.J. Stokes, G. Strazzulla, E.S. Thomson, H. Trinks, N. Uras-Aytemiz, *Reviews of Modern Physics*, **2012**, 84, 885.
4. V. Fuentes-Landete, C. Mitterdorfer, P.H. Handle, G.N. Ruiz, J. Bernard, A. Bogdan, M. Seidl, K. Amann-Winkel, J. Stem, S. Fuhrmann and T. Loerting, *Crystalline and amorphous ices*, Proceedings of the International School of Physics “Enrico Fermi”, Ed P.G. Debenedetti, M.A. Ricci and F. Bruni, IOS, Amsterdam, Bologna, **2015**.
5. W.F. Kuhs, M.S. Lehmann, *The structure of ice-Ih*, *Water Science Reviews* 2. Cambridge University Press, **1986**, pp. 1-66.
6. B.J. Murray, A.K. Bertram, *Physical Chemistry Chemical Physics*, **2006**, 8, 186.
7. T.L. Malkin, B.J. Murray, A.V. Brukhno, J. Anwar, C.G. Salzmann, *Proceedings of the National Academy of Sciences USA*, **2012**, 109, 1041.
8. Correction for Malkin et al., *Proceedings of the National Academy of Sciences USA*, **2012**, 109, 4020.
9. E.D. Isaacs, A. Shukla, P.M. Platzman, D.R. Hamann, B. Barbiellini, C.A. Tulk, *Physical Review Letters*, **1999**, 82, 600.
10. NIST Computational Chemistry Comparison and Benchmark Database, NIST Standard Reference Database Number 101. Release 16a, August 2013, Editor: Russell D. Johnson III. Available at: <http://cccbdb.nist.gov/> (<http://cccbdb.nist.gov/alldata2.asp?casno=7732185>)
11. R. Ludwig, *Angewandte Chemie International Edition*, **2001**, 40, 1808.
12. R.P. Wayne, *Chemistry of Atmospheres*, Oxford University Press: Oxford, **1991**.

13. A.V. Khakhalin, O.N. Gradoboeva, Y.N. Shirshov, *Moscow University Physics Bulletin*, **2012**, 67, 536.
14. L. Pauling, *The structure of water*, In: Hydrogen bonding, Ed. D. Hadzi, H.W. Thompson, Pergamon Press Ltd, London, **1959**, pp. 1-6.
15. D.J. Wales, M.P. Hodges, *Chemical Physics Letters*, **1998**, 286, 65.
16. R.J. Cooper, T.M. Chang, E.R. Williams, *The Journal of Physical Chemistry A*, **2013**, 117, 6571.
17. C.J. Burnham, M.K. Petersen, T.J.F. Day, S.S. Iyengar, G.A. Voth, *J. Chemical Physics*, **2006**, 124, 024327.
18. S.L. Clegg, P. Brimblecombe, *Journal of Physical Chemistry*, **1989**, 93, 7237.
19. Z. Latajka, S. Scheiner, *Journal of Physical Chemistry*, **1990**, 94, 217.
20. A.E. Galashev, *Journal of Physical Chemistry B*, **2013**, 7, 502.
21. D. Guerra, J. David, A. Restrepo, *Journal of Computational Methods in Science and Engineering*, **2014**, 14, 93.
22. D. Laage, J.T. Hynes, *Proceedings of the National Academy of Sciences USA*, **2007**, 104, 11167.
23. J. Cui, Y. Zhang, F. Zhao, J. Yang, G. Shen, Y. Xu, *Progress in Natural Science*, **2009**, 19, 41.
24. J.T. O'Brien, E.R. Williams, *Journal of the American Chemical Society*, **2012**, 134, 10228.
25. R. Fournier, *Journal of Computational Methods in Sciences and Engineering*, **2008**, 8, 331.
26. X.-M. Li, L.-B. Zhang, L.-Z. Zhou, X.-H. Kong, *Guang Pu Xue Yu Guang Pu Fen Xi/Spectroscopy and Spectral Analysis*, **2014**, 34, 1805.
27. T.M. Di Palma, A. Bende, *Chemical Physics Letters*, **2013**, 561, 18.
28. M.J. Ryding, K. Ruusuvoori, P.U. Andersson, A.S. Zatula, M.J. McGrath, T. Kurtén, I.K. Ortega, H. Vehkamäki, E. Uggerud, *The Journal of Physical Chemistry A*, **2012**, 116, 4902.
29. P. Hvelplund, T. Kurtén, K. Støchkel, M.J. Ryding, S. Brøndsted Nielsen, E. Uggerud, *The Journal of Physical Chemistry A*, **2010**, 114, 7301.
30. D.R. Hartree, *Mathematical Proceedings of the Cambridge Philosophical Society*, **1928**, 24, 89.
31. D.R. Hartree, *Mathematical Proceedings of the Cambridge Philosophical Society*, **1928**, 24, 111.
32. V.A. Fock, *Zeitschrift für Physik*, **1930**, 61, 126.
33. V.A. Fock, *Zeitschrift für Physik*, **1930**, 62, 795.
34. V.A. Fock, W. Hartree, *Proceedings of the Royal Society of London A*, **1935**, 150(869), 9.
35. R. Ditchfield, W.J. Hehre, J.A. Pople, *Journal of Chemical Physics*, **1971**, 54, 724.
36. W.J. Hehre, R. Ditchfield, J.A. Pople, *Journal of Chemical Physics*, **1972**, 56, 2257.
37. P.C. Hariharan, J.A. Pople, *Theoretica Chimica Acta*, **1973**, 28, 213.
38. A.V. Marenich, R.M. Olson, C.P. Kelly, C.J. Cramer, D.G. Truhlar, *Journal of Chemical Theory and Computation*, **2007**, 3, 2011.
39. C.J. Cramer, D.G. Truhlar, *Accounts of Chemical Research*, **2008**, 41(6), 760.
40. A.V. Marenich, C.J. Cramer, D.G. Truhlar, *Journal of Chemical Theory and Computation*, **2009**, 5, 2447.
41. R. Twarock, N.E. Grayson, A. Taormina, *Theoretical Computer Science*, **2009**, 410, 1440.

*Dedicated to Professor Mircea Diudea
on the Occasion of His 65th Anniversary*

OPTIMAL CONDITIONS FOR PREPARING CIGS THIN FILM THROUGH TWO-STEP PROCESS OF SPUTTERING FOLLOWED BY SELENIZATION

M. MORADI^a, M. ZAHEDIFAR^{a,b}, T. GHORBANI^{a,*},
M. SAADAT^a, K. ROSTAMI^a

ABSTRACT. Cu(In,Ga)Se₂ films were prepared via a sputtering route followed by a selenization process, on glass substrates. Having a layer sequence Mo/In/Cu-Ga with preferred thicknesses, the metallic layers were selenized at vacuum of 6×10^{-3} mbar and 1 atm pressure with a total gas inlet of 7 sccm. Under vacuum, only single-phase CIGS was observed while at 1 atm, other phases in addition to CIGS were formed. The metallic layers were selenized at several temperatures. Pure-phased CIGS films were obtained by selenization at 600°C. The crystallinity of the obtained films was further enhanced by increasing the selenization temperature. The produced CIGS films were studied by X-ray diffraction (XRD), scanning electron microscope (SEM) and energy dispersion spectroscopy (EDS) techniques.

Keywords: Cu(In,Ga)Se₂ thin film, sputtering, selenization.

INTRODUCTION

Chalcopyrite CuInGaSe₂ (CIGS), due to its high absorption coefficient ($\alpha \sim 10^5 \text{ cm}^{-1}$), is one of the most promising absorber materials for thin film solar cells tunable band gap and long-term stability [1, 2]. The band gap of CuInSe₂ is $E_g = 1 \text{ eV}$ and that of CuGaSe₂ is 1.7 eV . Therefore, a manipulation of the band gap between these two extremes makes it possible to prepare a wide variety

^a Institute of Nanoscience and Nanotechnology, University of Kashan, Kashan, Iran

^b Physics Department, University of Kashan, Kashan, Iran

* Corresponding Author: ghorbani.tayebeh@gmail.com

of absorber materials by simply adjusting the Ga/In ratio [3]. Here, the gallium ratio ($Ga/(Ga + In)$) could be adjusted by changing the thicknesses of the In and Cu-Ga films. The optimal Cu/(In+Ga) elemental ratio is typically between 0.8 to 0.9 [4,5] and that of Ga/In is about 0.3 corresponding to a band gap of 1.1 eV [6]. The hypothetical efficiency of polycrystalline solar cells increase with increasing the grain size of the absorber materials. Various methods such as chemical bath deposition [7], elemental co-evaporation [8], flash evaporation [9], single-source evaporation [10], RF sputtering [11,12], pulsed laser deposition [13], and electrodeposition [14,15] have been used to prepare CIGS thin films.

Another method to fabricate CIGS films is a two-step process, wherein the metallic films are deposited as the precursor films via the sputtering method followed by the selenization process. The first advantage of this method is that no precise control of the parameters is needed during the selenization process, as the metallic precursors absorb only the amount of selenium required by the stoichiometry [16-18]. The second is diffusion of Se into the Mo back-contact, thereby $MoSe_2$ is formed at the boundary of the active layer and the back-contact leading to an improved junction between the two materials [19]. The surface roughness of the absorber plays a vital role to form p-n junction between the absorber and window layer. A thin absorber layer with rough surface produces shunt path in the devices. On the other hand, a very smooth surface is not applicable because of reflection losses [4]. In this work, CIGS thin films were synthesized using the sputtering and post-selenization method. The layer sequence Mo/In/Cu-Ga with two different thicknesses was tested. The influence of annealing temperature and pressure were investigated and their optimum conditions for producing CIGS thin films were explored. The surface roughness of the prepared samples was also studied and the optimal conditions were obtained for the fabricated CIGS layer.

EXPERIMENTAL

Soda lime glass (SLG) substrates of $11 \times 26 \text{ mm}^2$ area and 1 mm thick were used for deposition. The substrates were scoured using detergent and ultrasonic cleaning by deionized water and acetone, followed by scrubbing with iso-propanol, drying with N_2 gas and immediately introducing into the vacuum chamber. Molybdenum (Mo) layer was deposited as back contact by RF magnetron sputtering onto the SLG substrate. Copper/Gallium (75:25 at%) alloy and pure indium targets were sequentially used for depositing the precursor films on SLG substrates via the sputtering route employing a RF magnetron sputtering system. The distance between the target and substrate was 20 cm and the substrates were fixed during deposition. The target power and voltage

were 250 W and 290 V respectively. In order to develop the CIGS films, the multi-layered precursor stacks were selenized in a closed steel container, where the evaporated selenium was loaded into an argon flux in a quartz tube. Selenium was supplied by placing 1.0 g of elemental selenium into the box prior to heating. The layer sequence Mo/In/Cu-Ga with two different thicknesses were tested: 300 nm/300 nm/160 nm (sample A) and 300 nm/300 nm/275 nm (sample B). Selenization procedure was carried out according to time-temperature profile shown in Figure 1.

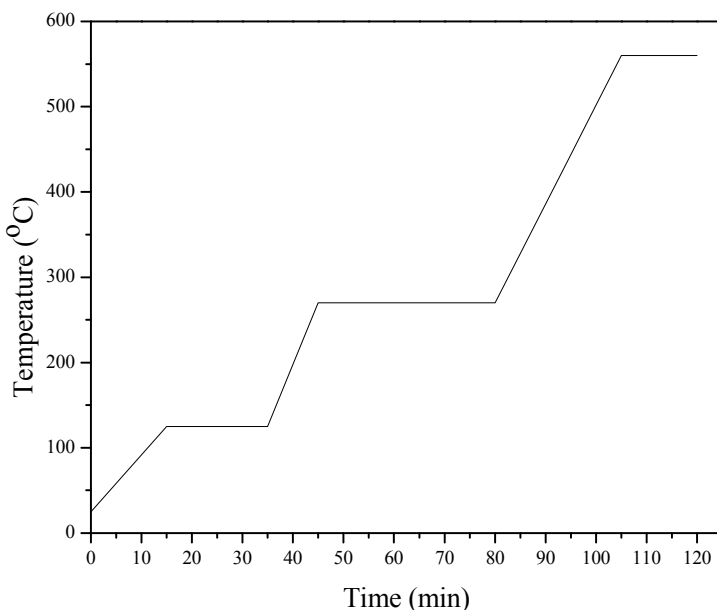


Figure 1. Schematic temperature profile used in selenization process.

The first step at 125 °C was conducted to obtain a good Cu–In/Ga alloy with stable physical properties [20]. In the second step, Se incorporation was allowed to diffuse into the alloy layer at 250 °C. The third step, was involved selenization and recrystallization process which was performed at an elevated temperature of 550 °C [21]. In order to investigate the atmosphere effect, the selenization process of sample B was performed at two conditions. First one at pressure of 1 atm and the second at the vacuum of 6×10^{-3} mbar, with a total gas inlet of 7 sccm each. Figure1 demonstrates the Selenization process.

Annealing temperature effect was examined by conducting the selenization process in a gas inlet of 7 sccm and vacuum of 2×10^{-3} mbar at 400, 450, 500, 600, 700, 800 °C. Phase evolution of the precursor and selenized

specimens was analyzed using a X-ray powder diffractometer (XRD, Philips X'Pert/PMD) and Cu K α radiation at 40 kV and 30 mA. The roughness of surface of the samples was studied by a Confocal Microscope. The scanning electron microscopy (SEM) and energy dispersive spectroscopy (EDS) measurements were carried out by a VEGA\TESCAN microscope.

RESULTS AND DISCUSSION

Figure 2 shows a typical XRD pattern of absorber layer prepared by sequential sputtering of sample A. According to this figure, the formation of a monophasic CuInSe $_2$ layer instead of CIGS phase, can be ascribed to low thickness of Cu-Ga layer. Therefore, the Cu-Ga layer thickness was increased to 275 nm (sample B).

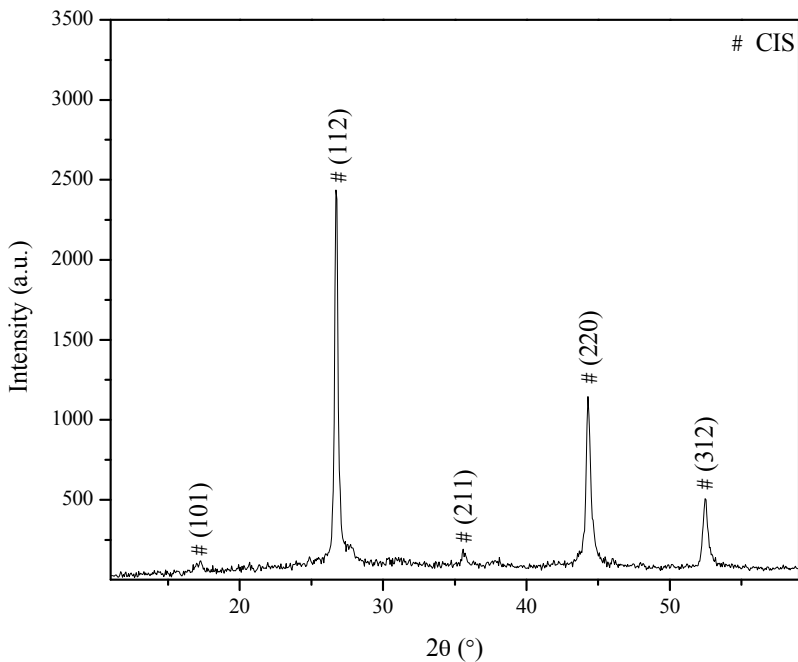


Figure 2. XRD patterns of sample A fairly coincides with that of single phase CIS thin film.

Figure 3 shows a typical XRD pattern of sample B, which reveals the main chalcopyrite diffraction peaks. The CIGS crystals with different compositions of Ga element have different positions of XRD reflection peaks.

The XRD pattern with two reflection peaks, indicates a non-uniform distribution Ga element in the CuInGaSe_2 absorber layer. The inset of Figure 3 shows an expanded view of positions of the (112) reflection peaks. The elemental composition distributions onto the surface and into the depth of the surface were investigated by EDS via two methods: Variation of EDS accelerating voltage and the cross-sectional depth composition of CIGS absorber. Variation of CIGS composition with EDS accelerating voltage is presented in Table 1. It is worth noting that gallium content increases from 0.29 near the surface to 1.92 at 25 kV which suggests diffusion of gallium toward the bottom of CIGS film.

Table 1. Atomic percentage of sample B for different EDS accelerating voltages.

Accelerating voltage (kV)	Cu (at %)	Ga (at %)	Se (at %)	In (at %)
5	19.37	0.29	41.25	39.09
10	23.56	0.87	49.68	25.89
15	24.43	0.42	51.27	23.88
20	22.69	1.28	52.11	23.92
25	22.41	1.92	50.8	24.87

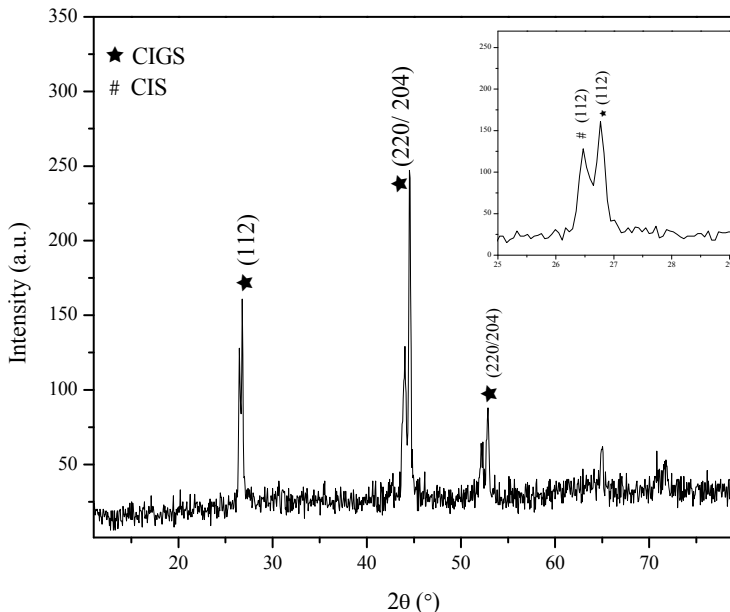


Figure 3. XRD patterns of CIGS thin film by sequential sputtering of sample B. The inset shows an expanded view of positions of the (112) reflection peak.

Figure 4 showing the cross-sectional depth composition of sample B is a result of EDS point analysis. The atomic concentrations measured by EDS analysis at 9 points are summarized in Table 2.

Table 2. The cross-sectional atomic % measured by EDS analysis at 9 points of sample B.

Point	Cu (%)	Ga (%)	Se (%)	In (%)
1	21.49	22.2	41.43	14.88
2	23.29	10.33	47.78	18.6
3	21.93	12.4	48.13	17.54
4	18.42	5.47	53.6	22.51
5	16.99	3.5	57.07	22.44
6	19.52	4.19	55.28	21.01
7	14.28	5.68	55.91	24.13
8	18.58	4.75	55.06	21.61
9	17.72	4.22	57.62	20.44

It is observed that the atomic concentration is considerably different along the depth, such that the Ga (In) concentration increases (decreases) slowly from the surface to the dept. Also apparent in Table 2 is that the amount of Se on the surface of CIGS film is larger than that in the interior, where the Cu concentration increases slowly from the surface to the inside.

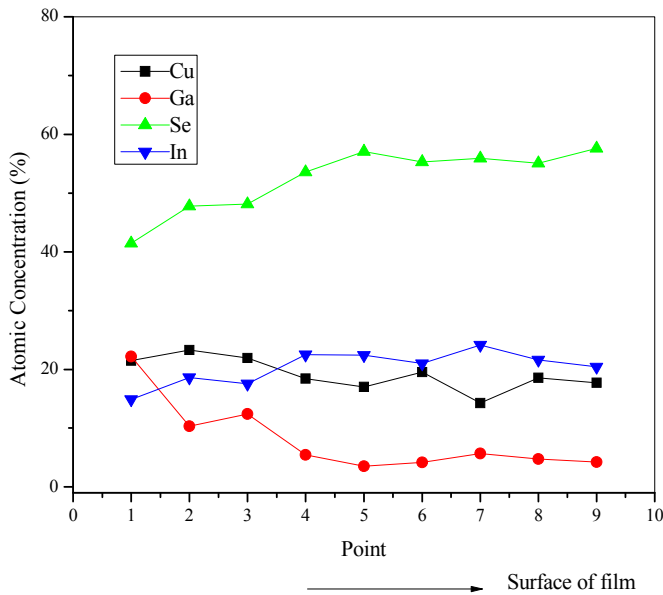


Figure 4. The EDS depth composition point analysis of sample B.

Figure 5 shows the SEM cross-section and top view of sample B. The film is dense and polycrystalline with compact 'facet-shaped' texture grain.

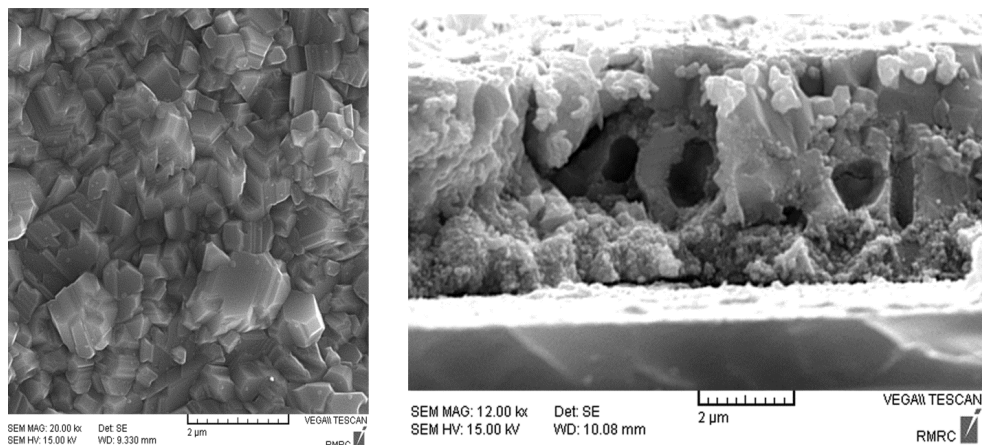


Figure 5. SEM cross-section and top view of sample B.

Figures 6 and 7 illustrate the X-ray diffraction patterns of sample B selenized respectively at the pressure of 10^{-3} mbar (medium vacuum) and 1000 mbar (atmosphere), each for 0.5 h. Under vacuum, only single-phase CIGS was observed but at 1 atm, other phases such as In_2O_3 compound was formed in addition to CIGS, which is due to presence of oxygen in the environment. Table 3 shows the EDS analysis of the sample selenized at 1 atm for 0.5 h.

Figure 8 illustrates the X-ray diffraction patterns of sample B selenized at various temperatures for 0.5h. Despite of formation of CIGS film following selenization at 400°C , In_2Se_3 and Cu_2In were also present in the sample. By increasing the selenization temperature to 450°C , In_2CuO_4 and In_2O_3 were found to coexist with CIGS in the prepared film. At 500°C , CuO and CIGS phases were formed. Monophasic CIGS was obtained by rising the selenization temperature to 600°C . The crystallinity of the obtained film was further enhanced by increasing the selenization temperature to 700°C .

Table 3. EDS analysis of sample B selenized at 1 atm for 0.5 h.

Element	O	Cu	Ga	Se	In
Atomic (%)	8.88	31.91	0.44	34.26	24.51

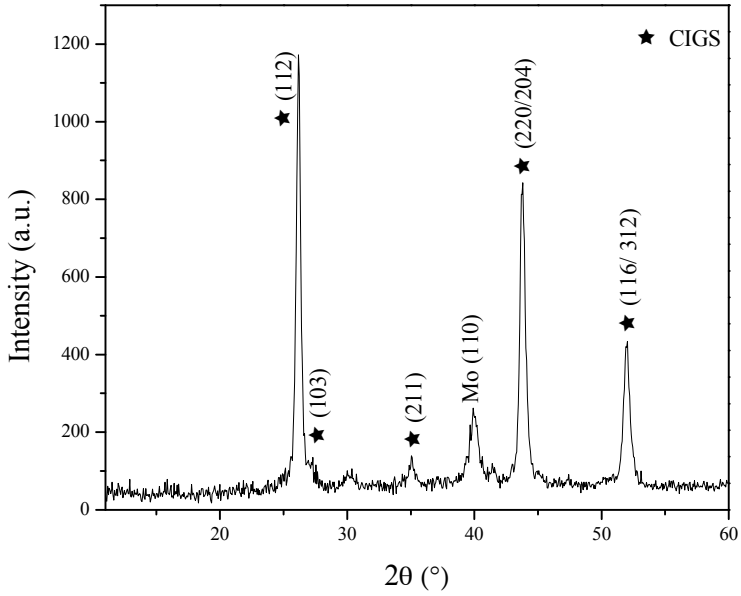


Figure 6. X-ray diffraction patterns of sample B selenized at pressure 10^{-3} mbar.

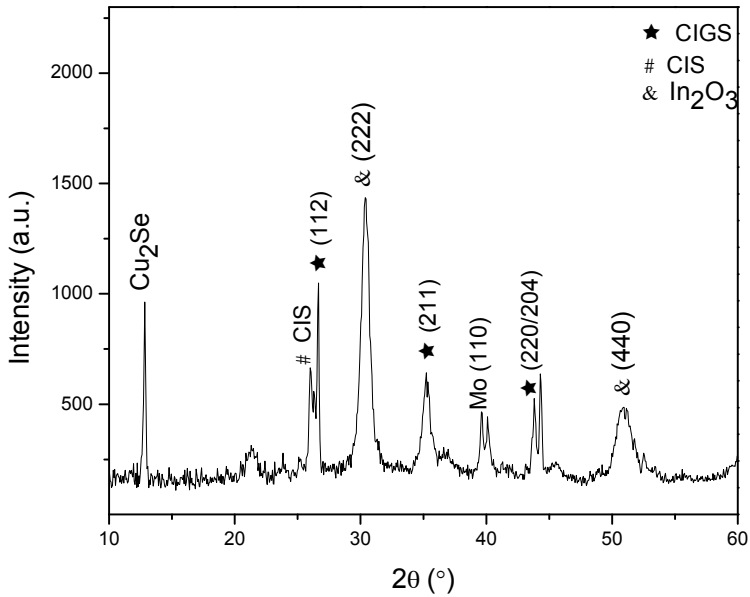


Figure 7. X-ray diffraction patterns of sample B selenized at 1 atm.

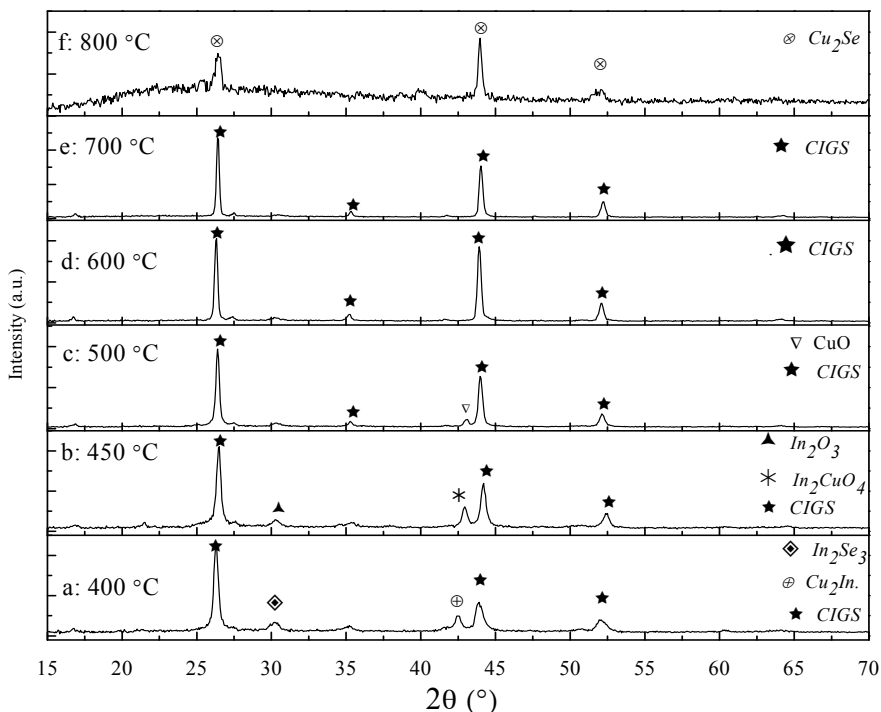


Figure 8. X-ray diffraction patterns of sample B selenized at different temperatures for 0.5h.

With more escalating the selenization temperature up to 800 °C, the CIGS phase disappeared, Cu_2Se was formed and the layer became amorphous like.

CIGS films were successfully formed at the selenization temperature of 450 °C. It was observed that increasing the selenization temperature from 400 to 450 °C resulted in a shift of the (112) diffraction peak toward higher angles. It was because Ga ions incorporated into CIGS to substitute indium ions, so that the lattice constants decreased due to the substitution of large In ion by small Ga ion [22]. Further increasing the temperatures led to increased intensity of (112) peak while its position shifted slightly to lower angles, justifying the sample selenized at 450 °C has the most Ga content.

Figure 9 shows the SEM cross-section and top view of sample B selenized at 400, 450, 500 and 700 °C. When the temperature of selenization increased, the geometry of the grain was changed from an agglomerated shape to a more compact 'facet-shaped' texture, and the crystallite size markedly increased. Selenization at 700 °C produced delamination of the CIGS absorber layer.

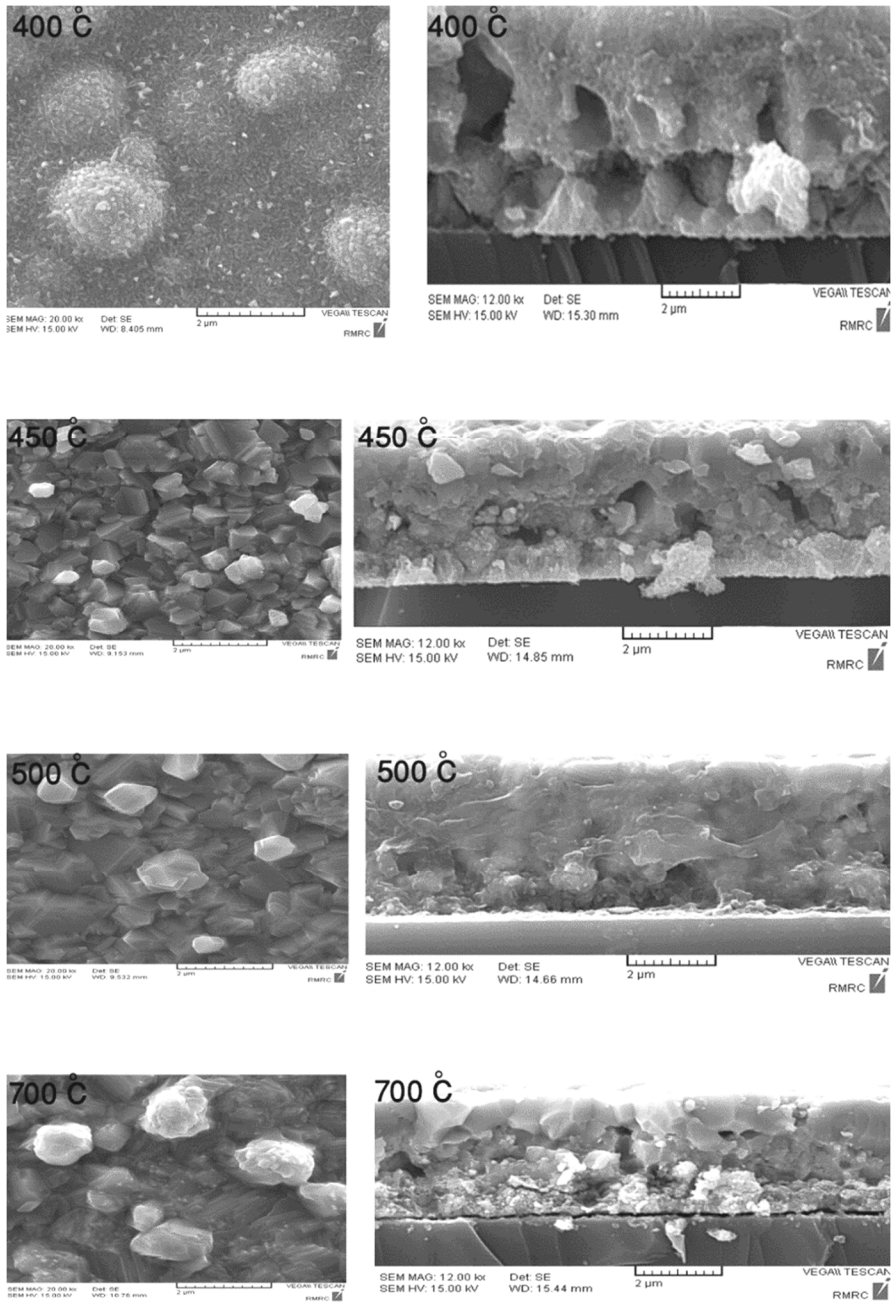


Figure 9. SEM cross-section (right) and top view (left) of sample B selenized at various temperatures for 0.5h.

OPTIMAL CONDITIONS FOR PREPARING CIGS THIN FILM

Figure 10 shows the surface roughness of sample B selenized at 400, 450, 500, 700 and 800 °C. The sample selenized at 400 °C has the lowest surface roughness, which could be due to presence of other phases. The decrease in surface roughness of CIGS layers with increasing selenizing temperature from 500 to 700 °C can be attributed to growing the grain size in higher temperature. At 800 °C the layer destroyed completely.

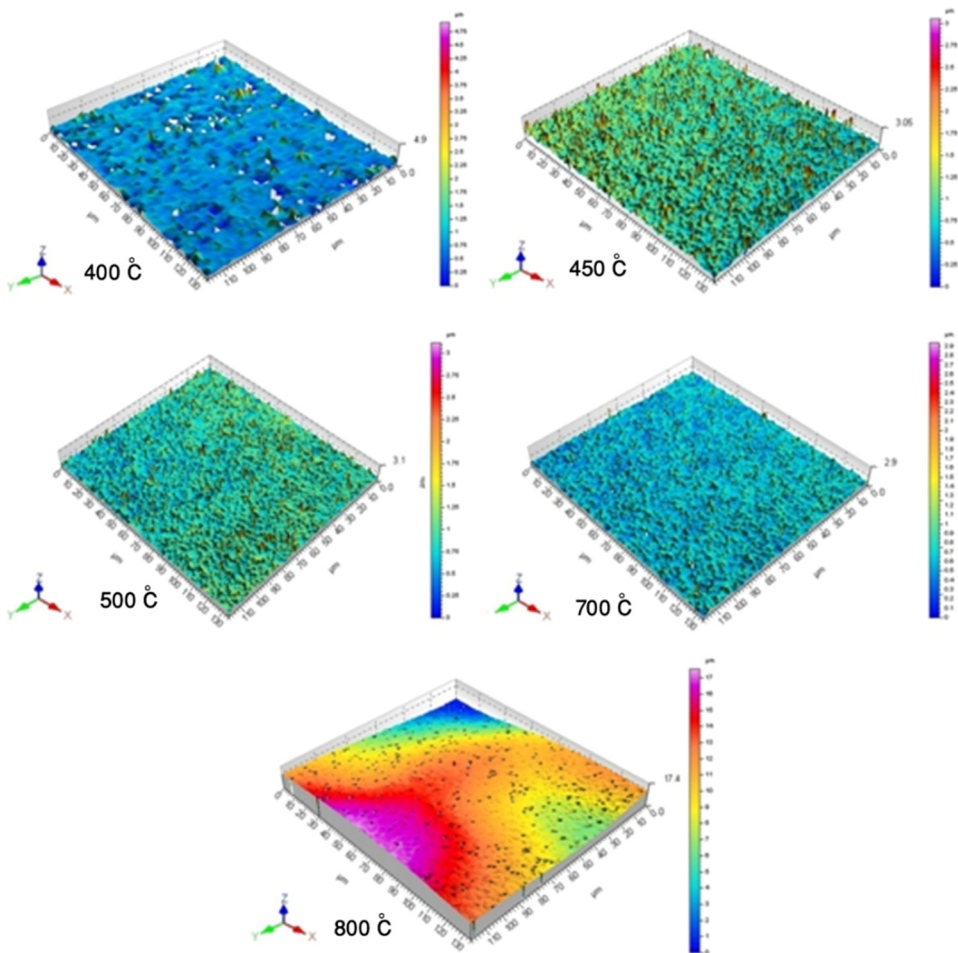


Figure 10. Surface roughness of sample B selenized at 400, 450, 500, 700 and 800 °C.

CONCLUSIONS

Cu(In,Ga)Se₂ films were prepared via the sputtering method followed by selenization process. Two samples with different Cu-Ga thicknesses of 160 and 275 nm were tested. In the former case, monophasic CuInSe₂ was obtained instead of CIGS phase and in the latter, CIGS was formed. By selenizing the samples prepared with 275 nm Cu-Ga at 1 atm, In₂O₃ compound in addition to CIGS were appeared but under vacuum, only single-phase CIGS was obtained. Therefore, a sputtering system coupled with the selenization process in a vacuum has a strong potential for preparation of high-quality CIGS films. The metallic layers were selenized at various temperatures for 0.5 h. Pure-phased CIGS films were obtained on selenization at 600 °C. The crystallinity of the prepared film was further enhanced by increasing the selenization temperature from 400 °C to 700 °C. With further rising the selenization temperature up to 800 °C, the CIGS phase disappeared, Cu₂Se formed and the layer became amorphous like. The lowest surface roughness belongs to the sample selenized at 400 °C and the surface roughness of CIGS layers decreased with increasing the selenizing temperature from 500 to 700 °C. At 800 °C the layer destroyed completely.

REFERENCES

1. C.A. Wolden, J. Kurtin, J.B. Baxter, I. Repins, S.E. Shaheen, J.T. Torvik, A.A. Rockett, V.M. Fthenakis, E.S. Aydil, *Journal of Vacuum Science & Technology A*, **2011**, 29, 801.
2. S. Niki, M. Contreras, I. Repins, M. Powalla, K. Kushiya, S. Ishizuka, K. Matsubara, *Research and Applications*, **2010**, 18, 453.
3. M. Klenk, O. Schenker, E. Bucher, *Thin Solid Films*, **2006**, 361-362, 229.
4. S.R. Kodigala, *Cu (In_{1-x}Ga_x) Se₂ based thin film solar cells*, Academic Press, **2011**.
5. A.M. Gabor, J.R. Tuttle, D.S. Albin, M.A. Contreras, R. Noufi, A.M. Hermann, *Applied Physics Letters*, **1994**, 65, 198.
6. M. Kemell, M. Ritala, M. Leskelä, *Critical Reviews in Solid State and Materials Sciences*, **2005**, 30, 1.
7. C. Huang, S.S. Li, W. Shafarman, C.-H. Chang, E. Lambers, L. Rieth, J. Johnson, S. Kim, B. Stanbery, T. Anderson, *Solar energy materials and solar cells*, **2001**, 69, 131.
8. O. Lundberg, J. Lu, A. Rockett, M. Edoff, L. Stolt, *Journal of Physics and Chemistry of Solids*, **2003**, 64, 1499.
9. J. Merino, M. León, F. Rueda, R. Diaz, *Thin Solid Films*, **2000**, 361, 22.

10. C. Xu, H. Zhang, J. Parry, S. Perera, G. Long, H. Zeng, *Solar Energy Materials and Solar Cells*, **2013**, *17*, 357.
11. H.K. Song, S.G. Kim, H.J. Kim, S.K. Kim, K.W. Kang, J.C. Lee, K.H. Yoon, *Solar Energy Materials and Solar Cells*, **2003**, *75*, 145.
12. S.M. Kong, R. Fan, S.H. Jung, C.W. Chung, *Journal of Industrial and Engineering Chemistry*, **2013**, *19*, 1320.
13. S.-C. Chen, D.-H. Hsieh, H. Jiang, Y.-K. Liao, F.-I. Lai, C.-H. Chen, C.W. Luo, J.-Y. Juang, Y.-L. Chueh, K.-H. Wu, *Nanoscale Research Letters*, **2014**, *9*, 280.
14. A. Kampmann, V. Sittinger, J. Rechid, R. Reineke-Koch, *Thin Solid Films*, **2000**, *361–362*, 309.
15. L. Zhang, F.D. Jiang, J.Y. Feng, *Solar Energy Materials and Solar Cells*, **2003**, *80*, 483.
16. M. Ganchev, J. Kois, M. Kaelin, S. Bereznev, E. Tzvetkova, O. Volobujeva, N. Stratieva, A. Tiwari, *Thin Solid Films*, **2006**, *511*, 325.
17. R. Caballero, C. Maffiotte, C. Guillen, *Thin Solid Films*, **2005**, *474*, 70.
18. G. Chen, J. Yang, Y. Chan, L. Yang, W. Huang, *Solar Energy Materials and Solar Cells*, **2009**, *93*, 1351.
19. D. Abou-Ras, G. Kostorz, D. Bremaud, M. Kälin, F. Kurdesau, A. Tiwari, M. Döbeli, *Thin Solid Films*, **2005**, *480*, 433.
20. T. Nakano, T. Suzuki, N. Ohnuki, S. Baba, *Thin Solid Films*, **1998**, *334*, 192.
21. S. Deok Kim, H.J. Kim, K. Hoon Yoon, J. Song, *Solar Energy Materials and Solar Cells*, **2000**, *62*, 357.
22. A. Kinoshita, M. Fukaya, H. Nakanishi, M. Sugiyama, S.F. Chichibu, *Physica Status Solidi (C)*, **2006**, *3*, 2539.

*Dedicated to Professor Mircea Diudea
on the Occasion of His 65th Anniversary*

BAND GAP MODULATION OF GRAPHENE AND GRAPHYNE VIA TETRACYANOETHYLENE ADSORPTION

ROYA MAJIDI^{a,*}, ALIREZA KARAMI^b

ABSTRACT. Adsorption of tetracyanoethylene molecule on graphene and graphyne was investigated in view of finding an effective way to control their electronic properties. The electronic properties of graphene, α -, β - and γ - graphyne were studied by using the density functional theory. The binding energy, equilibrium adsorption distance, amount of charge transfer, electronic band structure, and density of states were calculated. The small adsorption energy and large adsorption distance identified physisorption of tetracyanoethylene molecule on graphene and graphyne sheets. It was found that charge is transferred from sheets to tetracyanoethylene molecule. In the presence of this acceptor molecule, the graphene and α -, β - and γ -graphynes, with semimetallic properties, show semiconducting behaviour. The tetracyanoethylene molecule has no considerable effect on the semiconducting property of γ -graphyne. Our results reveal that adsorption of organic molecules, such as tetracyanoethylene, is a proper method to open a band gap in graphene and graphyne.

Keywords: *Organic molecule, Graphene, Graphyne, Band gap, Density functional theory.*

INTRODUCTION

Graphene is a class of two dimensional nanomaterials with exceptional electronic properties which make it a promising material for the next generation electronics [1].

^a *Department of Physics, Shahid Rajaee Teacher Training University, Lavizan, 16788-15811 Tehran, Iran*

^b *Department of Chemistry, Shahid Rajaee Teacher Training University, Lavizan, 16788-15811 Tehran, Iran*

* *Corresponding Author: r.majidi@srttu.edu, royamajidi@gmail.com*

The graphene structure is composed of carbon atoms packed into planar honeycomb lattice. Recently, new two dimensional carbon allotropes named graphyne were formed by introducing acetylenic linkages within the hexagonal lattice of graphene [2]. By varying concentrations of acetylenic linkages, several forms of graphyne so called α -, β - and γ - graphyne with different properties have been proposed [2-4]. It is found that α - and β - graphyne analogous to graphene are zero band gap semimetals while γ -graphyne is a semiconductor. It should be mentioned that lack of a band gap largely limits the application of graphene and graphyne in electronics. Thus, a band gap must be opened for the practical applications of these materials [5]. In the recent years, many physical and chemical approaches were suggested to open a band gap and provide suitable semiconducting properties in graphene [6-11]. For instance, it was found that chemical functionalization of graphene is a proper way to modify the electronic properties of graphene [6]. In addition, the use of underlying substrate such as silicon dioxide produced the shift from semimetal to semiconductor with a small energy band gap [7]. An alternative strategy is the organic molecule adsorption on graphene which may cause dramatic changes in electronic properties of graphene and induce a band gap. It is found that adsorption of organic molecules, such as tetracyanoethylene (TCNE), tetrakisdimethylamino-ethylene (TDAE), and tetracyanoquino-dimethane (TCNQ) provide a nondestructive way for controlling the carrier type and concentration of graphene via charge transfer between sheet and the adsorbed molecule [8, 11]. This result motivated us to study the effect of organic molecules on the electronic properties of graphene and graphyne; in the present work, we studied the adsorption of tetracyano-ethylene molecule on graphene and graphyne using density functional theory (DFT).

METHOD

The DFT calculations were performed using the openMX code [12]. The generalized gradient approximation (GGA) as parameterized by the Perdew-Burke-Ernzerhof (PBE) was used to take into account the exchange and correlation energy [13]. The cutoff energy was set to 150 Ry. The systems were relaxed until the residual forces arrived below 0.01 eV/Å. Charge transfer between the adsorbed molecule and sheet was estimated by Mulliken charge analysis. For calculations of the electronic properties, 51 k-points were used along of each high symmetry line. The graphene, α -, β - and γ - graphyne were selected as the host material for molecular adsorption. We have considered supercells of graphene and graphyne sheets as shown in Figure 1.

The periodic boundary condition was applied. A void with the height of 15 Å was put above the sheet to ensure that the distance between adjacent sheets

is large enough and interaction between them is negligible. The size of the simulation box, numbers of unit cell and carbon atoms in each supercell are listed in Table 1.

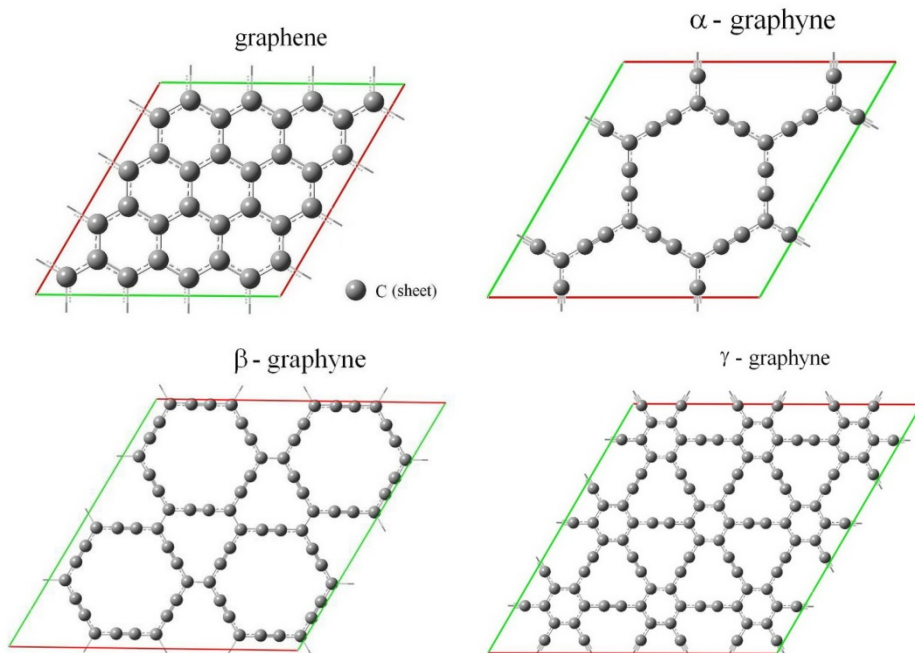


Figure 1. Structure of graphene and α -, β - and γ - graphynes.

Table 1. Size of simulation box, $a \times b \times c$, number of unit cell, n_u , and number of carbon atoms, n_c , per supercell.

Structure	$a \times b \times c$ (\AA^3)	n_u	n_c
graphene	$9.85 \times 9.85 \times 15$	4×4	32
α - graphyne	$13.96 \times 13.96 \times 15$	2×2	32
β - graphyne	$19.0 \times 19.0 \times 15$	2×2	72
γ - graphyne	$20.65 \times 20.65 \times 15$	3×3	108

RESULTS AND DISCUSSIONS

To evaluate adsorption state of tetracyanoethylene on sheets, the binding energy was calculated by $E_b = E_{\text{sheet+TCNE}} - (E_{\text{sheet}} + E_{\text{TCNE}})$. Here $E_{\text{sheet+TCNE}}$ and E_{sheet} are the total energies of sheet with and without tetracyanoethylene molecule,

respectively. The energy of an isolated tetracyanoethylene molecule is represented by E_{TCNE} .

Different initial configurations of tetracyanoethylene molecule adsorbed on sheets were considered and their binding energies were compared. The most stable configurations with the lowest binding energies are shown in Figure 2. The parameters of binding energy, equilibrium distance between molecule and sheet (defined as the nearest distance between molecule and sheet), and charge transfer are listed in Table 2. The small binding energy and large adsorption distance indicate that tetracyanoethylene molecule is physisorbed on graphene and graphyne sheets. The charge analysis demonstrates that electrons transfer occurred from sheets to tetracyanoethylene molecule. Such adsorption and charge transfer are similar to those reported in reference [8].

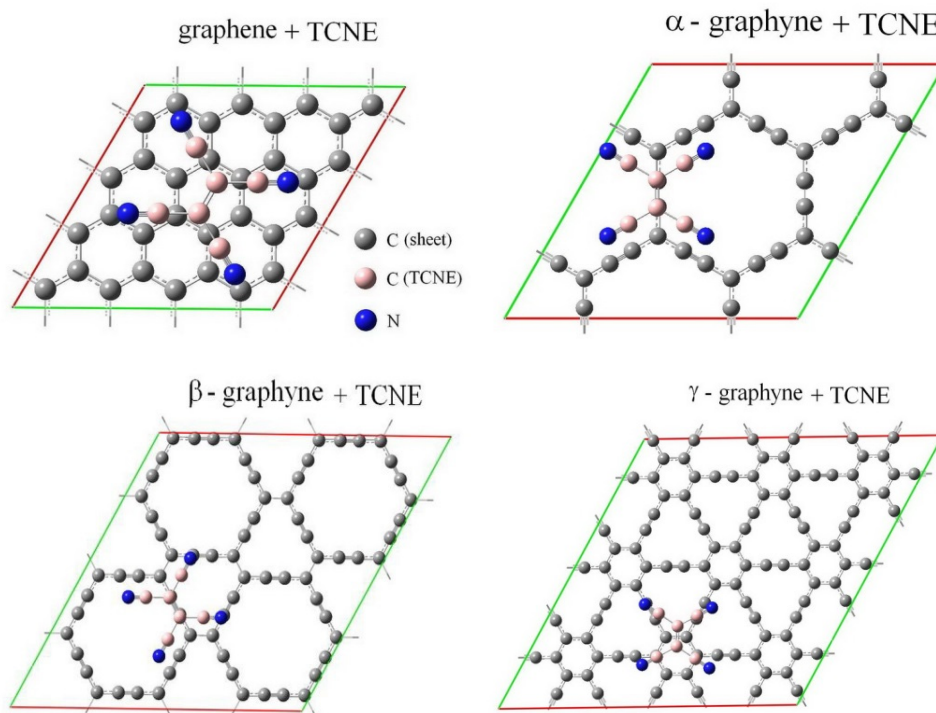


Figure 2. The most stable adsorption configurations of tetracyanoethylene on graphene and α -, β - and γ -graphynes.

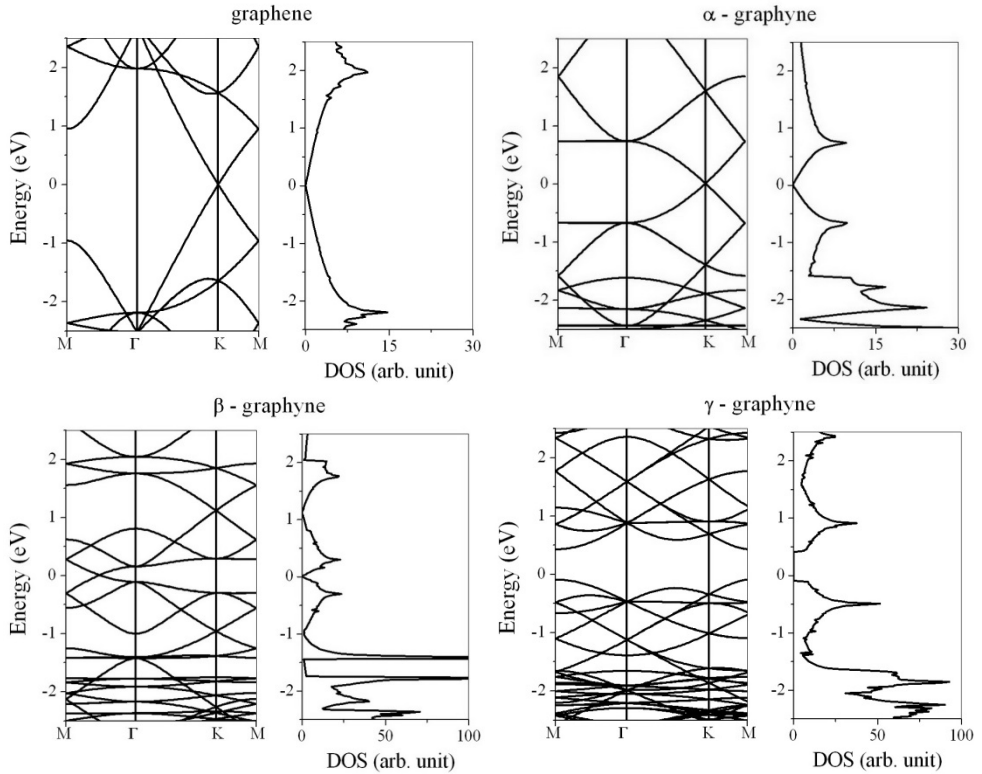


Figure 3. Electronic band structures and DOS of graphene and α -, β - and γ - graphynes. (The Fermi level is set to 0 eV.)

We have first studied the electronic properties of graphene and α -, β - and γ - graphyne sheets. The electronic band structures and density of states (DOS) of graphene and graphyne are presented in Figure 3. For graphene and α - and β - graphyne, the valence and conduction bands touch linearly at the Dirac cone and DOS is zero. Hence, graphene and α - and β - graphyne are semimetals with zero band gap. It is found that γ - graphyne is a semiconductor with a small energy band gap of 0.5 eV.

Next, we studied the effect of tetracyanoethylene molecule on the electronic properties of graphene and graphyne. The electronic band structures and DOS of graphene and α -, β - and γ - graphynes with tetracyanoethylene molecule are shown in Figure 4. In electronic band structures of graphene and α - and β - graphynes, small band gaps appeared, due to the presence of tetracyanoethylene molecule. The energy band gaps are listed in Table 2.

Therefore, graphene and, α - and β - graphynes show semiconducting behaviour in the presence of tetracyanoethylene molecule. This can be explained by the fact that adsorption of an acceptor molecule such as tetracyanoethylene decreases the carrier concentration and consequently the electrical conductivity of graphene and graphyne sheets with semimetallic properties. In contrast, adsorption of tetracyanoethylene has no considerable effect on the electronic band structure and energy band gap of γ - graphyne near the Fermi level. Hence, this type of graphyne is semiconductor before and after tetracyanoethylene adsorption.

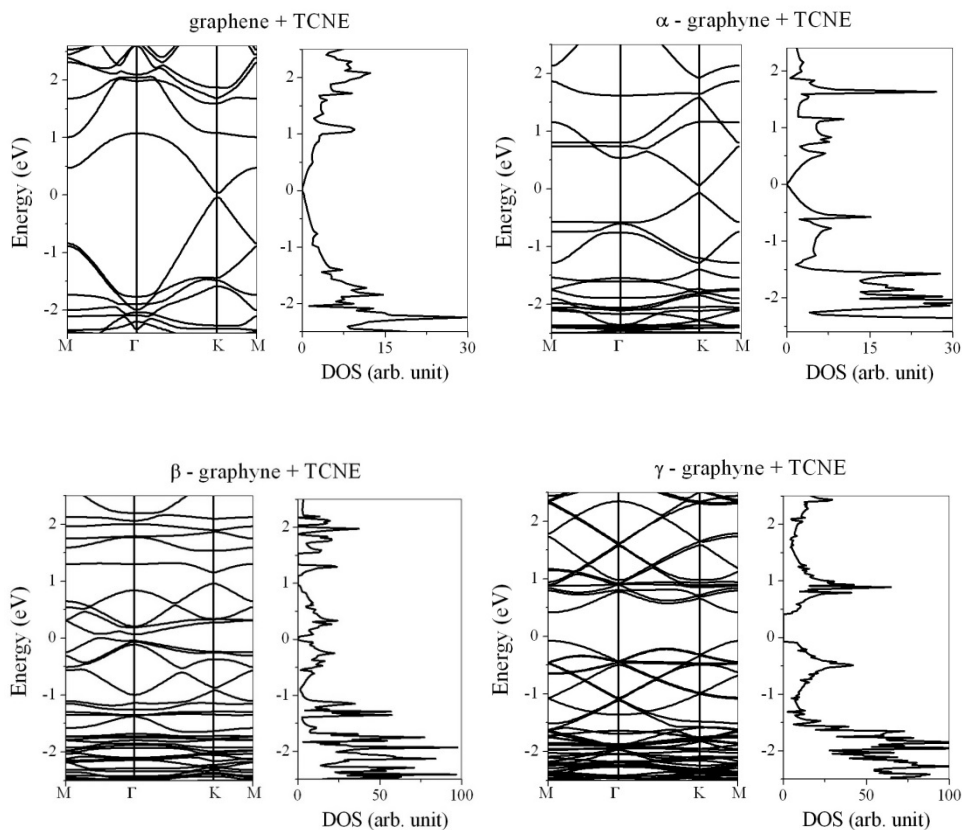


Figure 4. Electronic band structures and DOS of graphene and α -, β - and γ - graphynes in the presence of tetracyanoethylene. (The Fermi level is set to 0 eV.)

Table 2. Binding energy, E_b , adsorption distance, d , charge transfer, q , and band gap, E_g .

Structure	E_b (eV)	d (Å)	q (e)	E_g (eV)
graphene	1.8	2.6	0.85	0.1
α - graphyne	1.5	2.5	0.86	0.14
β - graphyne	0.8	2.5	0.16	0.07
γ - graphyne	1.1	2.6	0.03	0.5

CONCLUSIONS

Adsorption of tetracyanoethylene molecule on graphene and α -, β - and γ - graphynes was studied using DFT. The binding energy, equilibrium adsorption distance, charge transfer, electronic band structure, and DOS were calculated. The results show that tetracyanoethylene molecule is physisorbed on graphene and graphyne. The charge is transferred from sheets to tetracyanoethylene molecule. Adsorption of this acceptor molecule has a significant effect on the electronic properties of graphene and α - and β - graphyne sheets. These sheets with semimetallic character switch to semiconducting behaviour in the presence of tetracyanoethylene molecule. In contrast, the effect of tetracyanoethylene on electronic properties of γ - graphyne, with a priori semiconducting property, is not considerable. Our results provide an effective way to generate a band gap and produce semiconducting graphene and graphyne. This opens a gate for enormous technological and industrial areas for graphene and graphyne.

REFERENCES

1. H. Raza, "Graphene Nanoelectronics: Metrology, Synthesis, Properties and Applications", Springer, Berlin, **2012**.
2. A.L. Ivanovskii, *Prog. Solid State Chem.*, **2013**, *41*, 1.
3. D. Malko, C. Neiss, F. Vines, A. Gorling, *Phys. Rev. Lett.*, **2012**, *108*, 086804.
4. V. Ongun Ozcelik, S. Ciraci, *J. Phys. Chem. C*, **2013**, *117*, 2175.
5. Y. Li, F. Liv, Z. Chen, *J. Am. Chem. Soc.*, **2012**, *134*, 11269.
6. D. Haberer, D.V. Vyalikh, S. Taioli, B. Dora. M. Farjam, J. Fink, D. Marchenko, T. Pichler, K. Ziegler, S. Simonucci, M. S. Dresselhaus, M. Knupfer, B. Buchner, A. Gruneis, *Nano Lett.*, **2010**, *10*, 3360.
7. P. Shemella, S.K. Nayak, *Appl. Phys. Lett.*, **2009**, *94*, 032101.
8. M. Chi, Y-P. Zhao, *Comput. Mater. Sci.*, **2012**, *56*, 79.
9. K. Novoselov, *Nature Matter*, **2007**, *6*, 720.

10. Y.H. Lu, W. Chen, Y.P. Feng, P. M. He, *J. Phys. Chem. B*, **2009**, *113*, 2.
11. R. Majidi, A.R. Karami, *Physica E*, **2014**, *63*, 264.
12. T. Ozaki, H. Kino, J. Yu, M.J. Han, N. Kobayashi, M. Ohfuti, F. Ishii, et al. User's manual of OpenMX version 3.6, <http://www.openmx-square.org>.
13. J.P. Perdew, K. Burke, M. Ernzerhof, *Phys. Rev. Lett.*, **1996**, *77*, 3865.

*Dedicated to Professor Mircea Diudea
on the Occasion of His 65th Anniversary*

CHANGES IN PHYSICO-CHEMICAL CHARACTERISTICS OF HUMAN LOW DENSITY LIPOPROTEIN NANO-PARTICLES BY ELECTROMAGNETIC FIELD EXPOSURE

**SOHEILA ABDI^a, DAVOUD DORRANIAN^b, GHOLAM ALI NADERI^{c,*},
AMIRNADER EMAMI RAZAVI^d**

ABSTRACT. Studies on the effects of electromagnetic field (EMF) exposure on cardiovascular function have provided some evidence of a possible action. Low density lipoprotein (LDL) modifications appear as an early step in the promotion and progression of atherosclerosis, the most causes of death in cardiovascular disease (CVD) patients. This study aimed to evaluate the effects of extremely low frequency (ELF) of electromagnetic fields on LDL physico-chemical modifications. LDL was separated by sequential ultracentrifugation and its susceptibility to oxidation was evaluated by continuous monitoring of conjugated dienes formation, using a spectrophotometer. LDL size and zeta potential is determined by zetasizer instrument. The results indicated that moderate ELF-EMFs of 2-4 mT can induce the susceptibility of LDL to oxidation and aggregation. Weak ELF-EMFs of 0.125-0.5 mT caused a decrease in LDL zeta potential in a time and dose dependent manner while in moderate ELF-EMFs of 1-4 mT LDL zeta potential was started to increase after an initial decrease at the first hour of exposure. LDL oxidation and aggregation are two important modifications of LDL, involved in the promotion and progression of atherosclerosis. On the other hand, alteration of the LDL surface charge can interfere with the metabolism of LDL and its interaction with other molecules. Therefore with regard to the atherogenic effects of ELF-EMFs on LDL, it can be considered as a risk factor in atherosclerosis.

Keywords: *Electromagnetic field, LDL oxidation, LDL aggregation, LDL zeta potential, LDL mean size*

^a *Department of Physics, Safadasht Branch, Islamic Azad University, Safadasht, Tehran, Iran*

^b *Plasma Physics Research Center, Sciences and Research Branch, Islamic Azad University, Tehran, Iran*

^c *Cardiovascular Research Center, Isfahan Cardiovascular Research Institute, Isfahan University of Medical Sciences, Isfahan, Iran*

^d *Iran National Tumor Bank, Cancer Institute, Tehran University of Medical Sciences, Tehran, Iran*

* *Corresponding Author: naderi.crc@gmail.com*

INTRODUCTION

Recently, investigation on the biological effects and health implications of electric and magnetic fields becomes a subject of a public concern and private debate. However the effects of exposure to extremely low frequency (ELF) electromagnetic fields (EMFs) on human cardiovascular parameters remain undetermined. Studies indicate that the ELF-EMFs causes decrease in heart rate (HR) and increase in heart rate variability (HRV) in human subjects [1-3]. A cross sectional study on electricians revealed that long-time low-level exposure to ELF fields caused significantly frequent electrocardiogram (ECG) changes including arrhythmias, conduction disturbances, and myocardial ischemia changes [4]. However other investigations didn't find any significant changes in blood pressure and HR or cardiac arrhythmias following ELF magnetic field exposure [5-7]. Investigations indicate that local exposure of rabbits arterial sinocarotid baroreceptors to artificial static magnetic and natural geomagnetic field (GMF) will be effective in cardiovascular conditions with arterial hypertension and decreased baroreflex sensitivity [8].

Serum lipid and lipoprotein concentrations are associated with the risk of cardiovascular disease(CVD) [9-10]. A study on animals indicated that exposing to 15 Hz low-intensity pulsed magnetic fields for 8 weeks led to a significant decrease in serum triglycerides and cholesterol and increase in high density lipoprotein (HDL) levels in rabbits fed with high cholesterol diet [11]. Human studies indicated that serum lipids and lipoproteins could change under the exposure of EMFs and changes are depend on the time of exposure [12]. Among lipoproteins, low density lipoproteins (LDL) have been mostly investigated in terms of their role in atherosclerosis [13]. This is an inflammatory disease and the most cause of death in CVD patients. LDL readily enters the artery wall by crossing the endothelial membrane. Once on the arterial wall, if LDL accumulates, it is subject to a variety of modifications. LDL modification is an early step and very important event in the promotion of atherosclerosis [14]. The best known of these modifications is oxidation, both of the lipids and of the APO B [15]. LDL is also subject to other physical and chemical modifications such as aggregation [16] and glycation [17].

Investigations indicated that LDL characteristics such as particle size and its surface charge were related to the severity of CVD [18], and other related diseases like obesity metabolic syndrome and Diabetes [19].

There are a few studies that investigated the effects of ELF magnetic field on the generation and promotion of atherosclerosis. In previous studies we investigated the effects of weak and moderate static magnetic fields on the human LDL characteristics [20].

The aim of this study is to evaluate the effects of ELF-EMFs on LDL susceptibility to oxidation and aggregation. Because of the importance of LDL size and surface charge on their metabolism and interactions with other molecules such as apo lipoproteins, receptors, and enzymes, the effect of different intensities of ELF electromagnetic fields on the LDL particles mean size and surface charge was also investigated.

RESULTS

Figure 1 shows the oxidation curves of LDL samples under the exposure of different flux densities of EMF in comparison with control. *In vitro* oxidation of LDL is mediated by copper solution (70 $\mu\text{g/ml}$ LDL protein in iso-osmolar PBS with pH of 7.4, contain 10 μM CuSO_4) at 37 °C during a time frame of 180 min.

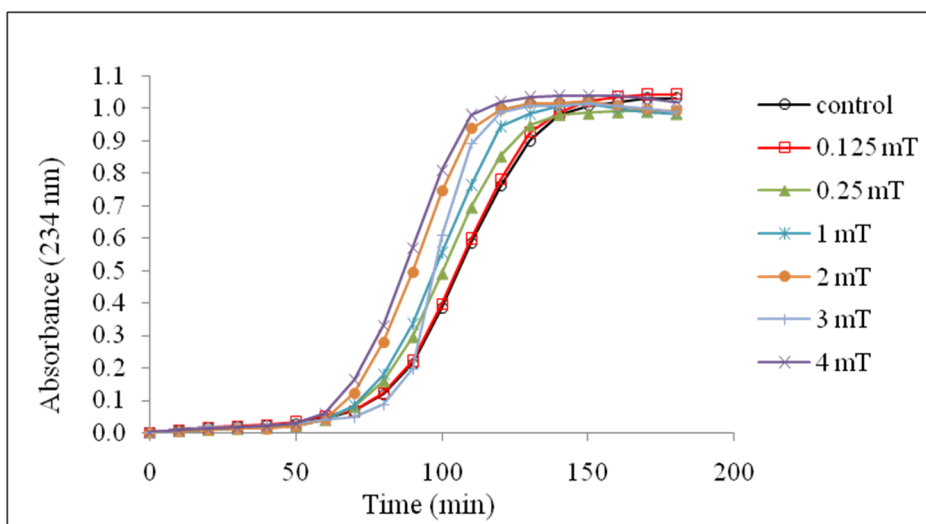


Figure 1. Effect of different electromagnetic flux densities on kinetics of copper-mediated oxidation of LDL, in comparison with the control.

Table 1 lists the parameters of LDL oxidation under the exposure at electromagnetic flux densities of 0.125, 0.25, 0.5, 1, 2, 3 and 4 mT in comparison with the control. LDL oxidation parameters were extracted from the oxidation curves and include the lag time (t_{lag}), time required for reaching half maximum dienes ($t_{1/2}$), maximum velocity (v_{max}) and maximum conjugated diene formation (d_{max}). The lag time and $t_{1/2}$ of LDL oxidation decreased parallel to the increase in electromagnetic flux density (except for magnetic flux density of 3 mT)

and this decrease is significant in 2 and 4 mT ($p < 0.01$). The propagation rate or v_{\max} was significantly increased to 745.8 ± 17.1 , 910.7 ± 7.6 and 734 ± 8.3 nmol/min under the exposure at magnetic flux densities of 2, 3 and 4 mT, respectively; data were compared to 622.6 ± 11.2 nmol/min in control samples (p value < 0.01). The production of conjugated dienes didn't show any changes under the exposure of different doses of EMF.

Table 1. Changes in LDL oxidation parameters under the exposure at different ranges of electromagnetic flux densities in comparison with the control.

Electromagnetic flux density (mT)	LDL oxidation parameters			
	Lag time (min)	$T_{1/2}$ (min)	Propagation rate (nmol/min)	Maximal diene (μmol)
Control	81.2 ± 2.6	112.3 ± 3.1	622.6 ± 11.2	35.0 ± 1.1
0.125	79.9 ± 2.1	11.4 ± 3.3	629.2 ± 12.1	35.5 ± 0.9
0.25	77.2 ± 2.9	100.4 ± 5.8	630.5 ± 14.1	33.6 ± 0.7
0.5	76.8 ± 1.9	101.5 ± 2.6	664.4 ± 19.3	34.7 ± 0.3
1	76.2 ± 2.0	98.1 ± 7.3	687.4 ± 10.8	34.4 ± 1.7
2	$69.1 \pm 2.6^{**}$	$91.7 \pm 5.4^{**}$	$745.8 \pm 17.1^{**}$	34.7 ± 0.9
3	86.2 ± 4.1	98.2 ± 8.1	$910.7 \pm 7.6^{**}$	34.4 ± 0.5
4	$66.4 \pm 2.4^{**}$	$87.3 \pm 5.1^{**}$	$734.2 \pm 8.3^{**}$	35.6 ± 0.45

Test samples were pre-incubated at 37°C under the exposure at electromagnetic flux densities of 0.125, 0.25, 0.5, 1, 2, 3 and 4 mT for one hour and control samples were pre-incubated at the same condition without magnetic field exposing. Oxidation of LDL (70 $\mu\text{g}/\text{ml}$ LDL protein in iso-osmolar PBS with a pH of 7.4) was initiated by addition of 10 μM CuSO_4 . Continuous monitoring of the formation of conjugated dienes at 234 nm was recorded at intervals of 10 min in 1 cm quartz cuvettes at 37°C for 3 h under the exposure of applied static magnetic field. The oxidation parameters were calculated from LDL oxidation curves. Data are represented as mean \pm SD obtained from 5 separate oxidation assays. * = p value < 0.05 and ** = p value < 0.01 .

Table 2 indicates the effect of different electromagnetic flux densities at different times of exposure on the LDL tendency to aggregation in comparison with controls. Data are represented as absorbance at 680 nm. Electromagnetic flux densities of 0.125 and 0.25 mg had no effect on the tendency of LDL particles to aggregation during the time of the experiment. The tendency of LDL to aggregation significantly increased after 3 h of incubation under the exposure at 0.5 mT ($p < 0.05$) and 2 h of incubation under the exposure of 1 mg ($p < 0.05$) when compared to that in control samples. Electromagnetic flux densities of 2, 3 and 4 mT caused a significant increase in the tendency of LDL particles to aggregation after the first h of exposure ($p < 0.01$), and this increase is time dependent.

Table 2. The effect of electromagnetic flux densities of 0.125, 0.25, 0.5, 1, 2, 3 and 4 mT at different times of exposure (60, 120 and 180 min) on the LDL tendency to aggregation in comparison with controls.

Electromagnetic flux density (mT)	Time of exposure (min)			
	0	60	120	180
0.125	0.34 ± 0.03	0.33 ± 0.02	0.34 ± 0.03	0.35 ± 0.04
0.25	0.32 ± 0.02	0.33 ± 0.03	0.34 ± 0.02	0.35 ± 0.03
0.5	0.32 ± 0.02	0.35 ± 0.03	0.36 ± 0.04	0.38 ± 0.03 *
1	0.34 ± 0.03	0.36 ± 0.04	0.38 ± 0.04 *	0.41 ± 0.03 **
2	0.34 ± 0.03	0.40 ± 0.04 **	0.42 ± 0.02 **	0.45 ± 0.03 **
3	0.33 ± 0.02	0.45 ± 0.03 **	0.49 ± 0.03 **	0.53 ± 0.02 **
4	0.34 ± 0.03	0.48 ± 0.03 **	0.55 ± 0.04 **	0.57 ± 0.03 **

Data are expressed as mean ± SD obtained from 5 separate determinations and the results are represented as Absorbance in 680 nm. * = p value <0.05 and ** = p value <0.01.

The LDL mean particle size isolated from pooled serum was 20.45 nm. No significant differences were found in the size of LDL under the exposure of different doses of electromagnetic field after the specified time in this research. The effect of different electromagnetic flux densities at different times of exposure on the LDL zeta potential is shown in Table 3. The results indicate that the zeta potential of LDL particles reduced under the exposure of 0.125 mT EMF and this reduction was significant at 180 min ($p < 0.05$).

Table 3. The effect of electromagnetic flux densities of 0.125, 0.25, 0.5, 1, 2, 3 and 4 mT at different times of exposure (60, 120 and 180 min) on the LDL zeta potential in comparison with controls.

Electromagnetic flux density (mT)	Time of exposure (min)			
	0	60	120	180
0.125	-22.4 ± 0.2	-22.2 ± 0.2	-21.2 ± 0.3	-21.3 ± 0.2 *
0.25	-22.4 ± 0.3	-21.3 ± 0.6 *	-20.5 ± 0.5 **	-19.2 ± 0.7 **
0.5	-22.9 ± 0.3	-20.2 ± 0.3 **	-19.9 ± 0.5 **	-19.5 ± 0.4 **
1	-23.0 ± 0.4	-19.4 ± 0.4 **	-19.1 ± 0.5 **	-20.8 ± 0.4 **
2	-22.9 ± 0.3	-18.7 ± 0.5 **	-19.3 ± 0.4 **	-21.4 ± 0.7
3	-22.8 ± 0.4	-18.2 ± 0.3 **	-20.4 ± 0.5 **	-22.3 ± 0.4
4	-23.0 ± 0.3	-19.2 ± 0.5 **	-21.8 ± 0.4 *	-23.1 ± 0.5

LDL zeta potentials represented as mv and the values are mean ± SD obtained from 5 separate determinations. * = p value <0.05 and ** = p value <0.01.

A significant reduction in LDL zeta potential also was seen after 60, 120 and 180 min under an exposure of 0.25, 0.5 and 1 mT ($p < 0.01$). Exposure to the electromagnetic flux densities of 2, 3 and 4 mT first lead to a significant reduction in LDL zeta potential after 60 min of incubation ($p < 0.01$). But with continuing the incubation the zeta potential started to increase, so that, there was no significant differences in LDL zeta potential after 180 min of exposure compared with control samples.

DISCUSSION

The possible cardiovascular effects of ELF-EMFs through the change in the LDL physico-chemical properties were herein investigated. LDL susceptibility to copper mediated oxidation under the exposure of ELF-EMFs with different intensities were evaluated at the first step. Our results indicated that the susceptibility of LDL to oxidation is increased under the exposure of weak intensities of EMFs in a dose dependent manner. Electromagnetic flux densities of 0.125 to 1 mT had no significant effect on the LDL susceptibility to oxidation, although can lead to a decrease in lag time and an increase in the propagation rate of LDL oxidation. Following to increase the electromagnetic flux density, the lag time was significantly decreased and reached 18.2 % reduction at 4 mT. Inverse v_{max} or propagation rate was decreased parallel to the increase of electromagnetic flux density and reached 46 % increase at 3 mT. Our previous study on the effects of static magnetic fields (SMF) on LDL susceptibility to oxidation has shown different results at magnetic flux densities of 0.25 and 0.5 mT [20]. At that investigation, weak SMFs of 0.25 and 0.5 mT opposite the moderate SMFs of 2-4 mT caused a significant decrease in the susceptibility of LDL to oxidation by increasing the lag time and decreasing the propagation rate [20].

The effect of an EMF on the living organism is a complex phenomenon. The initial mechanism is physico-chemical, but afterwards, biological effects develop. The physico-chemical action of an EMF consists in electron, ion, dipolar, macrostructural and electric polarization. Other factors may also play a role, such as molecular excitation, biochemical activation, generation of radicals, chemical bond weakening, hydration change, altered relaxation time of atom vibration, and altered spin of dipoles [21-23]. These physico-chemical changes could lead to different biological alterations that depend on the nature of the magnetic field, applied frequency, amplitude and time of exposure. The oxidative modification of LDL is a very important stage in the promotion and progression of atherosclerosis [15]. Free radical reactions are very important in the oxidation process of LDL and may require the generation of super oxide anion and

hydroxyl radicals through the Fenton reaction [24] and exert some of their deleterious effects by peroxidation of the lipids [25]. Enhanced pro-oxidant conditions and free radical formation have been suggested in different biological models as an important pathway of response induced by electromagnetic fields which modulates the turnover of oxyradicals, including induction of ROS-generating enzymes [26-28]. With regard to the effects of EMF on chemical reactions and free radicals [29-30], an increase in the free radicals production and stability may be the main cause of raising the susceptibility of LDL to oxidation in this investigation.

LDL aggregation is another lipoprotein modification with atherogenic properties. Aggregated LDL is taken up by macrophages at an increased rate, leading to foam cell formation [31]. In addition to oxidation, LDL aggregation also occurs in the arterial wall, but little is known about the mechanism responsible for this modification [32]. In this study the effects of ELF-EMFs on the tendency of LDL particles to aggregation were investigated. Electromagnetic flux densities of 0.125 and 0.25 mT had no significant effect on the tendency of LDL to aggregation in the experimental time frame. Electromagnetic flux densities of 2, 3 and 4 mT after the first hour, 1 mT after 2 h and 0.5 mT after 3 h of exposure can lead to a significant increase in LDL tendency to aggregation. In other words, the enhancing effects of ELF electromagnetic field on the LDL tendency to aggregation is a time and dose dependent process. Our previous study on the cardiovascular effects of SMF indicated the same result [20]. The surface charge of particles is an important factor in the stability of their suspension in colloids, decreasing the particles surface charge or zeta potential could lead to an increase in the tendency of particles to aggregation. The increase in the tendency of LDL to aggregation following the exposure to ELF-EMF could be the result of modifications in LDL structure or alterations in the electrostatic properties of surface molecules and LDL zeta potential.

LDL and other lipoprotein nano-particles have a distinctive electrical charge and changes in electrostatic properties directly affect the metabolism of the lipoprotein [33]. LDL zeta potential has a vital role in its structure, interaction with apolipoproteins, receptors, enzymes and finally in plasma lipid metabolism [34] and may change in different physiological and pathological conditions [35].

Size of LDL nano-particles is another physical characteristic of LDL that is very important in relation to CVD. Studies have indicated that individuals with predominantly small LDL particles have greater cardiovascular risk than those with predominantly large LDL [36]. In this study the effects of ELF-EMFs on LDL particles mean size and surface charge were evaluated *in vitro*. Our results showed that an ELF electromagnetic flux density of 0.125, 0.25 and 0.5 mT causes a decrease in LDL surface negative charge in a time and dose dependent manner. LDL zeta potential at electromagnetic flux densities of 1-4 mT, decreases at the first hour of exposure and then started to increase. Investigations indicated

that magnetic exposure reduced the zeta potential and diffusivity of nonmagnetic colloids [37]. It is not clear what is the reason for the decay in LDL zeta potential following the exposure to electromagnetic field in this study. It may be related to the physico-chemical alterations in LDL surface molecules including proteins and fatty acids and their interaction, that lead to decrease in negative charge density on the LDL surface. Investigations indicate that lipid peroxidation can lead to an increase in negative charge of LDL and HDL particles [38]. Thus, the increase of LDL zeta potential under the exposure at electromagnetic flux density of 1-4 mT, after the expected initial decay in LDL surface charge at the first hour of exposing, may be the result of lipid peroxidation induced by the production and stabilization of free radicals. It has been demonstrated that LDL tendency to aggregation is inversely related with the susceptibility of LDL to oxidation [39].

It should be considered that the degree of electromagnetic effect, in part, depends on the particle size and ions in the medium. Since different people have different size of LDL nano-particles and because LDL size distribution is associated with the risk of CVD and atherosclerosis, the effects of EMF on lipoprotein nano-particles physico-chemical characteristics and metabolism, and therefore its possible interaction with CVD may be different among individuals. However, further *in vivo* and *in vitro* studies are needed to demonstrate the adverse effects of ELF electromagnetic field as a risk factor in CVD.

CONCLUSIONS

Moderate ELF-EMFs can increase the susceptibility of LDL to oxidation through the decrease in the lag time and an increase in the propagation rate. The tendency of LDL to aggregation also is increased by ELF-EMF. LDL oxidation and aggregation are two important modifications of LDL involved in the promotion and progression of atherosclerosis. On the other hand, ELF-EMFs can alter the LDL surface charge and this alteration may interfere with the metabolism of LDL and its interaction with other molecules such as apolipoproteins, enzymes and receptors. If these atherogenic effects of ELF-EMF have been confirmed *in vivo*, it can be considered as a risk factor in CAD.

EXPERIMENTAL SECTION

Serum preparation and LDL separation. A pooled serum was prepared from 12 h fasting blood samples of 25 donors. In order of separation of LDL fraction including IDL ($1.006 \text{ g/cm}^3 < \rho < 1.063 \text{ g/cm}^3$), 5.9 ml of serum samples were poured into 8.9 ml polyallomer ultracentrifuge tubes (Optiseal, part number 361623, Beckman/Coulter, Fullerton, CA, USA) and a discontinuous density

gradient was made by overlaying the serum samples with 3 ml of Solution A [NaCl: 0.195 mM, NaOH: 0.62 mM, 0.01% ethylene diamine tetraacetic acid disodium salt (EDTA- Na_2), $d = 1.006 \text{ g/ml}$]. The tubes were centrifuged in a Beckman Coulter optima L-100 XP ultracentrifuge equipped with a type 90Ti fixed angle rotor, at 60000 rpm (462666 g) for 6 h at 16 °C, acceleration: "5" and deceleration: "7". After centrifugation, the very low density lipoprotein (VLDL) fraction (the white layer of the supernatant) accompanied by 3 ml of the upper layer solution in tubes was removed and residual content of tube was mixed with a solution B [containing 24.8 g sodium bromide (NaBr) in 100 ml of solution A, $d=1.182 \text{ g/cm}^3$]. The tubes were centrifuged at 60000 rpm for 12 h at 16 °C, acceleration: "9" and deceleration: "7". After centrifugation, the LDL fraction appears as a yellow-orange band at the supernatant [40].

LDL dialysis: The obtained LDL was carefully placed in special dialysis tubes (D6191-25EA, Sigma, St Louis, MO, USA) and dialyzed against iso-osmolar phosphate buffer solution (PBS) with a pH of 7.4 for 24 h at 4 °C under nitrogen gas and the dialysis buffer was exchanged three times [41]. After dialyzing, in order to reduce freeze-thawing effects including physical alteration and aggregation of LDL, 10% w/v sucrose was added to LDL [Rumsey et al., 1994]. The LDL protein content was determined according to a modified Lowry method and then LDL was aliquot and stored at -70 °C until further analysis [42].

Evaluation of the susceptibility of LDL to oxidation: Continuous monitoring of the formation of conjugated dienes was accomplished by using a spectrophotometer (UV 3100, Shimadzu, Kyoto, Japan) based on the technique proposed by Esterbauer et al. [43] at the wavelength of 234 nm. After thawing, LDL was adjusted to 70 μg protein/ml in iso-osmolar PBS buffer with a PH of 7.4. Test samples were pre-incubated at 37 °C under the exposure of different static magnetic flux densities of 0.125, 0.25, 0.5, 1, 2, 3 and 4 mT for one hour and control samples were pre-incubated at the same condition without magnetic field exposing. The oxidative modification of LDL was initiated by addition of freshly prepared 10 μM CuSO_4 . The kinetics of LDL oxidation were monitored every 10 min by measuring its absorbance at 234 nm for 3 h. The lag time (t_{lag}), the time period until the conjugated dienes began to increase, was determined graphically by the intercept of the tangents to the slow and fast increase of the diene absorption. The other LDL oxidation parameters are the time required for reaching half maximum dienes ($t_{1/2}$), and the maximum velocity (v_{max}) of lipid peroxidation. Every 0.01 unit change in absorbance per min equals to velocity of diene production of 0.03389. The maximum diene concentration ($\text{diene}_{\text{max}}$) is another parameter of LDL oxidation, and every 1 unit increase in absorption in 234 nm is equal to the production of 33.9 μM dienes. The conversion of absorption into concentrations is based on a molar absorptivity of $\epsilon_{234} = 29500 \text{ L}\cdot\text{mol}^{-1}\cdot\text{cm}^{-1}$ [43].

Evaluation of the LDL tendency to aggregation: In order to determine the effect of EMF on LDL aggregation, LDL samples (200 µg of protein/mL in iso-osmolar phosphate buffer with a pH of 7.4) were exposed to different electromagnetic flux densities of 0.125, 0.25, 0.5, 1, 2, 3 and 4 mT for 1, 2 and 3 h. At the end of exposure time, the tendency of LDL to aggregation was measured by LDL vortexing for a period of 60 s at 25 °C and monitoring the changes in absorbance at 680 nm in comparison with control samples [39].

Determination of the LDL mean particle size: A zetasizer nano ZS instrument (Malvern, Worcestershire, UK) equipped with a 532 nm green laser beam was used for determination of LDL particles mean size [44]. The scattered light was collected by detector at an angle of 173° using NIBS (Non-Invasive Back-Scatter) technology and directed to a correlator. The data were analyzed by zetasizer software (DTS, nano series, version 5.02, Malvern, Worcestershire, UK) and size information was reported as the Z-average by intensity [26]. All measurements were performed at 25°C, in duplicate with automatic duration measurements.

In order to measure LDL mean particle size by dynamic light scattering (DLS) methodology, isolated LDL samples were mixed gently with 1 ml of phosphate buffer, 0.2 M, pH 7.4 containing 0.1% (w/v) EDTA-Na₂ as dispersant at a final protein concentration of 200 µg/ml. The mixture was then passed through a syringe filter (Millipore cellulose acetate membrane, 30 mm, 0.2 µm pore size), prior to injection into a disposable polystyrene cell (Malvern, Worcestershire, UK) in order to remove dust particles and was then subjected to size determination. Viscosity and refractive index (RI) of water as the dispersant were applied to standard operating protocol (SOP) prior to size determination. The accuracy of size measurements was examined using standard size nano particles (Gold Nanoparticles, 20 nm, 0.01% (w/v) aqueous solution, Nanocs Inc, New York, NY, USA) under the same experimental conditions and the results were matched to the diameter quoted by the manufacturer. The within-assay coefficient of variation (CV %) for 10 measurements was 1.4% and between-assay CV for 10 measurements was 2.9%.

Zeta potential measurement: The LDL particles zeta potential was also detected by Zetasizer nano ZS instrument. The zeta potential was calculated by determining the electrophoretic mobility and then applying the Henry equation ($U_E = 2\varepsilon z f(ka)/3\eta$) where z = zeta potential, U_E = electrophoretic mobility, ε = dielectric constant, η = viscosity and $f(ka)$ = Henry's function. In aqueous solutions $f(ka)$ is 1.5 and is referred to as the Smoluchowski approximation, dielectric constant and viscosity also in considered 78.5 and 0.8872 cP respectively. The electrophoretic mobility was obtained by performing an electrophoresis experiment on the sample and measuring the velocity of the particles using Laser Doppler

Velocimetry (LDV). The data were analyzed by Zetasizer software DTS (nano) version 5.02 (Malvern). All measurements were performed at 25°C, with a dielectric constant of 78.5 in duplicate. Tris buffer (1 mM, pH 7.4) was used as the dispersant and viscosity of the samples was estimated to be that of water (0.887 cP). In order to measure the LDL zeta potential, isolated LDL were mixed gently with 1 ml of dispersant in a final concentration of 70 µg/ml protein and passed through a syringe filter (cellulose acetate membrane, 30 mm, pore size: 0.2 µm) while being injected into a special folded capillary cell (DTS1060, Malvern) to exclude dust particles. To investigate the effect of electromagnetic field on zeta potential modification, LDL samples inside the cells were placed in the center of the solenoid and incubated under the exposure of different electromagnetic flux densities at 25 °C for different times and then subjected to zeta potential measurement after each time point. The accuracy of zeta potential measurements was examined using standard nano particles with zeta potential of 50 ± 5 mv (Malvern) under the same experimental conditions and results were matched with the zeta potential quoted by the manufacturer. The within-assays coefficient of variation (CV %) for 10 measurements was 1.9% and between-assays CV was 2.1%.

The exposure system: Experimental setup for the static magnetic field exposure was consisted of a solenoid cylinder with a diameter of 12 cm, height of 30 cm and 1200 turns [20]. The solenoid was located inside a ventilated incubator (Parsazma, Tehran, Iran). The incubator temperature was set at 37 °C. For LDL oxidation experiments LDL samples (inside a quartz cuvette) were put in the center of the solenoid at the middle height of it by an especial sponge holder. In order to produce suitable electromagnetic flux densities, a voltage regulator AC power supply (model: TDGC2, 220v, 50-60 Hz, Delta International Electric Co, Shanghai, China) was used to provide variable AC currents. The produced electromagnetic field at the exact site of cuvette location in the middle center of the solenoid was measured by a digital tesla meter with a three-D sensor (Holaday, Eden Prairie, MN, USA). A small ventilator was improvised at the bottom of the solenoid in order to prevent temperature rising due to the electrical current in solenoid during the experiment.

Statistical analysis: All statistical analyses were performed with the SPSS statistical software, version 16.0 (SPSS, Chicago, IL, USA). Data were expressed as mean ± standard deviations. P value <0.05 was considered statistically significant. Comparison of data between control and exposed samples was examined by non parametric two-independent samples and Mann-Whitney-Wilcoxon test. Comparison of data between different static magnetic flux densities and different exposure times was examined by non parametric test for several independent samples and Kruskal-Wallis H test.

ACKNOWLEDGMENT

This study was supported by Grant no.r 90124 from Isfahan Cardiovascular Research Institute. The authors would like to thank Dr. Maryam Boshtam for her technical support and helpful comments on the manuscript.

REFERENCES

1. M.R. Cook, C. Graham, HD. Cohen, M.M. Gerkovich, *Bioelectromagnetics*, **1992**, 13, 261.
2. C. Graham, M.R. Cook, HD. Cohen, M.M. Gerkovich, *Bioelectromagnetics*, **1994**, 15, 447.
3. Z. Tabor, J. Michalski, E. Rokita, *Bioelectromagnetics*, **2004**, 25, 474.
4. R. Dănulescu, C. Goiceanu, E. Dănulescu, M. Mărgineanu, C. Croitoru, G. Bălăceanu, *J. Prev.*, **2004**, 12, 9.
5. S. Ghione, C. Del Seppia, L. Mezzasalma, M. Emdin, P. Luschi, *Bioelectro-magnetics*, **2004**, 25, 167.
6. S. Ghione, C.D. Seppia, L. Mezzasalma, L. Bonfiglio, *Neurosci. Lett.*, **2005**, 382, 112.
7. M.L. Sait, A.W. Wood, R.L. Kirsner, *Physiol. Measur.*, **2006**, 27, 73.
8. J. Gmitrov, C. Ohkubo, *Bioelectromagnetics*, **2002**, 23, 329.
9. J.E. Hokanson, M.A. Austin, *J. Cardiovasc. Risk*, **1996**, 3, 213.
10. P. Zimetbaum, W.H. Frishman, W.L. Ooi, M.P. Derman, M. Aronson, L.I. Gidez, H.A. Eder, *Arteriosclerosis, Thromb. Vascular Biol.*, **1992**, 12, 416.
11. E. Luo, G. Shen, K. Xie, X. Wu, Q. Xu, L. Lu, X.Jing, *Bioelectromagnetics*, **2007**, 28, 608.
12. B. Kula, A. Sobczak, R. Grabowska-Bochenek, D. Piskorska, *J. Occup. Health-Eng. Ed.*, **1999**, 41, 177.
13. D. Steinberg, N. Engl, *J. Med.*, **1989**, 320, 915.
14. D. Steinberg, *J. Lipid Res.*, **2009**, 50, S376.
15. H. Itabe, *Clin. Rev. Allergy Immunol.*, **2009**, 37, 4.
16. H.F. Hoff, J. O'Neil, Arteriosclerosis, *Thromb. Vascular Biol.*, **1991**, 11, 1209.
17. N. Rabbani, L. Godfrey, M. Xue, F. Shaheen, M. Geoffrion, R. Milne, P.J. Thomalley, *Diabetes*, **2011**, 60, 1973.
18. J. Vakkilainen, G. Steiner, J.-C. Ansquer, F. Aubin, S. Rattier, C. Foucher, A. Hamsten, M.-R. Taskinen, *Circulation*, **2003**, 107, 1733.
19. S.M. Grundy, *J. Clin. Endocrinol. Metab.*, **2004**, 89, 2595.
20. S. Abdi, D. Dorrnian, A.N. Emami Razavi, G.A. Naderi, M. Boshtam, M. Ghoran-Nevis, *Bioelectromagnetics*, **2012**, 9999, 1.
21. H. Berg, *Bioelectrochem. Bioenerg.*, **1993**, 31, 1.
22. D. Duda, J. Grzesik, K. Pawlicki, *J. Trace Elem. Electrolyt. Health Dis.*, **1991**, 5, 181.

23. B. Kula, *Bioelectrochem. Bioenerg.*, **1996**, 39, 27.
24. D. Steinberg, *J. Biol. Chem.*, **1997**, 272, 20963.
25. K. Zwirska-Korczała, J. Jochem, M. Adamczyk-Sowa, P. Sowa, R. Polaniak, E. Birkner, M. Latocha, K. Pilc, R. Suchanek, *J. Physiol. Pharmacol.*, **2005**, 56, 101.
26. K.J. Fernie, D.M. Bird, *Evidence Environ. Res.*, **2001**, 86, 198.
27. J. Rollwitz, M. Lupke, M. Simkó, *Biochim. Biophys. Acta*, **2004**, 1674, 231.
28. S. Roy, Y. Noda, V. Eckert, M.G. Traber, A. Mori, R. Liburdy, L. Packer, *FEBS Lett.*, **1995**, 376, 164.
29. R.K. Adair, *Bioelectromagnetics*, **1999**, 20, 255.
30. C.T.W. Eveson, B. Brocklehurst, P.J. Hore, R.K.A. McLaughlan, *Int. J. Rad. Biol.*, **2000**, 76, 1509.
31. J.W. Heinecke, A.G. Suits, M. Aviram, A. Chait, *Arterioscler., Thromb., Vasc. Biol.*, **1991**, 11, 1643.
32. D. Meyer, M. Mayans, P. Groot, K. Suckling, K. Bruckdorfer, S. Perkins, *Biochem. J.*, **1995**, 310, 417.
33. D.L. Sparks, C. Chatterjee, E. Young, J. Renwick, N.R. Pandey, *Chem. Phys. Lipids*, **2008**, 154, 1.
34. H.I. Nishida, H. Arai, T. Nishida, *J. Biol. Chem.*, **1993**, 268, 16352.
35. M. Yano, M. Inoue, E. Maehata, T. Shiba, M. Yamakado, Y. Hirabayashi, M. Taniyama, S. Suzuki, *Clin. Chim. Acta*, **2004**, 340, 93.
36. L. Kuller, A. Arnold, R. Tracy, J. Otvos, G. Burke, B. Psaty, D. Siscovick, D.S. Freedman, R. Kronmal, *Arterioscler., Thromb., Vasc. Biol.*, **2002**, 22, 1175.
37. K. Higashitani, H. Iseri, K. Okuhara, A. Kage, S. Hatade, *J. Coll. Interface Sci.*, **1995**, 172, 383.
38. O. Panasenko, M. Borin, O. Azizova, K. Arnol'd, *Biofizika*, **1985**, 30, 822.
39. I. Maor, T. Hayek, R. Coleman, M. Aviram, *Arterioscler. Thromb. Vasc. Biol.*, **1997**, 17, 2995.
40. T.J. Bronzert, H.B. Brewer, *Clin. Chem.*, **1977**, 23(11), 2089.
41. M.L. Rufail, S.C. Ramage, R. van Antwerpen, *FEBS Lett.*, **2006**, 580(22), 5155.
42. Markwell, Mary Ann K. et al., *Anal. Biochem.*, **1978**, 87(1), 206.
43. S.P. Gieseg, H. Esterbauer, *FEBS Lett.*, **1994**, 343(3), 188.
44. A. Emami Razavi, M. Pourfarzam, M. Ani, G.A. Naderi, *Biomarkers Med.*, **2013**, 7, 235.

***Dedicated to Professor Mircea Diudea
on the Occasion of His 65th Anniversary***

**THE AGGREGATION BEHAVIOR OF AN A₃B FREE BASE
PORPHYRIN AND ITS APPLICATION AS CHROMIUM(III)-SELECTIVE
MEMBRANE SENSOR**

**BOGDAN-OVIDIU ȚĂRANU^a, DANA VLASCICI^b,
IULIANA SEBARCHIEVICI^a, EUGENIA FĂGĂDAR-COSMA^{c,*}**

ABSTRACT. A polyvinyl chloride membrane chromium(III)-selective electrode based on a synthesized A₃B free base porphyrin, namely 5-(4-pyridyl)-10,15,20-tris(phenoxy-phenyl)porphyrin, as membrane carrier was formulated and evaluated. The electrode exhibits a near-Nernstian response over the chromium(III) concentration range of $3 \times 10^{-5} \div 1 \times 10^{-1}$ M and shows good selectivity with respect to a wide range of cations. The aggregation behavior of the porphyrin macrocycle was investigated using TEM and STEM analytic techniques and revealed the formation of different shapes of nanostructures. Electron tomography was also employed in the study of the porphyrin aggregates.

Keywords: *membrane carrier, A₃B porphyrin, aggregation behavior, electron tomography*

INTRODUCTION

The vast majority of metals and metallic complexes with industrial use present some type of ecological hazard. Of these, chromium is a pollutant of considerable concern, as it is highly toxic and finds widespread use in industrial fields, such as: leather tanning, electroplating, steel manufacturing, metal finishing,

^a *National Institute of Research-Development for Electrochemistry and Condensed Matter Timisoara, Dr. Aurel Paunescu Podeanu str., no. 144, 300569 Timisoara, Romania*

^b *Faculty of Chemistry-Biology-Geography, West University of Timisoara, Pestalozzi str., no. 16, 300115 Timisoara, Romania*

^c *Institute of Chemistry Timisoara of Romanian Academy, Mihai Viteazul Ave., no. 24, 300223 Timisoara, Romania*

* *Corresponding Author: efagadar@yahoo.com*

alloy manufacturing, wood treatment and oxidative dyeing. It is also an essential element in human nutrition, but exposure to high concentrations leads to irritation of skin and mucous membranes, ulcerations, liver and kidney damage, as well as lung cancer [1]. Chromium adds desirable properties in alloys with iron, nickel, and other metals, such as the hardness and corrosion resistance of chrome steel [2]. It can exist in trivalent and hexavalent states [3] and both forms have been found in industrial and environmental situations [1]. According to Sharma *et al.* [4] more than 80% of tanneries in South Asian and African countries engage in the leather tanning practice where the leather takes 50 to 60% chromium while the rest is discharged as waste. In South Asian tanneries about 50,000 metric tons of chromium salt is discharged into wastewater streams annually, causing environmental pollution.

Therefore, from an environmental point of view, there is a strong need to determine chromium ions using reliable methods. One such method is the potentiometric determination by ion-selective electrodes (ISEs) and it offers several advantages: it doesn't require any specialized equipment or sample pretreatment, it allows for a fast analysis, it's a low cost and nondestructive method, it can detect the target ion in a wide dynamic range and with fairly good selectivity.

A literature survey reveals that several chromium(III) selective ISEs have been reported in the last decades. These sensors were obtained using a variety of compounds as ionophores. In 1980 Masuda *et al.* reported for the first time on chromium(III) by studying the response of a PVC based electrode wire coated with Cr(III) and incorporating Aliquat 336S tetrakis-(thiocyanato)chromate(III) ion pair [5]. The electrode exhibited a Nernstian slope of 58 mV/pCr over the $10^{-5} \div 10^{-2}$ concentration range. In 1996 a PVC membrane based Cr(VI)-selective electrode incorporating nickel tris(1,10-batho-phenanthroline)hydrogen chromate as ionophore was developed. The sensor was used for sequential determination of Cr(VI) and Cr(III) by direct monitoring of Cr(VI) followed by oxidation of Cr(III) and measurement of the total chromium [6]. Another PVC based Cr(III)-selective electrode was reported by Singh *et al.* [7]. The ionophore for this sensor was 3,10-*c-meso*-3,5,7,7,10,12,14,14-octamethyl-1,4,8,11-tetraazacyclotetra-decane diperchlorate and the best results obtained by varying the composition of the membranes indicated that the Cr(III)-selective electrode can exhibit a Nernstian slope of 20 mV/decade of activity over the $1.77 \times 10^{-6} \div 10^{-1}$ M concentration range. Dimethylaminoazobenzene was also incorporated as membrane carrier in a PVC membrane during the development of a Cr(III)-selective electrode [8]. The sensor revealed a Nernstian response with a slope of 19.5 mV/decade over the $1.66 \times 10^{-6} \div 10^{-2}$ M concentration range. The construction of solid-contact Cr(III)-selective film electrodes based on

titanium diselenide and titanium ditelluride intercalated with chromium was also reported [9]. The electrode containing titanium diselenide proved to be a sensor for the determination of Cr(III) over the $5 \times 10^{-5} \div 10^0$ M concentration range. A PVC membrane based ISE using glyoxal bis(2-hydroxyanil) as ionophore was developed and studied as sensor for the determination of Cr(III) cations [10]. The electrode exhibited a Nernstian slope of 19.8 mV/decade over the $3 \times 10^{-6} \div 10^{-2}$ M concentration range with a detection limit of 6.3×10^{-7} M. In 2004 Sil *et al.* [11] tested tetraazacyclotetradecane, tetratosyltetraaza 12C4 and tritosyltriaza 9C3 as ionophores in PVC based coated wire Cr(III)-selective electrodes. The best performance was observed for the electrode incorporating tetratosyltetraaza 12C4 dibutyl phthalate plasticizer and PVC in the 5:60:35 (w/w) ratio. It exhibited a Nernstian slope of 20 mV/decade over the $10^{-7} \div 10^{-1}$ M concentration range with a detection limit of 6×10^{-8} M. The ionophore 2,10-dimethyl-4,12-diphenyl-1,5,9,13-tetraazacyclohexadeca-1,4,9,12-tetraene was incorporated in a polystyrene-based membrane and the selectivity of the resulting electrode was investigated in solutions containing Cr(III) ions. The best sensor had a Nernstian slope of 19.5 mV/decade over the $1.6 \times 10^{-6} \div 10^{-1}$ M concentration range [12]. In another study, a Cr(III)-specific potentiometric sensor was developed using a synthesized chelating resin, namely: Aurin tricarboxylic acid modified silica. A PVC membrane electrode of the modified silica was developed and evaluated as sensor for Cr(III) cations. It exhibited a Nernstian slope of 19 mV/decade of concentration over the $7 \times 10^{-6} \div 10^{-1}$ M concentration range [4]. Ganjali *et al.* used *N*-(1-thien-2-ylethylidene)benzene-1,2-diamine as ionophore in PVC membrane based electrodes that were subsequently tested as sensors for Cr(III) ions. The best sensor obtained after changing the ratio between the membrane components exhibited a Nernstian slope of 19.9 mV/decade over the $10^{-6} \div 10^{-1}$ M concentration range with a detection limit of 7×10^{-7} M [13]. In another report, a Cr(III)-selective electrode based on tri-*o*-thymotide in PVC matrix was manufactured and studied. The best sensor, obtained after changing the ratio between membrane components, showed a Nernstian slope of 20 mV/decade of activity over the $4 \times 10^{-6} \div 10^{-1}$ M concentration range with a detection limit of 2×10^{-7} M [14]. A PVC based Cr(III)-selective electrode incorporating di(benzylamino)glyoxime as ionophore was also studied. The sensor exhibited a Nernstian slope of 20.3 mV/decade over the $10^{-6} \div 10^{-1}$ M concentration range with a detection limit of 2×10^{-7} [15]. Zamani *et al.* [16,3,17,18] reported the development and evaluation of several Cr(III)-selective electrodes based on different compounds as carriers in PVC membranes: 4-amino-3-hydrazino-6-methyl-1,2,4-triazin-5-one; 1,3-diamino-2-hydroxypropane-*N,N,N'*, *N'*-tetraacetic acid; 5-amino-1-phenyl-1H-pyrazole-4-carboxamide and diethyl 2-phthalimidomalonate.

The reports published in the scientific literature outline the variety of membrane carriers used to manufacture Cr(III)-selective potentiometric sensors. However, to the best of our knowledge no Cr(III) ISE using a porphyrin as ionophore was ever developed. Porphyrins are macrocyclic compounds with properties that make them suitable to be used as membrane carriers in PVC membrane based potentiometric sensors [19-21]. Therefore, in the present work, a PVC membrane chromium(III)-selective electrode based on a synthesized A₃B free base porphyrin, namely 5-(4-pyridyl)-10,15,20-tris(phenoxy-phenyl)porphyrin, as ionophore was formulated and evaluated.

The aggregation behavior of the A₃B porphyrin from tetrahydrofuran solution was investigated using Transmission Electron Microscopy (TEM) and Electron Tomography. TEM is a valuable technique for studying materials at the submicron- and nanoscale [22-24], while electron tomography can be used to create 3D reconstructions from 2D projection images [25]. In the latter case, the projections are acquired at different tilt angles of the specimen, they undergo a process of alignment and the resulted tilt-series is used as input for a mathematical algorithm, such as Weighted Back-Projection (WBP) and Simultaneous Iterative Reconstruction Technique (SIRT) [26], leading to a 3D reconstruction.

RESULTS AND DISCUSSION

Investigation of porphyrin samples using electron microscopy.

TEM and STEM images obtained for the porphyrin samples in TEM Bright Field (BF) and STEM High-Angle Annular Dark Field (HAADF) modes are shown in Figures 1 and 2, respectively.

When the porphyrin aggregation behavior was investigated using electron microscopy, different types of structures were evidenced. Most aggregates resembled islands with circular and elliptical shapes (Figures 1a and 2a). Measurements performed on the circular formations revealed their diameters to range from the microscale all the way to the nanoscale (as small as 71.7 nm). These islands bear resemblance to other porphyrin structures reported in the literature as having their macrocycles oriented nearly parallel to the surface of the support [27]. The two types of structures further organize together into collections of aggregates bearing ovoidal shapes.

A few areas from the TEM grids also showed the presence of spherical aggregates (Figures 1b, 2b and 2c). The diameters of these spheres ranged from the submicron to the nanoscale. These structures can coexist with the other types of aggregates (Figures 2b and 2c) and even join with other spheres to form bundles (Figure 2c).

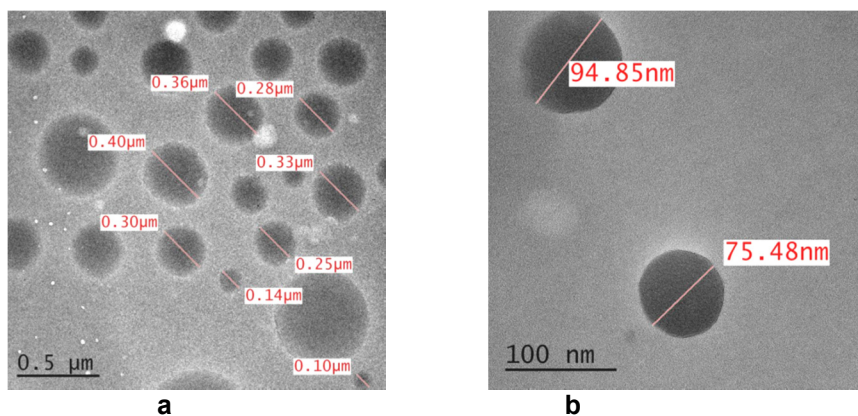


Figure 1. BF TEM images recorded for the porphyrin sample. a) Circular aggregates; b) Spherical aggregates

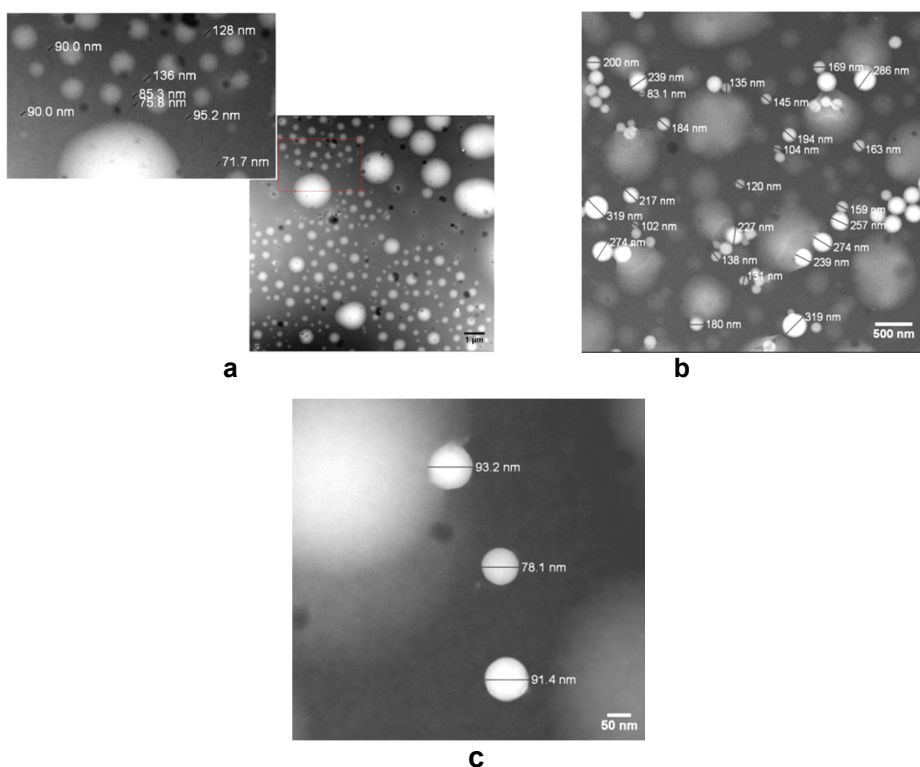


Figure 2. HAADF STEM images recorded for the porphyrin sample. a) Circular and elliptical aggregates. Inset showing enlarged area; b and c) Spherical aggregates with ovoidal aggregates in the background

Electron tomography of porphyrin aggregates. Figure 3a shows the porphyrin aggregate selected for 3D reconstruction using HAADF STEM Tomography and the reconstructed volume. The tilt series was recorded by setting the Max negative and positive tilts at -59° and 63° , respectively and the Low tilt step at 1° . The 3D reconstruction of the aggregate appears as a spheroid and it shows a slight elongation due to missing wedge artefacts generated by the limited spacing in between the pole pieces of the objective lens in the microscope column and by the tilt range selected for the holder during the acquisition. Even holders with tilt ranges higher than $\pm 80^\circ$ can cause an unsampled region in frequency space, referred to as the missing wedge region [28].

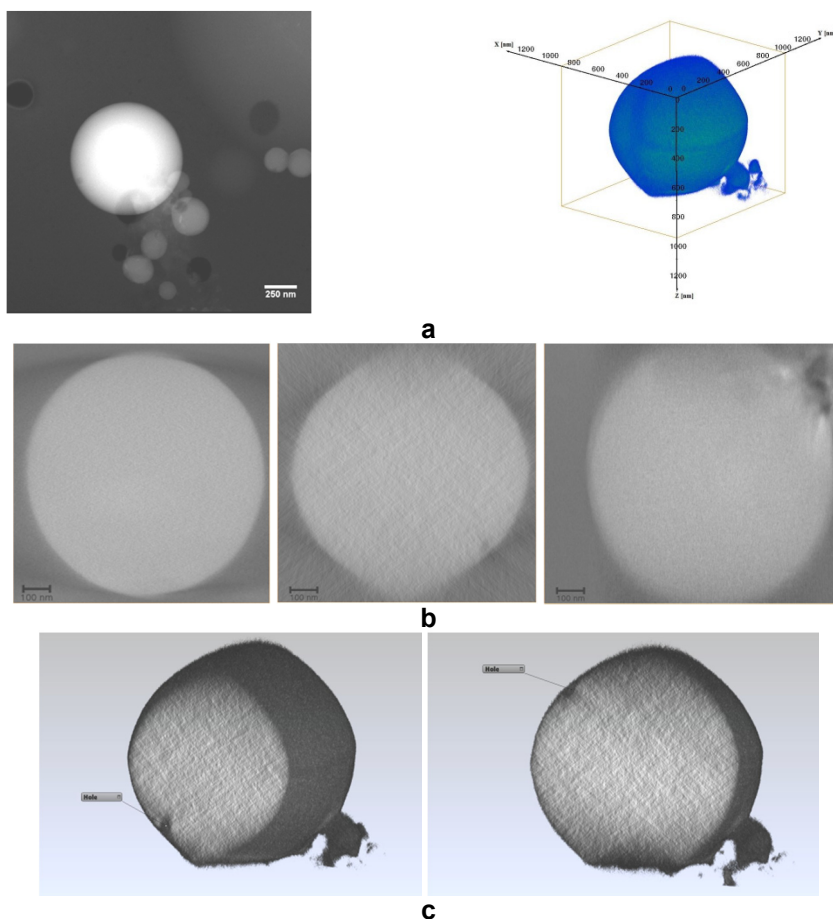


Figure 3. a) STEM image at 0° and the reconstructed volume ($955 \times 1,097 \times 957 \text{ nm}^3$) of porphyrin aggregate; b) XY, XZ and YZ orthoslices; c) sections through the 3D volume

Figure 3b shows the XY, XZ and YZ orthogonal slices half way through the reconstructed volume and together with Figure 3c reveals the interior of the object to be almost entirely filled. The only exceptions are a couple of holes located near the edge of the aggregate, with dimensions in the nanoscale.

Detection studies. 5-(4-pyridyl)-10,15,20-tris(phenoxy-phenyl)porphyrin was used as a ionophore for the obtaining of four potentiometric sensors different due to their composition and plasticizers used, which are presented in Table 1. The sensors were tested for a number of monovalent, divalent and trivalent cations and appear to be chromium-selective, having different working concentration ranges and different slope values (Table 1).

Table 1. Composition of the membranes and response characteristics of the sensors

Sensor	% Composition (w/w) of the membranes					Working concentration range (M)	Slope (mV/decade)
	Ionophore	PVC	NPOE	DOS	DOP		
1	1	33	66			$1 \times 10^{-1} \div 3 \times 10^{-5}$	18.11
2	1	33		66		$1 \times 10^{-2} \div 1 \times 10^{-5}$	21.91
3	1	33			66	$1 \times 10^{-1} \div 1 \times 10^{-6}$	42.88
4	1.4	32.87	65.73			$1 \times 10^{-1} \div 1 \times 10^{-4}$	17.92

According to the results presented in Table 1, a bigger amount of porphyrin does not improve the potentiometric answer of the sensor. In the terms of working concentration range, the best results were obtained for the sensor having dioctylphtalate as plasticizer, but in this case, the slope was double Nernstian, so the sensor is not useful. By meaning of both, working concentration range and slope, the optimum composition was obtained using *o*-nitrophenyloctylether as plasticizer with a slope of 18.11 mV/decade of concentration and working from $1 \times 10^{-1} \div 3 \times 10^{-5}$ M.

The potentiometric answer of the optimum composition sensor to all the cations used is presented in Figure 4 and the potentiometric response toward chromium(III) is presented in Figure 5.

The practical response time of the sensor to reach the equilibrium potential was obtained after successive immersion of the electrode in a series of chromium(III) solutions, each having a 10-fold difference in concentration. The response time was about 10 s as the concentration of chromium (III) varies from 10^{-3} to 10^{-2} M. The detection limit of the electrode having the optimum composition, established at the point of intersection of the extrapolated linear mid-range and final low concentration level segments of the calibration plot was 9×10^{-6} M.

The sensor was used for a period of 50 days, without significant changes in the values of the slope and no change in the working concentration range.

One important characteristic of a potentiometric sensor is the interference of other ions in the potentiometric answer of the main one. The values of the selectivity coefficients, calculated by separate solution method are presented in Table 2.

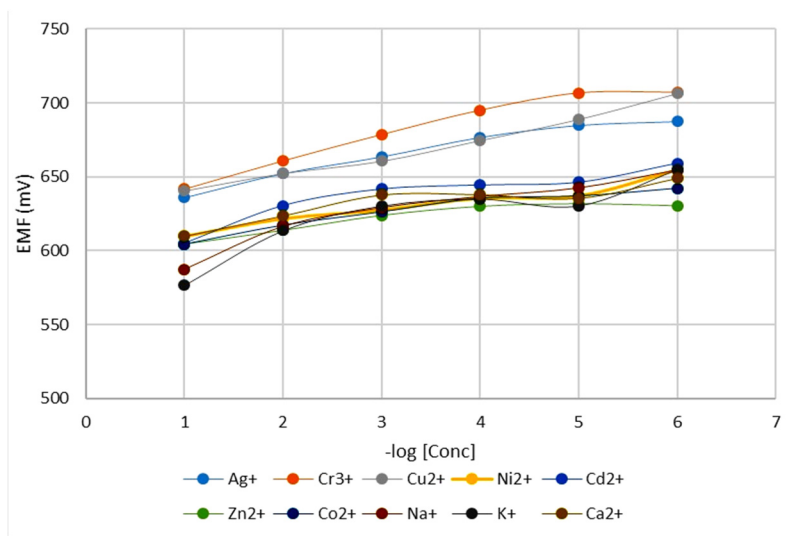


Figure 4. Potentiometric response of the sensor having the optimum composition of the membrane toward different metal ions.

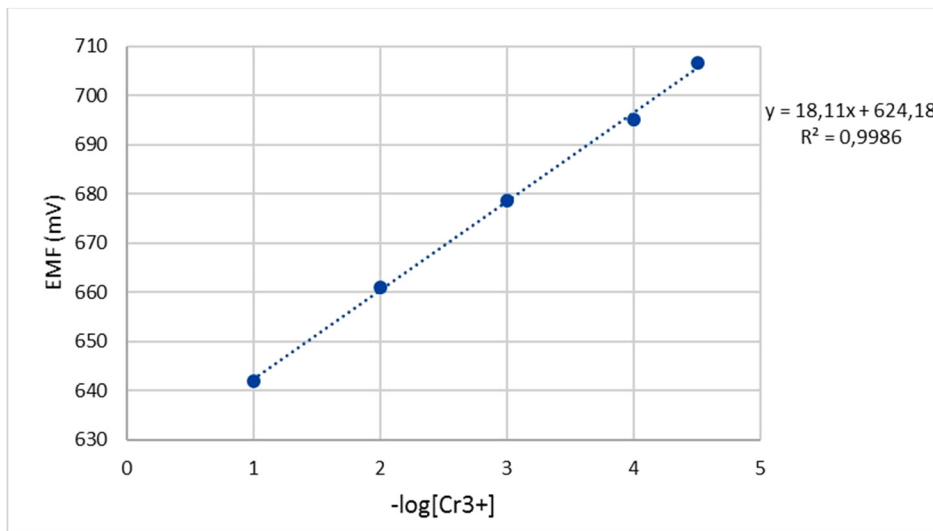


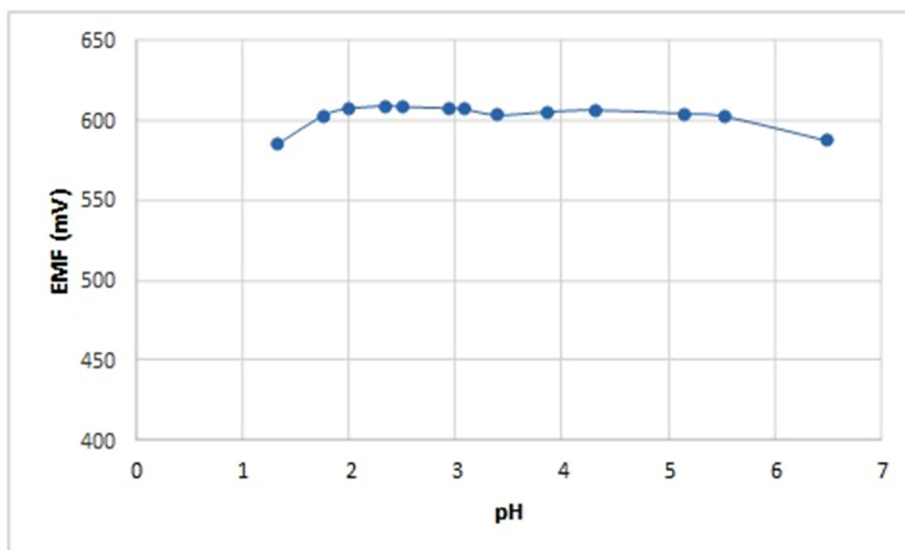
Figure 5. Potentiometric response to chromium of the optimum composition sensor

Table 2. The values of the selectivity coefficients

Interfering cation	$\log K_{Cr,Y}^{pot}$
Ag ⁺	-4.44
Cu ²⁺	-1.44
Ni ²⁺	-2.99
Cd ²⁺	-2.54
Zn ²⁺	-3.40
Co ²⁺	-3.31
Ca ²⁺	-2.90
Na ⁺	-6.26
K ⁺	-6.40

As it results from Table 2, the best composition sensor has very good values of the selectivity coefficients.

The pH function of the sensor was studied by using 10⁻² M chromium (III) solutions, adjusted with HCl and NaOH to pH ranges varying from 1.5 to 11 and the obtained results are presented in Figure 6.

**Figure 6.** Effect of the pH of chromium(III) solution on the potentiometric answer.

As it results, the sensor has a useful pH range from 2.0 to 5.5. Above this pH value the precipitation of chromium(III) hydroxide is taking place.

The analytical usefulness of the sensor was tested in three different synthetic solutions by direct potentiometry with good results, as it can be seen in Table 3.

Table 3. Analytical application of the chromium(III)-sensor in synthetic samples

Sample	Chromium in solution (g/L)	Chromium found by the electrode (g/L)	Recovery (%)
A	0.026	0.024	92.3
B	0.26	0.25	96.2
C	1.30	1.313	101.0

CONCLUSIONS

The aggregation behavior and ion detection properties of 5-(4-pyridyl)-10,15,20-tris(phenoxy-phenyl)porphyrin were investigated.

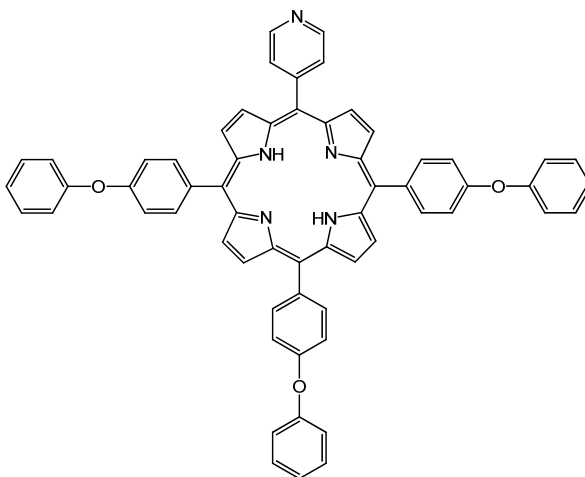
TEM and STEM analyses revealed the formation of circular, elliptical and spherical aggregates. The circular and elliptical structures group together into collections of aggregates bearing ovoidal shapes, while the spherical ones can join together into bunches. Diameter measurements revealed some of those aggregates to be in the nanoscale.

Electron tomography was used to obtain the 3D representation of a porphyrin aggregate. Sections through this structure reveal its interior to be almost entirely filled.

A PVC membrane-based chromium(III)-selective electrode incorporating the porphyrin as ionophore was formulated and evaluated. The sensor exhibited a slope of 18.11 mV/decade over the chromium concentration range of $3 \times 10^{-5} \div 10^{-1}$ M and it may be used in a pH range from 2.0 to 5.5 with very good values of the selectivity coefficients. With the aim of improving these results, future studies will focus on the use of gold nanoparticle-based microchip systems.

EXPERIMENTAL SECTION

Reagents. The synthesis, purification and characterization of the 5-(4-pyridyl)-10,15,20-tris(phenoxy-phenyl)porphyrin (Scheme 1) were previously published [29].



Scheme 1. The structure of 5-(4-pyridyl)-10,15,20-tris(phenoxy-phenyl)porphyrin

TEM samples were prepared using tetrahydrofurane (THF) purchased from Sigma Aldrich. PVC membranes incorporating the porphyrin ionophore were prepared using high molecular weight poly(vinyl)chloride, *o*-nitrophenyloctylether (NPOE), dioctylphthalate (DOP), bis(2-ethylhexyl)sebacate (DOS), sodium tetraphenylborate (NaTPB) and THF purchased from Fluka, Merck and Sigma Aldrich. All reagents (salts, acids and bases) were of analytical reagent grade. Double distilled water was used throughout the studies. The potentiometric response of each sensor was investigated in the $10^{-6} \div 10^{-1}$ M range of different cationic solutions. 0.1 M stock solutions were prepared by dissolving metal nitrates in double distilled water and standardized if necessary.

Preparation of TEM samples and analysis. The A₃B porphyrin was solubilized in THF and a solution of 0.15 mM was obtained. Drops of this solution were applied on TEM copper grids covered with continuous carbon film. The analysis was performed using a Titan G2 80-200 TEM/STEM microscope purchased from FEI Company in The Netherlands. The images were recorded in TEM and STEM modes at 80 and 200 kV acceleration voltages, using the software: Digital Micrograph v. 2.12.1579.0 and TEM Imaging & Analysis v. 4.7. The Electron Tomography tilt-series was obtained in STEM mode with the same microscope. Subsequent processing, including stack alignment and volume reconstruction, was performed using Inspect3D v. 4.0 software, while Avizo v. 9.0 was used for analyzing the 3D dataset.

Electrode membrane preparation and measurements. Three membranes having the composition: 1% ionophore, 33% PVC and 66% plasticizer were made. Sodium tetraphenylborate was used as additive (20 mol% relative to ionophore). Three different plasticizers: DOS, NPOE and DOP were used. One membrane was prepared in the composition 1,4% ionophore, 32,87% PVC and 65,73% plasticizer. Initially, the solvent mediator was mixed together with the porphyrin. Afterwards, the PVC with the appropriate amount of THF were added and mixed until a homogenous solution was obtained. This solution was transferred onto a glass plate and the THF was allowed to evaporate at room temperature until a tough and flexible membrane embedded in a PVC matrix was formed. Round shaped pieces of membranes (having diameters of 8 mm) were cut out and assembled on a Fluka electrode body. The measurements were performed at room temperature using a Hanna Instruments HI223 pH/mV-meter and the following cell setup:

Ag/AgCl/KCl (sat.) / sample solution / ion-selective membrane /
conductive support (Cu) / internal cable

Prior to the potentiometric measurements, all membrane based sensors were conditioned for 24 h by soaking in 10^{-2} M Cr^{3+} . The detection limit of each sensor was established at the intersection point of the extrapolated linear mid-range and final low concentration level segments of the calibration plot. Potentiometric selectivity coefficients were determined according to the separate solution method [30] using equation (1) with a theoretical slope of 19.73 mV/decade of activity for chromium(III) cation and the potential values obtained for 10^{-2} M cation solutions.

$$\log K_{X,Y}^{pot} = \frac{(E_Y - E_X) \cdot z_X \cdot F}{RT \ln 10} + \left(1 - \frac{z_X}{z_Y}\right) \cdot \lg a_X \quad (1)$$

The pH effect on the potentiometric response of the sensor was obtained by immersing the best chromium(III) sensor in solutions of NaOH and HCl in the 1.5 ÷ 11.0 pH range.

Analytical application. The best chromium(III) sensor was used for chromium detection in three synthetic solutions by direct potentiometry.

ACKNOWLEDGMENTS

The authors from the National Institute of Research-Development for Electrochemistry and Condensed Matter Timisoara kindly acknowledge Programme PN contract No. 09-34 02 07

REFERENCES

1. D.E. Kimbrough, Y. Cohen, A.M. Winer, L. Creelman, C.A. Mabuni, *Critical Reviews in Environmental Science and Technology*, **1999**, 29, 1.
2. McGraw-Hill, "Concise Encyclopedia of Science and Technology", 5th edition, McGraw-Hill, New York, **2004**.
3. H.A. Zamani, M.R. Ganjali, M.R. Abedi, P. Norouzi, *Sensor Letters*, **2007**, 5, 1.
4. R.K. Sharma, A. Goel, *Analytica Chimica Acta*, **2005**, 534, 137.
5. Y. Masuda, E. Ishida, K. Hiraga, *Nippon Kagaku Kaishi*, **1980**, 10, 1453.
6. S.S.M. Hassan, M.N. Abbas, G.A.E. Moustafa, *Talanta*, **1996**, 43, 797.
7. A.K. Singh, A. Panwar, S. Kumar, S. Baniwal, *Analyst*, **1999**, 124, 521.
8. A. Abbaspour, A. Izadyar, *Talanta*, **2001**, 53, 1009.
9. T.V. Velikanova, A.N. Titov, M.A. Malkova, *Journal of Analytical Chemistry*, **2001**, 56, 666.
10. M.B. Gholivand, F. Sharifpour, *Talanta*, **2003**, 60, 707.
11. A. Sil, V. S. Ijeri, A.K. Srivastava, *Analytical and Bioanalytical Chemistry*, **2004**, 378, 1666.
12. A.K. Singh, R. Singh, P. Saxena, *Sensors*, **2004**, 4, 187.
13. M.R. Ganjali, P. Norouzi, F. Faridbod, M. Ghorbani, M. Adib, *Analytica Chimica Acta*, **2006**, 569, 35.
14. V.K. Gupta, A.K. Jain, P. Kumar, S. Agarwal, G. Maheshwari, *Sensors and Actuators B*, **2006**, 113, 182.
15. M. Kia, H. Aghaie, M. Arvand, K. Zare, M. Aghaie, *Journal of Physical & Theoretical Chemistry Islamic Azad University of Iran*, **2006**, 3, 105.
16. H.A. Zamani, G. Rajabzadeh, M.R. Ganjali, *Sensors and Actuators B*, **2006**, 119, 41.
17. H.A. Zamani, G. Rajabzadeh, M. Masrornia, A. Dejbord, M.R. Ganjali, N. Seifi, *Desalination*, **2009**, 249, 560.
18. H.A. Zamani, S. Sahebhasagh, *International Journal of Electrochemical Science*, **2013**, 8, 3708.
19. V.K. Gupta, A.K. Jain, Z. Ishtaiwi, H. Lang, G. Maheshwari, *Talanta*, **2007**, 73, 803.
20. D. Vlascici, E. Fagadar-Cosma, I. Popa, V. Chiriac, M. Gil-Agusti, *Sensors*, **2012**, 12, 8193.
21. D. Vlascici, I. Popa, V.A. Chiriac, G. Fagadar-Cosma, H. Popovici, E. Fagadar-Cosma, *Chemistry Central Journal*, **2013**, 7, 111.
22. V. Snitka, M. Rackaitis, R. Rdaite, *Sensors and Actuators B*, **2005**, 109, 159.
23. Q. Liu, Y. Yang, H. Li, R. Zhu, Q. Shao, S. Yang, J. Xu, *Biosensors and Bioelectronics*, **2015**, 64, 147.
24. L. Yang, N. Larouche, R. Chenitz, G. Zhang, M. Lefevre, J.P. Dodelet, *Electrochimica Acta*, **2015**, 159, 184.
25. P.A. Midgley, R. Dunin-Borkowski, *Nature Materials*, **2009**, 8, 271.
26. G.S. Liu, S.D. House, J. Kacher, M. Tanaka, K. Higashida, I. M. Robertson, *Materials Characterization*, **2014**, 87, 1.

27. T. Djuric, T. Ules, S. Gusenleitner, N. Kayunkid, H. Plank, G. Hlawacek, C. Teichert, M. Brinkmann, M. Ramsey, R. Resel, *Physical Chemistry Chemical Physics*, **2012**, *14*, 262.
28. H.H. Mezerji, W.V. den Broek, S. Bals, *Ultramicroscopy*, **2011**, *111*, 330.
29. E. Fagadar-Cosma, G. Fagadar-Cosma, M. Vasile, C. Enache, *Current Organic Chemistry*, **2012**, *16*, 931.
30. Y. Umezawa, P. Buhlmann, K. Umezawa, K. Tohda, *Pure and Applied Chemistry*, **2000**, *72*, 1851.

*Dedicated to Professor Mircea Diudea
on the Occasion of His 65th Anniversary*

GC-MS METHODS FOR AMINO ACIDS DETERMINATION IN DIFFERENT BIOLOGICAL EXTRACTS

MONICA CULEA^{a,*}, ANDREEA MARIA IORDACHE^b, ELENA HORJ^a,
CORNELIA MESAROS^c, RAMONA BLEIZIFFER^a

ABSTRACT. Sensitive, precise and accurate analytical methods for free amino acids determination in biological samples were developed. Purification by ion exchange technique was followed by two steps derivatization method to obtain trifluoroacetyl ester derivatives. GC/MS analysis was performed by using scan or SIM mode. Known amounts of internal standard, the isotopic labelled analogue of glycine, methionine or isoleucine were added to the sample, before extraction, for the quantitative analysis, followed by matrix and regression curves calculation. The methods were validated using amino acid standard samples. Analyses of dairy, corn grain, fish plasma and meat are presented. Also a trace level (picogram) analysis method of blood spots, for diagnosis of inborn errors of metabolism, is described.

Keywords: *amino acids, GC-MS, isotopic dilution, blood*

INTRODUCTION

The paper presents the development of sensitive, simple and precise analytical methods for determination of amino acids in biological samples. The method involves different extraction methods, purification of extracts by

^a Babeş-Bolyai University, Faculty of Physics, 1 Kogălniceanu str., 400084 Cluj, Romania

^b National R&D Institute for Cryogenics and Isotopic Technologies, 4 Uzinei str., 240050 Râmnicu Vâlcea

^c University of Medicine and Pharmacy, 38 Gh. Marinescu St., Târgu Mureş, Romania, Cluj-Napoca, Romania

* Corresponding Author: monica.culea@phys.ubbcluj.ro

ion exchange technique, derivatization in two steps of the amino acids and gas chromatography-mass spectrometry (GC-MS) analysis. The derivatization was applied to obtain trifluoroacetyl ester derivatives [1-14]. Analytical methods by GC/MS was performed in the electron impact (EI) mode [2- 14]. The high sensitivity and specificity of GC-MS technique for volatile and semivolatile compounds was increased by one or two orders of magnitude when selected ion monitoring (SIM) mode was used. SIM-GC/MS is very useful for low level, nanogram and picogram, quantitative work and is usually achieved by isotopic dilution (ID).

Applications for the amino acids determination during some dairy processing, for free amino acid in corn grain, in fish plasma and for diagnosis of metabolic diseases are presented. GC-MS is an indispensable method for diagnosing inborn errors of metabolism. GC-MS quantitative determination method of five amino acids L-phenylalanine (Phe), L-tyrosine (Tyr), L-proline (Pro), L-leucine (Leu) and L-valine (Val) as n-butyl trifluoroacetyl esters was developed, to diagnose PKU, maple syrup urine disease (MSUD) and other aminoacidemias. Phenylketonuria (PKU) is caused by phenylalanine hydroxylase enzyme deficiency.

RESULTS AND DISCUSSION

Method validation

Methionine quantitative method gave a good linearity regression curve, $y=0.0355x + 0.1319$, $r=0.9995$, obtained with standards with known concentration of methionine, in the range $0-100\mu\text{g.mL}^{-1}$ and $20\mu\text{g.mL}^{-1}$ addition of internal standard. The internal standard ^{15}N -methionine, (99 atom % ^{15}N) and methionine required correction by deconvolution and matrix calculation. Fractional isotopic abundances for natural methionine and isotopomer were obtained experimentally [5,17-19] (Table 1).

Table 1. The matrix design (left) and the pseudoinverse matrix (right) used for methionine calculation [5]

methionine	[M]	[M+1]	methionine	[M]	[M+1]
n.a.	0.95	0.05	n.a.	1.05	-0.05
^{15}N	0.01	0.99	^{15}N	-0.01	1.01

Methionine was calculated by matrix and regression curve calculation. Very good correlation between the two methods was obtained, the correlation coefficient of 0.998. Precision and accuracy for methionine, measured for standards of 20 and 30 $\mu\text{g mL}^{-1}$ (n=7), showed very good results, lower than 6% and respectively 11%.

Method validation, using amino acid standards following the extraction and derivatization procedure (n=3), gave precision lower than 20% (R.S.D.), except Tyr and L.O.D. value 1ng of amino acid injected. Good linearity results for amino acids were found (Table 2).

Figure 1 presents the total ion chromatogram (TIC) of a standard solution of amino acids. The components were identified by using NIST library. The amino acids elution order was: alanine (Ala), glycine (Gly), threonine (Thr), serine (Ser), valine (Val), leucine (Leu), isoleucine (Ile), cysteine (Cys), gamma-aminobutyric acid (GABA), proline (Pro), hydroxyproline (Hy-Pro), methionine (Met), aspartic acid (Asp), ornitine (Orn), phenylalanine (Phe), lysine (Lys), glutamic acid (Glu), tyrosine (Tyr), histidine (His), tryptophan (Trp), cysteine (Cis).

Table 2. The regression curve and the coefficient of correlation, r, obtained for the studied amino acids [5]

Amino acid	Regression curve	r
Alanine (Ala)	$y = 1.017x + 12.567$	0.991
Glycine (Gly)	$y = 1.0682x + 13.166$	0.996
Threonine (Thr)	$y = 1.1285x + 15.058$	0.992
Serine (Ser)	$y = 1.1041x + 12.72$	0.995
Leucine (Leu)	$y = 1.0044x + 16.09$	0.995
Isoleucine (Ile)	$y = 0.8507x + 12.37$	0.994
Valine (Val)	$y = 1.5124x - 13.434$	0.980
Cysteine (Cys)	$y = 0.1667x - 6.512$	0.940
Gama-aminobutyric acid(GABA)	$y = 2.207x - 8.8747$	0.980
Proline (Pro)	$y = 1.0331x + 20.49$	0.991
Hydroxyproline (Hy-Pro)	$y = 1.3504x - 4.257$	0.993
Ornitine (Orn)	$y = 0.7645x + 8.7581$	0.997
Phenylalanine (Phe)	$y = 0.6542x + 26.844$	0.978
Tyrosine (Tyr)	$y = 0.3209x - 5.2564$	0.973
Lysine(Lys)	$y = 1.2868x - 10.384$	0.978
Histidine (His)	$y = 0.6916x - 10.196$	0.957

Amino acids in meat

The method was applied for determination of free amino acid in beef, pork and a salami mixture meat, as presented in Table 3.

Significant differences were observed between the amino acid levels measured in different sorts of meat. Essential amino acids were higher in beef and pork meat while flavor amino acids were higher in mixture meat [5].

Table 3. Comparative values of amino acids levels in a mixture, beef and pork meat [5]

	mg/g	mixture	pork	beef
1	Ala ³	1.18	1.29	2.43
2	Gly ³	0.33	0.42	0.67
3	Thr ^{1,3}	0.24	0.29	0.55
4	Ser ³	0.13	0.10	0.18
5	Val ¹	4.89	7.60	6.39
6	Leu ¹	0.5	0.56	1.38
7	Ile ¹	0.44	0.43	1.08
8	Pro	0.57	0.59	1.06
9	Met ¹	0.06	0.01	0.01
10	Asp ¹	0.51	0.48	1.18
11	Phe ^{1,4}	0.32	0.36	0.85
12	Orn ¹	0.11	0.00	0.15
13	Glu ²	15.83	4.95	13.77
14	Lys ¹	1.23	1.09	2.21
15	Tyr ⁴	0.1	0.33	0.20
16	His ¹	4.86	10.01	12.29
	total(mg/g)	31.29	28.51	44.40
	eAA	12.84	20.46	25.23
	fAA	15.83	4.95	13.77
	sAA	1.64	1.81	3.29
	frAA	0.42	0.70	1.05

Note: ¹-essential amino acids (eAA); ²-flavor-related amino acids (fAA); ³-sacharinity-related AA(sAA); ⁴-fragrant-related amino acids (frAA)

Cheese amino acids

Application for study the free amino acids (FAA) in cheese at various stages of ripening, by using two different starter enzymes, a lipolytic (L) one and a proteolytic (P) one, in comparison with a control (M) cheese was performed. The main amino acids identified in all samples were: Ala, Gly, Thr, Ser, Val, Leu, Ile, Pro, Asp, Phe, Orn, Glu, Lys, Tyr. Proteolytic cheese showed higher quantity of Ala, Thr, Ser, Pro, (sweet amino acids) and much higher Tyr (bitter

taste) than in control sample. These amino acids had no cheese taste, but they can contribute to the complex taste of maturated cheese. The use of different starter bacteria caused differences in the quality of cheese and the starter culture had contributed to proteolysis at different degrees [7].

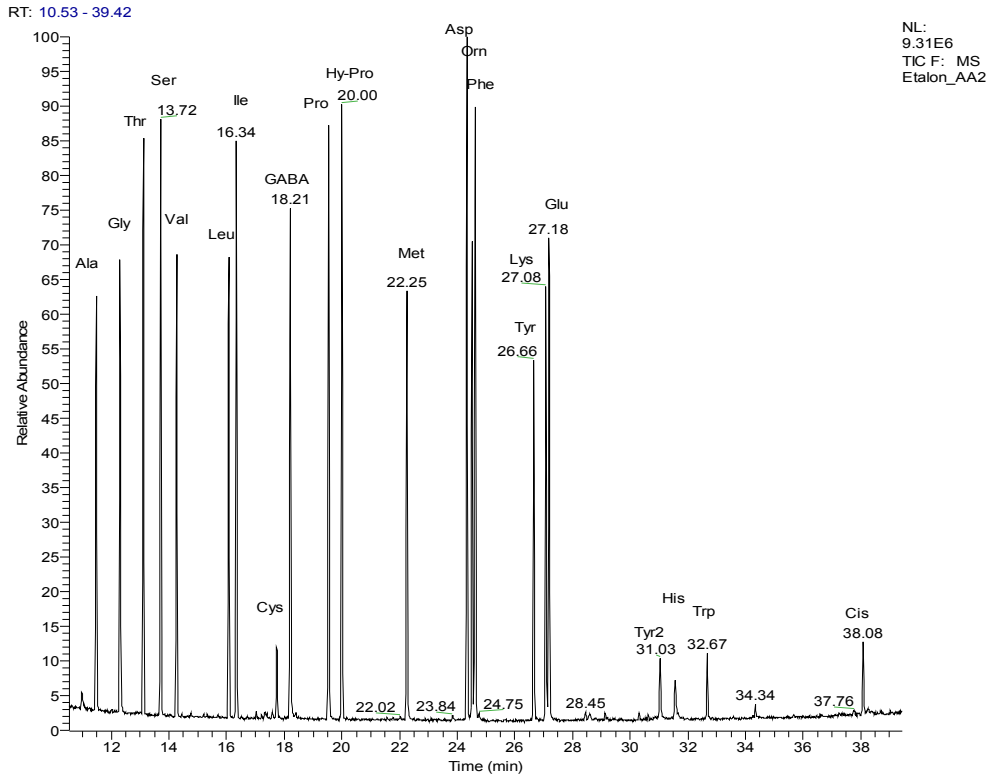


Figure 1. GC-MS amino acids standard separation and identification [5]

Yoghurt amino acids

The method was applied for the study of different steps in the technical processes of preparation of some dairy products, after protein hydrolysis (yoghurt (I), “sana” (S), butter milk (LB)). Significant differences among the three steps tested in the concentration of the amino acids were found. In the fermentation processes amino acids from proteins were changed, especially Phe, Tyr, Pro, Leu [8].

Salami amino acids

The salami samples of different days of storage (dry fermentation) were purchased from a local producer as meat mixture after reddening (r, day 0), salami (day 0), salami (day 14), salami (day 30), salami (day 45) and preserved at - 20°C, until analysis. Two salami samples, extracted twice, were used for a day of study. Batches containing 0.3% glucono delta-lactone (GDL) and 0.05% sodium ascorbate (ASC), and batches containing only 0.1 % sodium ascorbate were manufactured. The content of FAA (Figure 2) was measured at different time intervals over 45 days of storage.

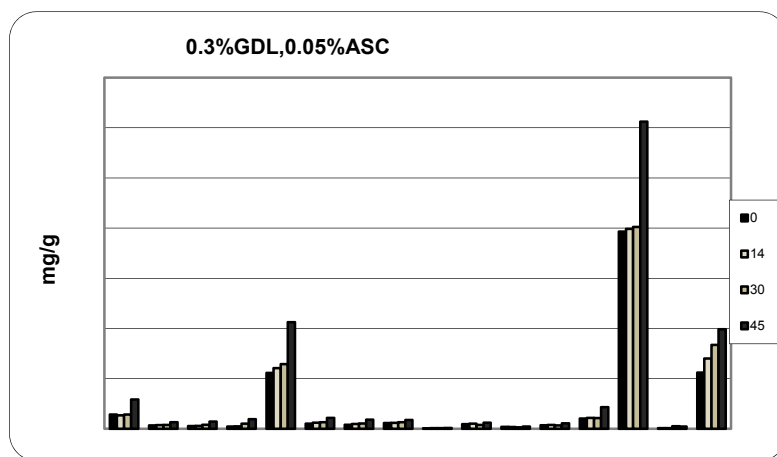


Figure 2. Comparison of FAA in a salami variety

The amino acids increased significantly with storage especially in GDL variety. A higher increase with fermentation time was observed especially for glutamic acid (flavor-related amino acid), serine, tyrosine (fragrant-related amino acid), isoleucine, threonine, lysine, alanine and glycine. The total amount of free amino acids may be influenced by the pH decrease of salami containing GDL and by fermentation time.

The method is suitable (e.g. RSD was lower than 20% for precision and lower than 23% for accuracy, LOD lower than 1ng and linearity ($r > 0.98$),) for different purposes as: food quality control, food processing control, animals' diet control and metabolic studies [12,16].

Corn grain amino acids

The method was used for the determination of free amino acids from corn inbred lines flour (25 samples have been compared).

Table 4. FAA values, in $\mu\text{g}\cdot\text{g}^{-1}$, in corn seed nucleus and inbred lines*

1.1	2.1	3.1	4.1	5.1
1293.39±15.22	713.44±7.13	2404.68±31.49	5798.44±44.89	933.87±9.79
1.2	2.2	3.2	4.2	5.2
1315.09±7.76	2075.06±6.14	4785.51±20.39	1556.46±20.39	977.90±6.28
1.3	2.3	3.3	4.3	5.3
831.67±4.36	1898.42±6.82	4443.38±80.20	1551.73±14.72	772.43±7.86
1.4	2.4	3.4	4.4	5.4
1858.99±19.14	3911.90±47.82	4290.14±39.53	2123.28±26.84	1685.26±12.66
1.5	2.5	3.5	4.5	5.5
1285.69±7.71	1226.75±8.00	4284.74±39.98	1317.92±8.63	924.76±3.28

* FAA: total free amino acids; the corn inbred lines were noted: 1.2, 1.3, 1.4, 1.5; and similar 2.2- 2.5; 3.2- 3.5; 4.2- 4.5; 5.2- 5.5. Seed nucleus: 1.1, 2.1, 3.1, 4.1, 5.1.

Among the free amino acids determined, the highest were aspartic acid, proline, gamma-aminobutyric acid, lysine, alanine, glutamic acid and histidine. The study established the variation of the free amino acids within the different inbred lines. The results suggest that FAA determination in inbred lines studied (Table 4) could help the selection of genotype and may improve its functional and nutritional qualities [13].

Fish amino acids

We have determined seasonal differences of blood plasma amino acids concentration of rainbow trout (*Oncorhynchus mykiss*). The essential amino acids determined were: threonine, valine, leucine, isoleucine, methionine, phenylalanine, tyrosine and lysine. Nonessential amino acids determined was: alanine, glycine, serine, proline, hydroxiprolin, ornithine, aspartic acid and glutamic acid. For most amino acids, their concentration decreased in summer, compared with those recorded in the spring season[14].

Also the free amino acids in two carp varieties (Galitian and Lausitz) occurred at a dietary Se-methionine level of 0.05 mg/kg was compared with control carp plasma. A significant increase of about 3.8 times of methionine was observed in Galitian carp experimental group in comparison with control. Galitian carp variety showed almost two times higher values for total free amino acids in experimental fish than control, and also higher values were obtained in experimental Lausitz variety in comparison with control. The methods are very useful for nutrient and diet control [15].

Diagnosis of inborn errors of metabolism

Isotopic dilution GC-MS rapid method developed for the early diagnosing of inborn error of metabolism of some neonatal diseases was used for the screening of phenylketonuria or maple syrup urine disease in newborns. ID-GC-MS is a fast and reliable method which has the advantages of using small volumes of neonatal blood spots. The blood samples were derivatized as trifluoroacetylbutyl esters and analyzed by gas chromatography coupled with mass spectrometry in the selected ion monitoring (SIM) mode. Regression curves for standard amino acids were used for quantitative determination of valine, leucine, proline, phenylalanine and tyrosine using ^{15}N -isoleucine as internal standard.

Good regression curves were obtained by injecting standard solutions containing amino acids in concentration of 1, 5, 10, 20, 30 and 40 $\mu\text{g}/\text{ml}$ with 25 μg of ^{15}N -Ile, added to each standard solution and per ml of blood sample. The regression curves obtained were very good, with coefficient of correlation over 0.998 for Val, Leu, Pro, Phe except Tyr ($r=0.984$). Precision studied for standard of 30 and 40 $\mu\text{g}/\text{ml}$ gave R.S.D. values between 9-12.9% for 30 $\mu\text{g}/\text{ml}$ and 6.7-18.6 % for 40 $\mu\text{g}/\text{ml}$. Accuracy values were lower than 5.5 for 40 $\mu\text{g}/\text{ml}$ ($n=4$). The limit of detection (L.O.D.) was lower than 0.1 $\mu\text{g}/\text{ml}$.

Significant differences between PKU subjects and control was observed. In control subjects ($n=53$) the ratio of Phe/Tyr was less than 1 while the PKU positive blood ($n=20$) gave more than 2. MSUD cases was not found in our study [3,4,9-11].

CONCLUSIONS

The methods developed are useful for the analysis of nutrients from different biological media. Good validation parameters, linearity, correlation coefficients, precision, accuracy, were obtained in the range of interest.

The use of isotopic labeled internal standard increased precision and avoids the overlapping of analytes with different contaminants.

Important differences in the free amino acids among varieties of meat and dairy products were observed. The free amino acids determined during the ripening period could characterise the quality of cheese. FAA determination in corn inbred lines studied could help the selection of genotype and may improve its nutritional qualities. The methods are useful for nutrient and diet control.

The minim invasive method was used for amino acids quantitation from dried blood spots. Diagnosis in the first 3 months of newborn saves lives (MSUD) or normal intellectual development (PKU) and also the treatment and diet could be controlled for this patients.

EXPERIMENTAL SECTION

A gas chromatograph coupled with a quadrupole mass spectrometer Trace DSQ (Thermo Finnigan, Proanalysis, Bucharest, Romania) was equipped with a capillary column using an adequate temperature program (Table 5).

Table 5. Amino acid analytical conditions

Capillary column	Temperature program	MS conditions:
Rtx-5MS had 30 m x 0.25 mm I.D., film thickness of 0.25 μ m; split mode (10:1)	50°C for 1 min, 6°C/min to 100°C, 4°C/min to 200°C, 20°C/min to 300°C, 300°C for 3 min. Carrier gas: He, 6.0; 1ml/min.	Mode: EI; electron energy: 70 eV; emission current: 100 μ A. Mass range: 50-500 a.m.u. Transfer line: 250°C, injector: 200°C; ion source: 250°C.

The amino acids extraction and derivatization steps were followed as presented in Table 6.

Table 6. Extraction procedure of amino acids from sample

Amino acids extraction [1]	Amino acids derivatization	
cation exchange resin Dowex 50W-X8 100mesh, 40x2mm column; Activation of resin; sample+IS; Elution: 2ml 3M NH ₄ OH; Evaporate	1. esterification:100 μ l butanol/HCl 3M for 1h, 110°C;	2. acetylation:100 μ l TFAA, 80°C, 20 min; dry at 4°C; 1ml ethyl acetate

One microliter of each sample was injected into the GC/MS by using a TriPlus autosampler (Proanalysis, Bucharest, Romania).

The blood spot samples were separated on the same capillary column in a temperature gradient of 14 min. and in the selected ion monitoring (SIM) mode. The following important ions from the mass spectra of Phe, Pro, Val, Leu and Tyr were used: m/z 91, 148, 204 for Phe, m/z 166 for Pro, m/z 168 for Val, m/z 182 Leu, m/z 203, 260, 316 for Tyr and m/z 183 for the internal standard. This minimum invasive method was based on profiling and quantitative determination of some amino acids in blood samples of 20 μ l by using filter paper blood specimens and the GC-MS technique [4].

REFERENCES

1. D. Roach, C.W. Gehrke, *J. Chromatogr. A*, **1969**, *44*, 269.
2. T. Hodisan, M. Culea, C. Cimpoiu, A. Cot, *J. Pharm. Biomed. Anal.*, **1998**, *18*, 319.
3. C. Deng, C. Sang, Y. Hu, X. Zhang, *J. Chromatogr. B*, **2002**, *775*, 115.
4. C. Deng, Y. Deng, *J. Chromatogr. B*, **2003**, *792* (2), 261.
5. E. Horj, A. Iordache, M. Culea, *Studia UBB. Physica*, **2010**, *LV*, 2, 61.
6. T. Hodisan, M. Culea, C. Cimpoiu, A. Cot, *J. Pharm. Biomed. Anal.*, **1998**, *18*, 319.
7. A. Iordache, M. Culea, M. Jimborean, A. Pintea, M. Chiriac, *JEPE*, **2009**, *10*, 149.
8. M. Iosin, M. Culea, A. Rotar, O. Cozar, L. Petrusca, *An. Stiint. Univ. Al.I. Cuza Iasi*, **2005**, 101.
9. M. Culea, A. Iordache, C. Mesaros, *Chem. Listy*, **2008**, *102*, s936.
10. M. Culea, M. Chiriac, E. Culea, C. Lehene, A. Iordache, *Rom. J. Biophys.*, **2007**, *17*, 169.
11. M. Culea, E. Horj, A. Iordache, D. Florescu, *Chem. Listy*, **2011**, *105*, s1047.
12. L. Bara, C. Pop, E. Horj, A. Iordache, C. Laslo, M. Culea, *Bulletin UASVM Agriculture*, **2010**, *67*(2), 162.
13. M. Culea, S. Scrob, S. Suvar, P. Podea, I. Has, S. Muste, *Anal Lett.*, **2015**, *48*, 37.
14. D. Cocan, E. Horj, M. Culea, V. Miresan, A. Pintea, *Bulletin UASVM Agriculture*, **2010**, *67*, 132.
15. A. Iordache, M. Culea, E. Horj, O. Cozar, *Rom. J. Phys.*, **2011**, *56*, 7-8, 963.
16. S.K. Jin, I.S. Kim, H.J. Jung, D.H. Kim, Y.J. Choi, S.J. Hur, *Poultry Sci.*, **2007**, *86*, 2676–2684.
17. J.I. Brauman, "Spectral Analysis: Methods and Techniques", Ed. by J.A. Blackburn, Marcel Dekker, New York, **1970**.
18. K. Nakamura, D.L. Hachey, C.S. Kreek, C.S. Irving, P.D. Klein, *J. Pharm. Sci.*, **1982**, *71*, 40.
19. M. Culea, D. Hachey, *Rapid Commun. Mass Spectrom.*, **1995**, *9*, 655.

*Dedicated to Professor Mircea Diudea
on the Occasion of His 65th Anniversary*

CORRELATION STUDY AMONG BOILING TEMPERATURE AND HEAT OF VAPORIZATION

**MIHAELA L. UNGUREȘAN^a, LORENA L. PRUTEANU^b,
LORENTZ JÄNTSCHI^{a,b,*}, SORANA D. BOLBOACĂ^c**

ABSTRACT. In this paper, a preliminary result from a property-property analysis on a series of chemical compounds in regards of quantitative relationship between two properties is communicated. The study was conducted on a series of 190 inorganic chemical compounds for which both properties taken into study are known. The correlation analysis revealed that is a strong relationship between the boiling point and the heat of vaporization at the boiling temperature, having the variance in the paired series of data explained over 90%.

Keywords: *Property-property relationship, Distribution analysis, Regression analysis*

INTRODUCTION

Regression analysis and error distribution

Even the first studies about binomial expressions were made by Euclid [1], the mathematical basis of the binomial distribution study was put by Jacob Bernoulli [1654-1705]. The Bernoulli's studies, with significance for the theory of probabilities [2], were published 8 years later after his death by his nephew,

^a *Technical University of Cluj-Napoca, Faculty of Material Sciences, 103-105 Muncii Blvd., RO-400641, Cluj-Napoca, Romania*

^b *Babeș-Bolyai University, Faculty of Chemistry and Chemical Engineering, 11 Arany Janos str., RO-400028, Cluj-Napoca, Romania*

^c *Iuliu Hațieganu University of Medicine and Pharmacy, Department of Medical Informatics and Biostatistics, 6 Louis Pasteur str., RO-400349, Cluj-Napoca, Romania*

* *Corresponding author: lorentz.jantschi@gmail.com*

Nicolaus Bernoulli. In *Doctrinam de Permutationibus & Combinationibus* section of this fundamental work he demonstrated the Newton binomial series expansion. Later, Abraham De Moivre [1667-1754] put the basis of approximated calculus for binomial distribution approximation using the normal distribution [3]. Later, Johann Carl Friedrich Gauss [1777-1855] put the basis of mathematical statistics [4].

The simplest association model is linear. The model assumes that there exists a relationship between two paired characteristics expressed by a straight line. The expression of this association is given by the implicit equation of a straight line: $aX + bY + c = 0$. If $a = 0$ then the equation of the line reduces to $bY + c = 0$. Next, if $c \neq 0$ results in a relationship which defines the mean of Y associated characteristic but no relationship with X . Similarly if $b = 0$ then the equation of line reduces to $aX + c = 0$ and if further $c \neq 0$ leads to a relationship which defines the mean of X associated characteristic but no relationship with Y . The remained case, if $c = 0$ defines a degenerated linear model in which there is no intercept between the characteristics X and Y .

Which expression of the linear equation should be used is a matter of experimental error treatment. Going further, if a linear model defines the relationship between the X and Y characteristics, then if we take samples $(x_i, y_i)_{1 \leq i \leq n}$ of these two (X and Y) characteristics, a relationship in terms of experimental errors would be defined.

The information related to the error distribution is very important. A common assumption is to expect an error ε_i (or η_i) to occur in an equal probability as its pair error $-\varepsilon_i$ (or $-\eta_i$), and accordingly the distribution of the experimental errors is symmetrical.

An experiment design that gives different weights to the errors led to a weighted regression. Usually the weights are function of the observable and/or expectance ($v_i = f(x_i, \hat{x}_i)$, $w_i = g(y_i, \hat{y}_i)$). Weighted errors involve data normalization, e.g. normalization of errors distribution or at least having a known error distribution; knowledge on error distribution is essential in the estimation of population parameters.

Structure-activity relationships

Building of the first (big) family of molecular descriptors was described in [5] and, about ten years after, the usage potential of this sort of methodology investigating structure-activity relationships was significantly increased by joining with genetic algorithms [6].

Relationships commonly called property-property relationships have been developed due to the intrinsic relations between some thermodynamic functions (see for details [7]).

Non-linear relationships are possible but are less desirable, being less efficient in prediction than the linear ones, also more difficult to interpret, even in some cases may over perform the linear models (see [8]).

Physico-chemical properties such as the heat of vaporization are of technical interest for designing devices that work at the phase transition between gaseous and liquid state [9-11].

Data on the measured physico-chemical parameters are available for relatively few chemical compounds (a representative source is given in [12]); this is one of the legitimate reasons for developing relationships among properties.

In this paper, a computational study was drawn for a series of 190 inorganic chemical compounds to relate the molar enthalpy (heat) of vaporization ($\Delta_{\text{vap}}H$) at the normal boiling point (t_b) referred to a pressure of 101.325 kPa (760 mmHg) with their boiling point. Our aim was to find if variable transformation leading to normal error distribution would provide significantly simple regression models, able to links the boiling temperature with the heat of vaporization.

RESULTS AND DISCUSSION

The error distribution analysis of the boiling temperature revealed that the normal distribution is rejected at all conventional levels of significance over 20% risk to be in error (Table 1). The analysis of lognormal distribution, has found that the location parameter determined by the maximum likelihood estimation is -309.79. This value is near to -273.15 and suggests that a transformation of the scale from Celsius degrees to Kelvin degrees will lead to normalization of data. Indeed, after this transformation ($T=t^{\circ}\text{C}+273.15$) the data series became lognormal distributed, and the hypothesis of the distribution cannot be rejected at a significance level of 5%. Thus, the probability associated with the Anderson-Darling A-D statistic is 9.31% and the probability associated with the Kolmogorov-Smirnov K-S statistic is 13.34%. Therefore, the data were further transformed by the logarithmic function and analysed again. The probability associated with Anderson-Darling statistic become 9.07%, the probability associated with Kolmogorov-Smirnov statistic become 12.81% (see Figure 1 below) while the estimations of population statistics were $\mu=6.0873$ and $\sigma=0.90038$.

Table 1. H_0 (Data follow normal distribution): Results for different significance levels α

Reject H_0 ?	Boiling temperature				Heat of vaporization			
	$\alpha=0.2$	$\alpha=0.1$	$\alpha=0.05$	$\alpha=0.01$	$\alpha=0.2$	$\alpha=0.1$	$\alpha=0.05$	$\alpha=0.01$
K-S	Yes	Yes	Yes	Yes	Yes	Yes	Yes	Yes
A-D	Yes	Yes	Yes	Yes	Yes	Yes	Yes	Yes
CS	Yes	Yes	Yes	Yes	Yes	Yes	Yes	Yes

K-S = Kolmogorov-Smirnov; A-D = Anderson-Darling; CS = Chi-square

The distribution analysis of the heat of vaporization also revealed that the normal distribution is rejected at all conventional levels of significance over 20% risk of error (Table 1). Looking for lognormal distribution, the three parameters of lognormal distribution (with the location parameter determined by the maximum likelihood estimation method) were found as being -3.3553. This value was used to transform the observed data. After this transformation ($\Delta H_1 = \Delta H(t_b) + 3.3553$) the data series became lognormal distributed, when the hypothesis of the distribution cannot be rejected at 5% risk of error. Thus, the probability associated with the Anderson-Darling statistic is 23.53%, and the probability associated with the Kolmogorov-Smirnov statistic is 16.34%. Therefore, the data were further transformed by the logarithmic function and analyzed again. The probability associated with the Anderson-Darling statistic became 23.95%, the probability associated with the Kolmogorov-Smirnov statistic became 16.31% (see Figure 2), and the estimations of the population statistics were $\mu = 3.8313$ and $\sigma = 0.84324$.

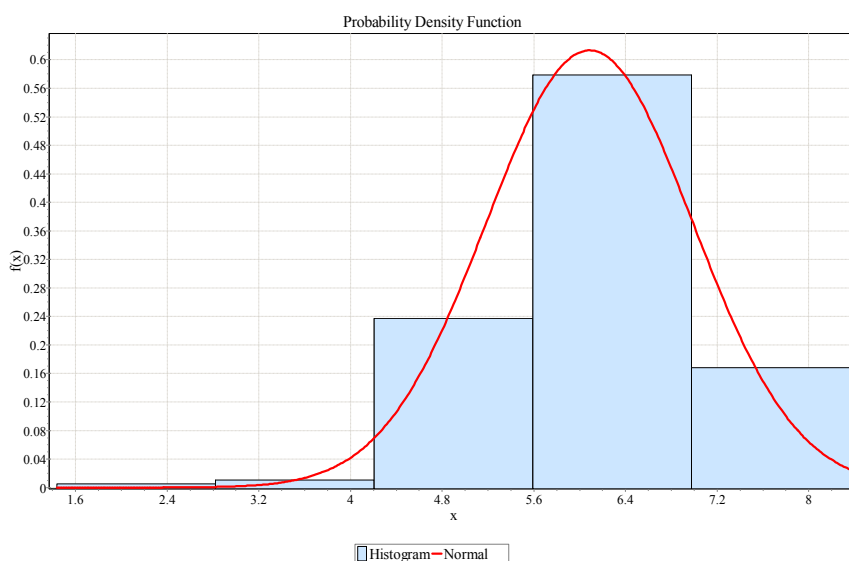


Figure 1. Distribution fit for the transformed boiling temperatures as $\ln(\text{b.p.}(K))$

Regression analysis was applied on the original data set and normalized data set and the derived equations were analysed to see if significant differences between models exist. Both the investigated models (created using original and transformed data) proved to be significant (Table 2), with a higher contribution to the intercept for the model obtained on original data and of the heat of vaporization on the model with transformed data.

CORRELATION STUDY AMONG BOILING TEMPERATURE AND HEAT OF VAPORIZATION

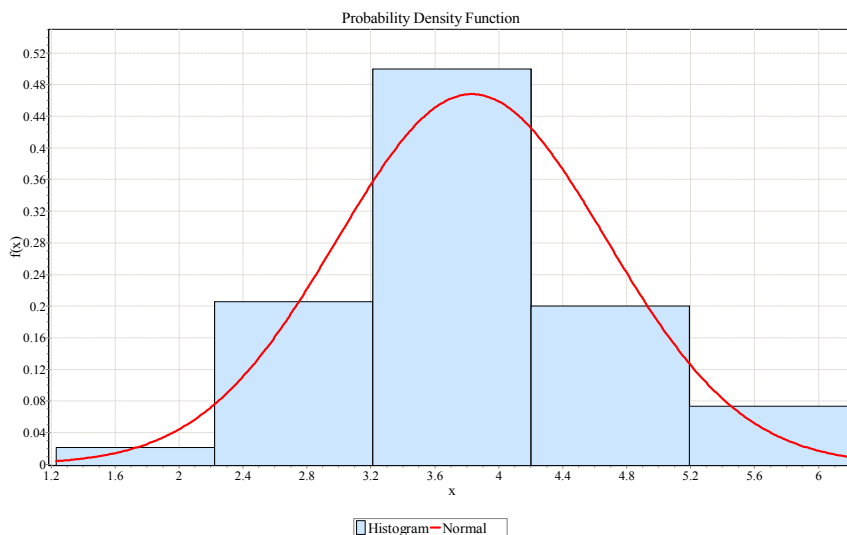


Figure 2. Distribution fit for the transformed heat of vaporization as $\ln(\Delta_{\text{vap}}H + 3.3553 \text{ kJ/mol})$

Table 2. Characteristics of obtained models

Model	Original data	Normalized data
R^2	0.9574	0.9259
R^2_{adj}	0.9572	0.9255
RMSE	14.16	0.23
MAE	38.86	0.63
MAPE	7.77	0.18
F (p)	4224 (<0.0001)	2349 (<0.0001)
Int [95%CI]	24.80 [22.46; 27.14]	-1.65 [-1.88; -1.43]
Coeff [95%CI]	0.11 [0.10; 0.11]	0.90 [0.86; 0.94]

R^2 = determination coefficient; R^2_{adj} = adjusted determination coefficient;
 RMSE = root mean square error; MAE = mean absolute error;
 F = Fisher's statistic; p = probability to be in error;
 Int = intercept; 95%CI = 95% confidence interval;
 Coeff = the value of coefficient associated to heat of vaporization

Our findings showed that the model created on original data ($R=0.9785$) had a significantly ($p=0.0059$) higher correlation coefficient compared with the model obtained on transformed data ($R=0.9622$). However, the values of the root mean square error (RMSE) and the mean absolute error (MAE) showed that the model obtained on transformed data is more reliable (small values of both RMSE and MAE).

The leave-one-out analysis was carried out to assess the internal validity of the models; the main characteristics of the models are given in Table 3.

Table 3. Characteristics of models in the leave-one-out analysis

Model	Q ²	RMSE	MAE	MAPE	F _{loo} (p _{loo})
Original data	0.9551	14.47	7.69	0.40	3995 (p<0.0001)
Transformed data	0.9182	0.24	0.15	0.05	2104 (p<0.0001)

Q² = determination coefficient in leave-one-out (loo) analysis

RMSE = root mean square error; MAE = mean absolute error;

MAPE = mean absolute percentage error

The root mean square error RMSE, mean absolute error MAE and mean absolute percent error MAPE are smaller in the model with transformed data (Table 3), thus supporting the validity and reliability of this procedure, even the determination coefficient is smaller compared to that obtained on original data.

A training and test analysis was conducted to assess the validity of the identified model, with 126 compounds in the training set and 64 in the test set. The equation for model with original data is given in Eq(3)

$$\hat{Y} = 25.218 + 0.107 * X \quad \text{Eq(3)}$$

$$R^2_{Tr} = 0.9741; n = 126$$

$$R^2_{Ts} = 0.9334; n = 64$$

where \hat{Y} approximates the heat of formation at boiling point temperature ($\hat{Y} \sim \Delta H(t_b)$) and X is the boiling point temperature ($X = t_b$, in Celsius degrees).

The equation for model with transformed data is given in Eq(4):

$$\hat{Y} = -2.145 + 0.982 * X \quad \text{Eq(4)}$$

$$R^2_{Tr} = 0.9633; n = 126$$

$$R^2_{Ts} = 0.8888; n = 64$$

where \hat{Y} approximates the logarithm of the heat of formation at boiling point temperature ($\hat{Y} \sim \ln(\Delta H(T_b) + 3.3553)$) and X is the logarithm of the boiling point temperature ($X = \ln(T_b)$, in Kelvin).

Graphical representation of performances in the training and test analysis is shown in Figure 3 for original data while in Figure 4 for transformed data.

CORRELATION STUDY AMONG BOILING TEMPERATURE AND HEAT OF VAPORIZATION

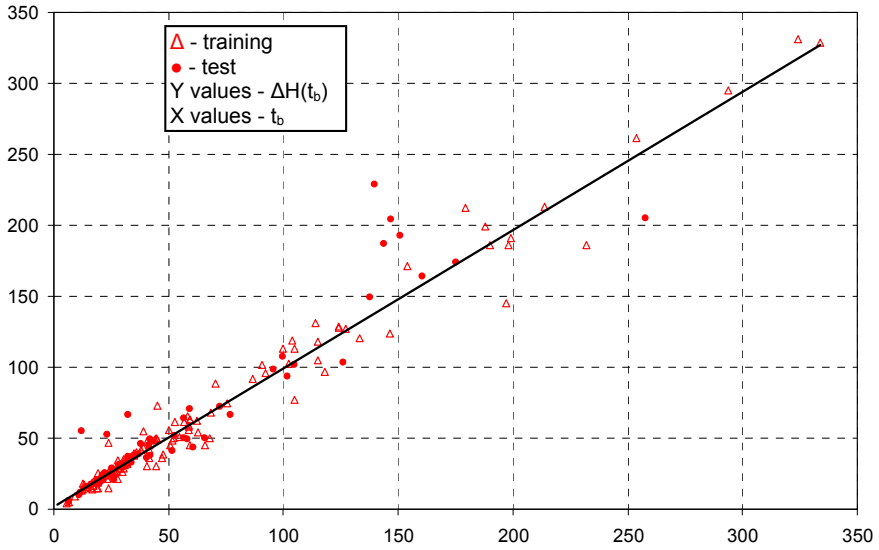


Figure 3. Training vs. test analysis: original data

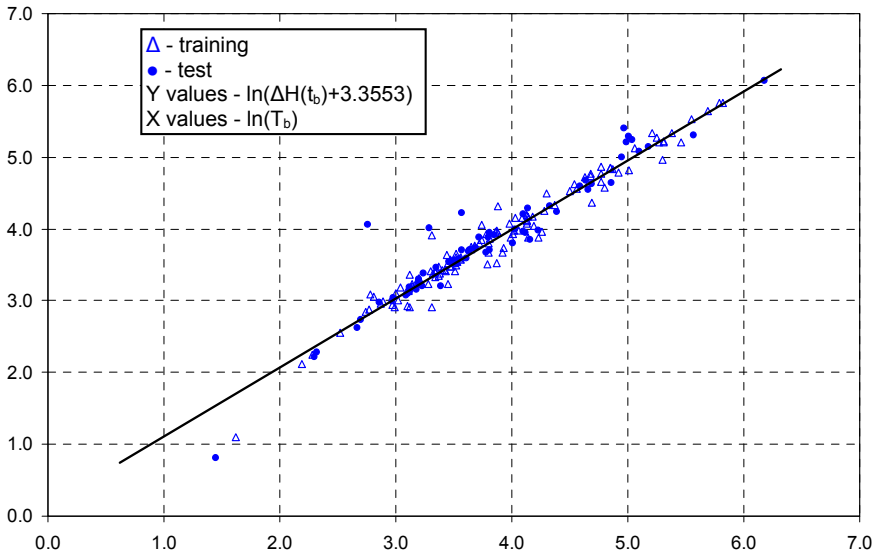


Figure 4. Training vs test analysis: transformed data

The training vs test analysis shows an apparently better agreement in both training and test sets (see Eq3 and Eq4) when the untransformed data are used. This should not lead to the conclusion that is better to be used the untransformed data, because for the untransformed data the assumptions of the linear regression are not accomplished. Also, the measurement units for the transformed data are not the same with the measurement units for original data. For instance, turning back to the original measurement units (by raising to the exponent of Y and \hat{Y} values) the determination in the test set (between Y and \hat{Y}) for transformed data becomes 0.9321, a much closer value to that given in Eq3. This case - of having lower agreement when the data are properly transformed to accomplish the requirements of the regression analysis - is much more important than it seems – because, usually, the agreements are reported without checking the accomplishment of the requirements. The explanation of this fact relies on the intrinsic procedure of obtaining the coefficients, namely on the minimization of the sum of squares between observed and estimated values. If there exists some points at ends of the interval of values with large departures (differences between observed and estimated values, see for instance [12]) then the minimization of the sum of squares has the tendency to follow it, ignoring and penalizing other departures, and the same idea applies for the correlation coefficient.

CONCLUSIONS

As can be concluded from this analysis, it seems that these two properties (boiling point and heat of vaporization at the boiling point) have a large part of their variance explained by one to each other and are suitable for a more detailed study meant to increase the explanatory power.

Conducting of the analysis without checking the assumptions of the analysis may lead to incorrect results, usually tending to produce more explanatory power than it is.

MATERIALS AND METHODS

Data were taken from a recent edition of the serial containing reference physical and chemical data [13] and refers to both the boiling point and the heat of vaporization, the primary study reporting these values being [14,15].

The chemical compounds included in the study, listed in the ascending order of their boiling point, are: helium (He), hydrogen (H_2), Neon (Ne), Nitrogen (N_2), Fluorine (F_2), Argon (Ar), Oxygen (O_2), Krypton (Kr), Fluorine monoxide (F_2O),

Nitrogen trifluoride (NF₃), Silane (SiH₄), Xenon (Xe), Phosphorus(III) fluoride (PF₃), Chlorine fluoride (ClF), Boron trifluoride (BF₃), Fluorosilane (SiFH₃), Trifluorosilane (SiF₃H), Diborane (B₂H₆), Germane (GeH₄), Phosphine (PH₃), Hydrogen chloride (HCl), Phosphorus(V) fluoride (PF₅), Difluorosilane (SiF₂H₂), Tetrafluorohydrazine (N₂F₄), Chlorotrifluorosilane (SiClF₃), Hydrogen bromide (HBr), Arsine (AsH₃), Nitrosyl fluoride (NFO), Hydrogen sulfide (H₂S), Difluorine dioxide (F₂O₂), Arsenic(V) fluoride (AsF₅), Phosphorothioc trifluoride (PSF₃), Stannane (SnH₄), Phosphorus(III) chloride difluoride (PClF₂), Perchloryl fluoride (ClFO₃), Thionyl fluoride (SOF₂), Hydrogen selenide (H₂Se), Sulfur tetrafluoride (SF₄), Hydrogen iodide (HI), Chlorine (Cl₂), Tetrafluorodiborane (B₂F₄), Ammonia (NH₃), Dichlorodifluorosilane (SiCl₂F₂), Chlorosilane (SiClH₃), Stibine (SbH₃), Disilane (Si₂H₆), Sulfur dioxide (SO₂), Nitrosyl chloride (NClO), Hydrogen telluride (H₂Te), Bromosilane (SiBrH₃), Chlorine monoxide (Cl₂O), Thionitrosyl fluoride (FNS), Dichlorosilane (Cl₂H₂Si), Chlorine dioxide (ClO₂), Chlorine trifluoride (ClF₃), Boron trichloride (BCl₃), Phosphorus(III) dichloride fluoride (PCl₂F), Tungsten(VI) fluoride (WF₆), Tetraborane(10) (B₄H₁₀), Bromine fluoride (BrF), Digermane (Ge₂H₆), Trichlorosilane (SiHCl₃), Rhenium(VI) fluoride (ReF₆), Molybdenum(VI) fluoride (MoF₆), Hydrazoic acid (HN₃), Bromine pentafluoride (BrF₅), Aluminum borohydride (AlB₃H₁₂), Sulfur trioxide (SO₃), Osmium(VI) fluoride (OsF₆), Vanadium(V) fluoride (VF₅), Trisilane (Si₃H₈), Iridium(VI) fluoride (IrF₆), Arsenic(III) fluoride (AsF₃), Tetrachlorosilane (SiCl₄), Bromine (Br₂), Diphosphine (P₂H₄), Pentaborane(11) (B₅H₁₁), Dibromosilane (SiBr₂H₂), Sulfuryl chloride (SO₂Cl₂), Hydrogen disulfide (H₂S₂), Thionyl chloride (SOCl₂), Phosphorus(III) chloride (PCl₃), Germanium(IV) chloride (GeCl₄), Boron tribromide (BBr₃), Water (H₂O), Iodine pentafluoride (IF₅), Selenium tetrafluoride (SeF₄), Phosphoryl chloride (PCl₃O), Tribromosilane (SiHBr₃), Trigermane (Ge₃H₈), Hydrazine (N₂H₄), Tin(IV) chloride (SnCl₄), Chromium(VI) dichloride dioxide (CrCl₂O₂), Bromine trifluoride (BrF₃), Vanadyl trichloride (VOCl₃), Arsenic(III) chloride (AsCl₃), Titanium(IV) chloride (TiCl₄), Hydrogen peroxide (H₂O₂), Vanadium(IV) chloride (VCl₄), Tetrabromosilane (SiBr₄), Rhenium(VI) oxytetrafluoride (ReF₄O), Phosphorus(III) bromide (PBr₃), Iodine (I₂), Rhenium(VII) dioxytrifluoride (ReF₃O₂), Tungsten(VI) oxytetrafluoride (WOF₄), Molybdenum(VI) oxytetrafluoride (MoF₄O), Germanium(IV) bromide (GeBr₄), Phosphoryl bromide (PBr₃O), Gallium(III) chloride (GaCl₃), Tin(IV) bromide (SnBr₄), Boron triiodide (BI₃), Molybdenum(V) fluoride (MoF₅), Antimony(III) chloride (SbCl₃), Arsenic(III) bromide (AsBr₃), Rhenium(V) fluoride (ReF₅), Phosphorus(III) iodide (PI₃), Tantalum(V) fluoride (TaF₅), Tungsten(VI) oxytetrachloride (WOCl₄), Osmium(V) fluoride (OsF₅), Titanium(IV) bromide (TiBr₄), Niobium(V) fluoride (NbF₅), Tantalum(V) chloride (TaCl₅), Niobium(V) chloride (NbCl₅), Aluminum bromide (AlBr₃), Molybdenum(V) chloride (MoCl₅), Gallium(III) bromide (GaBr₃), Phosphorus (P), Tetraiodosilane (SiI₄), Antimony(III) bromide (SbBr₃), Mercury(II) chloride (HgCl₂), Mercury(II) bromide (HgBr₂), Tungsten(VI) chloride (WCl₆), Gallium(III) iodide (GaI₃), Tantalum(V) bromide (TaBr₅), Mercury(II) iodide (HgI₂), Mercury (Hg), Tin(IV) iodide (SnI₄), Titanium(IV) iodide (TiI₄), Aluminum iodide (AlI₃), Tellurium tetrachloride (TeCl₄), Antimony(III)

iodide (SbI_3), Arsenic(III) iodide (AsI_3), Bismuth trichloride ($BiCl_3$), Sulfur (S), Bismuth tribromide ($BiBr_3$), Beryllium chloride ($BeCl_2$), Beryllium iodide (BeI_2), Tin(II) chloride ($SnCl_2$), Tin(II) bromide ($SnBr_2$), Indium(I) bromide ($BrIn$), Zinc bromide ($ZnBr_2$), Selenium (Se), Indium(I) iodide (InI), Tin(II) iodide (SnI_2), Thallium(I) chloride ($ClTI$), Zinc chloride ($ZnCl_2$), Cadmium iodide (CdI_2), Cadmium (Cd), Thallium(I) bromide ($BrTI$), Thallium(I) iodide (ITI), Cadmium bromide ($CdBr_2$), Lead(II) iodide (PbI_2), Lead(II) bromide ($PbBr_2$), Thorium(IV) chloride ($ThCl_4$), Titanium(III) chloride ($PbCl_2$), Titanium(III) chloride ($TiCl_3$), Cadmium chloride ($CdCl_2$), Tellurium (Te), Chromium(II) chloride ($CrCl_2$), Molybdenum(VI) oxide (MoO_3), Lead(II) fluoride (PbF_2), Thallium(I) sulfide (STI_2), Sodium hydroxide (NaOH), Titanium(II) chloride ($TiCl_2$), Zinc fluoride (ZnF_2), Silver(I) bromide (AgBr), Silver(I) iodide (AgI), Silver(I) chloride (AgCl), Bismuth (Bi), Lithium hydroxide (LiOH), Lithium fluoride (LiF), Thorium(IV) fluoride (ThF_4), Lead (Pb), Cadmium fluoride (CdF_2), Barium (Ba), Gallium (Ga), Aluminum (Al), Germanium (Ge), Gold (Au), and Boron (B).

In order to relate the properties, the following methodology of analysis was applied:

- Analyses the distribution of the boiling temperature values; if the values are not normally distributed, then find the transformation which normalizes it;
- Analyses the distribution of the heat of vaporization values; if the values are not normally distributed, then find the transformation which normalizes it;
- On the normalized data, by keeping the association given by the chemical compound on which these properties were measured, draw the regression analysis;
- After identification of the regression model, use the inverse of the transformations, which normalizes the data to analyses the model.

The analysis of the distribution was conducted by EasyFit [16] and the analysis of regression was conducted by Excel [17]. The distribution parameters were estimated using the Maximum Likelihood Method (MLE, [18]), and the agreement between the observations and the model were measured using Anderson-Darling statistic ([19]) and Kolmogorov-Smirnov statistic ([20, 21]).

ACKNOWLEDGMENTS

This paper is dedicated to Prof. Mircea V. Diudea with the occasion of his 65th birthday.

REFERENCES

1. J.L. Coolidge, *The American Mathematical Monthly*, **1949**, 56(3), 147.
2. J. Bernoulli, "Ars Conjectandi", Thurnisius, Basel, **1713**.
3. A. De Moivre, "Approximatio ad Summam Terminorum Binomii $(a+b)^n$ in Seriem expansi" (presented privately to some friends in 1733), In: *The Doctrine of Chance: or The Method of Calculating the Probability of Events in Play* (2nd ed.), London, W. Pearson, **1738**, p. 235-243.
4. J.C.F. Gauss, *Comment. Societ. R. Sci. Gottingensis Recentiores*, **1823**, 5, 33.
5. L. Jäntschi, Prediction of Physical, Chemical and Biological Properties using Mathematical Descriptors (in Romanian). PhD Thesis in Chemistry (PhD Advisor: Prof. Dr. Mircea V. Diudea). Cluj-Napoca: Babeş-Bolyai University, **2000**.
6. L. Jäntschi, Genetic Algorithms and their Applications (in Romanian). PhD Thesis in Horticulture (PhD Advisor: Prof. Dr. Radu E. Sestraş). Cluj-Napoca: University of Agricultural Sciences and Veterinary Medicine, **2010**.
7. L. Jäntschi, S.D. Bolboacă, *Journal of Computational Science*, **2014**, 5(4), 597.
8. L. Jäntschi, S.D. Bolboacă, *Studia Universitatis Babeş-Bolyai Chemia*, **2010**, LV(4), 61.
9. C.N. Markides, R.B. Solanki, A. Galindo, *Applied Energy*, **2014**, 124, 167.
10. L.R. Erickson, E.K. Ungar, *AIAA SPACE 2013 Conference and Exposition*, **2013**, 99748.
11. M. Son, J. Koo, W. Cho, E. Lee, *Journal of Thermal Science*, **2012**, 21(5), 428.
12. S.D. Bolboacă, L. Jäntschi, *Combinatorial Chemistry & High Throughput Screening*, **2013**, 16(4), 288.
13. W.M. Haynes (Ed.), *CRC Handbook of Chemistry and Physics*. 95th Edition, Chapman and Hall/CRCnetBASE, Boca Raton, FL, Internet Version, **2015**.
14. D.R. Lide, *CRC Handbook of Chemistry and Physics*, 90th Edition Internet Version. Boca Raton, FL: Chapman and Hall/CRCnetBASE, **2010**.
15. M.W. Chase, Jr., C.A. Davies, J.R. Downey, Jr. D.J. Frurip, R.A. McDonald, A.N. Syverud, *Journal of Physical and Chemical Reference Data*, **1985**, 14(S1), 1856p.
16. MathWave Technologies, 2009. EasyFit Professional v.5.2 (software). Web site: <http://mathwave.com>
17. Microsoft® Excel® 2002 SP3, Copyright© Microsoft Corporation 1987-2001.
18. R.A. Fisher, *Messenger of Mathematics*, **1912**, 41, 155.
19. T.W. Anderson, D.A. Darling, *Annals of Mathematical Statistics*, **1952**, 23(2), 193.
20. A. Kolmogorov, *Annals of Mathematical Statistics*, **1941**, 12(4), 461.
21. N.V. Smirnov, *Annals of Mathematical Statistics*, **1948**, 19(2), 279.

*Dedicated to Professor Mircea Diudea
on the Occasion of His 65th Anniversary*

COMPARATIVE STUDY OF NANOCRYSTALLINE DIAMOND GROWTH USING PECVD AND HFCVD TECHNIQUES

ZAHRA KHALAJ^a

ABSTRACT. Diamond coating is one of the hot research topic due to its various industrial applications; for the diamond growth, several techniques, such as PECVD and HFCVD, have been reported. In this paper, we investigate the effects of different CVD techniques on synthesis of diamond crystals, grown on silicon and aluminum substrates, at temperature of 550° C and the reaction pressure of 30 Torr, in which CH₄ and H₂ act as a source and diluting gases, respectively. The hydrogen was used as the etching gas to enhance the diamond nucleation. As a result, we obtained a high distribution of nanodiamond with (111) crystallite structure on gold-coated silicon in HFCVD system. The samples were analyzed using AFM, SEM and XRD.

Keywords: *Hot filament chemical vapor deposition; Plasma enhanced chemical vapor deposition; Etching gas; NCD.*

INTRODUCTION

Diamond coating is a hot research topic because of its high thermal conductivity, large band gap, excellent hardness, robustness, low friction coefficient and stable chemical properties [1-13]. Most of the researches reported the growth of nano crystalline diamond (NCD) and films on silicon substrate, scratching by diamond powder to increase the diamond nucleation by PECVD and HFCVD techniques [13-18]. One of the suitable gases for etching the substrate is the hydrogen. It can increase the ratio of diamond nucleation without using diamond powder. According to some references, the

^a *Department of Physics, Shahr-e-Qods Branch, Islamic Azad University, Tehran, I. R. Iran,
e-mail: khalaj.z@gmail.com*

presence of hydrogen may improve the quality of diamond films, by reducing the graphite content in diamond films [19, 20]. It is generally believed that methyl radicals play the most important role in standard CVD diamond growth, by abstracting the hydrogen from the diamond surface. Therefore, a high concentration of atomic hydrogen at the surface in addition to CH_3 radicals is a prerequisite for a successful microcrystalline diamond deposition [21-26].

In the present paper, we study the effects of simultaneous HFCVD and PECVD systems on the growth of diamond nano structures with (111) crystallite on conductive substrates. Gold coated on silicon and aluminum was used as the substrates in this experiment. Hydrogen gas was used for etching treatment of the substrates. A mixture of methane and hydrogen were used for the growing process in the both systems.

RESULTS AND DISCUSSION

XRD analysis of surface was carried to estimate the crystalline structure of the deposits. Figures 3 and 4 show XRD patterns of diamond grown by HFCVD and PECVD systems on substrates with 2θ angles ranging from 35° to 85° . The study of the parameters show a major peak corresponding to diamond (111) at $2\theta=44.62^\circ$ and $2\theta=44.46^\circ$ on aluminum and gold coated on silicon respectively, performed at $T_F=1800^\circ\text{C}$ by HFCVD system (Fig. 1). The same result for the other aluminum substrate obtained in PECVD system at $2\theta\approx 44.50^\circ$ but here the hydrogen plasma was used for etching the substrate (Fig. 2a). However, we cannot see the diamond peak of (111) crystallinity in the last sample, made by PECVD, but the pattern displays a peak with $2\theta\approx 41.91^\circ$ indicating the diffraction from (101) diamond (See Fig. 2b).

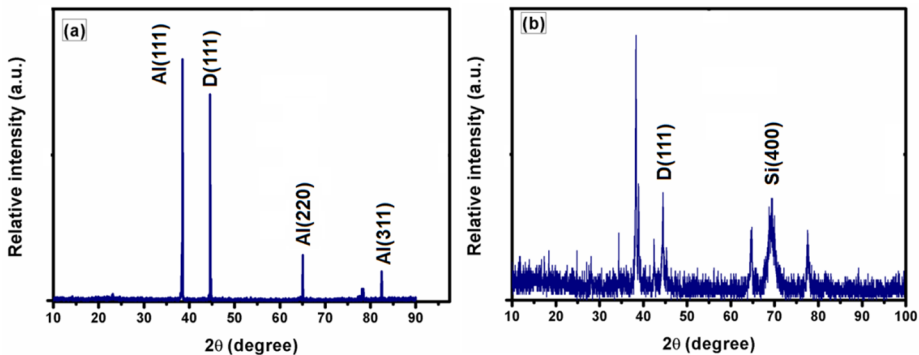


Figure 1. XRD pattern for diamond crystals grown by HFCVD system: (a) Al substrate and (b) Gold coated on silicon.

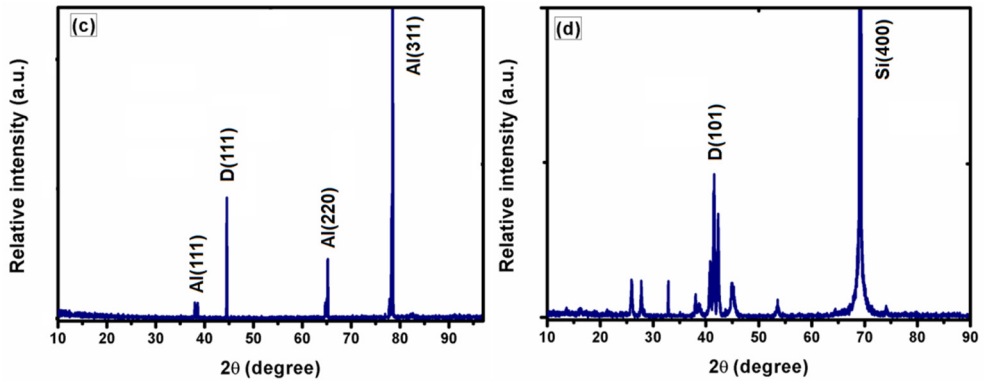


Figure 2. XRD pattern for diamond crystals grown by PECVD system: (a) Al substrate and (b) Gold coated on silicon.

One of the best factors for crystallite quality is Full Width Half Maximum (FWHM) of the XRD patterns. In fact, sharp peaks with small FWHM indicate a high crystal quality [28]. The sharp peaks with small FWHM in Al samples confirm this idea. But a better result in Al sample refers to the sample grown by HFCVD system. The high ratio of reactive gases is the essential parameter for growing diamond nano crystals. Because of the hot filament in HFCVD system, the ionization rate of the reactive gases is much higher than in the case of plasma system of PECVD. On the other hand, in PECVD, in the case of gold coated on silicon substrate, different types of diamond crystals were obtained when different CVD systems were used. The SEM micrographs, in Fig. 3, show the morphology of diamond nano and micro structures, grown on aluminum and gold coated on silicon substrates.

As we can see, diamond single crystals grow in the case of Al substrate, in both the systems (Fig. 3(a)-(b)), whereas a high comparative distribution of nano crystalline diamond can be observed in the case of using gold coated on silicon (Fig. 3(c)). Fig. 3(d) shows some dendritic structures which led to crystals with a regular distribution of nano and micro diamond crystals.

According to Scherer formula, the grain size (T) of diamond crystals is calculated by $T=0.9\lambda/\Delta(2\theta) \cos \theta$, where $\Delta(2\theta)$ is the FWHM in radians and λ is the wavelength in nm [29].

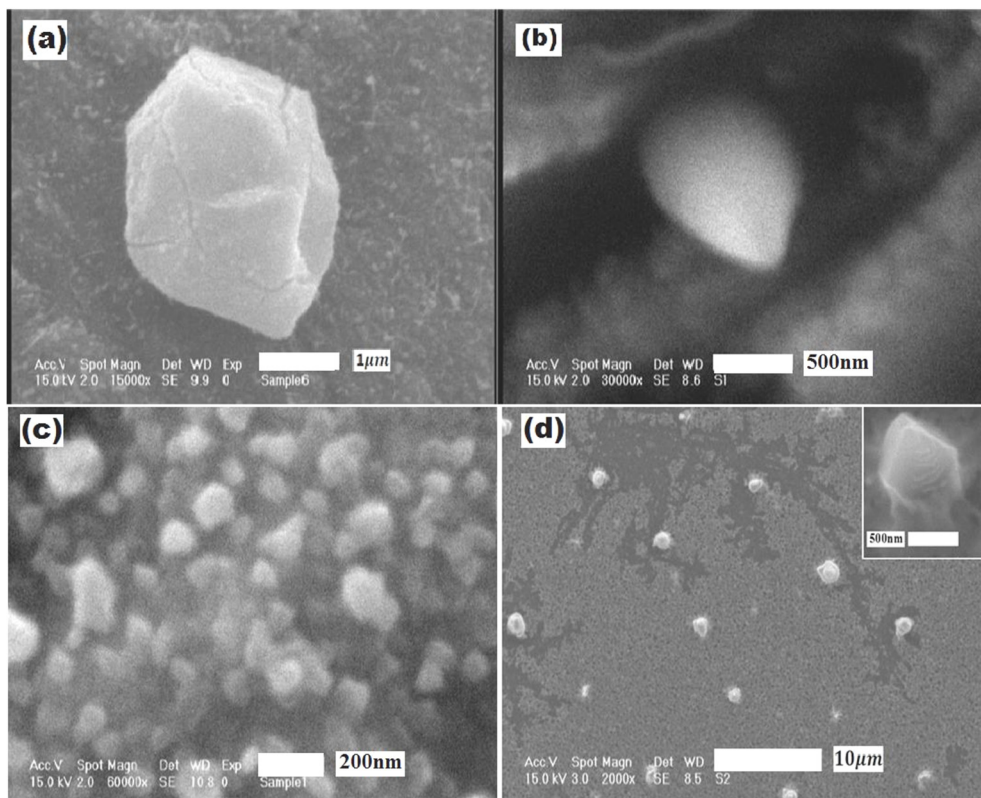


Figure 3. SEM images of nano and microcrystalline diamond grown on: (a) Al substrate by HFCVD, (b) Al substrate by PECVD, (c) Si coated by gold substrate by HFCVD, (d) Si coated by gold substrate by PECVD.

Table 1. Result of XRD studies for diamond crystals grown on gold coated on silicon and aluminum substrates.

Sample	Orientation of plane	$\Delta(2\theta)$ (deg)	T(nm)
Si(HFCVD)	[111]	0.196	44.70
Si(PECVD)	[101]	0.136	66
Al(PECVD)	[111]	0.15	57.75
Al(HFCVD)	[111]	0.09	106.61

The calculated grain size for the diamond crystals grown on the silicon and aluminum substrates measured less than 110 nm. Detailed data for the grain size of the diamond were listed in Table 1.

CONCLUSIONS

In this work, growth of diamond nanocrystals with orientation in (111) plane on gold coated on silicon and aluminum was investigated by two different CVD techniques. Using HFCVD technique, diamond nano and micro crystals with (111) crystallinity were grown on Al and Si substrates. By PECVD technique, a high quality (111) diamond was obtained on Al substrate and (101) diamond crystals on gold coated on silicon. The XRD patterns shown a good quality for the diamond structures grown on aluminum in both techniques, as proved by high intensity and small FWHM in diamond peaks; however, the high concentration and distribution of the diamond nanocrystals on the substrate with lower grain size of the particles were obtained in gold coated on silicon substrates, synthesized by HFCVD. It was proved that the ionization rate of reaction gases has a great influence on diamond nucleation. This is achieved in the case of HFCVD, the hot filament providing a high concentration of ionized gas. It was shown that the usage of H₂ as etching gas in different CVD methods results in diamond nanocrystals, with high concentration of distribution and crystalline quality, on gold coated on silicon substrates.

MATERIALS AND METHODS

Silicon wafers [Si-P typed] with (10mm×10mm) and aluminum (5mm x 5mm) with 99.99% purity were used as substrates in this experiment and pretreated in two steps. For aluminum pretreatment, all the substrates were polished with diamond paste to obtain a smooth surface. Before loading into deposition chamber, the Al substrates were ultrasonically cleaned in a bath of acetone, ethanol and de-ionized water for 15 minutes. The Si samples were ultrasonically cleaned with acetone and ethanol for 15 minutes and a gold nanolayer of 13nm thickness was deposited on the silicon substrate as a catalyst nano layer. Gold deposition was made by a direct magnetron sputtering system, consisting of a cylindrical glass tube and two parallel disks as cathode and anode in its chamber in which a uniform magnetic field was induced for Au coating from outside. In this case, the applied voltage was 2000 V. The argon gas was used as a sputtering gas and the operation pressure was set at 5×10^{-2} Torr. Figure 4 represents the 2D and 3D Atomic Force Microscopy (AFM) image of the gold sputtered substrate; the roughness of the substrate after coating with gold can be seen. The average roughness for the gold coated on silicon was 8.33 Å; this was 15.5 Å for Al polished by diamond paste.

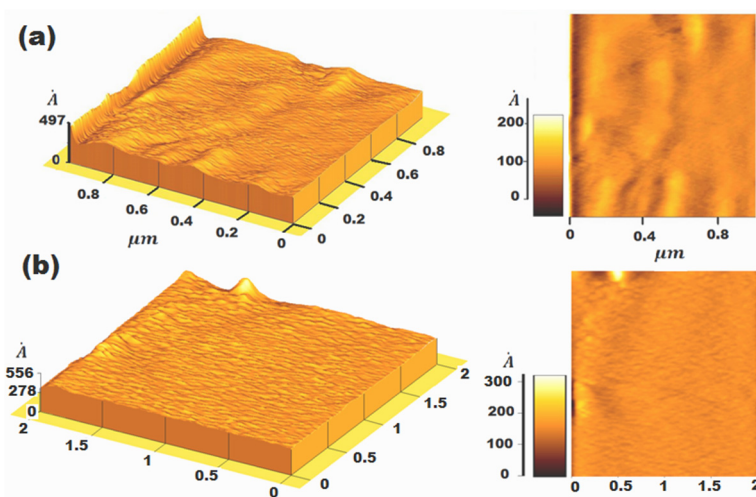


Figure 4. AFM image of the: (a) Aluminum polished by 1 μm diamond paste; (b) Gold coated on silicon substrate.

Deposition of diamond structures carried out in the Hot Filament Chemical Vapor Deposition (HFCVD) and Plasma Enhanced Chemical Vapor Deposition (PECVD) systems. The HFCVD system consists of a gas dispersion system inside a horizontal stainless steel (S.S.316) cylinder as a reaction chamber, a filament network, and an aperture support plate for the substrate (Fig. 5(a)).

The parallel tungsten filaments were employed for activation of gas-phase reactions. The Si coated by gold nanolayer and Al substrates were placed 5mm below to five 0.5mm diameter hot filaments. After the base pressure reached to near to 10^{-5} Torr, the substrate temperature and the temperature of the filament increased up to 450°C and 1600°C, respectively. The hydrogen gas was used for etching the substrates to enhance the diamond nucleation. The H_2 gas was fed into the reaction chamber, at 10 Torr, as the etching pressure, for 45 minutes. For growing the diamond structures, a combination of CH_4/H_2 with 5% flow ratio was fed into the reaction chamber. Prior to diamond deposition, a carbonized interlayer was formed. This layer plays an important and complex role in the diamond nucleation [27]. The reaction pressure and temperature of the filament, for the growth process, were 30 Torr and $\approx 1800^\circ\text{C}$, respectively; the time taken for the growth was 60 minutes. These conditions were preserved for all the samples herein studied. We have done the same experiment in parallel with PECVD system to compare the result of diamond deposition by different CVD methods.

Fig. 5(b) shows the schematic diagram of the DC-PECVD system. After the chamber was pre-evacuated by rotary pump, the base pressure of the system was kept at 1×10^{-2} Torr. The substrate was placed on a furnace right under the anode. The applied voltage and current were 400 V and 25 mA, respectively. The other experimental conditions were same as in the case of HFCVD system. The temperatures of the substrates in both systems were monitored by two thermo-couples, separately.

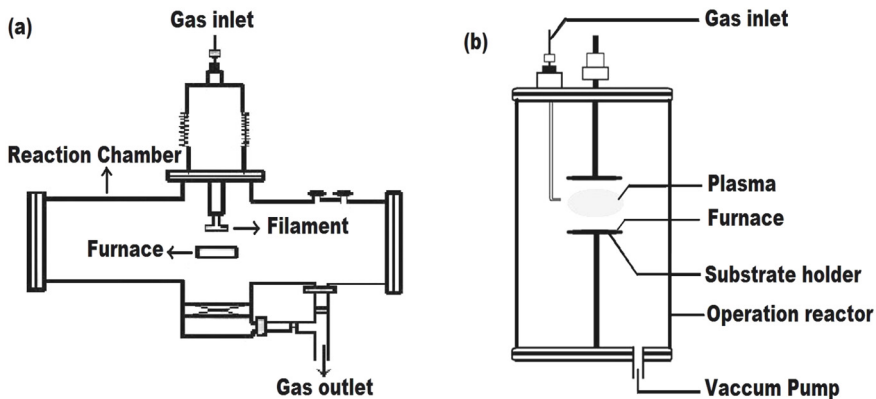


Figure 5. Schematic diagram of: (a) the HFCVD and (b) PECVD, systems.

The morphology of the diamond structures was observed by SEM (XL30, Phillips, Holland), and the crystallinity of the samples was studied by XRD ($\text{CuK}\alpha$, $\lambda=0.154\text{nm}$, $D/\text{Max}=2200$, X-ray diffractometer) analysis.

ACKNOWLEDGMENT

Many thanks are addressed to Professor Mircea V. Diudea for his valuable advice and to Plasma Physics Research Center, Tehran, for technical support.

REFERENCES

1. D. Rommel, F. Scherm, Ch. Kuttner, U. Glatzel, *Surface & Coatings Technology*, **2016**, 291, 62.
2. K. Yamazaki, K. Furuichi, I. Tsumura, Y. Takagi, *Crystal Growth*, **2008**, 310, 1019.
3. A.M. Alexeev, R.R. Ismagilov, E.E. Ashkinazi, A.S. Orekhov, S.A. Malykhin, A.N. Obraztsov, *Diamond and Related Materials*, **2016**, 65, 13.

4. X. Sun, Y. Li, B. Wan, L. Yang, Q. Yang, *Surface and Coatings Technology*, **2015**, *284*, 139.
5. H.E. Zhoutong, Y. Shumin, L. Qintao, Z. Dezhang, G. Jinlong, *Nuclear Science and Technology*, **2008**, *19*, 83.
6. Y. Takano, M. Nagao, T. Takenouchi, H. Umezawa, I. Sakaguchi, M. Tachiki, H. Kawarada, *Diamond and Related Materials*, **2005**, *14*, 1936.
7. B. Aldwell, Sh. Yin, K.A. McDonnell, D. Trimble, T. Hussain, R. Lupoi, *Scripta Materialia*, **2016**, *115*, 10.
8. L.G. Wang, L.W. Jiang, L. Ren, J. M. Liu, Q.F. Su, R. Xu, H.Y. Peng, W.M. Shi, Y.B. Xia, *Transactions of Nonferrous Metals Society of China*, **2006**, *16*, 289.
9. N. Kohmura, K. Sudoh, K. Sato, K.K. Hirakuri, K. Miyake, G. Friedbacher, *Diamond and Related Materials*, **2005**, *14*, 283.
10. A. Bogus, I.C. Gebeshuber, A. Pauschitz, M. Roy, R. Haubner, *Diamond and Related Materials*, **2008**, *17*, 1998.
11. M.S. You, F.C.N. Hong, Y.R. Jeng, S.M. Huang, *Diamond and Related Materials*, **2009**, *18*, 155.
12. I.E. Monje, E. Louis, J.M. Molina, *Scripta Materialia*, **2016**, *115*, 159.
13. S. Yang, Z. He, Q. Li, D. Zhu, J. Gong, *Diamond and Related Materials*, **2008**, *17*, 2075.
14. C.J. Tang, A.J. Neves, S. Pereira, A.J.S. Fernandes, J. Gracio, M.C. Carmo, *Diamond and Related Materials*, **2008**, *17*, 72.
15. S.A. Rakha, S. Yang, Z. He, I. Ahmed, D. Zhu, J. Gong, *Current Applied Physics*, **2009**, *9*, 698.
16. J. Hirnke, S. Schwarz, C. Rottmair, S.M. Rosiwal, R.F. Singer, *Diamond and Related Materials*, **2006**, *15*, 536.
17. X.T. Zhou, H.L. Lai, H.Y. Peng, C. Sun, W.J. Zhang, N. Wang, I. Bello, C.S. Lee, S.T. Lee, *Diamond and Related Materials*, **2000**, *9*, 134.
18. A. Bogus, I.C. Gebeshuber, A. Pauschitz, M. Roy, R. Haubner, *Diamond and Related Materials*, **2008**, *17*, 1998.
19. K.C. Yang, Y.B. Xia, L.J. Wang, J.M. Liu, I.F. Su, R. Xu, H.Y. Peng, W.M. Shi, *Transactions of Nonferrous Metals Society of China*, **2006**, *16*, 321.
20. Y. Yamazaki, K. Ishikawa, N. Mizuochi, S. Yamasaki, *Diamond and Related Materials*, **2005**, *14*, 1939.
21. Yu. A. Mankelevich, P.W. May, *Diamond and Related Materials*, **2008**, *17*, 1021.
22. O. Matsumoto, H. Tushima, Y. Kanzaki, *Thin solid films*, **1985**, *128*, 341.
23. B.V. Spitsyn, L.L. Bouilov, B.V. Derjaguin, *Crystal Growth*, **1981**, *52*, 219.
24. M. Tsuda, M. Nakajima, S. Oikawa, *Japanese Journal Applied Physics*, **1987**, *26*, L527.
25. M. Frenklach, *Applied Physics*, **1989**, *65*, 5142.
26. Y. Mitsuda, Y. Kojima, T. Yoshida, K. Akashi, *Material Science*, **1987**, *22*, 1557.
27. K.I. Itoh, C. Morishima, K. Ubukata, A. Chiba, H. Aida, O. Matsumoto, *Diamond and Related Materials*, **2000**, *9*, 140.
28. S. Schwarz, C. Rottmair, J. Hirnke, S. Rosiwal, R.F. Singer, *Crystal Growth*, **2004**, *271*, 425.
29. M. Pandey, R. D'Cunha, A.K. Tyagi, *Alloys and Compounds*, **2002**, *333*, 260.

***Dedicated to Professor Mircea Diudea
on the Occasion of His 65th Anniversary***

ON (3,6) AND (4,6)–FULLERENE CAYLEY GRAPHS

ALI REZA ASHRAFI^a, AMIR LOGHMAN^{b,*} AND MOJGAN MOGHARRAB^c

ABSTRACT. An (r, s) –fullerene graph is a planar 3–regular graph with only C_r and C_s faces, where C_n denotes a cycle of length n . In this paper the $(3,6)$ –fullerene Cayley graphs constructed from finite groups are classified. A characterization of $(4,6)$ –fullerene Cayley graphs is also presented.

Keywords: Fullerene, Cayley graph, finite group.

INTRODUCTION

In this paper, the word graph refers to a finite, undirected graph without loops and multiple edges.

Let G be a group and S a subset of G not containing the identity element. We define the Cayley digraph $X = \text{Cay}(G, S)$ of G with respect to S by $V(X) = G$ and $E(X) = \{(g, gs) \mid g \in G, s \in S\}$. It is not so difficult to prove that X is undirected if and only if $S = S^{-1} = \{s^{-1} \mid s \in S\}$. In the latter case, we call X a Cayley graph.

The notion of a map satisfies the originally intuitive problem of “drawing a graph without intersections”. Let us denote the group of all map–automorphism of M by $\text{Aut}(M)$. If $\text{Aut}(M)$ contains a subgroup that acts regularly on the vertex set then M is called a Cayley map. Since $\text{Aut}(M) \leq \text{Aut}(X)$ we clearly have that the underlying graph X of a Cayley map is a Cayley graph. Equivalently,

^a Department of Mathematics, Statistics and Computer Science, Faculty of Science, University of Kashan, Kashan 87317-51167, I. R. Iran; Institute of Nanoscience and Nanotechnology, University of Kashan, Kashan 87317-53153, I. R. Iran

^b Department of Mathematics, Payame Noor Universtiy, PO BOX 19395-3697 Tehran, Iran

^c Department of Mathematics, Persian Gulf University, Bushehr, I. R. Iran

* Corresponding Author: amirloghman@pnu.ac.ir

a Cayley map is an embedding of a Cayley graph onto an oriented surface having the same cyclic rotation of generators around each vertex. These are studied extensively in literature, see [1–3] for more details on this subject.

A graph which can be drawn in the plane in such a way that edges meet only at points corresponding to their common ends is called a planar graph. An (r,s) -fullerene graph is a planar 3-regular graph with only r - and s -faces, where an n -face is a face of size n . Suppose p , h , n and m are the number of r -faces, s -faces, vertices and edges, respectively, in a given (r,s) -fullerene, where $(r,s) = (3,6);(4,6)$. Since each vertex in an (r,s) -fullerene graph lies in exactly 3 faces and each edge lies in 2 faces, the number of vertices is $n = (rp + sh)/3$, the number of edges is $m = (3/2)n = (rp + sh)/2$ and the number of faces is $f = p + h$. By the Euler's formula $n - m + f = 2$, one can deduce that $(rp + sh)/3 - (rp + sh)/2 + p + h = 2$, and therefore the number of 3-faces in $(3,6)$ -fullerenes is four while the number of 4-faces in $(4,6)$ -fullerenes is six. This implies that $(3,6)$ -fullerenes have exactly four triangles and $n/2 - 2$ hexagons. Similarly, $(4,6)$ -fullerenes have exactly 6 squares and $n/2 - 4$ hexagons. The $(4,6)$ -fullerenes with isolated squares are called ISR-fullerenes. The name is taken from [4] in which the authors used the name IPR-fullerene for those with disjoint pentagons.

Computations were carried out by the aid of GAP [5]. The motivation for this study is outlined in [3,6–8] and the reader is encouraged to consult these papers for background material as well as for basic computational techniques. Our notation is standard and taken mainly from [4].

RESULTS AND DISCUSSION

Since the discovery of C_{60} fullerene in 1985 by Kroto *et al.*, the fullerenes became the subject of interest of scientists all over the world [9,10]. The aim of this section is to characterize the $(3,6)$ - and $(4,6)$ -fullerene Cayley graphs [11]. We begin by $(3,6)$ -fullerene Cayley graphs.

Theorem 1. Let $X = \text{Cay}(G,S)$ be a $(3,6)$ -fullerene Cayley graph on a group G . Then, either G is isomorphic to an abelian group of order 4 and X is isomorphic to the complete graph K_4 , or G is isomorphic to the alternating group A_4 and X is isomorphic to the graph shown in Figure 1.

Proof. By Euler's formula X contains a 3-cycle. Since X is cubic and undirected, then S is of cardinality 3 and $S=S^{-1}$. If S consists of three involutions a , b and c then a 3-cycle in X must arise from the relation $abc = e$, which implies that $c = ab$ and consequently $G = \langle a, b, c \rangle = \langle a, b \mid a^2 = b^2 = (ab)^2 = e \rangle \cong Z_2 \times Z_2$

and $X \cong K_4$. If however S consists of an involution a , a non-involution x and the inverse of this non-involution then a 3-cycle in X arises either from the relation $x^3 = e$ or from the relation $x^2a = e$. In the former case the edge with end vertices e and x must lie on a 6-cycle arising from the relation $(ax)^3 = e$ and thus $G = \langle a, x \mid a^2 = x^3 = (ax)^3 = e \rangle \cong A_4$ and X is isomorphic to the graph shown in Figure 1. In the latter case $G = \langle x \mid x^4=e \rangle \cong Z_4$ and $X \cong K_4$. This completes our proof.

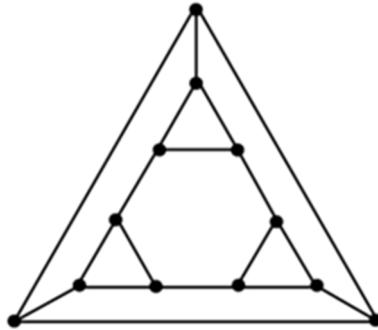


Figure 1. The (3,6)-fullerene Cayley graph on the alternating group A_4 .

Theorem 2. Let $X = \text{Cay}(G,S)$ be a (4,6)-fullerene Cayley graph on group G .

Then

- I. G is isomorphic to the dihedral group D_8 or $Z_2 \times Z_4$ with a Cayley graph isomorphic to the cube Q_3 ,
- II. G is a finite quotient of an infinite group H presented as follows:

$$H = \langle a, b, c \mid a^2 = b^2 = c^2 = e, (ab)^2 = e \rangle,$$

- III. G is a finite quotient of the free product group $Z_2 \diamond Z_2$,
- IV. G is isomorphic to the symmetric group S_4 with a Cayley graph isomorphic to an ISR-fullerene on 24 vertices depicted in Figure 2,
- V. G is isomorphic to the dihedral group D_{12} with a Cayley graph isomorphic to a 6-prism depicted in Figure 3,
- VI. G is a finite quotient of an infinite group H isomorphic to an extension of $Z_2 \times Z_2$ by Z_2 .

Proof. Suppose $X = \text{Cay}(G,S)$ is a (4,6)-fullerene. Since X is 3-regular, we can assume that $S = \{a, b, c\}$. By similar argument as Theorem 1, we consider the following cases:

Case 1. $a^2 = b^2 = c^2 = e$. A tedious calculation shows that we can assume that the 4–face of X arise from $(ab)^2 = e$ or $abac = e$. If $(ab)^2 = e$ then $ab = ba$ and G has the following presentation:

$$G = \langle a, b, c \mid a^2 = b^2 = c^2 = e, (ab)^2 = e \rangle.$$

We now compute the abelian invariants of G and G' as follows:

$$\frac{G}{G'} \cong Z_2 \times Z_2 \times Z_2, \text{ and}$$

$$\frac{G'}{G''} \cong Z \times Z \times Z.$$

Therefore, G is infinite, as desired. If $abac = e$ then $aba = c$ and so

$$G = \langle a, b, c \mid a^2 = b^2 = c^2 = e, aba = c \rangle$$

$$= \langle a, b \mid a^2 = b^2 = e \rangle \cong Z_2 \diamond Z_2,$$

Where $Z_2 \diamond Z_2$ denotes the free product of Z_2 by Z_2 , which is an infinite group.

Case 2. $a^2 = b^4 = e$ and $c = b^{-1}$. In this case, $b^2 = c^2$ and by existence of a face of length 4, $(ab)^2 = e$ or $aba = b$. If $(ab)^2 = e$ then G has the following presentation:

$$G = \langle a, b \mid a^2 = b^4 = e, (ab)^2 = e \rangle \cong D_8.$$

Therefore, the Cayley graph X on G is isomorphic to the cube Q_3 . If $aba = b$ then G has the following presentation:

$$G = \langle a, b \mid a^2 = b^4 = e, ab = ba \rangle \cong Z_2 \times Z_4,$$

and X is isomorphic to Q_3 .

Suppose that the 4–faces in X arise only from the relation $b^4=e$. We now consider combinations of generators of length 6. Then $(ab)^3 = e$, or $ab^3ab=e$, or $(ab)^2 = e$ or $(ab^2)^2 = e$. If $ab = ba$ then G is abelian and so it is isomorphic to $Z_2 \times Z_4$ and $X = \text{Cay}(G,S) \cong Q_3$. If $(ab)^3 = e$ then G is presented by $\langle a, b \mid a^2 = b^4 = (ab)^3 = e \rangle$. It is well–known that this group is isomorphic to the symmetric group on four symbols, S_4 . A simple GAP program [5] shows that the Cayley graph of G is the following ISR (4,6)–fullerene of Figure 2.

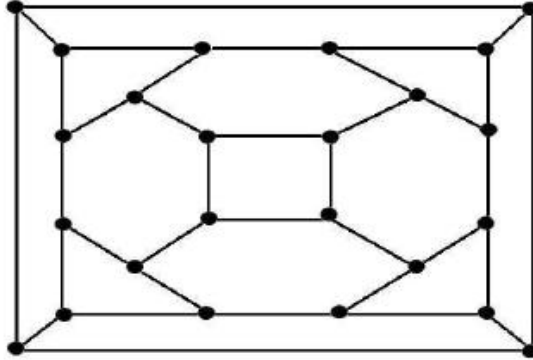


Figure 2. An ISR-Fullerene on 24 vertices.

If $(ab)^2 = e$ then $G = \langle a, b \mid a^2 = b^4 = (ab)^2 = e \rangle \cong D_8$ and $X \cong Q_3$. Finally, if $(ab^2)^2 = e$ then $b^2 \in Z(G)$. Consider the factor group $G/\langle b^2 \rangle$. Then a simple calculation shows that this group can be presented by $\langle a, b \mid a^2 = b^2 = e \rangle \cong Z_2 \diamond Z_2$.

Case 3. $a^2 = b^6 = e$ and $c = b^{-1}$. In this case using a similar argument as those given in Cases 1 and 2, one can see that $(ab)^2 = e$ and so G can be presented as follows:

$$G = \langle a, b \mid a^2 = b^6 = (ab)^2 = e \rangle \cong D_{12},$$

giving the 6-fold prism as its Cayley graph, Figure 3. This completes our argument.

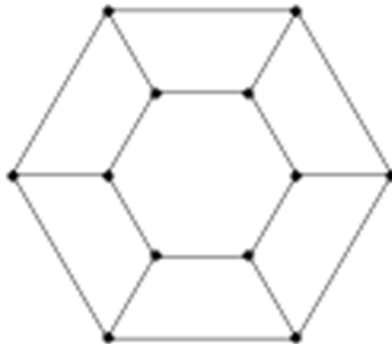


Figure 3. The 6-Prism Graph.

ACKNOWLEDGMENTS

The first author is supported by the University of Kashan under grant no. 364988/36. The research of the second author was in part supported by a grant from Payame Noor Universtiy.

REFERENCES

1. M.E. Conder, *Quart. J. Math. Oxford*, **1987**, 38, 427.
2. H.H. Glover, D. Marusic, *J. Eur. Math. Soc.*, **2007**, 9, 775.
3. M.–H. Kang, *Discrete Math.*, **2011**, 311, 2384.
4. P.W. Fowler, D.E. Manolopoulos, "An atlas of Fullerenes", The Clarendon Press, Oxford, **1995**.
5. The GAP Team, GAP, Groups, Algorithms and Programming, Lehrstuhl De für Mathematik, RWTH, Aachen, **1995**.
6. B. Kostant, *Notices of the AMS*, **1995**, 42, 959.
7. B. Kostant, *Proc. Natl. Acad. Sci.*, **1994**, 91, 11714.
8. B. Kostant, *Selecta Mathematica, New Series*, **1995**, 1, 163.
9. H.W. Kroto, J.R. Heath, S.C. O'Brien, R.F. Curl, R.E. Smalley, *Nature*, **1985**, 318, 162.
10. H.W. Kroto, J.E. Fichier, D.E. Cox, "The Fullerene", Pergamon Press, New York, **1993**.
11. A.R. Ashrafi, G.H. Fath-Tabar, *Appl. Math. Lett.*, **2011**, 24, 337.

***Dedicated to Professor Mircea Diudea
on the Occasion of His 65th Anniversary***

NATURE OF POLYETHYLENEIMINE-GLUCOSE OXIDASE INTERACTIONS

B. SZEFLER^{a,*}, M.V. DIUDEA^b AND I.P. GRUDZINSKI^c

ABSTRACT. The nature of interactions between Polyethylenimine and glucose oxidase 3QVR enzyme was studied by docking and Molecular dynamics procedures. The docking procedure evidenced two active sites, one located inside the enzyme body and the second at the enzyme surface. In view of deeply understand the interactions ligand – enzyme, a Molecular dynamics study followed to the docking. This provided a detailed information on the type, intensity and frequency of these interactions.

Keywords: PEI, 3QVR, Glucose oxidase (GOx), Docking, Molecular Dynamics

INTRODUCTION

Glucose oxidase (GOx) is an enzyme produced by several fungi, such as *Aspergillus*, *Penicillium* and other species. It catalyzes the oxidation of beta-D-glucose to D-glucono-1,5-lactone, which further hydrolyzes to produce the gluconic acid. A coproduct of this enzymatic reaction is the hydrogen peroxide (H₂O₂) [1-3]. GOx has found several applications in Chemistry and Pharmaceutics, in production of biosensors that use this enzyme immobilized on different nanomaterials, like the carbon nanotubes and/or biopolymers such as polyethylenimine PEI, polyethilene glycol PEG, polyaminoamide PAMAM, etc [4-6].

^a Department of Physical Chemistry, Faculty of Pharmacy, Collegium Medicum, Nicolaus Copernicus University, Kurpiskiego 5, 85-096 Bydgoszcz, Poland

^b Department of Chemistry, Faculty of Chemistry and Chemical Engineering, Babes-Bolyai University, 400028 Cluj, Romania

^c Faculty of Pharmacy, Medical University of Warsaw, 02-097 Warsaw, Poland

* Corresponding Author: beatas@cm.umk.pl

The problem of GOx immobilization is to retain the enzyme native activity despite its immobilization onto the polymer surface. In this respect, knowledge of the intimate interaction between the enzyme and ligands, in vary conditions, is of great importance.

In this paper, a coupled study of docking and Molecular Dynamics was conducted and the results were collected and interpreted.

METHODS

Docking Procedure

Using the AutoDockVina software [7], the protein molecule was loaded and stored as “protein.pdb” after assigning hydrogen bonds [8]. The investigated ligand was loaded and its torsions along the rotatable bonds were assigned; then the files were saved as “ligand.pdbqt”. The grid menu is next toggled [9]; after loading “protein.pdbqt”, the map files were selected directly with setting up the grid points, for the search of ligand-protein interactions. The enzyme allows several interactions with ligands, that’s why a map of ligand - enzyme interactions was made, for all area of enzyme, by changing parameters of grid box, step by step. The docking parameter files were completed by using the Lamarckian genetic algorithm [10].

Molecular Dynamics Method

A Molecular Dynamics (MD) procedure was applied to a complex enzyme–ligand [11]. The structure of ligand and enzyme was characterized by using the Amber force field parameters; the atomic charges were calculated according to the Merz-Kollmann scheme, via the RESP procedure [12] at HF/6-31G* level of theory. Each system was neutralized and immersed in a periodic TIP3P water box. The considered systems were heated up to 300K by 100 ps of initial MD simulation, while the temperature was controlled by the Langevin thermostat [13]. The periodic boundary conditions and SHAKE algorithm [14] were applied to 70 ns of molecular dynamic simulation: the first 10 ns of the simulation time was considered as the equilibration interval while the next 60 ns of trajectory were used for the analysis of interactions ligand-enzyme. Structural analysis was performed by the VMD package [15]. The energetic characterization of the interactions between the ligand and active sites was obtained by the Molecular Mechanic/Poisson-Boltzmann Surface Area (MMPBSA) method [16]. In all MD simulations, the AMBER 11 package [17] was used.

RESULTS AND DISCUSSION

Docking results

Based on crystal data, one can see that 3QVR/GOx enzyme can establish many interactions with a ligand, in all its area (Figure 1) [11]. That's why a docking study of PEI - 3QVR complex was made in all area of GOx enzyme, by changing parameters of grid box, step by step.

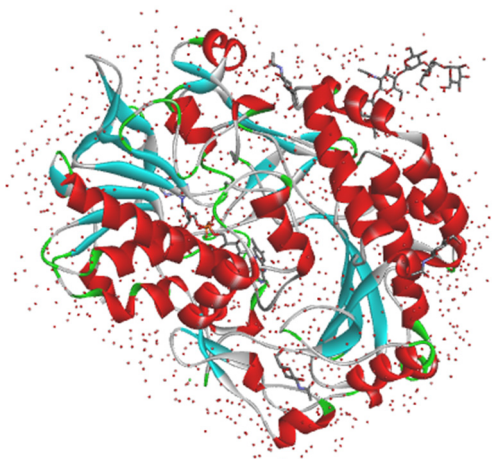


Figure 1. The protein 3QVR (RCSB PDB, GOx - molecule of the month, May, 2006) [11]

As ligands, three types of PEI molecules were considered: branched (B), linear (L) and dendrimer (D) (Figure 2).

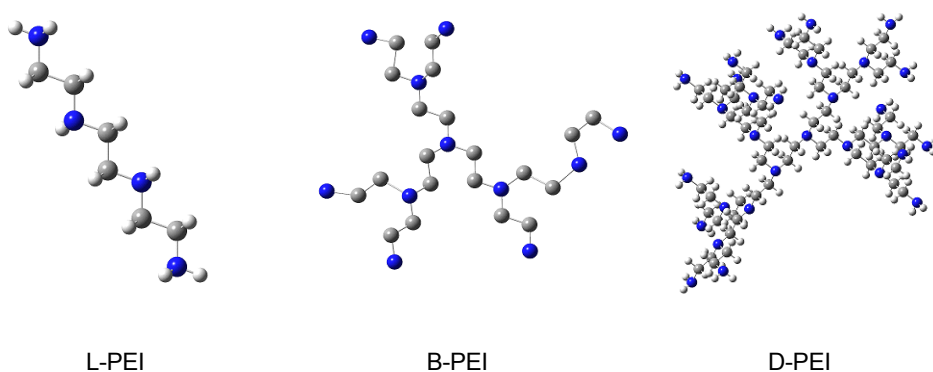


Figure 2. Examples of PEI molecules: linear L (left); branched B (middle) and dendrimer D (right).

Among these 3 groups, the strongest affinity to GOx enzyme shows B-PEI (mean value -7.9 kcal/mol - Figure 3). The groups of ligands D-PEI and L-PEI exhibit less affinity to enzyme, in comparison to B-PEI (Figure 3). Only D3-PEI-C26N14 and L-PEI-C26N14 exhibit an affinity close to the ligands of B-PEI group (at about -7 kcal/mol) (Figure 3); the rest of ligands of the two groups D-PEI and L-PEI exhibit similar values, at about -5kcal/mol.

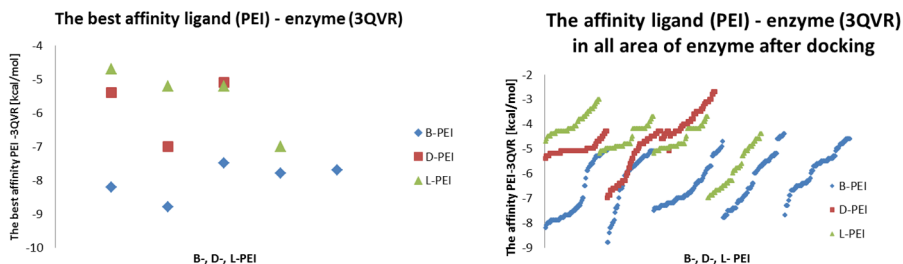


Figure 3. Energy (in kcal/mol) of the best affinity ligand (PEI) - enzyme (3QVR) complex, (left), and energy of all the docked ligand (PEI) - enzyme (3QVR) complexes, in all area of the enzyme (right), for B-, D-, and L-PEI.

Therefore, to simulate the DM, only one ligand of the B-PEI structures, namely the polymer PEI_C14N8_07_B22 (Figure 4) was used.

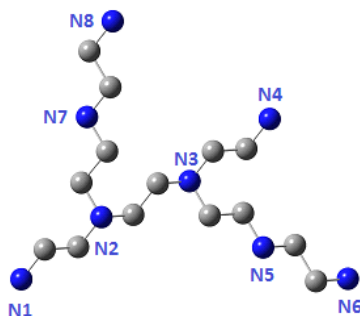


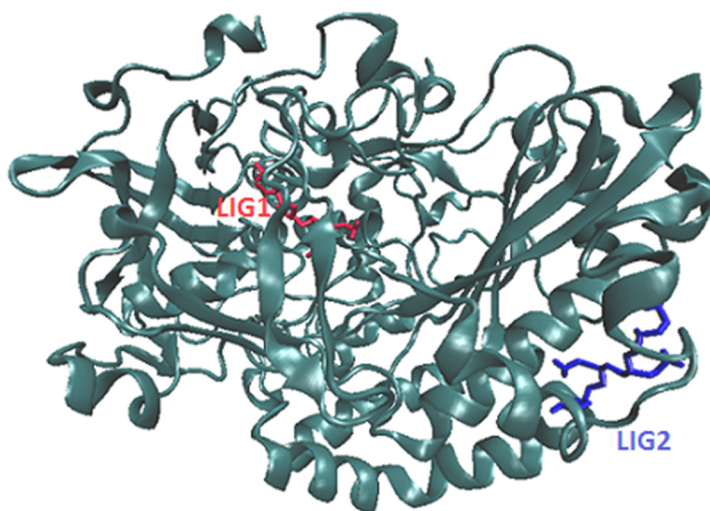
Figure 4. The ligand PEI_C14N8_07_B22.

The values of binding free energy were collected in the vicinity of the protein active site, where the ligand PEI_C14N8_07_B22 (Figure 4) was docked; data are listed in Table 1.

Table 1. The best binding energy of ligand PEI_C14N8_07_B22 at the active sites LIG1 and LIG2 of 3QVR, during the nine explored conformations.

Ligand binding site	1	2	3	4	5	6	7	8	9	Best docking Energy (kcal/mol)
LIG1	-5.8	-5.8	-5.6	-5.6	-5.6	-5.5	-5.5	-5.5	-5.5	-5.8
LIG2	-4.5	-4.3	-4.2	-4.2	-4.2	-4.2	-4.2	-4.1	-4.1	-4.5

Based on the best docked energies: -5.8 and -4.5 kcal/mol, two sites were differentiated on the protein body, which show the best affinity to PEI (Table 1). In the first case, the ligand is bound to amino acids inside of the protein area (LIG1, Figure 5), while in the second case the binding takes place outside of the enzyme surface (LIG2, Figure 5). That's why the Molecular Dynamics will be performed for the first and second active places of this protein, separately. Thus, the docking study gave information about the type and number of interactions between ligand and amino acid residuals of the enzyme. The results obtained during the docking procedure became the starting point in molecular dynamics study.

**Figure 5.** Two sites of the most important interaction ligand - enzyme (3QVR): inside of the protein, named LIG1, and on its surface, named LIG2. As a ligand, the molecule PEI_C14N8_07_B22 was used (see Figure 4).

Molecular Dynamics results

The Molecular Dynamics simulations allow to study the interactions within the enzyme – ligand complex, in the natural environment and in a large number of conformations of this complex, as well [18]. During MD, the time evolution of ligand PEI_C14N8_07_B22 lying in two active sites of the conformational space of 3QVR protein, inside (LIG1) and on its surface (LIG2) (Figure 5) was followed. The 60 ns of collected trajectories were used for structural analysis. In both cases, the first 10 ns of MD simulation show considerable fluctuations, while in the remaining time of simulation, the trajectories seem stabilized, meaning the equilibrium stage was attained (Figure 6).

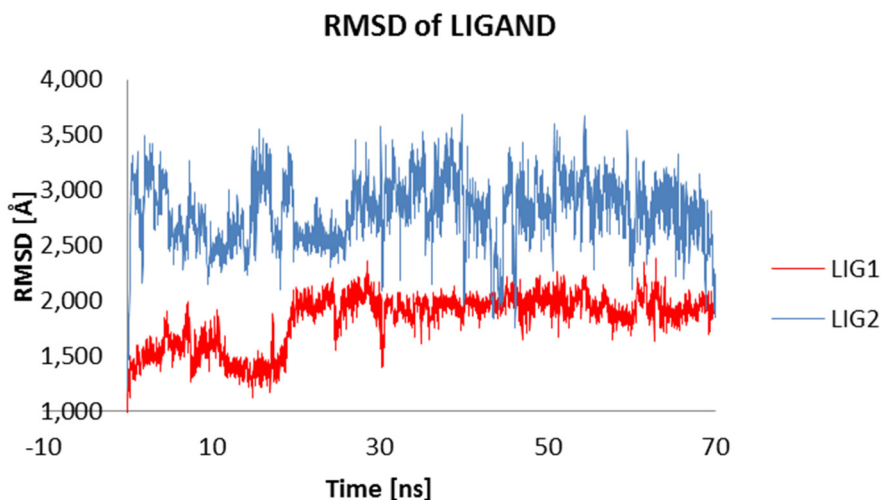
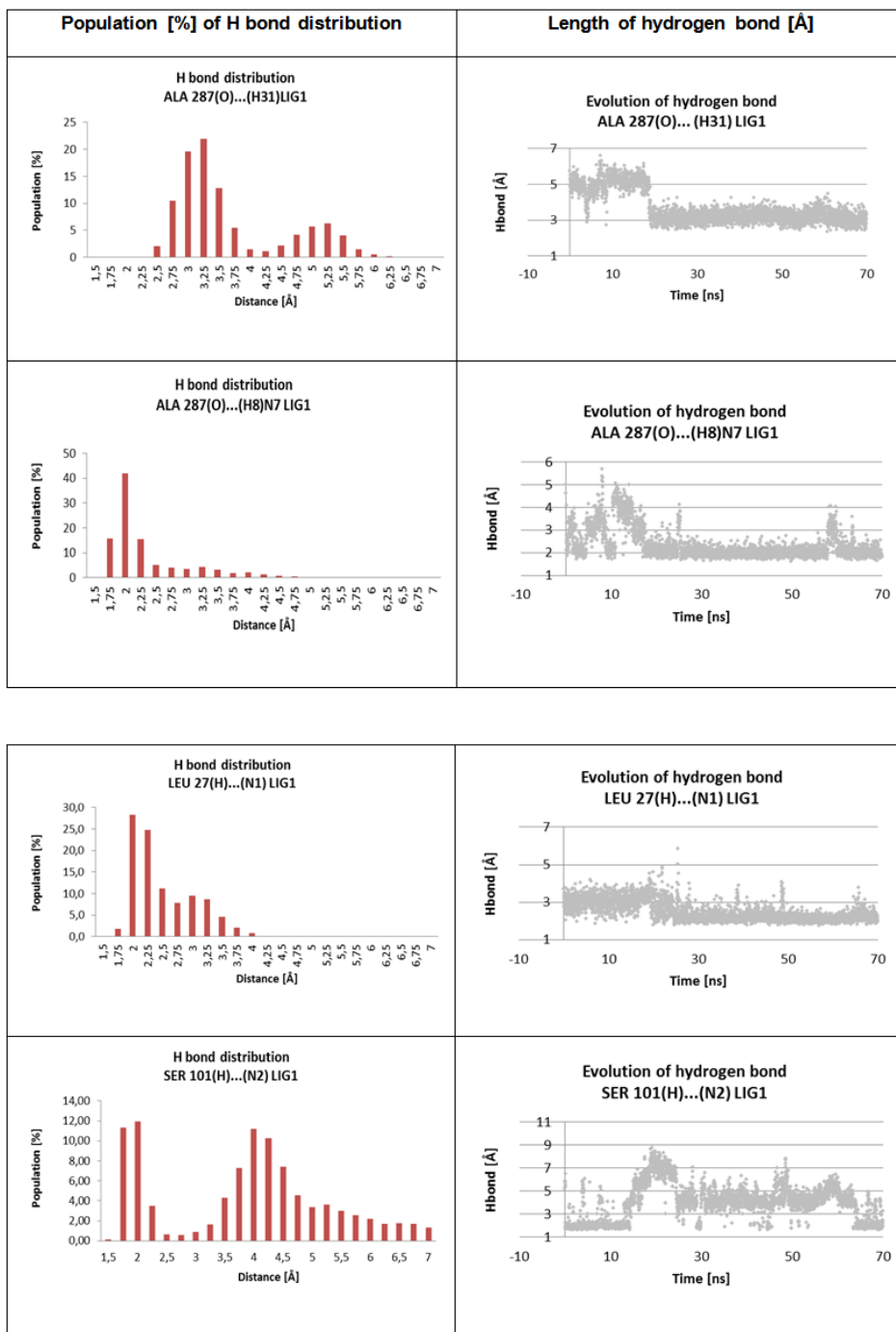


Figure 6. RMSD distribution of ligand: values characterizing the ligand interaction at the first active site (LIG1, red color) of 3QVR enzyme, inside the protein and at the second active site (LIG2, blue color), on the protein surface.

In case of complex located inside the protein body (LIG1, Figure 5) the MD simulation found five amino acids: ALA287, LEU27, SER101, SER94 and SER289 that interact with the ligand and stabilize the complex 3QVR – PEI; in case of complex located outside, on the enzyme surface (LIG2, Figure 5) only three amino acids ASN471, ASP358 and GLU354 have been found. In the first case, the number of formed hydrogen bonds HB is six while in the second, this number is seven.

NATURE OF POLYETHYLENEIMINE-GLUCOSE OXIDASE INTERACTIONS



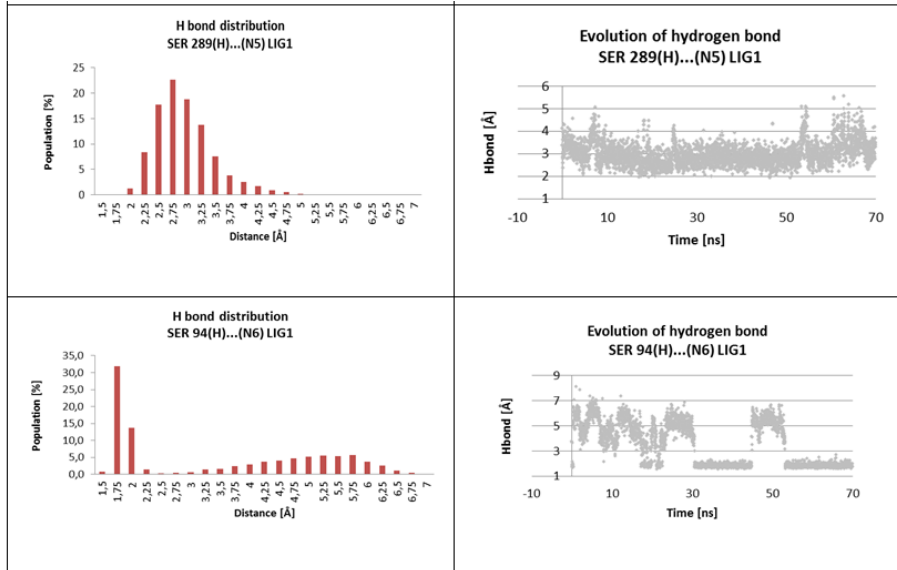
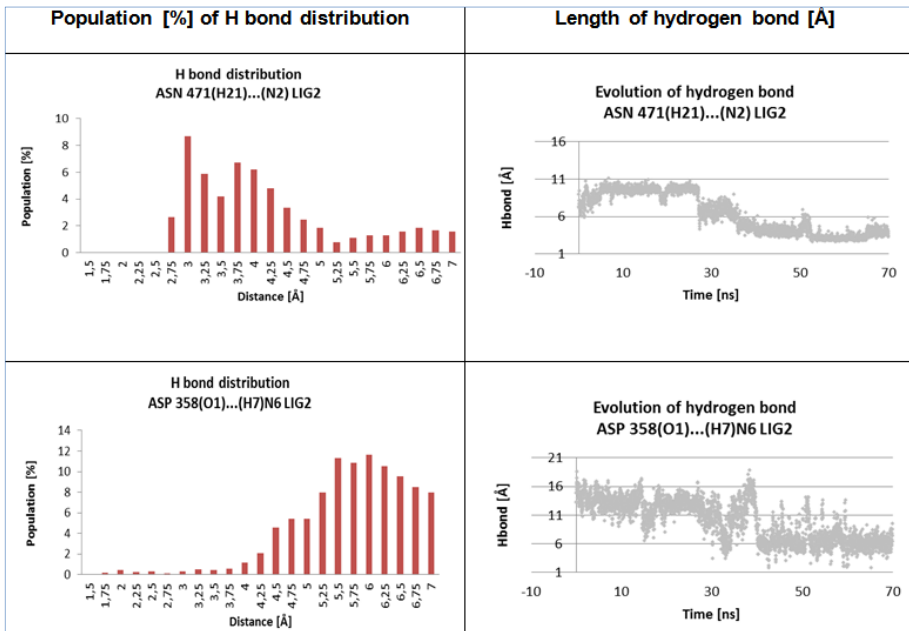
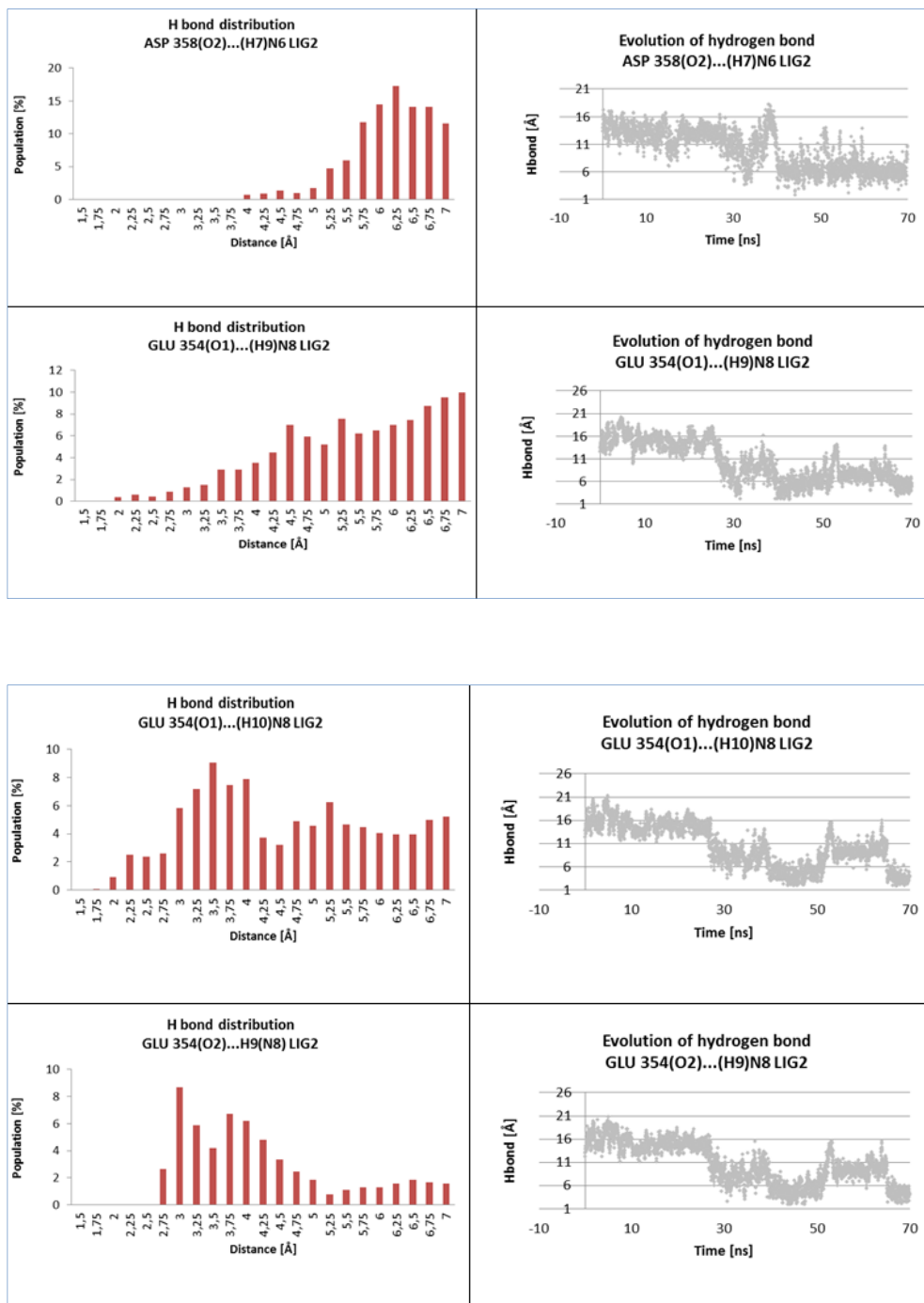


Figure 7. Distribution of hydrogen bonds length during the MD simulation time, created by PEI_C14N8_07_B22 with selected amino acids from the LIG1 active site of 3QVR inside of this protein (left) and evolution of hydrogen bonds as a function of time [ns] of MD.



NATURE OF POLYETHYLENEIMINE-GLUCOSE OXIDASE INTERACTIONS



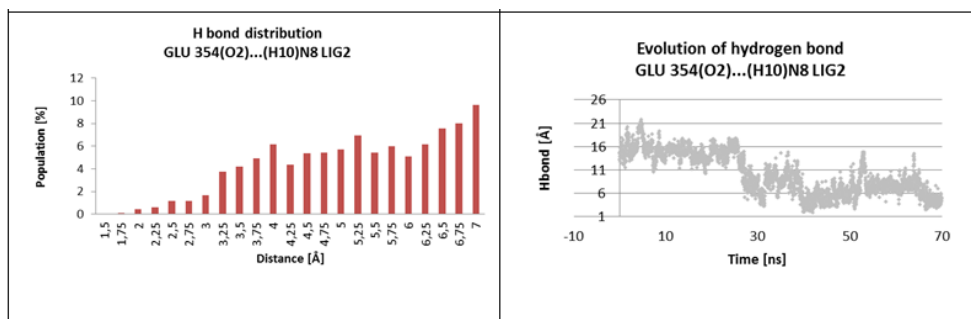


Figure 8. Distribution of hydrogen bonds length during the MD simulation time, created by PEI_C14N8_07_B22 with selected amino acids from the LIG2 active site of 3QVR on the surface of this protein (left) and evolution of hydrogen bonds as a function of time [ns] of MD (right).

In the first active side, LIG1, (Figure 7) of enzyme, there are five different aminoacids: ALA 287, LEU 27, SER 101, SER 289, SER 94 that form HBs in their interaction with the ligand (PEI_C14N8_07_B22). In case of ALA 287, LEU 27 and SER 101, such interactions appear at about 20 ns of the trajectory while in case of SER 289 they occur during all the time of simulation (Figures 7). Only the behavior of SER 94 is quite different ((Figure 7, bottom). Here HB appear from 30 ns of MD simulation but in the meantime disappear for about 10 ns. One can see the formation of strong HB (1.7Å) from 30 to 40 ns and next from 50 to 70 of simulation of DM. Aminoacid ALA 287 creates two HBs: ALA(O)...(H31) LIG1 and ALA(O)...(H8) LIG1 with ligand PEI_C14N8_07_B22, of the length 2.75-3Å (with 3Å having the largest distribution) and 1.75 Å -2.25 Å (with 2Å the largest distribution), respectively (Figures 7, left).

For other aminoacids: LEU27, SER101, SER289 and SER 94, the interactions of ligand PEI_C14N8_07_B22 with different N atoms and different H atoms of the amino acids in the enzyme are strong and medium ones (Figures 7, left). H atom of LEU27 creates a hydrogen bond with the nitrogen atom N1 of length 2Å-2.25Å (LEU 27(H)...(N1) LIG1). In case of interactions SER 101(H)...(N2) LIG1, SER 289(H)...(N5) LIG1, SER 94(H)...(N6) within LIG1, the length of hydrogen bonds are 1.75 Å -2 Å (with 1.75 Å showing the largest distribution), 2.5 Å -3 Å (with 2.75 Å the largest distribution) and 1.75 Å -2 Å (with 1.75 Å the largest distribution), respectively (Figures 7, left). In the LIG2 active side of enzyme (Figure 5), located on its surface, there are only three different amino acids: ASN 471, ASP 358, GLU 354.

In case of ligand docked at the enzyme surface, more precisely at LIG2, the interactions ligand - enzyme appear relatively late, during MD simulations, at about 30-40 ns (Figures 8, left) and all the formed HB are of medium and low strength (Figures 8, right). In addition, the formed bonds tend to disappear and re-appear during MD simulation (Figures 8, right).

In the interior of enzyme, at LIG1, there are two kinds of HB, formed between the enzyme and ligand: “amino acid (O) ... (H) ligand” and “amino acid (H) ... (N) ligand”. In these cases, two amino groups, N₁H₂ and N₆H₂, are involved in the formation of hydrogen bonds (Figure 7). On the surface of enzyme, at LIG2, formation of HB of the type „amino acid NH (H) ... (N) ligand” involves the nitrogen atoms N₈ and N₆ of amino groups, while HB of the type „amino acid NH (H) ... (N) ligand” are provided by the nitrogen atoms of the amino groups N₆H₂ and N₂ (Figure 8)

Thus, the number and the type of amino groups NH₂ of ligand, involved in the formation of a complex with the enzyme, are two parameters that control the interaction ligand – enzyme. The stabilization of ligand – protein complex depends not only on the strength of the created HB but also on the number of each type of the created of hydrogen bonds.

CONCLUSIONS

The nature of interactions between Polyethylenimine and glucose oxidase 3QVR enzyme was studied by docking and Molecular dynamics techniques.

The docking procedure evidenced two places of major interaction of the protein with the polymer PEI: (LIG1), of -5.8 kcal/mol and (LIG2), of -4.5 kcal/mol, located inside the enzyme and on its surface, respectively. It was found that the hydrogen bonds HB, formed between enzyme and ligand, are shorter (i.e., stronger) inside of the protein compared to HB formed on the protein surface, which are, consequently, longer and weaker ones. The number and type of HB formed by the ligand with the active sites of the enzyme are important factors in the stabilization of the complex ligand – enzyme; also important are the dynamics of HB formation/breaking, within environmental conditions consideration.

ACKNOWLEDGEMENTS

This work was financially supported by GEMNS project granted in the European Union’s Seventh Framework Programme under the frame of the ERA-NET EuroNanoMed II (European Innovative Research and Technological Development Projects in Nanomedicine).

REFERENCES

1. C. Sittiwet, M. Srisa-ard and Y. Baimark, *Polymer J.*, **2010**, *5*, 108.
2. T. Homma, T. Ichimura, M. Kondo, T. Kuwahara, M. Shimomura, *Eur. Polymer J.*, **2014**, *51*, 130.
3. M. Shimomura, N. Kojima, K. Oshima, T. Yamauchi, S. Miyauchi, *Polymer J.*, **2001**, *33*, 629.
4. M. Poplawska, M. Bystrzejewski, I.P. Grudzinski, M.A. Cywinska, J. Ostapko, A. Cieszanowski, *CARBON*, **2014**, *74*, 180.
5. V.A. Karachevtsev, A.Y.U. Glamazda, E.S. Zarudnev, M.V. Karachevtsev, V.S. Leontiev, A.S. Linnik, O.S. Lytvyn, A.M. Plokhotnichenko, S.G. Stepanian, *Ukr. J. Phys.*, **2012**, *57*, 700.
6. A. Kasprzak, M. Poplawska, M. Bystrzejewski, O. Łabędź, I.P. Grudziński, *Royal Soc. Chem. Adv.*, **2015**, *5*, 85556.
7. O. Trott, A.J. Olson, *J. Comp. Chem.*, **2010**, *31*, 455.
8. O. Trott, A.J. Olson, *J. Comput. Chem.*, **2010**, *31*, 455.
9. K. Dhananjayan, K. Kalathil, A. Sumathy, P. Sivanandy, *Der Pharma Chemica*, **2014**, *6* (2), 378.
10. R. Abagyan, M. Totrov, *Curr. Opin. Chem. Biol.*, **2001**, *5*, 375.
11. RCSB PDB, GOx - molecule of the month, May 2006.
12. C.I. Bayly, P. Cieplak, W.D. Cornell, P.A. Kollman, *J. Phys. Chem.*, **1993**, *97*, 10269.
13. S.A. Adelman, J.D. Doll, *J. Chem. Phys.*, **1976**, *64*(6), 2375.
14. J.P. Ryckaert, G. Ciccotti, H.J.C. Berendsen, *J. Comput. Phys.*, **1977**, *23*(3), 327.
15. W. Humphrey, A. Dalke and K. Schulten, *J. Molec. Graphics*, **1996**, *14*, 33.
16. B.R. Miller, T.D. McGee, J.M. Swails, N. Homeyer, H. Gohlke, A.E. Roitberg, *J. Chem. Theory. Comput.*, **2012**, *8* (9), 3314.
17. D.A. Case, T.A. Darden, T.E. III Cheatham, C.L. Simmerling, J. Wang, R.E. Duke, R. Luo, R.C. Walker, W. Zhang, K.M. Merz, B. Roberts, B. Wang, S. Hayik, A. Roitberg, G. Seabra, I. Kolossváry, K.F. Wong, F. Paesani, J. Vanicek, J. Liu, X. Wu, S.R. Brozell, T. Steinbrecher, H. Gohlke, Q. Cai, X. Ye, J. Wang, M.J. Hsieh, G. Cui, D.R. Roe, D.H. Mathews, M.G. Seetin, C. Sagui, V. Babin, T. Luchko, S. Gusarov, A. Kovalenko, and P.A. Kollman. AMBER 11, University of California, San Francisco, **2010**.
18. G. Todde, S. Hovmoller, A. Laaksonen, F. Mocci, *Proteins*, **2014**, *82*, 353.

*Dedicated to Professor Mircea Diudea
on the Occasion of His 65th Anniversary*

POLYHEDRAL GRAPHS UNDER AUTOMORPHISM GROUPS

MODJTABA GHORBANI^{a,*} AND MARDJAN HAKIMI-NEZHAAD^a

ABSTRACT. A modified Wiener number was proposed by Graovać and Pisanski. It is based on the full automorphism group of a graph. In this paper, we compute the difference between these topological indices for some polyhedral graphs.

Keywords: *automorphism, polyhedral graphs, topological indices.*

INTRODUCTION

A topological index is a numerical value associated to a chemical constitution purporting for correlation of chemical structure with various physical properties, chemical reactivity or biological activity. In an exact phrase, if Σ denotes the class of all finite graphs then a topological index is a function Top from Σ into real numbers with the property that $\text{Top}(I_1) = \text{Top}(I_2)$, if the graphs I_1 and I_2 are isomorphic. Obviously, the number of vertices and the number of edges may be considered as topological indices. Wiener index is the first reported distance based topological index defined as half sum of the distances between all the pairs of vertices in a molecular graph. Topological indices are abundantly used in QSPR and QSAR researches. So far, a variety of topological indices have been described. The Wiener number is one of them. It is the first reported distance based topological index. The Wiener number is defined as the half sum of distances between all the pairs of vertices in a molecular graph [1]. Randić defined the hyper-Wiener index

^a *Department of Mathematics, Faculty of Science, Shahid Rajaee Teacher Training University, Tehran, 16785-136, I. R. Iran*

* *Corresponding Author: mghorbani@srttu.edu*

of acyclic graphs [2], and then Klein et al. [3] generalized Randić's definition for all connected graphs, as a generalization of the Wiener index. It is defined as:

$$WW(\Gamma) = 1/2W(\Gamma) + 1/2 \sum_{\{x,y\}} (d(x,y))^2. \tag{1}$$

We refer to [4-6] for mathematical properties and chemical meaning of this topological index.

An automorphism of the graph Γ is a bijection α on it, which preserves the edge set E i.e., if $e=uv$ is an edge, then $\alpha(e)=\alpha(u)\alpha(v)$ is an edge of E . Here the image of vertex u is denoted by $\alpha(u)$. We denote the set of all automorphisms of Γ by $\text{Aut}(\Gamma)$ and this set, under the composition of mappings, forms a group. This group acts transitively on the set of vertices, if for any pair of vertices $u, v \in V$, there is an automorphism α such that $\alpha(u)=v$.

By means of automorphism group, Graovać and Pisanski proposed the modified Wiener index [7,8], as follows:

$$\hat{W}(\Gamma) = \frac{|V(\Gamma)|}{2|G|} \sum_{x \in V(\Gamma)} \sum_{\alpha \in G} d(x, \alpha(x)), \tag{2}$$

In [9], a modified hyper-Wiener index was defined as:

$$\hat{W}W(\Gamma) = \frac{1}{2} \hat{W}(\Gamma) + \frac{|V(\Gamma)|}{4|G|} \sum_{u \in V(\Gamma), \alpha \in G} d(u, \alpha(u))^2. \tag{3}$$

Theorem 1 [7]. Let Γ be a graph with automorphism group $G = \text{Aut}(\Gamma)$ and the vertex set $V(\Gamma)$. Let V_1, V_2, \dots, V_k be all orbits of action of G on $V(\Gamma)$. Then

$$\hat{W}(\Gamma) = |V(\Gamma)| \sum_{i=1}^k \frac{W(V_i)}{|V_i|}. \tag{4}$$

Corollary 2. Let Γ be a vertex-transitive graph, then $W(\Gamma) = \hat{W}(\Gamma)$.

It is easy to see that the Wiener index is equal to the modified Wiener index if Γ is vertex-transitive and the modified Wiener index is zero if and only if $\text{Aut}(\Gamma)$ is trivial. For a given graph Γ , the difference between Wiener and modified Wiener indices is [10,11]:

$$\delta(\Gamma) = W(\Gamma) - \hat{W}(\Gamma). \tag{5}$$

Similarly, the difference between hyper-Wiener and modified hyper-Wiener indices can be written as:

$$\delta\delta(\Gamma) = WW(\Gamma) - \hat{W}W(\Gamma). \tag{6}$$

Example 3 [8]. Wiener index of Circumcoronenes with $5n^2$ vertices, for $n \geq 2$ is:

$$W(C_{5n^2}) = \frac{1}{6}(124n^5 - 35n^3 + n),$$

and the modified-Wiener index of circumcoronenes for $n \geq 2$ is:

$$\hat{W}(C_{5n^2}) = \frac{1}{3}n^3(n^2 - 10).$$

Then, we have

$$\delta(C_{5n^2}) = \frac{n}{6}(14n^4 - 15n^2 + 1).$$

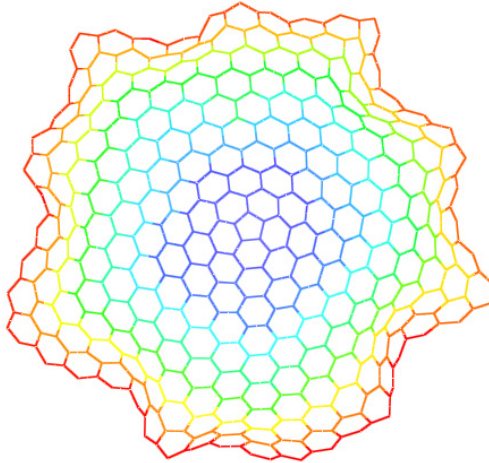


Figure 1. Circumcoronene; $n=9$.

Example 4 [8]. Wiener index of circumcoronenes with $6n^2$ vertices, for $n \geq 1$, is:

$$W(C_{6n^2}) = \frac{n}{5}(164n^4 - 30n^2 + 1)$$

and the modified-Wiener index of circumcoronenes for $n \geq 1$ is:

$$\hat{W}(C_{6n^2}) = 30n^5 - 3n^3.$$

Hence, we can deduce that

$$\delta(C_{6n^2}) = \frac{n}{5}(14n^4 - 15n^2 + 1).$$

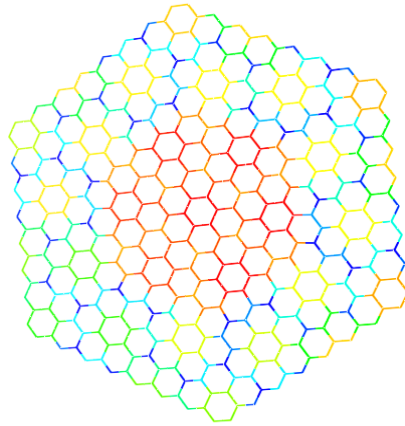


Figure 2. Circumcoronene; $n=8$.

RESULTS AND DISCUSSION

A planar graph is the one that can be drawn on the plane in such a way that its edges intersect only at their endpoints. Let Γ be a planar graph and n, m, f are respectively the number of vertices, edges and faces. Then by Euler theorem, we have

$$n - m + f = 2 \tag{7}$$

A general polyhedron is the one that satisfies the Euler relation. If a cubic polyhedron has no face of size greater than 6, then it has a positive curvature. In [12], Ghorbani introduced a new class of fullerene graphs with pentagons and heptagons. In this paper, we also introduce a class of polyhedral graphs with squares, pentagons and hexagons (Figures 3;4).

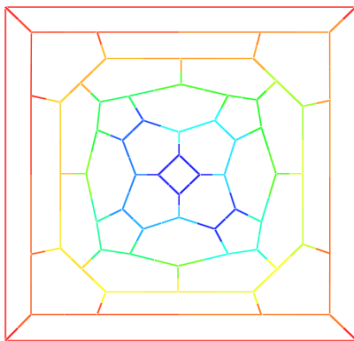


Figure 3. The Case of $n = 4$ in C_{16n} .

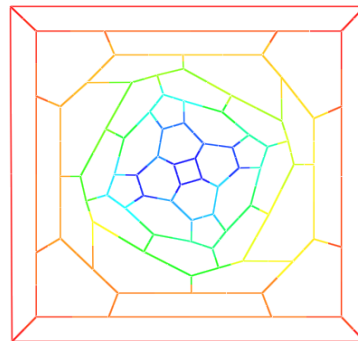


Figure 4. The Case of $n = 5$ in C_{16n} .

This class of polyhedral graphs has exactly $16n$ vertices, where n is an integer greater than or equal with 4, herein denoted by C_{16n} . By Euler's formula, we can conclude that this graph has exactly 2 squares, 8 pentagons and $8(n-1)$ hexagons, for $n \geq 4$.

Theorem 5. For $n \geq 4$, the automorphism group of graph C_{16n} is isomorphic to

$$Aut(C_{16n}) \cong \begin{cases} D_{16} & n \mid 2 \\ D_8 & n \nmid 2 \end{cases}$$

Proof. At first we compute the order of $G = Aut(C_{16n})$ of symmetries of the polyhedral graph C_{16n} , for $n=4$ depicted in Figure 5; the automorphism group of C_{16n} for $n \geq 5$ and $n \nmid 2$ can be computed similarly. If α denotes the rotation of C_{16n} for 45° and β is a reflection over the central vertical line, then $G = \langle \alpha, \beta \rangle$. On the other hand, $|\langle \alpha, \beta \rangle| = 16$ where $\alpha^8 = \beta^2 = 1$, $\beta\alpha\beta = \alpha^{-1}$. This leads us to conclude that $G = \langle \alpha, \beta \rangle \cong D_{16}$.

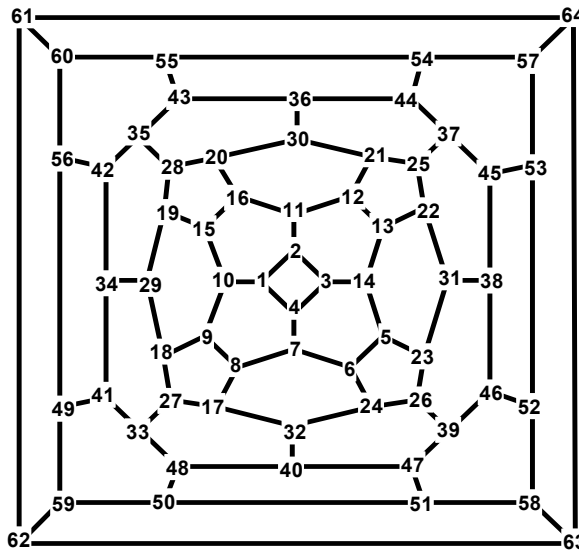


Figure 5. Labeling of cubic polyhedral graph C_{16n} for $n=4$.

Similarly, for $n \nmid 2$, $G \cong D_8$ and the proof is completed.

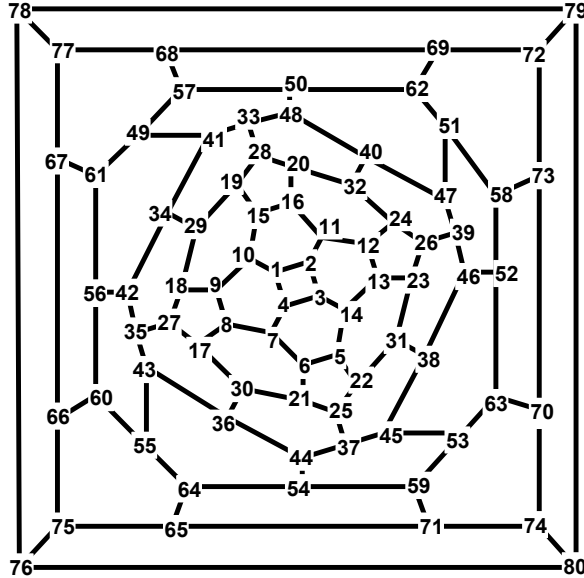


Figure 6. Labeling of cubic polyhedral graph C_{16n} for $n=5$.

Now, we prove that the Wiener index of this class of polyhedral graphs for $n \geq 9$ is:

$$W(C_{16n}) = \frac{256}{3}n^3 + \frac{8384}{3}n - 7432. \quad (8)$$

The Wiener index of this class of polyhedral graphs is computed for the first time in this paper. We can also apply our method to compute the other classes of polyhedral graphs. In [13], a method to obtain a polyhedral graphs from a zig – zag or armchair nanotubes, is described. Here, by continuing this method, we can construct an infinite class of polyhedral graphs and then compute its Wiener number. The symbol $T_z[m,n]$ means a zig–zag nanotube with m rows and n columns of hexagons (see Figure 7). Combine a nanotube $T_z[8,n]$ with two copies of cap B (Figure 8) as shown in Figure 9; the resulted graph is a polyhedral graph with $16n$ vertices, for $n \geq 9$.

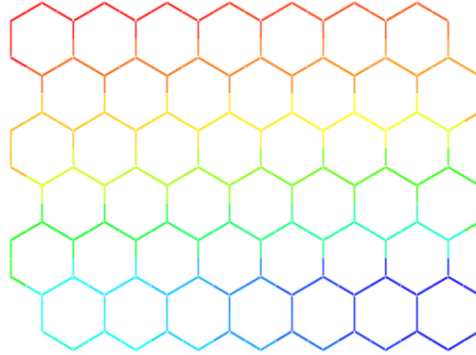


Figure 7. 2D graph of a zig-zag nanotube $T_z[m, n]$, for $m = 8$; $n = 6$.

A block matrix can be written in terms of smaller matrices. In the following theorem, the Wiener index of the $G = T_z[8, n]$ nanotube for $n \geq 9$ is computed, see Figure 9.

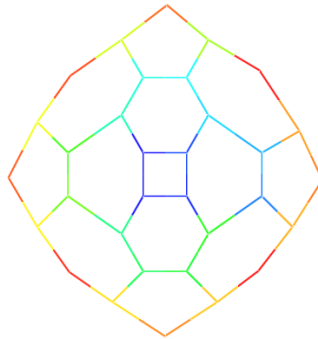


Figure 8. Cap B .

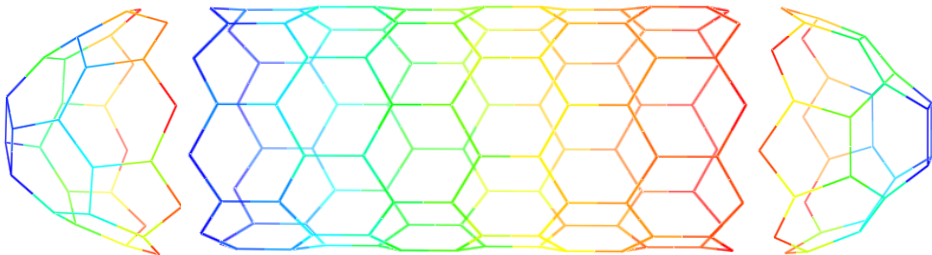


Figure 9. Polyhedral graph C_{16n} constructed by combining two copies of cap B , and the zig-zag nanotube $T_z[8, n]$.

Theorem 6. For $n \geq 9$,

$$W(T_z[8, n]) = \frac{256}{3}n^3 - 512n^2 + \frac{11072}{3}n - 11392. \quad (9)$$

Proof. According to Figure 9, there are $n + 1$ rows of vertices. We suppose the vertices of the last row are $U = \{u_1, u_2, \dots, u_{16}\}$. To compute the Wiener index of this nanotube we use a recursive sequence method. Let t_n be the two times of Wiener index of $G = T_z[8, n]$. A straightforward computation yields the recurrence

$$\begin{aligned} 2W(G) = t_n &= \sum_{x,y \in U} d(x,y) + \sum_{x,y \in V \setminus U} d(x,y) + 2 \sum_{x \in U, y \in V \setminus U} d(x,y) \\ &= 1024 + t_{n-1} + 2 \sum_{x \in U, y \in V \setminus U} d(x,y). \end{aligned} \quad (10)$$

To compute the summation $\sum_{x \in V, y \in V \setminus U} d(x,y)$ by using the symmetry of graph we have

$$\sum_{x \in U, y \in V \setminus U} d(x,y) = 8(d(u_1) + d(u_2)), \quad (11)$$

where $d(u_1) = \sum_{y \in V \setminus U} d(u_1, y)$ and $d(u_2)$ defines the similarly (see Figure 10).

By computing these values, one can see that:

$$\begin{aligned} d(u_1) &= 16n^2 - 72n + 184, \quad n \geq 9, \\ d(u_2) &= 16n^2 - 88n + 288, \quad n \geq 10. \end{aligned} \quad (12)$$

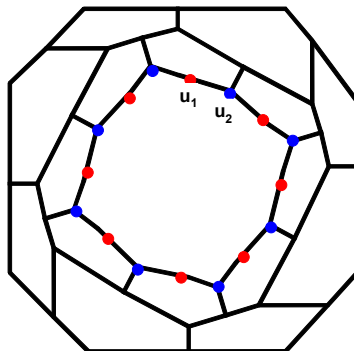


Figure 10. 2-D graph of the nanotube $T_z[8,2]$.

This implies that $t_{n+1} = 1024 + t_n + 8(d(u_1) + d(u_2))$. The solution of this recurrence is

$$W(G) = \frac{256}{3}n^3 - 512n^2 + \frac{11072}{3}n - 11392. \quad (13)$$

Theorem 7. For $n \geq 9$,

$$W(C_{16n}) = \frac{256}{3}n^3 + \frac{8384}{3}n - 7432. \quad (14)$$

Proof. From Figure 9, one can see that the distance matrix of polyhedral graph C_{16n} can be written as a block matrix as follows:

Suppose $\{v_1, v_2, \dots, v_r\}$, $\{u_1, \dots, u_s\}$ and $\{w_1, \dots, w_r\}$ be the set of vertices of the first cap, vertices of $T_z[8, n]$ and vertices of the second cap, respectively. The distance matrix D can be broken to the following form:

$$D = \begin{bmatrix} V & B & W \\ B & U & B \\ W & B & V \end{bmatrix},$$

where V , B and W are distances between vertices of the first cap with the vertices of $T_z[8, n]$ and vertices of the second cap. The matrix U is the distance matrix of vertices $\{u_1, \dots, u_s\}$. In other words, U is the distance matrix of $T_z[8, n]$. This matrix was computed in Theorem 6. It is easy to see that the Wiener index is equal to the half-sum of distances of the distance matrix D between all pairs of vertices. For any polyhedral graph C_{16n} the matrix V is constant, as shown in Figure 11. The summation of entries of matrix V is 3880. Obviously, the distance matrices B , U and W are dependant to the number of rows in the nanotube $T_z[8, n]$. In other words, if w_n and w_{n-1} be the Wiener indices of the polyhedral graphs C_{16n} and $C_{16(n-1)}$, respectively, then similar to the proof of the Theorem 1, for $n \geq 10$, we have

$$w_{10} - w_9 = 25920, w_{11} - w_{10} = 31040, w_{12} - w_{11} = 36672, w_{13} - w_{12} = 42816.$$

Again, a straightforward computation yields the recurrence

$$w_n - w_{n-1} = 256n^2 - 256n + 2880. \quad (15)$$

and the solution of this recurrence is

$$W(C_{16n}) = \frac{256}{3}n^3 + \frac{8384}{3}n - 7432. \quad (16)$$

This completes the proof.

Corollary 8. For polyhedral graph C_{16n} , we have

$$\delta(C_{16n}) = \begin{cases} \frac{64}{3}n^3 - 256n^2 + \frac{6704}{3}n - 7432, & n = 4k, k \geq 3 \\ \frac{64}{3}n^3 - 256n^2 + \frac{6896}{3}n - 7432, & \text{otherwise} \end{cases}, \quad (17)$$

$$\hat{\delta}(C_{16n}) = \begin{cases} \frac{32}{3}n^3 - 864n^2 + \frac{41800}{3}n - 60524, & 2 | n, n = 4k, \\ \frac{32}{3}n^3 - 864n^2 + \frac{43432}{3}n - 60524, & 2 | n, n = 2(2k - 1). \\ \frac{32}{3}n^3 - 896n^2 + \frac{43144}{3}n - 60524, & 2 \nmid n \end{cases} \quad (18)$$

Proof. At first by a direct computation, we have

$$\begin{aligned} W(C_{64}) &= 9984, W(C_{80}) = 17520, W(C_{96}) = 27864, W(C_{112}) = 41436, W(C_{128}) = 58624, \\ WW(C_{64}) &= 34100, WW(C_{80}) = 65976, WW(C_{96}) = 114684, WW(C_{112}) = 185496, \\ WW(C_{128}) &= 283916, WW(C_{144}) = 417748. \end{aligned}$$

By applying the methods of [6], we have:

$$\begin{aligned} W(C_{16n}) &= \frac{256}{3}n^3 + \frac{8384}{3}n - 7432, \quad n \geq 9 \\ WW(C_{16n}) &= \frac{128}{3}n^4 + \frac{128}{3}n^3 + \frac{352}{3}n^2 + \frac{52576}{3}n - 60524, \quad n \geq 10. \end{aligned} \quad (19)$$

On the other hand, by using Theorem 5, we have:

$$\begin{aligned} \hat{W}(C_{64}) &= 9760, \hat{W}(C_{80}) = 16480, \hat{W}(C_{96}) = 25824, \hat{W}(C_{112}) = 37912, \hat{W}(C_{128}) = 53568, \\ \hat{WW}(C_{64}) &= 36128, \hat{WW}(C_{80}) = 67280, \hat{WW}(C_{96}) = 113568, \\ \hat{WW}(C_{112}) &= 184352, \hat{WW}(C_{128}) = 281728. \end{aligned}$$

and for $n \geq 9, k \geq 3$ we have:

$$\hat{W}(C_{16n}) = \begin{cases} 64n^3 + 256n^2 + 560n, & n = 4k \\ 64n^3 + 256n^2 + 496n, & \text{otherwise} \end{cases},$$

$$\widehat{WW}(C_{16n}) = \begin{cases} \frac{128}{3}n^4 + 32n^3 + \frac{2944}{3}n^2 + 3592n, & 2 \mid n, n = 4k, \\ \frac{128}{3}n^4 + 32n^3 + \frac{2944}{3}n^2 + 3048n, & 2 \mid n, n = 2(2k - 1). \\ \frac{128}{3}n^4 + 32n^3 + \frac{3040}{3}n^2 + 3144n, & 2 \nmid n \end{cases} \quad (20)$$

The proof can be drawn from (19) and (20).

V =	0, 1, 2, 1, 4, 3, 2, 3, 2, 1, 2, 3, 4, 3, 2, 3, 4, 3, 3, 4, 4, 5, 5, 4, 5, 5, 4, 4, 4, 5, 6, 5
	1, 0, 1, 2, 3, 4, 3, 4, 3, 2, 1, 2, 3, 2, 3, 2, 5, 4, 4, 3, 3, 4, 4, 5, 4, 4, 5, 5, 4, 5, 6
	2, 1, 0, 1, 2, 3, 2, 3, 2, 3, 2, 1, 4, 3, 4, 5, 5, 4, 4, 3, 3, 4, 4, 5, 5, 4, 4, 5, 5, 6, 5, 4, 5
	1, 2, 1, 0, 3, 2, 1, 2, 3, 2, 3, 4, 3, 2, 3, 4, 3, 4, 4, 5, 5, 4, 4, 3, 3, 4, 4, 5, 5, 6, 5, 4, 4
	4, 3, 2, 3, 0, 1, 2, 3, 4, 5, 4, 3, 2, 1, 6, 5, 4, 5, 7, 6, 6, 4, 3, 1, 2, 4, 2, 5, 7, 6, 6, 5, 2, 3, 3
	3, 4, 3, 2, 1, 0, 1, 2, 3, 4, 5, 4, 3, 2, 5, 6, 3, 4, 6, 7, 5, 4, 2, 1, 5, 2, 4, 7, 5, 6, 5, 6, 3, 2, 2
	2, 3, 2, 1, 2, 1, 0, 1, 2, 3, 4, 5, 4, 3, 4, 3, 4, 1, 2, 4, 5, 7, 6, 4, 1, 2, 4, 5, 7, 6, 4, 3, 6, 4, 3, 3
	3, 4, 3, 2, 3, 2, 1, 0, 1, 2, 5, 6, 5, 4, 3, 4, 4, 1, 2, 4, 5, 7, 6, 4, 1, 2, 4, 5, 7, 6, 4, 3, 6, 5, 2
	2, 3, 4, 3, 4, 3, 2, 1, 0, 1, 4, 5, 6, 5, 2, 3, 2, 1, 3, 4, 6, 7, 5, 4, 7, 5, 2, 4, 2, 5, 6, 3, 2, 5, 6, 3
	1, 2, 3, 2, 5, 4, 3, 2, 1, 0, 3, 4, 5, 4, 1, 2, 3, 2, 2, 2, 3, 5, 6, 6, 6, 5, 6, 6, 6, 3, 3, 4, 7, 4
	2, 1, 2, 3, 4, 5, 4, 5, 4, 3, 0, 1, 2, 3, 3, 2, 1, 6, 5, 3, 2, 2, 3, 5, 6, 6, 6, 6, 6, 3, 3, 4, 7, 4
	3, 2, 3, 4, 3, 4, 5, 6, 5, 4, 1, 0, 1, 2, 3, 2, 7, 6, 4, 3, 1, 2, 4, 4, 3, 1, 2, 4, 5, 2, 5, 2, 3, 6
	4, 3, 2, 3, 2, 3, 4, 5, 6, 5, 2, 1, 0, 1, 4, 3, 6, 7, 5, 4, 2, 1, 3, 4, 2, 4, 7, 5, 6, 6, 3, 3, 2, 5
	3, 2, 1, 2, 1, 2, 3, 4, 5, 4, 3, 2, 1, 0, 5, 4, 5, 6, 6, 5, 3, 3, 2, 2, 3, 3, 3, 6, 6, 7, 4, 3, 4
	2, 3, 4, 3, 6, 5, 4, 3, 2, 1, 2, 3, 4, 5, 0, 1, 4, 3, 1, 2, 4, 5, 7, 6, 6, 5, 7, 4, 2, 2, 3, 6, 5
	3, 2, 3, 4, 5, 6, 5, 4, 3, 2, 1, 2, 3, 4, 5, 4, 1, 0, 5, 4, 2, 1, 3, 4, 6, 7, 4, 7, 5, 2, 3, 2, 5, 6
	4, 5, 4, 3, 4, 3, 2, 1, 2, 3, 6, 7, 6, 5, 4, 5, 0, 2, 4, 6, 8, 6, 4, 2, 7, 3, 1, 5, 3, 7, 5, 1
	3, 4, 5, 4, 5, 4, 3, 2, 1, 2, 5, 6, 7, 6, 6, 3, 4, 2, 0, 2, 4, 6, 8, 6, 4, 7, 5, 1, 3, 1, 5, 7, 3
	3, 4, 5, 4, 7, 6, 5, 4, 3, 2, 3, 3, 4, 5, 6, 1, 2, 4, 2, 0, 2, 4, 6, 8, 6, 6, 5, 7, 3, 1, 1, 5, 7, 5
	4, 3, 4, 5, 6, 7, 6, 5, 4, 3, 2, 3, 4, 5, 2, 1, 6, 4, 2, 0, 2, 4, 6, 8, 6, 3, 7, 5, 1, 3, 1, 5, 7
	4, 3, 4, 5, 4, 5, 6, 7, 6, 5, 2, 1, 2, 3, 4, 3, 8, 6, 4, 2, 0, 2, 4, 6, 1, 5, 7, 3, 5, 1, 3, 7
	5, 4, 3, 4, 3, 4, 5, 6, 7, 6, 6, 3, 2, 1, 2, 5, 4, 6, 8, 6, 6, 4, 2, 0, 2, 4, 1, 3, 7, 5, 7, 3, 1, 5
	5, 4, 3, 4, 1, 2, 3, 4, 5, 6, 5, 4, 3, 2, 7, 6, 4, 6, 8, 6, 6, 4, 2, 0, 2, 3, 1, 5, 7, 7, 5, 1, 3
	4, 5, 4, 3, 2, 1, 2, 3, 4, 5, 6, 5, 4, 3, 6, 7, 2, 4, 6, 8, 6, 4, 2, 0, 2, 5, 1, 3, 7, 5, 7, 3, 1
	5, 4, 4, 5, 4, 5, 6, 7, 6, 3, 2, 2, 3, 5, 4, 7, 7, 5, 3, 1, 1, 3, 5, 0, 4, 8, 4, 6, 2, 2, 6
	5, 5, 4, 4, 2, 2, 3, 4, 5, 6, 6, 5, 4, 3, 7, 7, 3, 5, 7, 7, 5, 3, 1, 1, 4, 0, 4, 8, 6, 6, 2, 2
	4, 5, 5, 4, 5, 4, 3, 2, 2, 3, 6, 7, 7, 6, 4, 5, 1, 1, 3, 5, 7, 7, 5, 3, 8, 4, 0, 4, 2, 6, 6, 2
	4, 4, 5, 5, 7, 7, 6, 5, 4, 3, 3, 4, 5, 6, 2, 2, 5, 3, 1, 1, 3, 5, 7, 7, 4, 8, 4, 0, 2, 2, 6, 6
	4, 5, 6, 5, 6, 5, 4, 3, 2, 3, 4, 5, 6, 7, 2, 3, 3, 1, 1, 3, 5, 7, 7, 5, 6, 6, 2, 2, 0, 4, 8, 4
	5, 4, 5, 6, 5, 6, 7, 6, 5, 4, 3, 2, 3, 4, 3, 2, 7, 5, 3, 1, 1, 3, 5, 7, 2, 6, 6, 2, 4, 0, 4, 8
6, 5, 4, 5, 2, 3, 4, 5, 6, 7, 4, 3, 2, 3, 6, 5, 5, 7, 7, 5, 3, 1, 1, 3, 2, 2, 6, 6, 8, 4, 0, 4	
5, 6, 5, 4, 3, 2, 3, 2, 3, 4, 7, 6, 5, 4, 5, 6, 1, 3, 5, 7, 7, 5, 3, 1, 6, 2, 2, 6, 4, 8, 4, 0	

Figure 11. Matrix V(C_{16,n})

CONCLUSION

In this paper, a new family of cubic polyhedral graphs was introduced and then its modified Wiener index was computed. Also, their Wiener index was computed and, finally, the difference between two topological indices was derived.

ACKNOWLEDGEMENT

This research is partially supported by the Shahid Rajaei Teacher Training University.

REFERENCES

1. H.J. Wiener, *J. Am. Chem. Soc.*, **1947**, 69, 17.
2. M. Randić, X. Guo, T. Oxley, H. Krishnapriyan, L. Naylor, *J. Chem. Inf. Comput. Sci.*, **1994**, 34, 361.
3. D.J. Klein, I. Lukovits, I. Gutman, *J. Chem. Inf. Comput. Sci.*, **1995**, 35, 50.
4. J.E. Graver, *DIMACS Ser. Discrete Math. Theoret. Comput. Sci.*, *Amer. Math. Soc.*, Providence, RI, **2005**, 69, 167.
5. I. Gutman, L. Šoltés, *Z. Naturforsch.*, **1991**, 46a, 865.
6. M. Ghorbani, T. Ghorbani, *Studia Univ. Babeş-Bolyai, Chemia*, **2013**, 58, 43.
7. A. Graovac, T. Pisanski, *J. Math. Chem.*, **1991**, 8, 53.
8. M. Ghorbani, S. Klavžar, *Ars Math. Contemp.*, accepted.
9. F. Koorepazan-Moftakhar, A.R. Ashrafi, *Match*, **2015**, 75, 259.
10. M. Hakimi-Nezhaad, M. Ghorbani, *J. Math. Nanosci.*, **2014**, 4, 19.
11. M. Ghorbani, M. Hakimi-Nezhaad, *Fullerenes, Nanotubes and Carbon Nanostructures*, accepted.
12. M. Ghorbani, *J. Math. Nanosci.*, **2013**, 3, 33.
13. H. Zhang, D. Ye, *J. Math. Chem.*, **2007**, 41, 123.

*Dedicated to Professor Mircea Diudea
on the Occasion of His 65th Anniversary*

ON THE EDGE VERSION OF GEOMETRIC-ARITHMETIC INDEX OF NANOCONES

MUHAMMAD FAISAL NADEEM^{a,*}, SOHAIL ZAFAR^b, ZOHAIB ZAHID^b

ABSTRACT. In this paper, the edge version geometric-arithmetic index of certain nanocones is presented.

Keywords: *Geometric-arithmetic (GA) index, GA_e index, Nanocones*

INTRODUCTION

A numerical quantity that can be used to characterize the structure of a molecular graph is called a Topological Index. The obvious candidates for topological indices are the number of vertices and edges. Topological indices are invariant under the graph isomorphism. The importance of topologically indices is generally related to quantitative structure property relationship (QSPR) and quantitative structure activity relationship (QSAR).

In this article we will consider only simple graphs without loop and multiple edges. Let G be a simple graph, with the vertex set $V(G)$ and edge set $E(G)$. The line graph $L(G)$ of a graph G is the graph whose vertices are the edges of G and two vertices e and f are incident if and only if they have a common end vertex in G . The degree d_u of a vertex u is the number of vertices adjacent to u . Also, the degree d_e of an edge e of $E(G)$ is the number of its joining vertices in $V(G)$. The distance $d(u,v)$ between two vertices u and v is the length of the shortest path between u and v in G .

For a natural number k , we define the partitions

$$V_k(G) = \{u \in V(G) | d_u = k\} \text{ and } E_k(G) = \{e = uv \in E(G) | d_u + d_v = k\}.$$

^a *Department of Mathematics, Comsat Institute of Information Technology, Lahore Pakistan*

^b *University of Management and Technology (UMT), Lahore Pakistan*

* *Corresponding Author: mfaisalnadeem@gmail.com*

The first member of geometric-arithmetic index class was introduced in [1]:

$$GA_1(G) = \sum_{uv \in E(G)} \frac{2\sqrt{d_u \times d_v}}{d_u + d_v}.$$

The second member of this class was defined in [2]:

$$GA_2(G) = \sum_{uv \in E(G)} \frac{2\sqrt{n_u \times n_v}}{n_u + n_v}$$

where $n_u = \left| \left\{ y \mid y \in V(G), d(u, y) < d(y, v) \right\} \right|$ and $|A|$ denotes the number of elements of a set A .

The third member of this class was considered in [3]:

$$GA_3(G) = \sum_{uv \in E(G)} \frac{2\sqrt{m_u \times m_v}}{m_u + m_v}$$

where $m_u = \left| \left\{ x \mid x \in E(G), d(u, x) < d(x, v) \right\} \right|$.

The fourth member of the class of GA index was introduced by M. Ghorbani et al. in [4]:

$$GA_4(G) = \sum_{uv \in E(G)} \frac{2\sqrt{\epsilon_u \times \epsilon_v}}{\epsilon_u + \epsilon_v}$$

where ϵ_u is the eccentricity of a vertex u and defined as the maximum graph distance between u and any other vertex v of G .

The fifth member of the class of GA index was introduced in [5]:

$$GA_5(G) = \sum_{uv \in E(G)} \frac{2\sqrt{S_u \times S_v}}{S_u + S_v}$$

$$S_u = \sum_{v \in N_u} d_v \text{ where } N_u = \left\{ v \in V(G) \mid uv \in E(G) \right\}.$$

The sixth member of this class, also known as edge version of GA index, was launched in [6]:

$$GA_e(G) = \sum_{uv \in L(E(G))} \frac{2\sqrt{d_e \times d_f}}{d_e + d_f}.$$

For further results on geometric-arithmetic index we address to the articles [7-14]. The aim of this paper is to study the edge version of geometric-arithmetic index GA_e of nanocones $CNC_K[n]$.

RESULTS AND DISCUSSION

The following lemma is useful for finding the degree of a vertex of line graph.

Lemma 1. [14] Let G be a graph, $u \in V(G)$ and $e = uv \in E(G)$. Then:

$$d_e = d_u + d_v - 2.$$

Theorem 1. Let G be a graph of $CNC_3[n]$ nanocones for $n \geq 1$ with $3(n+1)^2$ vertices and $3\left(\frac{3}{2}n^2 + \frac{5}{2}n + 1\right)$ edges. Then:

$$GA_e(G) = \frac{12}{5}\sqrt{6} + 6n - 3 + \frac{24}{7}n\sqrt{3} + 9n^2.$$

Proof. The edge version of GA index is equivalent to GA_1 index of its line graph. The graph of $CNC_3[n]$ nanocones and its line graph are shown in Fig. 1. Now we will partition the vertex set and edge set of G as follows:

$$V_2(G) = \{u \in V(G) | d_u = 2\} \Rightarrow |V_2(G)| = 3(n+1),$$

$$V_3(G) = \{u \in V(G) | d_u = 3\} \Rightarrow |V_3(G)| = 3(n^2 + n),$$

$$E_4(G) = \{e = uv \in E(G) | d_u + d_v = 4\} \Rightarrow |E_4(G)| = 3,$$

$$E_5(G) = \{e = uv \in E(G) | d_u + d_v = 5\} \Rightarrow |E_5(G)| = 6n \text{ and}$$

$$E_6(G) = \{e = uv \in E(G) | d_u + d_v = 6\} \Rightarrow |E_6(G)| = \frac{3n(3n+1)}{2}.$$

On the other hand it is easy to see that

$$|V(L(G))| = 3\left(\frac{3}{2}n^2 + \frac{5}{2}n + 1\right), \text{ so we can partition the } V(L(G)) \text{ by using}$$

Lemma 1, as follows:

$$V_2(L(G)) = \{e \in V(L(G)) | d_e = 2\} \Rightarrow |V_2(L(G))| = 3,$$

$$V_3(L(G)) = \{e \in V(L(G)) | d_e = 3\} \Rightarrow |V_3(L(G))| = 6n \text{ and}$$

$$V_4(L(G)) = \{e \in V(L(G)) | d_e = 4\} \Rightarrow |V_4(L(G))| = \frac{3n(3n+1)}{2}.$$

And we get

$$|E(L(G))| = \frac{2 \times 3 + 3 \times 6n + 2 \times 3n(3n+1)}{2} = 3(n+1)(3n+1).$$

Now we split $E(L(G))$ as follows:

$$\begin{aligned}
 E_5(L(G)) &= \{ef \in E(L(G)) \mid d_e + d_f = 5\} \Rightarrow |E_5(L(G))| = 2|V_2(L(G))| = 6, \\
 E_6(L(G)) &= \{ef \in V(L(G)) \mid d_e + d_f = 6\} \\
 &\Rightarrow |E_6(L(G))| = |V_3(L(G))| - |V_2(L(G))| = 6n - 3, \\
 E_7(L(G)) &= \{ef \in E(L(G)) \mid d_e + d_f = 7\} \Rightarrow |E_7(L(G))| = |V_3(L(G))| = 6n \\
 &\text{and } E_8(L(G)) = \{ef \in E(L(G)) \mid d_e + d_f = 8\} \\
 &\Rightarrow |E_8(L(G))| = |E(L(G))| - |E_5(L(G))| - |E_6(L(G))| - |E_7(L(G))| = 9n^2.
 \end{aligned}$$

Since $GA_e(G) = \sum_{uv \in L(E(G))} \frac{2\sqrt{d_e \times d_f}}{d_e + d_f}$, then

$$GA_e(G) = 6 \frac{2\sqrt{2 \times 3}}{2+3} + 3(2n-1) \frac{2\sqrt{3 \times 3}}{3+3} + 6n \frac{2\sqrt{3 \times 4}}{3+4} + 9n^2 \frac{2\sqrt{4 \times 4}}{4+4}$$

After simplification we get

$$GA_e(G) = \frac{12}{5}\sqrt{6} + 6n - 3 + \frac{24}{7}n\sqrt{3} + 9n^2.$$

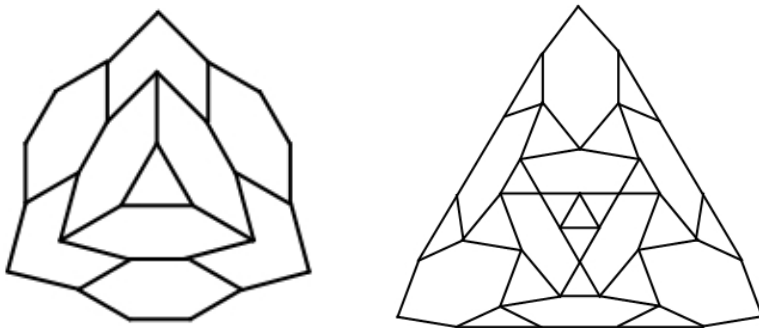


Figure 1. Graph of $CNC_3[2]$ nanocone (left); Graph of $L(CNC_3[2])$ (right)

Theorem 2. Let G be a graph of $CNC_4[n]$ nanocones for $n \geq 1$ with $4(n+1)^2$ vertices and $4\left(\frac{3}{2}n^2 + \frac{5}{2}n + 1\right)$ edges. Then

$$GA_e(G) = \frac{16}{5}\sqrt{6} + 8n - 4 + \frac{32}{7}n\sqrt{3} + 12n^2.$$

Proof. The graph of $CNC_4[n]$ nanocones and its line graph are shown in Fig. 2. Now we will partition the vertex set and edge set of G as follows:

$$V_2(G) = \{u \in V(G) | d_u = 2\} \Rightarrow |V_2(G)| = 4(n+1),$$

$$V_3(G) = \{u \in V(G) | d_u = 3\} \Rightarrow |V_3(G)| = 4(n^2 + n),$$

$$E_4(G) = \{e = uv \in E(G) | d_u + d_v = 4\} \Rightarrow |E_4(G)| = 4,$$

$$E_5(G) = \{e = uv \in E(G) | d_u + d_v = 5\} \Rightarrow |E_5(G)| = 8n \text{ and}$$

$$E_6(G) = \{e = uv \in E(G) | d_u + d_v = 6\} \Rightarrow |E_6(G)| = \frac{4n(3n+1)}{2}.$$

On the other hand it is easy to see that

$$|V(L(G))| = 4\left(\frac{3}{2}n^2 + \frac{5}{2}n + 1\right),$$

so we can partition the $V(L(G))$ by using Lemma 1, as follows:

$$V_2(L(G)) = \{e \in V(L(G)) | d_e = 2\} \Rightarrow |V_2(L(G))| = 4,$$

$$V_3(L(G)) = \{e \in V(L(G)) | d_e = 3\} \Rightarrow |V_3(L(G))| = 8n \text{ and}$$

$$V_4(L(G)) = \{e \in V(L(G)) | d_e = 4\} \Rightarrow |V_4(L(G))| = \frac{4n(3n+1)}{2}.$$

And it is easy to see that:

$$|E(L(G))| = 4(n+1)(3n+1).$$

Now we split $E(L(G))$ as follows:

$$E_5(L(G)) = \{ef \in E(L(G)) | d_e + d_f = 5\} \Rightarrow |E_5(L(G))| = 2|V_2(L(G))| = 8,$$

$$E_6(L(G)) = \{ef \in E(L(G)) | d_e + d_f = 6\}$$

$$\Rightarrow |E_6(L(G))| = |V_3(L(G))| - |V_2(L(G))| = 8n - 4,$$

$$E_7(L(G)) = \{ef \in E(L(G)) | d_e + d_f = 7\} \Rightarrow |E_7(L(G))| = |V_3(L(G))| = 8n$$

$$\text{and } E_8(L(G)) = \{ef \in E(L(G)) | d_e + d_f = 8\}$$

$$\Rightarrow |E_8(L(G))| = |E(L(G))| - |E_5(L(G))| - |E_6(L(G))| - |E_7(L(G))| = 12n^2.$$

$$\text{Since } GA_e(G) = \sum_{uv \in E(G)} \frac{2\sqrt{d_u \times d_v}}{d_u + d_v}, \text{ then}$$

$$GA_e(G) = 8 \frac{2\sqrt{2 \times 3}}{2+3} + 4(2n-1) \frac{2\sqrt{3 \times 3}}{3+3} + 8n \frac{2\sqrt{3 \times 4}}{3+4} + 12n^2 \frac{2\sqrt{4 \times 4}}{4+4}$$

After simplification we get

$$GA_e(G) = \frac{16}{5}\sqrt{6} + 8n - 4 + \frac{32}{7}n\sqrt{3} + 12n^2.$$

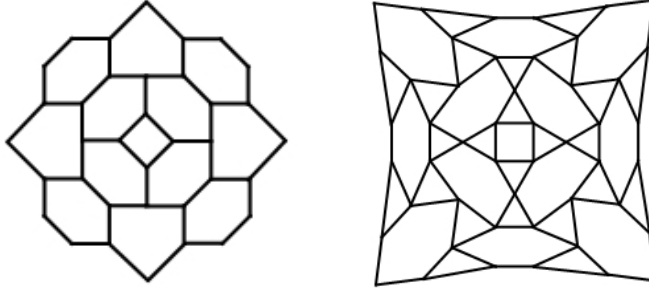


Figure 2. Graph of $CNC_4[2]$ nanocone (left); Graph of $L(CNC_4[2])$ (right)

Theorem 3. Let G be a graph of $CNC_5[n]$ nanocones for $n \geq 1$ with $5(n+1)^2$ vertices and $5\left(\frac{3}{2}n^2 + \frac{5}{2}n+1\right)$ edges. Then

$$GA_e(G) = 4\sqrt{6} + 10n - 5 + \frac{40}{7}n\sqrt{3} + 15n^2.$$

Proof. The graph of $CNC_5[n]$ nanocones and its line graph are shown in Fig. 3. At first we will partition the vertex set and edge set of G as follows:

$$V_2(G) = \{u \in V(G) | d_u = 2\} \Rightarrow |V_2(G)| = 5(n+1),$$

$$V_3(G) = \{u \in V(G) | d_u = 3\} \Rightarrow |V_3(G)| = 5(n^2 + n),$$

$$E_4(G) = \{e = uv \in E(G) | d_u + d_v = 4\} \Rightarrow |E_4(G)| = 5,$$

$$E_5(G) = \{e = uv \in E(G) | d_u + d_v = 5\} \Rightarrow |E_5(G)| = 10n \text{ and}$$

$$E_6(G) = \{e = uv \in E(G) | d_u + d_v = 6\} \Rightarrow |E_6(G)| = \frac{5n(3n+1)}{2}.$$

On the other hand it is easy to see that

$$|V(L(G))| = 5\left(\frac{3}{2}n^2 + \frac{5}{2}n+1\right),$$

so we can partition the $V(L(G))$ by using Lemma 1, as follows:

$$V_2(L(G)) = \{e \in V(L(G)) \mid d_e = 2\} \Rightarrow |V_2(L(G))| = 5,$$

$$V_3(L(G)) = \{e \in V(L(G)) \mid d_e = 3\} \Rightarrow |V_3(L(G))| = 10n \text{ and}$$

$$V_4(L(G)) = \{e \in V(L(G)) \mid d_e = 4\} \Rightarrow |V_4(L(G))| = \frac{5n(3n+1)}{2}.$$

And we can obtained

$$|E(L(G))| = 5(n+1)(3n+1)$$

Now we split $E(L(G))$ as follows:

$$E_5(L(G)) = \{ef \in E(L(G)) \mid d_e + d_f = 5\} \Rightarrow |E_5(L(G))| = 2|V_2(L(G))| = 10,$$

$$E_6(L(G)) = \{ef \in V(L(G)) \mid d_e + d_f = 6\}$$

$$\Rightarrow |E_6(L(G))| = |V_3(L(G))| - |V_2(L(G))| = 10n - 5,$$

$$E_7(L(G)) = \{ef \in E(L(G)) \mid d_e + d_f = 7\} \Rightarrow |E_7(L(G))| = |V_3(L(G))| = 10n$$

$$E_8(L(G)) = \{ef \in E(L(G)) \mid d_e + d_f = 8\} \text{ and}$$

$$\Rightarrow |E_8(L(G))| = |E(L(G))| - |E_5(L(G))| - |E_6(L(G))| - |E_7(L(G))| = 15n^2.$$

Since $GA_e(G) = \sum_{uv \in E(G)} \frac{2\sqrt{d_u \times d_v}}{d_u + d_v}$, then

$$GA_e(G) = 10 \frac{2\sqrt{2 \times 3}}{2+3} + 5(2n-1) \frac{2\sqrt{3 \times 3}}{3+3} + 10n \frac{2\sqrt{3 \times 4}}{3+4} + 15n^2 \frac{2\sqrt{4 \times 4}}{4+4}$$

After simplification we get

$$GA_e(G) = 4\sqrt{6} + 10n - 5 + \frac{40}{7}n\sqrt{3} + 15n^2.$$

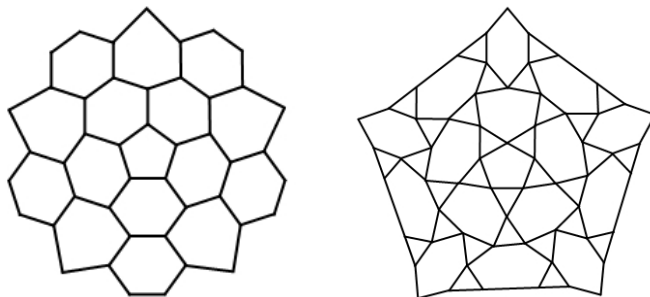


Figure 3. Graph of $CNC_5[2]$ nanocone (left); Graph of $L(CNC_5[2])$ (right)

Theorem 4. Let G be a graph of $CNC_k[n]$ nanocones for $n \geq 1$ and $k \geq 3$ with $5(n+1)^2$ vertices and $5\left(\frac{3}{2}n^2 + \frac{5}{2}n + 1\right)$ edges. Then

$$GA_e(G) = 3kn^2 + n\left(2k + \frac{8}{7}k\sqrt{3}\right) + \frac{4}{5}k\sqrt{6} - k.$$

Proof. The graph of $CNC_k[n]$ nanocones and its line graph are shown in Fig. 4 (a) and (b) respectively. At first we will partition the vertex set and edge set of G as follows:

$$V_2(G) = \{u \in V(G) | d_u = 2\} \Rightarrow |V_2(G)| = k(n+1),$$

$$V_3(G) = \{u \in V(G) | d_u = 3\} \Rightarrow |V_3(G)| = k(n^2 + n),$$

$$E_4(G) = \{e = uv \in E(G) | d_u + d_v = 4\} \Rightarrow |E_4(G)| = k,$$

$$E_5(G) = \{e = uv \in E(G) | d_u + d_v = 5\} \Rightarrow |E_5(G)| = 2kn \text{ and}$$

$$E_6(G) = \{e = uv \in E(G) | d_u + d_v = 6\} \Rightarrow |E_6(G)| = \frac{kn(3n+1)}{2}.$$

On the other hand it is easy to see that $|V(L(G))| = k\left(\frac{3}{2}n^2 + \frac{5}{2}n + 1\right)$,

so we can partition the $V(L(G))$ by using Lemma 1, as follows:

$$V_2(L(G)) = \{e \in V(L(G)) | d_e = 2\} \Rightarrow |V_2(L(G))| = k,$$

$$V_3(L(G)) = \{e \in V(L(G)) | d_e = 3\} \Rightarrow |V_3(L(G))| = 2kn \text{ and}$$

$$V_4(L(G)) = \{e \in V(L(G)) | d_e = 4\} \Rightarrow |V_4(L(G))| = \frac{kn(3n+1)}{2}.$$

And we can obtained

$$|E(L(G))| = \frac{2 \times k + 3 \times 2kn + 2 \times kn(3n+1)}{2} = k(n+1)(3n+1)$$

Now we split $E(L(G))$ as follows:

$$E_5(L(G)) = \{ef \in E(L(G)) | d_e + d_f = 5\} \Rightarrow |E_5(L(G))| = 2|V_2(L(G))| = 2k,$$

$$E_6(L(G)) = \{ef \in V(L(G)) | d_e + d_f = 6\}$$

$$\Rightarrow |E_6(L(G))| = |V_3(L(G))| - |V_2(L(G))| = k(2n-1),$$

$$E_7(L(G)) = \{ef \in E(L(G)) \mid d_e + d_f = 7\} \Rightarrow |E_7(L(G))| = |V_3(L(G))| = 2kn$$

$$\text{and } E_8(L(G)) = \{ef \in E(L(G)) \mid d_e + d_f = 8\}$$

$$\Rightarrow |E_8(L(G))| = |E(L(G))| - |E_5(L(G))| - |E_6(L(G))| - |E_7(L(G))| = 3kn^2$$

Since $GA_e(G) = \sum_{uv \in E(G)} \frac{2\sqrt{d_u \times d_v}}{d_u + d_v}$, then

$$GA_e(G) = 2k \frac{2\sqrt{2 \times 3}}{2+3} + k(2n-1) \frac{2\sqrt{3 \times 3}}{3+3} + k(2n) \frac{2\sqrt{3 \times 4}}{3+4} + k(3n^2) \frac{2\sqrt{4 \times 4}}{4+4}$$

After simplification we get

$$GA_e(G) = 3kn^2 + n \left(2k + \frac{8}{7}k\sqrt{3} \right) + \frac{4}{5}k\sqrt{6} - k.$$

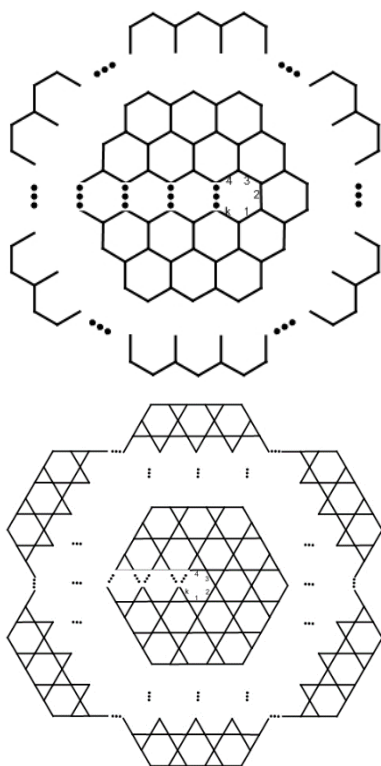


Figure 4. Graph of $CNC_k[n]$ nanocone (top) Graph of $L(CNC_k[n])$ (bottom)

CONCLUSION

In this article the edge version of geometric-arithmetic (GA) index was studied for the case of nanocones, $CNC_k[n]$. In future, we will pay attention to some new classes of nanostructures and study their topological indices which will be practically helpful to identify their underlying topologies.

REFERENCES

1. D. Vukičević, B. Furtula, *J. Math. Chem.*, **2009**, *46*, 1369.
2. G. Fath-Tabar, B. Furtula, I. Gutman, *J. Math. Chem.*, **2010**, *47*, 477.
3. B. Zhou, I. Gutman, B. Furtula, Z. Du, *Chem. Phys. Lett.*, **2009**, *153*, 482.
4. M. Ghorbani, A. Khaki, *Optoelectron. Adv. Mater.-Rapid Commun.* **2010**, *4*(12), 2212.
5. A. Graovac, M. Ghorbani, M.A. Hosseinzadeh, *J. Math. Nanosciences*, **2011**, *1*, 33.
6. A. Mahimiani, O. Khormali, A. Iranmanesh, *Digest J. Nanomater. Biostruct.*, **2012**, *7*, 411.
7. S. Chen, W. Liu, *J. Comput. Theor. Nanosci.*, **2010**, *7*, 1993.
8. M.R. Farahani, *Acta Univ. Apulensis*, **2013**, *36*, 277.
9. A. Madanshekaf, M. Ghaneeei, *Optoelectron. Adv. Mater.-Rapid Commun.* **2010**, *4*(12), 2200.
10. M. Ghorbani, H. Mesgarani, S. Shakeraneh, *Optoelectron. Adv. Mater.-Rapid Commun.*, **2011**, *5*(3), 324.
11. A. Khaksar, M. Ghorbani, H.R. Maimani, *Optoelectron. Adv. Mater.-Rapid Commun.*, **2010**, *4*(11), 1868.
12. S. Hayat, M. Imran, *Studia UBB Chemia*, **2014**, *59* (3), 113.
13. M.R. Farahani *Proc. Rom. Acad., Series B*, **2013**, *15*, 95.
14. A. Mahimiani, O. Khormali, *Int. J. Ind. Math.*, **2013**, *5*, 259.

*Dedicated to Professor Mircea Diudea
on the Occasion of His 65th Anniversary*

ON BIPARTITE EDGE FRUSTRATION OF CARBON AND BORON NANOTUBES

SAKANDER HAYAT^{a,*}, HAFIZ MUHAMMAD AFZAL SIDDIQUI^b

ABSTRACT. The measure of bipartivity is one of the important topological and structural property which describes the chemical stability of underlying chemical structures. Bipartite edge frustration is one of the topological descriptors which calculate measure of bipartivity of a chemical structure. Carbon hexagonal nanotubes, boron triangular nanotubes and boron α -nanotubes are important nanostructures, which have been studied extensively by both of the theoretical and computational chemists. In this article, we consider carbon hexagonal nanotubes, boron triangular nanotubes and boron α -nanotubes for the study of bipartite edge frustration.

Keywords: *Bipartite edge frustration, Carbon hexagonal nanotube, Boron triangular nanotube, Boron α -nanotube*

INTRODUCTION

Nanotechnology works with structures of size in the range 1 to 100 nanometers. Nanotechnology creates many new materials and devices with a variety of applications in medicine, electronics, and computer. The most significant nano structures are carbon nanotubes, boron triangular nanotubes and boron α -nanotubes (Figure 1).

^a *School of Mathematical Sciences, University of Science and Technology of China (USTC), Hefei, Anhui, China*

^b *Department of Mathematics, School of Natural Sciences, National University of Sciences and Technology (NUST), H-12 Sector, Islamabad, Pakistan*

* *Corresponding Author: sakander1566@gmail.com*

The recent discovery of pure boron triangular nanotubes challenges the monopoly of carbon. The first boron triangular nanotubes were created in 2004 and consist of triangular sheets [1,2]. Figure 1b shows a boron triangular sheet.

Let $G=(V,E)$ be a simple graph, a graph without multiple edges and loops. A subgraph H of G is a graph whose set of vertices and set of edges are all subsets of G . A spanning subgraph is a subgraph that contains all the vertices of the original graph.

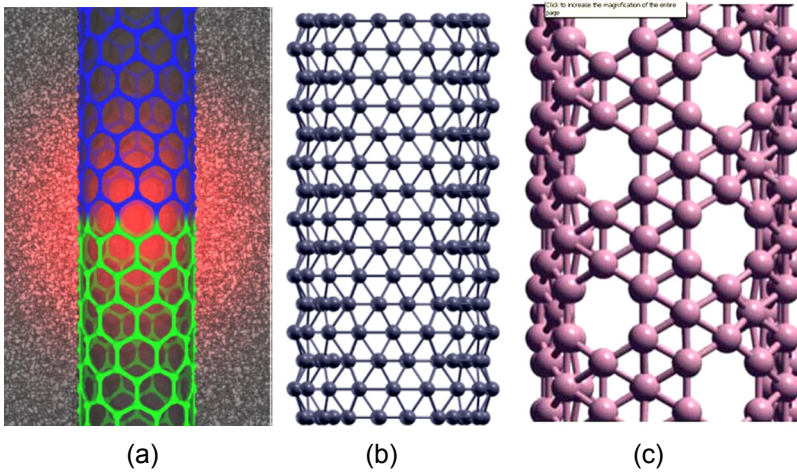


Figure 1. Carbon hexagonal nanotube (a); Boron triangular nanotube (b); Boron α -nanotube (c).

The graph G is called bipartite if the vertex set V can be partitioned into two disjoint subsets V_1 and V_2 such that all edges of G have one endpoint in V_1 and the other in V_2 . Bipartite edge frustration of a graph G denoted by $\phi(G)$, is the minimum number of edges that need to be deleted to obtain a bipartite spanning subgraph.

It is easy to see that $\phi(G)$ is a topological index and G is bipartite if and only if $\phi(G) = 0$. Thus $\phi(G)$ is a measure of bipartivity. It is well-known that a graph G is bipartite if and only if it does not have odd cycles. Holme *et al.* introduced the edge frustration as a measure in the context of complex network [3].

Fajtlowicz claimed that the chemical stability of fullerenes is related to the minimum number of vertices/edges that need to be deleted to make a fullerene graph bipartite [4,5]. However, Schmalz *et al.* [6] observed that the isolated pentagon fullerenes (IPR fullerenes) have the best stability. Doslic [7]

presented some computational results to confirm this relationship. So it is natural to ask about relationship between the degree of non-bipartivity and stability of chemical structures such as nanotubes.

Throughout this paper all the considered graphs are finite and simple. Our notation is standard and taken mainly from [8,9]. We encourage the reader to consult papers by Doslic [7,10,11] for background material and more information on the problem. Also, the reader is referred to papers [12-15] for some background material as well as basic computational methods on mathematical properties of nanomaterials and chemical networks.

RESULTS AND DISCUSSION

Bipartite edge frustration is probably related to the chemical stability of nanostructures, like fullerenes or nanotubes.

Ashrafi *et al.* [16] computed the bipartite edge frustration of various families of carbon nanotubes. Doslic *et al.* [2,10] studied the bipartite edge frustration of fullerenes. In this paper, the bipartite edge frustration of carbon and boron nanotubes is studied.

Carbon Polyhex Nanotubes

There are different shapes of carbon polyhex nanotubes CNT, such as armchair, chiral and zigzag [2] based on the rolling of 2D carbon polyhex sheet. A CNT of order $n \times m$ is a tube obtained from a carbon polyhex sheet of n rows and m columns by merging the vertices of last column with the respective vertices of first column (Figure 2).

A zig-zag CNT is a nanotube of order $n \times m$ in which carbon atoms are arranged in zig-zag pattern (Figure 2a). Similarly, an armchair carbon hexagonal nanotube is a carbon nanotube in which carbon atoms are arranged in an armchair pattern (Figure 2b). It can easily be seen that a carbon hexagonal nanotube has only odd number of rows and even number of columns.

A complete regular hexagon with six vertices is called full-hexagon. An incomplete hexagon with four vertices is called a half-hexagon. The first row (last row) of an armchair CNT of order $n \times m$ has $m/2$ number of half-hexagons. For the sake of simplicity we denote zig-zag carbon hexagonal nanotube with CNT_1 and armchair carbon hexagonal nanotube with CNT_2 . In a CNT of order $n \times m$, there are $m(n-2)/2$ full hexagons and m half hexagons. The number of vertices and edges in such a CNT are nm and $m(3n-2)/2$ respectively.

In the following, we prove that both of these carbon hexagonal nanotubes have zero bipartite edge frustration.

Theorem 2.1.1. Let CNT_1 and CNT_2 be the zig-zag and armchair carbon hexagonal nanotubes respectively, then

$$\phi(CNT_1) = \phi(CNT_2) = 0$$

Proof. A graph G is bipartite if and only if $\phi(G) = 0$, thus, it suffices to prove them bipartite. Figure 2 shows a 2-coloring of CNT_1 , in which bold vertices can be put in one partition and rest of them in the other partition. This clearly shows that CNT_1 is bipartite. Similarly, the bipartivity is proven for CNT_2 .

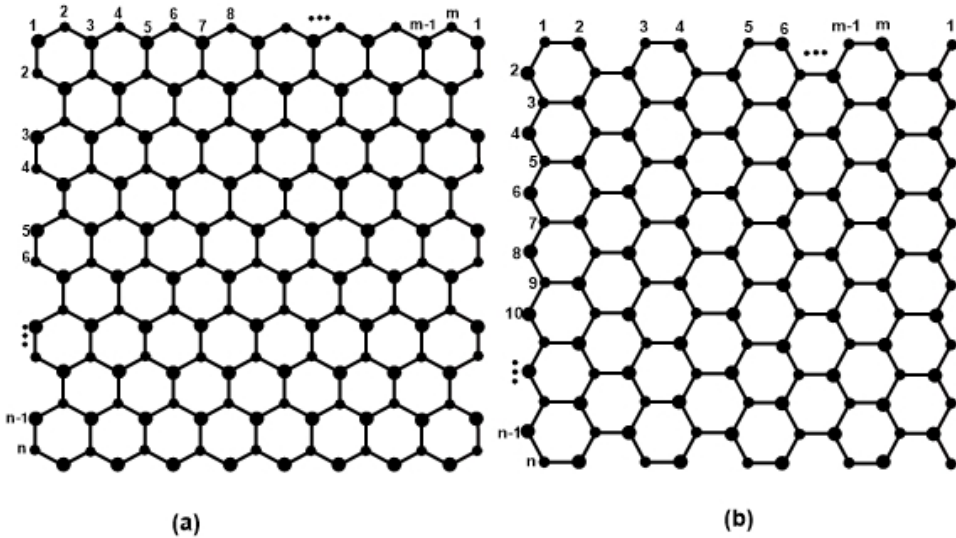


Figure 2. 2D models of: Zig-zag CNT (a); Armchair CNT (b).

Boron Triangular Nanotubes

A boron triangular nanotube, of order $n \times m$, is drawn from a hexagonal nanotube of the same order by adding a new vertex at the center of each hexagon and join it with the original points of the hexagon. Figure 3 shows the way of construction of a boron triangular nanotube.

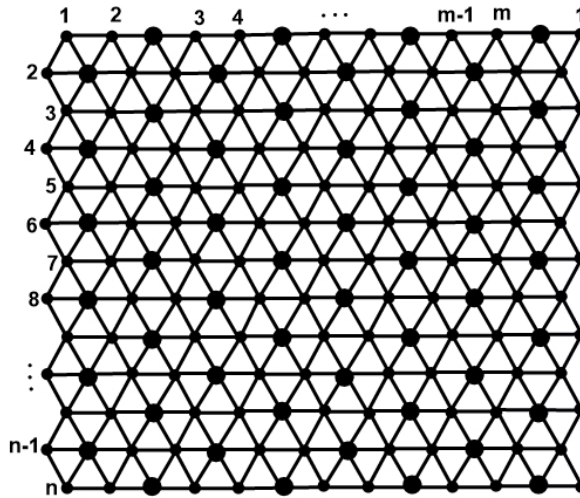


Figure 3. Boron triangular nanotube of order (n, m) .

We denote the boron triangular nanotube of order $n \times m$ as $BNT_t[n, m]$, in which n is the number of rows and m is the number of columns. Since, there are $m(n-2)/2$ full hexagons and m half hexagons, the number of vertices is $3nm/2$ while that of edges is $3m(3n-2)/2$.



Figure 4. The dotted edges which need to be deleted from a full and a half hexagons.

Now we compute bipartite edge frustration of boron triangular nanotube.

Theorem 1. Let $BNT_t[n, m]$ be the boron triangular nanotube with defining parameters n and m , then

$$\phi(BNT_t[n, m]) = \frac{m}{2}(3n - 2)$$

Proof. Consider G be a boron triangular nanotube. There exist no 2-coloring of G which results in $\phi(G) > 0$. To prove that it is exactly $\frac{m}{2}(3n-2)$, we need to prove both of the inequalities i.e. $\phi(G) \geq \frac{m}{2}(3n-2)$ and $\phi(G) \leq \frac{m}{2}(3n-2)$. Since a CNT has zero bipartite edge frustration, the problem is with the newly added edges. If one deletes three newly added alternating edges from a full hexagon and two newly added alternating edges from half hexagon that makes both full and half hexagons bipartite spanning subgraphs. Figure 4 exhibits the edges which need to be deleted from a full and a half hexagon. Since, there are $m(n-2)/2$ full hexagons and m half hexagons in a boron triangular nanotube, this implies that $\phi(G) \leq \frac{m}{2}(3n-2)$. On the other hand, one can easily be seen that there is no less number of edges to make the edges deleted subgraph a bipartite spanning subgraph. This turns out that $\phi(G) \geq \frac{m}{2}(3n-2)$ thus proving the theorem.

Boron α -Nanotubes

A boron α -nanotube of order $n \times m$ is obtained from a hexagonal nanotube of order $n \times m$ by deleting the central point of some hexagons of a triangular nanotube. We denote an (n, m) -boron α -nanotube as $BNT_{\alpha}[n, m]$ (Figure 5).

Lemma 2. In an (n, m) -dimensional boron α -nanotube:

- There are $\frac{m}{2} \left(\frac{n}{3} - 1 \right)$ empty full hexagons.
- There are $\frac{m}{2} \left(\frac{2n}{3} - \frac{3}{2} \right)$ filled full hexagons.
- There are $\frac{4nm}{3}$ vertices, when n is a multiple of 3.
- There are $\frac{m(7n-4)}{2}$ edges, when n is a multiple of 3.

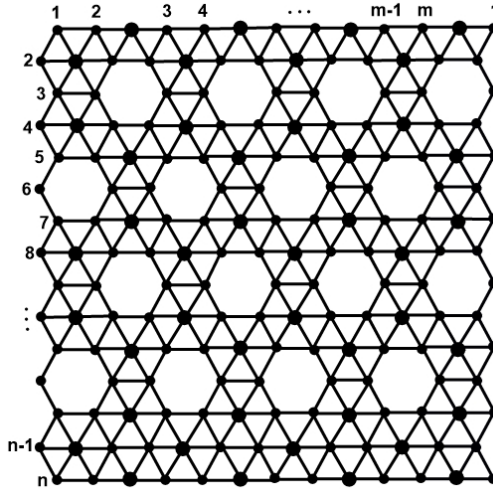


Figure 5. A 2D model of boron α -nanotube of order (n, m) .

Let present the bipartite edge frustration of boron α -nanotube, $BNT_\alpha[n, m]$.

Theorem 3. Let $BNT_\alpha[n, m]$ be the (n, m) -dimensional boron α -nanotube, then

$$\phi(BNT_\alpha[n, m]) = \frac{m}{2}(2n + 1)$$

Proof. Let G be the (n, m) -dimensional boron α -nanotube. Since we do not find any 2-coloring of G , it results that $\phi(G) > 0$. We prove both of the inequalities $\phi(G) \geq \frac{m}{2}(2n + 1)$ and $\phi(G) \leq \frac{m}{2}(2n + 1)$, to prove it is exactly $\frac{m}{2}(2n + 1)$. If we delete three newly added alternative edges from a full hexagon and two newly added alternative edges from half hexagon it results in both full and half hexagons bipartite spanning subgraphs. Figure 4 exhibits the edges which need to be deleted from a full and a half hexagon.

Since, there are $\frac{m}{2}(\frac{n}{3} - 1)$ empty full hexagons and $\frac{m}{2}(\frac{2n}{3} - \frac{3}{2})$ filled hexagons in an (n, m) -dimensional boron α -nanotube, this implies that

$\phi(G) \leq \frac{m}{2}(2n+1)$. On the other hand, it can easily be seen that there is no less number of edges to make its edge deleted subgraph a bipartite spanning subgraph. This turns out that $\phi(G) \geq \frac{m}{2}(2n+1)$, which completes the proof.

CONCLUSIONS

Evaluating the bipartivity in chemical structures provides important information about their topology and eventually about chemical stability. While carbon polyhex nanotubes have zero bipartite edge frustration, the boron nanotubes have non-zero bipartivity.

ACKNOWLEDGMENTS

The first author is supported by CAS-TWAS president fellowship at USTC, China. The second author is partially supported by NUST, Pakistan.

REFERENCES

1. S. Battersby, <http://www.newscientist.com>.
2. J. Kunstmann, A. Quandt, *Phys. Rev. B*, **2006**, 74, 354.
3. P. Holme, F. Liljeros, G.R. Edling, B.J. Kim, *Phys. Rev. E*, **2003**, 68, 056107.
4. S. Fajtlowicz, <http://www.math.uh.edu/~clarson/fajt>.
5. S. Fajtlowicz, C. E. Larson, *Chem. Phys. Lett.*, **2003**, 177, 485.
6. T.G. Schmalz, W.A. Seitz, D.J. Klein, G.E. Hite, *Chem. Phys. Lett.*, **1986**, 130, 203.
7. T. Doslic, *Chem. Phys. Lett.*, **2008**, 412, 336.
8. P.W. Fowler, D.E. Manolopoulos, *Clarendon Press, Oxford*, **1995**.
9. F. Harary, *Graph Theory*, *Addison-Wesley, Reading, MA*, **1969**.
10. T. Doslic, *J. Math. Chem.*, **2002**, 31, 187.
11. T. Doslic, D. Vukicevic, *Discrete Appl. Math.*, **2007**, 155, 1294.
12. S. Hayat, A. Khan, F. Yousafzai, M. Imran, *Optoelectron. Adv. Mater. Rapid Commun.*, **2015**, 9, 869.
13. S. Hayat, M. Imran, *J. Comput. Theor. Nanosci.*, **2015**, 12(1), 70.
14. S. Hayat, M. Imran, *App. Math. Comp.*, **2014**, 240, 213.
15. S. Hayat, M. Imran, *Studia UBB Chemia*, LIX, **2014**, 3, 113.
16. M. Ghojavand, A. R. Ashrafi, *Dig. J. Nanomater. Biostruc.*, **2008**, 3, 209.

*Dedicated to Professor Mircea Diudea
on the Occasion of His 65th Anniversary*

TOPOLOGICAL INDICES IN HYPERTUBES OF HYPERCUBES

KHADIJEH FATHALIKHANI^a, ATENA PÎRVAN-MOLDOVAN^b,
MIRCEA V. DIUDEA^{b,*}

ABSTRACT. A topological index is a single number descriptor that characterizes the molecular graph topology up to isomorphism. Hyper-tubes, open or closed, consisting of hyper-cubes of n -dimensions have been designed and formulas for some topological indices, counting vary substructures or characteristics, were established.

Keywords: *graph, topological index, n-cube, hyper-tube, hyper-torus, n-dimensional space*

INTRODUCTION

Schläfli [1] was the first scientist that described spaces of dimension higher than three, namely the six regular 4D-polytopes, also called polychora. These are as follows: 5-Cell {3,3,3}; 8-Cell {4,3,3}; 16-Cell {3,3,4}; 24-Cell {3,4,3}; 120-Cell {5,3,3} and 600-Cell {3,3,5}. Five of them can be associated to the Platonic solids but the sixth one, the 24-cell has no a 3D equivalent; it consists of 24 octahedral cells, 6 cells meeting at each vertex. Among the four dimensional polytopes, 5-Cell and 24-Cell are self-dual while the others are pairs: (8-Cell & 16-Cell); (120-Cell & 600-Cell). In the above, $\{p, q, r\}$ are the Schläfli symbols: the symbol $\{p\}$ denotes a regular polygon for integer p , or a

^a Department of Pure Mathematics, Faculty of Mathematical Sciences, University of Kashan, Kashan 87317-51167, I. R. Iran

^b Department of Chemistry, Faculty of Chemistry and Chemical Engineering, Babes-Bolyai University, 400028 Cluj, Romania

* Corresponding Author: diudea@chem.ubbcluj.ro

star polygon for rational p ; the symbol $\{p, q\}$ denotes a 3D-object tessellated by p -gons while q is the vertex-figure (i.e., the number of p -gons surrounding each vertex); the symbol $\{p, q, r\}$ describes a 4D-structure, in which r 3D-objects join at any edge (r being the edge-figure) of the polytope, and so on. The Schläfli symbol has the nice property that its reversal gives the symbol of the dual polytope.

In dimensions 5 and higher, there are only three kinds of convex regular polytopes; no non-convex regular polytopes exist [2-4]. In the following, some details are given.

The **n -simplex** [2] has the Schläfli symbol $\{3^{n-1}\}$, and the number of its k -faces is given by the combinatorial formula $\binom{n+1}{k+1}$; it is a generalization of the triangle or tetrahedron to any dimensions. For example, a 0-simplex is a point, a 1-simplex is a line segment, a 2-simplex is a triangle, a 3-simplex is the tetrahedron, and a 4-simplex is the 5-cell.

The **hypercube** [2] is a generalization of the 3-cube to n -dimensions and is also called an n -Cube Q_n . It is a regular polytope with mutually perpendicular sides, thus being an orthotope. Its Schläfli symbol is $\{4, 3^{n-2}\}$ and k -faces are counted by the formula $2^{n-k} \binom{n}{k}$. The hypercube can also be expressed as the Cartesian product of the complete graph K_2 : $Q_n = \square_{i=1}^n K_2$.

The **n -orthoplex or cross-polytope** [2] has the Schläfli symbol $\{3^{n-2}, 4\}$ and its k -faces are counted by the formula $2^{k+1} \binom{n}{k+1}$; it is the dual of Q_n , in any n -dimensions. The facets of a cross-polytope are simplexes of the previous dimensions, while its vertex figures are other cross-polytopes of lower dimensions.

To investigate an n -dimensional polytope, a formula, due to Euler [5] (see also Schläfli [1]) is used:

$$\sum_{i=0}^{n-1} (-1)^i f_i = 1 - (-1)^n \tag{1}$$

For $n=3$, eq (1) reduces to the simpler (well-known) Euler relation

$$v - e + f = 2(1 - g) \tag{2}$$

with v , e , f and g being the vertices, edges, 2-faces and the genus, respectively; $g=0$ for the sphere and $g=1$ for the torus.

It was conjectured by Diudea [6, 7] that the alternating sum for objects embedded in surfaces other than the sphere accounts for the genus of the embedding surface:

$$\sum_{k=0}^n (-1)^k f_k = \chi(M) = 2(1 - g); \quad n > 1; k = 0, 1, \dots, n. \tag{3}$$

It means that summation by (1) gives 2 and zero (for odd and even dimension, respectively) because the embedding surface was the sphere (see also (2)). In tori, with $g=1$, $\chi=0$ irrespective of the dimension of the embedded structure.

HYPERCUBES IN HIGH-DIMENSIONAL TUBULAR STRUCTURES

It is well-known [2] that the number of k -cubes $Q_n(k)$ contained in the hypercube Q_n can be calculated by

$$Q_n(k) = 2^{n-k} \binom{n}{k}; \quad k = 0, \dots, n-1 \quad (4)$$

Hypercube (Figure 1) is isomorphic to the Hasse diagram of a finite Boolean algebra [2].

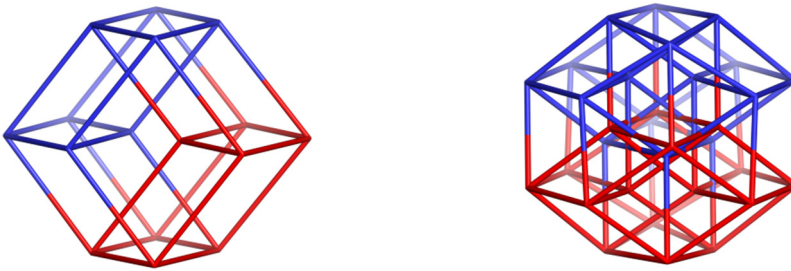


Figure 1. Hypercubes: the Tesseract or Q_4 .16 hypercube (left) and Q_5 .32 hypercube (right).

Open Tubes

In a recent paper [8], Moldovan and Diudea proposed the embedding of n -Cube in surfaces other than the sphere (Figures 2 and 3).



Figure 2. A hyper-tube $TU(4,5), Q_4.40$ (left) and a hyper-tube $TU((4,8,5), Q_3.80)$ (right)

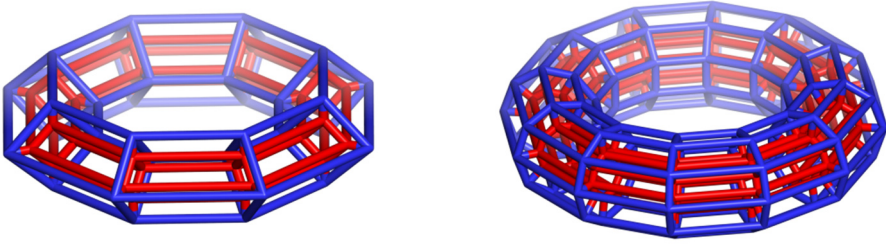


Figure 3. An elementary double-wall torus $T((4,8), Q_4.64)$, of square section (left) and $T((4,9,12), Q_3.216)$, with octagonal section and 16 units $T((4,9,1), Q_3.36)$ (right)

The k -dimensional substructures of a simple hyper-tube $TU((4,r), Q_n)$ (Figure 2, left) are counted from the hypercube $Q_n(k)$ substructures by formulas:

$$f_r = (r/2 - 1) / n \quad f_k = (r/2) + k \cdot f_r \quad k = 0, 1, \dots, n-1 \quad (5)$$

$$TU((4,r), Q_n, k) = Q_n(k) \cdot f_k; \quad TU((4,r), Q_n, (k+1)) = r$$

From Table 1, one can see that the alternation sum of figures (equaling the value of χ) gives: zero for even dimension and 2 for the even dimension “Dim” of the hyper-tube. It means that the elementary hyper-tube $TU((4,r), Q_n)$ is like the sphere (*i.e.*, both having the genus $g=0$).

Table 1. Figure count in two hyper-tubes embedding hyper-cubes

Structure \ k	0	1	2	3	4	5	6	χ	Dim
TU((4,5), Q₅).80	80	224	248	136	37	5	-	0	6
Q_5	32	80	80	40	10	0	-	2	5
f_k	2.5	2.8	3.1	3.4	3.7	4	-	-	-
$Q_5 \times f_k \& r$	80	224	248	136	37	5	-	0	6
TU((4,5), Q₆).160	160	528	720	520	210	45	5	2	7
Q_6	64	192	240	160	60	12	-	0	6
f_k	2.5	2.75	3	3.25	3.5	3.75	4	-	-
$Q_6 \times f_k \& r$	160	528	720	520	210	45	5	2	7

In a more complex hyper-tube (Figure 2, right), each unit in the tube $TU((4,r,s), Q_n)$ is an elementary hyper-torus $T((4,r), Q_n)$ (Figure 3, left) while there are s -units along the tube.

The k -dimensional substructures of a complex hyper-tube $TU((4,r,s),Q_n)$ are counted from the previous dimensional substructures of the elementary hyper-torus $T((4,r),Q_n)$, by formulas:

$$TU((4,r,1),Q_n,k) = T((4,r),Q_{n-1},k) + T((4,r),Q_{n-1},(k-1)) \tag{6}$$

$$TU((4,r,s),Q_n,k) = s \times TU((4,r,1),Q_n,k) + T((4,r),Q_{n-1},k); \tag{7}$$

$$k = 0, 1, \dots, n-1; n > 3$$

Table 2 gives details of the calculation of substructures in case of the hyper-tube $TU((4,9,7),Q_5)$.504. Formulas work for any integer $n > 3$.

Table 2. Figure count in the hyper-tube $TU((4,9,7),Q_5)$.504

Structure \ k	0	1	2	3	4	5	χ	Dim
$TU((4,9,7),Q_5)$.504	504	1692	2214	1413	441	54	0	6
$T((4,9),Q_4)$.72	72	180	162	63	9	-	0	5
-	-	72	180	162	63	9	-	-
$TU((4,9,1),Q_5)$.72	72	252	342	225	72	9	0	6
$TU((4,9,1),Q_5) \times 6$	432	1512	2052	1350	432	54	-	-
+ $T((4,9),Q_4)$.72	72	180	162	63	9	0	-	-
Sum	504	1692	2214	1413	441	54	0	6

Tori

When the end-faces of a hypertube are identified, it results in a closed hyper-tube or a hyper-torus (Figure 3). We studied particularly the tori $T(4,r)$ and $T(4,r,s)$, according to Diudea’s discretization procedure [9].

The k -dimensional substructures of a simple hyper-torus $T((4,r),Q_n)$ (Figure 3, left) are counted on the basis of the hypercube $Q_n(k)$ substructures by the following formulas:

$$f_r = (r/2) / n \quad f_k = (r/2) + k \cdot f_r \quad k = 0, 1, \dots, n-1 \tag{8}$$

$$T((4,r),Q_n,k) = Q_n(k) \cdot f_k; \quad T((4,r),Q_n,(k+1)) = r$$

Formulas can be easily verified from data listed in Table 3. The hyper-torus $T((4,r),Q_n,k)$ is herein named “elementary” because it is a constituent of the more complex hyper-tubes and hyper-tori built up on the ground of hyper-cubes.

Table 3. Figure count for the hyper-torus $T((4,8),Q_n)$

<i>Torus \ k</i>	0	1	2	3	4	5	6	7	f_r	Deg(v)	χ
Q ₃	8	12	6	0	0	0	0	0	0	3	2
Q ₄	16	32	24	8	0	0	0	0	0	4	0
Q ₅	32	80	80	40	10	0	0	0	0	5	2
Q ₆	64	192	240	160	60	12	0	0	0	6	0
Q ₃ T ₄	32	64	40	8	0	0	0	0	4/3	4	0
Q ₄ T ₅	64	160	144	56	8	0	0	0	4/4	5	0
Q ₅ T ₆	128	384	448	256	72	8	0	0	4/6	6	0
Q ₆ T ₇	256	896	1280	960	400	88	8	0	4/6	7	0

The number of rings R around any point in the hyper-torus is given by formula

$$R(T((4, r), Q_n)) = 4^{(n-1)(n+2)/2} \tag{9}$$

The vertex degree in the hyper-torus $T((4,r),Q_n)$ equals $(n+1)$. The torus is vertex transitive but its edges f_1 and faces f_2 are split in two equivalence classes.

In a more complex hyper-torus (see Figure 3, right); each unit $T((4,r,1),Q_n)$ in the torus $T((4,r,s),Q_n)$ is an elementary hyper-torus $T((4,r),Q_n)$ while there are s -units around the central hollow.

The k -faces of a hyper-torus $T((4,r,s),Q_n)$ are counted from the previous dimensional substructures of the elementary hyper-torus $T((4,r),Q_n)$, by formulas:

$$T((4, r, 1), Q_n, k) = T((4, r), Q_{n-1}, k) + T((4, r), Q_{n-1}, (k - 1)) \tag{10}$$

$$T((4, r, s), Q_n, k) = s \times T((4, r, 1), Q_n, k); k = 0, 1, \dots, n - 1; n > 3 \tag{11}$$

Details are given in Table 4; formulas work for any integer $n > 3$.

Table 4. Figure count in the hyper-torus $T((4,8,16),Q_7).4096$

Structure \ k	0	1	2	3	4	5	6	7	χ
$T((4,8),Q_6).256$	256	896	1280	960	400	88	8	0	0
	-	256	896	1280	960	400	88	8	-
$T((4,8,1),Q_7).256$	256	1152	2176	2240	1360	488	96	8	0
$T((4,8,16),Q_7).4096$	4096	18432	34816	35840	21760	7808	1536	128	0

The vertex degree in the hyper-torus $T((4,r,s),Q_n)$ equals $(n+2)$. This torus is vertex transitive but its edges f_1 and faces f_2 are split in three equivalence classes.

Note the difference between the hyper-cube and $TU((4,r),Q_n)$ on one hand and the hyper-tube $TU(4,r,s),Q_n$, on the other hand: the figure sum gives alternating 0 and 2 for the hyper-cube, at even and odd n -dimension, respectively (Table 3), while the last structures provide zero, irrespective of n parity. This is because torus has the genus $g=1$ [10].

OMEGA POLYNOMIAL AND CI INDEX

A counting polynomial [11] is a representation of a graph $G(V,E)$, with the exponent a showing the extent of partitions $p(G)$, $\cup p(G) = P(G)$ of a graph property $P(G)$ while the coefficient $p(a)$ is related to the number of partitions of extent a .

$$P(x) = \sum_a p(a) \cdot x^a \tag{12}$$

Let G be a connected graph, with $V(G)$ and $E(G)$ being the vertex set and edge set, respectively. Two edges $e=(u,v)$ and $f=(x,y)$ of G are *codistant* (briefly: *e co f*) if they fulfill the relation [12]

$$d(v, x) = d(v, y) + 1 = d(u, x) + 1 = d(u, y) \tag{13}$$

where d is the shortest-path distance function. The relation *co* is reflexive (*e co e*) and symmetric (*e co f*) for any edge e of G but is not necessarily transitive. A graph is called a *co-graph* if the relation *co* is also transitive and thus *co* is an equivalence relation.

Let $C(e) := \{f \in E(G); f \text{ co } e\}$ be the set of edges in G , codistant to $e \in E(G)$. The set $C(e)$ is provided by an orthogonal edge-cutting procedure: take a straight line segment, orthogonal to the edge e , and intersect it and all other edges (of a polygonal plane graph) parallel to e . The set of these intersections is called an *orthogonal cut* of G , with respect to e . If G is a *co-graph* then its orthogonal cuts C_1, C_2, \dots, C_k form a partition of $E(G)$:

$$E(G) = C_1 \cup C_2 \cup \dots \cup C_k, \quad C_i \cap C_j = \emptyset, \quad i \neq j \tag{14}$$

A subgraph $H \subseteq G$ is called *isometric* if $d_H(u, v) = d_G(u, v)$, for any $(u, v) \in H$; it is *convex* if any shortest path in G between vertices of H belongs to H . The relation *co* is related to Djoković \sim [13] and Winkler Θ [14] relations (see also [15]).

Two edges e and f of a plane graph G are in relation *opposite*, e *op* f , if they are opposite edges of an inner face of G . Then e *co* f holds by the assumption that faces are isometric. The relation *co* is defined in the whole graph while *op* is defined only in faces/rings. Relation *op* will partition the edges set of G into *opposite edge strips ops*, as follows. (i) Any two subsequent edges of an *ops* are in *op* relation; (ii) Any three subsequent edges of such a strip belong to adjacent faces; (iii) In a plane graph, the inner dual of an *ops* is a path (however, in 3D networks, the ring/face interchanging will provide *ops* which are no more paths); (iv) The *ops* is taken as maximum possible, irrespective of the starting edge. The choice about the maximum size of face/ring, and the face/ring mode counting, will decide the length of the strip. Note that *ops* are *qoc* (quasi orthogonal cuts), meaning the transitivity relation is, in general, not obeyed.

The Omega polynomial $\Omega(x)$ [16-18] is defined on the ground of opposite edge strips *ops* S_1, S_2, \dots, S_k in the graph. Denoting by m the number of *ops* of cardinality/length $s=|S|$, we can write

$$\Omega(x) = \sum_s m \cdot x^s \quad (15)$$

The first derivative (in $x=1$) can be taken as a graph invariant or a topological index:

$$\Omega'(1) = \sum_s m \cdot s = |E(G)| \quad (16)$$

An index, called Cluj-Ilmenau $CI(G)$ [12], was defined on $\Omega(x)$:

$$CI(G) = \{[\Omega'(1)]^2 - [\Omega'(1) + \Omega''(1)]\} \quad (17)$$

In tree graphs, the Omega polynomial counts the non-opposite edges, all being included in the term of exponent $s=1$. Omega polynomial was thought to describe the covering of polyhedral nano-structures or the tiling of crystal-like lattices, as a complementary description of the crystallographic one.

In n -dimensional space, Omega polynomial could be useful in topological characterization of structures in which formulas for k -substructures are not known, the polynomial being more easily to count.

The following tables provide analytical formulas for the hyper-cubes (Tables 5 and 6), hyper-tubes (Tables 7 to 10) and hyper-tori (Tables 11 to 14) and numerical examples as well.

Table 5. Formulas for Omega polynomial in hyper-cubes Q_n

1	$\Omega(Q_n, x) = n \cdot x^{2^{n-1}}$
2	$\Omega'(1) = e(Q_n) = E(Q_n) = n \cdot 2^{n-1}$
3	$\Omega''(1) = n \cdot 2^{n-1} \cdot (2^{(n-1)} - 1)$
4	$CI(T((4, r), Q_n)) = n(n-1) \cdot 4^{n-1}$

Table 6. Omega polynomial in hyper-cubes Q_n ; examples

Vertices	Edges	Q_n	Deg(v)	Omega polynomial	CI
16	32	4	4	$4X^8$	768
32	80	5	5	$5X^{16}$	5120
64	192	6	6	$6X^{32}$	30720

Table 7. Formulas for Omega polynomial in hyper-tubes $((4,r),Q_n)$

1	$\Omega(TU((4,r),Q_n),x) = (r-1) \cdot x^{4 \cdot 2^{n-3}} + (n-1) \cdot x^{2r \cdot 2^{n-3}}$
2	$\Omega'(1) = e(TU((4,r),Q_n)) = 2^{n-3} \cdot (2r + 2rn - 4)$
3	$v(TU((4,r),Q_n)) = 4r \cdot 2^{n-3}$
4	$\Omega''(1) = 2^{n-4}(4r - 4 \cdot 2^n \cdot r + 4 \cdot 2^n + 2^n \cdot r^2 + 4nr - 2^n \cdot nr^2 - 8)$
5	$CI(TU((4,r),Q_n)) = 4^{n-2}(n^2r^2 + nr^2 - 4nr + 2r^2 - 8r + 8)$

Table 8. Omega polynomial in $TU((4,r),Q_n)$

Structure	Vertices	Edges	Q_n	Omega polynomial	CI
TU(4,5)	20	36	3	$4X^4+2X^{10}$	1032
	40	92	4	$4X^8+3X^{20}$	7008
	80	224	5	$4X^{16}+4X^{40}$	42752
TU(4,6)	24	44	3	$5X^4+2X^{12}$	1568
	48	112	4	$5X^8+3X^{24}$	10496
	96	272	5	$5X^{16}+4X^{48}$	63488

Table 9. Formulas for Omega polynomial in hyper-tubes $TU((4,r,s),Q_n)$

1	$\Omega(TU((4,r,s),Q_n),x) = r \cdot x^{2s \cdot 2^{n-3}} + (s-1) \cdot x^{2r \cdot 2^{n-3}} + (n-2) \cdot x^{rs \cdot 2^{n-3}}$
2	$\Omega'(1) = e(TU((4,r,s),Q_n)) = 2^{n-3} \cdot (2rs - 2r + nrs)$
3	$v(TU((4,r,s),Q_n)) = 2rs \cdot 2^{n-3}$
4	$\Omega''(1) = 2^{n-6} \cdot r \cdot (16s + 4 \cdot 2^n \cdot r - 4 \cdot 2^n \cdot s^2 + 8 \cdot n \cdot s + 2 \cdot 2^n \cdot r \cdot s^2 - 4 \cdot 2^n \cdot r \cdot s - 2^n \cdot n \cdot r \cdot s^2 - 16)$
5	$CI(TU((4,r,s),Q_n)) = 4^{n-3} \cdot r \cdot (8r + 6r \cdot s^2 - 4s^2 - 12r \cdot s + n^2 \cdot r \cdot s^2 - 4n \cdot r \cdot s + 3n \cdot r \cdot s^2)$

Table 10. Omega polynomial in $TU((4,r,s),Q_n)$

Structure	Vertices	Edges	Q_n	Omega polynomial	r	s	CI
TU(5,5)	50	115	3	$5X^{10}+4X^{10}+1X^{25}$	5	5	11700
	100	280	4	$5X^{20}+4X^{20}+2X^{50}$	5	5	69800
	200	660	5	$5X^{40}+4X^{40}+3X^{100}$	5	5	391200
TU(9,7)	126	297	3	$9X^{14}+6X^{18}+1X^{63}$	9	7	80532
	252	720	4	$9X^{28}+6X^{36}+2X^{126}$	9	7	471816
	504	1692	5	$9X^{56}+6X^{72}+3X^{252}$	9	7	2613024

Table 11. Formulas for Omega polynomial in hyper-tori $T((4,r), Q_n)$

1	$\Omega(T((4,r), Q_n), x) = r \cdot x^{(2^{n-1})} + (n-1) \cdot x^{(r \cdot 2^{n-2})}$
2	$\Omega'(1) = e(T((4,r), Q_n)) = r(n+1) \cdot 2^{n-2}$
3	$v(T((4,r), Q_n)) = r \cdot 2^{n-1}$
4	$\Omega''(1) = (-)r \cdot 2^{n-4} (4n + r \cdot 2^n - 2^{n+2} - r \cdot n \cdot 2^n + 4)$
5	$CI(T((4,r), Q_n)) = r \cdot 4^{n-2} (r \cdot n^2 + r \cdot n + 2r - 4)$

Table 12. Omega polynomial in hyper-tori $T((4,r), Q_n)$; examples

Vertices	Edges	Q_n	Deg(v)	Omega polynomial	CI
T(4,8)					
32	64	3	4	$8X^4+2X^{16}$	3456
64	160	4	5	$8X^8+3X^{32}$	22016
128	384	5	6	$8X^{16}+4X^{64}$	129024
T(4,9)					
288	1008	6	7	$9X^{32}+5X^{144}$	903168
576	2304	7	8	$9X^{64}+6X^{288}$	4773888
1152	5184	8	9	$9X^{128}+7X^{576}$	24403968

Table 13. Formulas for Omega polynomial in hyper-tori $T((4,r,s), Q_n)$

1	$\Omega(T((4,r,s), Q_n), x) = s \cdot x^{r \cdot 2^{n-2}} + r \cdot x^{s \cdot 2^{n-2}} + (n-2) \cdot x^{rs \cdot 2^{n-3}}$
2	$\Omega'(1) = e(T((4,r,s), Q_n)) = rs(n+2) \cdot 2^{n-3}$
3	$v(T((4,r,s), Q_n)) = rs \cdot 2^{n-2}$
4	$\Omega''(1) = (-)2^{n-6} rs(8n - 2^{n+2}r - 2^{n+2}s + 2^{n+1}rs - 2^n nrs + 16)$
5	$CI(T((4,r,s), Q_n)) = 2^{2(n-3)} rs(rsn^2 + 3rsn - 4r - 4s + 6rs)$

Table 14. Omega polynomial in hyper-tori $T((4,r,s), Q_n)$; examples

Vertices	Edges	Q_n	Deg(v)	Omega polynomial	CI
T(4,5,15)					
150	375	3	5	$15X^{10}+5X^{30}+1X^{75}$	129000
300	900	4	6	$15X^{20}+5X^{60}+2X^{150}$	741000
600	2100	5	7	$15X^{40}+5X^{120}+3X^{300}$	4044000
T(4,8,8)					
128	320	3	5	$16X^{16}+1X^{64}$	94208
256	768	4	6	$16X^{32}+2X^{128}$	540672
512	1792	5	7	$16X^{64}+3X^{256}$	2949120

CLUJ POLYNOMIAL AND RELATERD INDICES

In bipartite graphs, the coefficients of *CJ* polynomial [19,20] can be calculated by an orthogonal edge-cut procedure [20,21]. In this respect, a more theoretical background is needed.

A graph *G* is a *partial cube* if it is embeddable in the hypercube $C(n)$. For any edge $e=(u,v)$ of a connected graph *G* let n_{uv} denote the set of vertices lying closer to *u* than to *v*: $n_{uv} = \{w \in V(G) \mid d(w,u) < d(w,v)\}$. It follows that $n_{uv} = \{w \in V(G) \mid d(w,v) = d(w,u) + 1\}$. The sets (and subgraphs) induced by these vertices, n_{uv} and n_{vu} , are called *semicubes* of *G*; the *semicubes* are called *opposite semicubes* and are disjoint [22,23]. A graph *G* is bipartite if and only if, for any edge of *G*, the opposite *semicubes* define a partition of *G*: $n_{uv} + n_{vu} = v = |V(G)|$. These *semicubes* are just the vertex proximities of (the endpoints of) edge $e=(u,v)$, which CJ_e polynomial counts. In partial cubes, the *semicubes* can be estimated by an orthogonal edge-cutting procedure.

Function of the mathematic operation, three polynomials can be written with these *semicubes*:

(i) *Cluj-Sum*, symbolized *CJS* (obtained by summation) [24-26]:

$$CJS(x) = \sum_e (x^{v_k} + x^{v-v_k}) \tag{18}$$

(ii) PI_v (vertex, Padmakar-Ivan index [27]) polynomial (obtained by pairwise summation) [28-30]

$$PI_v(x) = \sum_e x^{v_k + (v-v_k)} \tag{19}$$

(iii) *Cluj-Product*, symbolized *CJP* (obtained by pairwise product). [19,20,26,32]. It was also named *Szeged* polynomial SZ_v [29,30,33]:

$$CJP(x) = SZ_v(x) = \sum_e x^{v_k(v-v_k)} \tag{20}$$

In hypercubes, the formulas for calculating the Cluj-related polynomials and derived topological indices (as the first derivative, in $x=1$) are given in Table 15 while examples are provided in Tables 16 to 18. Observe that the first derivative of *CJs* and PI_v are the same (Tables 16 and 17) but the second derivative (in $x=1$) is however, different.

Table 15. Formulas for Cluj and PI_v polynomial in hyper-cubes

Formulas	
1	$v(Q_n) = V(Q_n) = 2^n ; e(Q_n) = E(Q_n) = n \cdot 2^{n-1}$
2	$CJS(Q_n, x) = n(v/2)x^{v/2} + n(v/2)x^{v/2} = n(2^{n-1}) \cdot x^{2^{n-1}} + n(2^{n-1}) \cdot x^{2^{n-1}} = n \cdot 2^n \cdot x^{2^{n-1}}$
3	$CJS'(1) = n \cdot 2^{2n-1}$
4	$CJS''(1) = n \cdot 2^{2(n-1)} \cdot (2^n - 2)$
5	$PI_v(Q_n, x) = ex^v = n \cdot 2^{n-1} \cdot x^{2^n}$
6	$PI_v'(1) = n \cdot 2^{2n-1}$
7	$PI_v''(1) = n \cdot 2^{2n-1} \cdot (2^n - 1)$
8	$CJP(Q_n, x) = n(v/2)x^{(v/2)(v/2)} = n \cdot 2^{n-1} \cdot x^{2^{2(n-1)}}$
9	$CJP'(1) = n \cdot 2^{n-1} \cdot 2^{2(n-1)} = SZ_v$

Table 16. Cluj polynomial CJS in hypercube Q_n

$Q_n : n$	CJS(x)	CJS'	CJS''
3	$12x^4 + 12x^4$	96	288
4	$32x^8 + 32x^8$	512	3584
5	$80x^{16} + 80x^{16}$	2560	38400
6	$192x^{32} + 192x^{32}$	12288	380928

Table 17. PI_v polynomial in hypercube Q_n

$Q_n : n$	$PI_v(x)$	PI_v'	PI_v''
3	$12x^8$	96	672
4	$32x^{16}$	512	7680
5	$80x^{32}$	2560	79360
6	$192x^{64}$	12288	774144

Table 18. Cluj polynomial CJP in hypercube Q_n

$Q_n : n$	CJP(x)	$CJP'=SZ_v$
3	$12x^{(4*4)}$	192
4	$32x^{(8*8)}$	2048
5	$80x^{(16*16)}$	20480
6	$192x^{(32*32)}$	196608

COMPUTATIONAL DETAILS

The design and properties of the studied structures was performed by our original Nano Studio [34] software program.

The numerical data resulted in calculation of polynomials and related topological indices appeared as integer sequences. To find the corresponding analytical formulas, we made use of OEIS, "The On-Line Encyclopedia of Integer Sequences" [35].

CONCLUSIONS

In this paper, several polynomials and the corresponding topological indices have been computed for tubular and toroidal hyper-structures made from hyper-cube units. Analytical formulas were established and numerical examples given.

REFERENCES

1. L. Schläfli, "Theorie der vielfachen Kontinuität Zürcher und Furrer", Zürich, **1901** (Reprinted in: Ludwig Schläfli, 1814-1895, "Gesammelte Mathematische Abhandlungen", Verlag Birkhäuser, Basel, **1950**, Band 1).
2. http://en.wikipedia.org/wiki/Convex_hull; <http://en.wikipedia.org/wiki/Simplex>; <http://en.wikipedia.org/wiki/Cross-polytope>; <http://en.wikipedia.org/wiki/Hypercube>. (accessed 12.05.2015)
3. H.S.M. Coxeter, "Regular Polytopes", 3rd ed. New York: Dover, **1973**.
4. B. Grünbaum, "Convex Polytopes", Graduate Texts in Mathematics (2nd ed.), Springer, **2003**.
5. L. Euler, *Novi Comm. Acad. Scient. Imp. Petrop.*, **1758**, 4, 109.
6. M.V. Diudea, "Multi-shell polyhedral clusters", Springer, **2016** (in preparation).
7. C.L. Nagy, M.V. Diudea, *MATCH Commun. Math. Comput. Chem.*, **2016** (in press).
8. A. Parvan-Moldovan, M. V. Diudea, *Iran. J. Math. Chem.*, **2015**, 6, 163.
9. M.V. Diudea, *Bull. Chem. Soc. Japan*, **2002**, 75, 487.
10. F. Harary, "Graph Theory", Addison-Wesley, Reading, MA, **1969**.
11. M.V. Diudea, "Nanomolecules and Nanostructures - Polynomials and Indices", MCM, No. 10, Univ. Kragujevac, **2010**.
12. P.E. John, A.E. Vizitiu, S. Cigher, M.V. Diudea, *MATCH Commun. Math. Comput. Chem.*, **2007**, 57, 479.
13. D.Ž. Djoković, *Combin. J. Theory Ser. B*, **1973**, 14, 263.
14. P.M. Winkler, *Discrete Appl. Math.*, **1984**, 8, 209.
15. M.V. Diudea, S. Klavžar, *Acta Chem. Sloven.*, **2010**, 57, 565.

16. M.V. Diudea, *Carpath. J. Math.*, **2006**, 22, 43.
17. M.V. Diudea, S. Cigherand, P.E. John, *MATCH, Commun. Math. Comput. Chem.* **2008**, 60, 237.
18. M.V. Diudea, S. Cigher and A.E. Vizitiu, M.S. Florescu, P.E. John, *J. Math. Chem.*, **2009**, 45, 316.
19. M.V. Diudea, in: Gutman I., Furtula B., (Eds) "Novel Molecular Structure Descriptors-Theory and Applications I", Univ Kragujevac, Kragujevac, **2010**, 191.
20. M.V. Diudea in: Gutman I., Furtula B., (Eds) "Novel Molecular Structure Descriptors-Theory and Applications II", Univ Kragujevac, Kragujevac, **2010b**, 57.
21. I. Gutman, S. Klavžar, *J. Chem. Inf. Comput. Sci.*, **1995**, 35, 1011.
22. M.V. Diudea, S. Cigher, P.E. John, *MATCH Commun. Math. Comput. Chem.*, **2008**, 60, 237.
23. M.V. Diudea, S. Klavžar, *Acta Chem. Sloven.*, **2010**, 57, 565.
24. M.V. Diudea, A.E. Vizitiu, D. Janežič, *J. Chem. Inf. Model.*, **2007**, 47, 864.
25. M.V. Diudea, *J. Math. Chem.*, **2009**, 45, 295.
26. M.V. Diudea, N. Dorosti, A. Iranmanesh, *Carpath. J. Math.*, **2010**, 4, 247.
27. P.V. Khadikar, *Nat. Acad. Sci. Lett.*, **2000**, 23, 113.
28. M.H. Khalifeh, H. Yousefi-Azari, A.R. Ashrafi, *Discrete Appl. Math.*, **2008**, 156, 1780.
29. A.R. Ashrafi, M. Ghorbani, M. Jalali, *J. Theor. Comput. Chem.*, **2008**, 7, 221.
30. T. Mansour, M. Schork, *Discr. Appl. Math.*, **2009**, 157, 1600.
31. M.V. Diudea, A. Ilić, M. Ghorbani, A.R. Ashrafi, *Croat. Chem. Acta*, **2010**, 83, 283.
32. M.V. Diudea, *J. Chem. Inf. Comput. Sci.*, **1997**, 37, 300.
33. M.H. Khalifeh, H. Yousefi-Azari, A.R. Ashrafi, *Linear Algebra Appl.*, **2008**, 429, 2702.
34. C.L. Nagy, M.V. Diudea, NANO–Studio, Babes-Bolyai Univ., Cluj, **2009**.
35. <https://oeis.org/>, "The On-Line Encyclopedia of Integer Sequences" (accessed 12.05.2015).

***Dedicated to Professor Mircea Diudea
on the Occasion of His 65th Anniversary***

QSAR STUDY OF PHENOTHIAZINES

ATENA PÎRVAN MOLDOVAN^{a,*}, SARA ERSALI^a, RALUCA POP^b

ABSTRACT. A QSAR study on a set of 30 phenothiazines performed within a hypermolecule frame, to model their logP and LD₅₀ values, is reported. The initial set of molecules was split into a training set and the test set; Cluj topological indices and some quantum mechanical descriptors have been used to derive the models, which were next tested for predictability by LOO, external validation and similarity clustering.

Key words: phenothiazine, hypermolecule, LD₅₀, logP, topological indices.

INTRODUCTION

Phenothiazine is an organic heterocyclic compound, of the class of thiazines, with the brute formula S(C₆H₄)₂NH, of which skeleton occurs in various antipsychotic, antihistaminic, antiemetic, etc. drugs. Phenothiazine was synthesized by Bernthsen in 1883 by melting the diphenylamine with sulfur; its medicamentous derivatives are currently synthesized by the cyclization of substituted diphenylamines or diphenyl sulfides. Synthesis of methylene blue was reported in 1876 and is still used as antiseptic, anthelmintic drug.

Phenothiazine antipsychotics, like chlorpromazine and prochlorperazine, are used to treat serious mental and emotional disorders, including schizophrenia and other psychotic disorders. Phenothiazine antipsychotics are classified into three groups, differing with respect to the substituent on nitrogen: the aliphatic compounds, piperidine compounds and piperazine derivatives. As antihistaminic, the promethazine is the most used phenothiazine.

^a Babeş-Bolyai University, Faculty of Chemistry and Chemical Engineering, 11 Arany Janos str., RO-400028, Cluj-Napoca, Romania

^b University of Medicine and Pharmacy "Victor Babes" Timisoara, Faculty of Pharmacy, E. Murgu Square 2, 300041 Timisoara, Romania

* Corresponding Author: atenamoldovan99@gmail.com

Several water-soluble phenothiazines, such as methylene blue, methylene green, thionine, etc. can be electropolymerized, the resulted polymer finding industrial applications [1].

Quantitative structure–activity relationship (QSAR) studies, attempt to predict (in the light of the paradigm that relates a biological activity, or a physicochemical property, of a compound to its chemical structure) the activity of tested compounds and to suggest structural features which could enhance that biological activity, in the process of drug design [2-4]. The concept of similarity is used in grouping chemical compounds according to their molecular structure, biological effects or physicochemical properties; it has found extensive use in drug discovery [4].

Topological indices are molecular descriptors, useful in QSAR studies; they are integer or real-valued numbers, derived from the connectivity and other topological matrices computed on the molecular graph associated to a molecule. Among thousands of topological indices, the Cluj indices, defined by Diudea [5, 6], are among the most simple and versatile ones in coding the chemical information of a molecular graph. Indices are calculated from the Cluj topological matrices, as half sum of matrix entries, by using the original TopoCluj software [7].

The octanol–water partition coefficient ($\log P$) describes the chemical lipophilic/hydrophilic characteristics. $\log P$ is the ratio of a chemical concentration in the octanol phase to its concentration in the aqueous phase of a two-phase system at equilibrium. $\log P$ is involved in the passive transport of a drug molecule through cell membrane [3].

This QSAR study was performed following Diudea's algorithm [8]; it is based on the alignment of molecules over a hypermolecule [9] and a correlation weighting procedure [10, 11] coupled with a predictive validation of the model descriptors within similarity clusters [12] performed for each molecule in the test set. The algorithm can be extended with other powerful statistical tools (e.g. PLS or PCA) but we limited here to the more common multi linear regression in achieving the best prediction of a chosen property, like $\log P$ or LD_{50} .

COMPUTATIONAL

The structures have been optimized at Hartree-Fock HF (6-31g(d,p)) level of theory, in gas phase, by Gaussian 09 [13]. Topological indices have been computed by TOPOCLUJ software [7]. The modeled properties: $\log P$ and LD_{50} , along with some of the molecular descriptors, like Charges, D3D, Detour, Distance, IE[CfMax], IP[CfMin], IP[CfMax], E HOMO (a.u.), HL gap (eV), Chemical potential (eV), Hardness (eV), Electrophilicity (eV), are listed in Tables 1 and 2, respectively.

RESULTS AND DISCUSSION

Data set

A hypermolecule (Figure 1) was built up by superposing all the 30 molecules under study. The hypermolecule is considered to mimic the investigated statistical hyperspace [9] and works like a biological receptor, over which the ligands are aligned. According to this alignment, *binary vectors* were constructed, with 1 when for a given position of the hypermolecule exists an atom in the current molecule, and zero, otherwise. In the above binary vectors, the values 1 are next replaced by mass fragments. Table 1 lists the phenothiazines of the data set, with the properties to be modeled: logP and LD₅₀ (intraperitoneal, mouse).

Table 1. List of studied phenothiazines with their name, CID and properties logP and LD₅₀.

No.	CID	logP	LD50 mg/kg	Name	Canonical Smiles
1	2726	5.41	14	chlorpromazine	CN(C)CCCN1C2=CC=CC=C2SC3=C1C=C(C=C3)Cl
2	2801	5.19	150	clomipramine	CN(C)CCCN1C2=CC=CC=C2CCC3=C1C=C(C=C3)Cl
3	2995	4.90	85	desipramine	CNCCCN1C2=CC=CC=C2CCC3=CC=CC=C31
4	3089	3.34	190	fonazine/dimethothiazine	CC(CN1C2=CC=CC=C2SC3=C1C=C(C=C3)S(=O)(=O)N(C)C)N(C)C
5	3781	3.66	62	isothipendyl	CC(CN1C2=CC=CC=C2SC3=C1N=CC=C3)N(C)C
6	4066	4.70	54	mequitazine	C1CN2CCC1C(C2)CN3C4=CC=CC=C4SC5=CC=CC=C53
7	4744	4.10	185	perazine	CN1CCN(CC1)CCCN2C3=CC=CC=C3SC4=CC=CC=C42
8	4747	3.52	115	periciazine	C1CN(CCC1O)CCCN2C3=CC=CC=C3SC4=C2C=C(C=C4)C#N
9	4748	4.20	64	perphenazine	C1CN(CCN1CCCN2C3=CC=CC=C3SC4=C2C=C(C=C4)Cl)CCO
10	4917	4.88	120	prochlorperazine	CN1CCN(CC1)CCCN2C3=CC=CC=C3SC4=C2C=C(C=C4)Cl
11	4926	4.55	140	promazine	CN(C)CCCN1C2=CC=CC=C2SC3=CC=CC=C31
12	4927	4.81	124	promethazine	CC(CN1C2=CC=CC=C2SC3=CC=CC=C3)N(C)C
13	5452	5.90	65	thioridazine	CN1CCCC1CCN2C3=CC=CC=C3SC4=C2C=C(C=C4)SC
14	5566	5.03	120	trifluoperazine	CN1CCN(CC1)CCCN2C3=CC=CC=C3SC4=C2C=C(C=C4)C(F)(F)F
15	6075	5.60	140	mepazine/pecazine	CN1CCCC(C1)CN2C3=CC=CC=C3SC4=CC=CC=C42
16	6077	4.20	350	acetylpromazine	CC(=O)C1=CC2=C(C=C1)SC3=CC=CC=C3N2CCCN(C)C
17	6761	4.40	80	pipamazine	C1CN(CCC1C(=O)N)CCCN2C3=CC=CC=C3SC4=C2C=C(C=C4)Cl
18	10646	4.70	190	pyrathiazine	C1CCN(C1)CCN2C3=CC=CC=C3SC4=CC=CC=C42
19	14670	3.40	135	prothipendyl	CN(C)CCCN1C2=CC=CC=C2SC3=C1N=CC=C3
20	14677	5.23	183	methdilazine	CN1CCC(C1)CN2C3=CC=CC=C3SC4=CC=CC=C42
21	16414	4.80	119	7-hydroxycloprpromazine	CN(C)CCCN1C2=C(C=C(C=O)O)SC3=C1C=C(C=C3)Cl
22	19396	3.40	185	oxomemazine	CC(CN1C2=CC=CC=C2S(=O)(=O)C3=CC=CC=C3)N(C)C
23	19675	4.21	98	piperacetazine	CC(=O)C1=CC2=C(C=C1)SC3=CC=CC=C3N2CCCN4CCC(CC4)CCO
24	65535	4.90	225	diethazine	CCN(CC)CCN1C2=CC=CC=C2SC3=CC=CC=C31
25	65750	5.90	90	chlorprothazine	CCN(CC)CCCN1C2=CC=CC=C2SC3=C1C=C(C=C3)Cl
26	68223	4.20	115	fenethazine	CN(C)CCN1C2=CC=CC=C2SC3=CC=CC=C31
27	69500	3.80	210	difazin	CCN(CC)CC(=O)N1C2=CC=CC=C2SC3=CC=CC=C31
28	70413	3.90	163	opromazine	CN(C)CCCN1C2=CC=CC=C2S(=O)C3=C1C=C(C=C3)Cl
29	72287	4.68	58.5	levomepromazine	C[C@H](CN1C2=CC=CC=C2SC3=C1C=C(C=C3)OC)N(C)C
30	94280	4.96	206	dimetacrine	CC1(C2=CC=CC=C2N(C3=CC=CC=C3)CCCN(C)C)

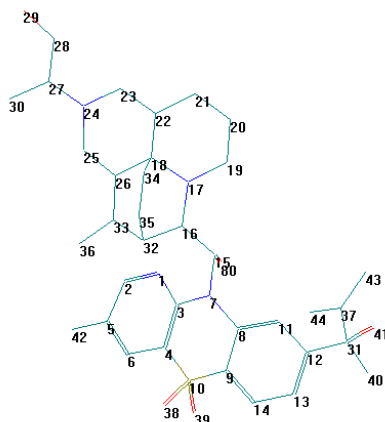


Figure 1. Hypermolecule comprising the features of the dataset

Table 2. The modeled properties: logP and LD₅₀ and some of the molecular descriptors computed for 30 phenothiazines

Mol	logP	LD50 mg/kg	Charges	D3D	Detour	Distance	IE[CiMax]	IP[CiMin]	IP[CiMax]	E HOMO (a.u.)	HL gap (eV)	Chem.pot (eV)	Hardness (eV)	E.phil (eV)	SD(logP)	SD(LD50)
1	5.20	~	-0.105	959	2450	896	201	4630	1260	-0.297	11.040	-2.560	5.520	0.590	-54.235	~
2	5.20	150	-0.379	1040	2860	995	212	5030	1350	-0.302	11.340	-2.550	5.670	0.570	-53.820	-9000.05
3	4.90	85	0.060	800	2330	759	144	3770	958	-0.295	11.430	-2.450	5.720	0.520	-54.097	-9033.07
4	3.80	190	-0.280	1550	3810	1540	366	8090	2070	-0.308	10.680	-3.030	5.320	0.860	-55.200	-8928.76
5	3.50	62	-0.668	740	2150	744	156	3730	974	-0.297	11.040	-2.550	5.520	0.590	-55.528	-9040.66
6	4.60	54	-0.162	1130	3320	1090	219	8580	1670	-0.291	11.436	-2.203	5.718	0.424	-54.476	-9059.29
7	4.10	185	-0.341	1370	3500	1390	320	9070	2440	-0.291	11.170	-2.340	5.580	0.490	-54.779	-8932.61
8	3.50	115	-0.034	1610	4200	1720	398	11300	2980	-0.304	10.616	-2.947	5.308	0.818	-55.463	-9015.74
9	4.20	64	-0.065	1910	4560	2000	486	13500	3690	-0.294	11.284	-2.346	5.642	0.488	-54.828	-9034.78
10	4.90	120	-0.098	1530	3840	1540	353	10100	2670	-0.294	11.280	-2.347	5.640	0.488	-54.208	-8976.6
11	4.50	140	-0.196	874	2200	789	178	4030	1130	-0.293	11.180	-2.380	5.590	0.510	-54.807	-8956.05
12	4.80	124	-0.267	759	2150	744	156	3730	974	-0.273	10.690	-2.090	5.350	0.410	-54.571	-9007.79
13	5.90	65	-0.334	1560	3860	1440	311	9490	2390	-0.297	10.900	-2.620	5.450	0.610	-53.196	-9048.29
14	4.70	120	0.636	2110	4940	2080	492	13700	3610	-0.304	10.950	-2.800	5.480	0.720	-54.707	-8989.26
15	5.60	140	-0.268	1070	2870	982	162	6450	1420	-0.294	11.180	-2.410	5.590	0.520	-53.606	-8973.29
16	4.30	350	-0.065	1240	2990	1150	268	6080	1630	-0.301	10.360	-3.010	5.180	0.870	-54.393	-8762.6
17	4.40	80	0.074	1870	4540	1980	474	13300	3590	-0.267	10.471	-2.013	5.235	0.387	-54.529	-9045.99
18	4.70	190	-0.275	959	2560	889	176	5340	1280	-0.286	11.700	-2.107	5.673	0.391	-54.243	-8906.66
19	3.40	135	-0.642	807	2200	789	178	4030	1130	-0.280	10.610	-2.320	5.300	0.510	-55.764	-8988.92
20	4.60	183	-0.208	833	2540	859	146	5280	1130	-0.280	10.770	-2.240	5.380	0.470	-54.455	-8930.29
21	4.80	119	-0.192	1060	2720	1020	224	5300	1420	-0.297	11.020	-2.560	5.510	0.600	-54.235	-9000.05
22	3.40	185	0.123	1140	2880	1080	255	5450	1550	-0.333	11.220	-3.460	5.610	1.070	-55.560	-8931.28
23	4.00	~	-0.013	2250	5380	2410	595	16500	4480	-0.299	10.340	-2.960	5.170	0.850	-55.355	~
24	4.90	225	-0.286	951	2410	894	215	4570	1330	-0.291	11.080	-2.360	5.540	0.500	-54.243	-8906.66
25	5.90	90	-0.221	1170	2980	1190	314	6280	1940	-0.297	11.030	-2.560	5.510	0.590	-53.199	-9000.05
26	4.20	115	-0.228	711	1950	658	128	3300	832	-0.287	11.350	-2.122	5.675	0.397	-54.883	-8980.16
27	3.80	210	0.033	990	2610	979	242	4950	1450	-0.304	11.300	-2.620	5.650	0.610	-55.296	-8906.66
28	3.90	163	-0.048	1020	2690	993	223	5110	1390	-0.309	10.970	-2.930	5.480	0.780	-55.299	-8947.64
29	4.80	58.5	-0.323	1150	2950	1130	268	5900	1620	-0.282	10.920	-2.220	5.460	0.450	-54.273	-9038.46
30	5.40	206	-0.536	1020	2650	973	221	4930	1380	-0.262	10.510	-1.870	5.250	0.330	-53.731	-8906.92

Data reduction

In this step, the descriptors with variance <10% and intercorrelation > 0.80 (two descriptors highly correlated bring quite the same information on the molecule, one of them being sufficient) were discarded.

Correlation weighting was performed as follows: the correlation coefficients of the statistically significant positions in the hypermolecule were used to multiply the local descriptors, thus resulting new weighted vectors CD_{ij} . Next, these new descriptors are summed to give a global descriptor, $SD_i = \sum_j CD_{ij}$ which is a linear combination of the local correlating descriptors for the significant positions in the hypermolecule (for logP model, significant positions are 1, 10, 12, 18, 19, 21, 23, 24, 26, 27, 28, 30, 31, 32, 40, 80; for LD₅₀ model, these are: 1, 12, 16, 18, 19, 21, 27, 28, 31, 32, 33, 34, 37, 38, 40, 41).

Basic equations that describe the relationships between values of property or biological activity of compounds and their structures were obtained:

$$\log P = 59.096 + SD_{\log P} \quad (1)$$

n=30; R²=0.946; s=0.165; F=488.078

$$LD_{50} = 9113.289 + SD_{LD_{50}} \quad (2)$$

n=28; R²=0.956; s=13.964; F=566.487
(molecules 1 and 23 were outliers)

QSAR models (for case log P)

The models were performed on the training set (structures 11-30) and the best results (in decreasing order of R²) are listed below in Tables 3 and 4.

Table 3. The best bivariate models for logP in the training set

Property	Descriptors	R ²
logP	SD(logP) IP[CfMax]	0.9487
	SD(logP) Detour	0.9482
	SD(logP) D3D	0.9480
	SD(logP) El.phil (eV)	0.9480
	SD(logP) IE[CfMax]	0.9479
	SD(logP) IE[CjMax]	0.9479
	SD(logP) Chem.pot.(eV)	0.9474
	SD(logP) E HOMO (a.u.)	0.9469
	SD(logP) Charges	0.9467
	SD(logP) Hardness(eV)	0.9465

Table 4. The best trivariate models for logP in the training set

Property	Descriptors	R ²
logP	IP[CfMin] Chem.pot (eV) SD(logP)	0.95114
	Chem.pot (eV) SD(logP) IP[CjMin]	0.95110
	IP[CjMax] Chem.pot (eV) SD(logP)	0.95109
	Chem.pot (eV) SD(logP) IP[CjMax]	0.95109
	Distance Chem.pot (eV) SD(logP)	0.95060
	Chem.pot (eV) SD(logP) IE[CfMax]	0.95026
	Hardness (eV) SD(logP) Detour	0.94954
	D3D Hardness (eV) SD(logP)	0.94920

Property	Descriptors		R ²
SD(logP)	Detour	E HOMO (a.u.)	0.94919
Charges	Chem.pot (eV)	SD(logP)	0.94919
E HOMO (a.u.)	SD(logP)	D3D	0.94905
E HOMO (a.u.)	SD(logP)	Distance	0.94904
E HOMO (a.u.)	SD(logP)	Charges	0.94833
Chem.pot (eV)	SD(logP)	E HOMO (a.u.)	0.94755

I. Monovariate regression

$$\log P = 57.266 + 0.966 \times \text{SD}_{\log P} \quad (3)$$

n=20; R²=0.946; s=0.172; F=317.17

II. Bivariate regression

$$\log P = 57.299 + 0.968 \times \text{SD}_{\log P} + 3.54 \times 10^{-5} \times \text{IP}[\text{CfMax}] \quad (4)$$

n=20; R²=0.949; s=0.173; F=157.155

III. Trivariate regression

$$\log P = 56.341 + 0.948 \times \text{SD}_{\log P} + 1.26 \times 10^{-5} \times \text{IP}[\text{CfMin}] + 0.097 \times \text{Chem.pot.} \quad (5)$$

n=20; R²=0.951; s=0.174; F=103.82

QSAR models (for case LD₅₀)

The models were performed on the training set and the best results (in decreasing order of R²) are listed below in Tables 5 and 6.

I. Monovariate regression

$$\text{LD}_{50} = 9444.65 + 1.037 \times \text{SD}_{\text{LD}_{50}} \quad (6)$$

n=19; R²=0.940; s=13.534; F=265.126

II. Bivariate regression

$$\text{LD}_{50} = 9415.945 + 1.033 \times \text{SD}_{\text{LD}_{50}} - 0.0266 \times \text{IE}[\text{CfMax}] \quad (7)$$

n=19; R²=0.943; s=13.607; F=131.573

Table 5. The best bivariate models for LD₅₀ in the training set

Property	Descriptors		R ²
LD ₅₀	SD(LD ₅₀)	IE[CfMax]	0.9427
		SD(LD ₅₀)	0.9424
		SD(LD ₅₀)	0.9424
		IP[CfMax]	0.9422
		IP[CjMax]	0.9421
		SD(LD ₅₀)	0.9414
		SD(LD ₅₀)	0.9413
		SD(LD ₅₀)	0.9412
		SD(LD ₅₀)	0.9412
		Detour	0.9407
		SD(LD ₅₀)	0.9401
		SD(LD ₅₀)	0.9398

QSAR STUDY OF PHENOTHIAZINES

Property	Descriptors		R ²
	Hardness (eV)	SD(LD ₅₀)	0.9398
	SD(LD ₅₀)	E.phil (eV)	0.9398
	SD(LD ₅₀)	Chem.pot (eV)	0.9398
	SD(LD ₅₀)	E HOMO (a.u.)	0.9397

III. Trivariate regression

$$LD_{50}=9606.267+1.055\times SD_{LD_{50}}-0.2024\times IE[CfMax]+0.047\times Distance \quad (8)$$

n=19; R²=0.947; s=13.498; F=89.557

Table 6. The best trivariate models for LD₅₀ in the training set

Property	Descriptors			R ²
LD ₅₀	Distance	SD(LD ₅₀)	IE[CfMax]	0.9471
	D3D	SD(LD ₅₀)	Detour	0.9448
	IE[CfMax]	HL gap (eV)	SD(LD ₅₀)	0.9432
	IE[CfMax]	Hardness (eV)	SD(LD ₅₀)	0.9432
	SD(LD ₅₀)	E.phil (eV)	IE[CfMax]	0.9429
	SD(LD ₅₀)	Chem.pot (eV)	IE[CfMax]	0.9428
	SD(LD ₅₀)	E HOMO (a.u.)	IE[CfMax]	0.9427
	Chem.pot (eV)	Distance	SD(LD ₅₀)	0.9415
	IP[CjMin]	SD(LD ₅₀)	E HOMO (a.u.)	0.9412
	SD(LD ₅₀)	Detour	Chem.pot (eV)	0.9407

Model validation

(a) Leave-one-out

The performances in leave-one-out analysis [14] related to the models listed as best in Tables 3-6 are shown in Tables 7 and 8 .

Table 7. Leave-one-out analysis for the best logP models

	Descriptors	Q ²	R ² - Q ²
1	SD(logP)	0.9378	0.0085
2	SD(logP), IP[CfMax]	0.9285	0.0208
3	SD(logP), IP[CfMin], Chem.pot.	0.9096	0.0410

Table 8. Leave-one-out analysis for the best LD₅₀ models

	Descriptors	Q ²	R ² - Q ²
1	SD(LD ₅₀)	0.9306	0.0092
2	SD(LD ₅₀), IE[CfMax]	0.9251	0.0176
3	SD(LD ₅₀), IE[CfMax], Distance	0.9188	0.0301

(b) External Validation

The values of logP and LD₅₀ for the test sets (structures 1-10 for logP; structures 8, 11, 12, 16, 18, 20, 24, 26, 28 for LD₅₀) of phenothiazines were calculated by using Eqs 5 and 8, respectively.

The monivariate correlations are plotted in Figures 2 and 3.

$$\log P_{\text{exp}} = -0.674 + 1.132 \times \log P_{\text{calc}} \quad (9)$$

(n=10, R²=0.940, s=0.171, F=126.298)

$$LD_{50\text{exp}} = 10.945 + 0.916 \times LD_{50\text{calc}} \quad (10)$$

(n=9, R²=0.944, s=18.942, F=116.983)

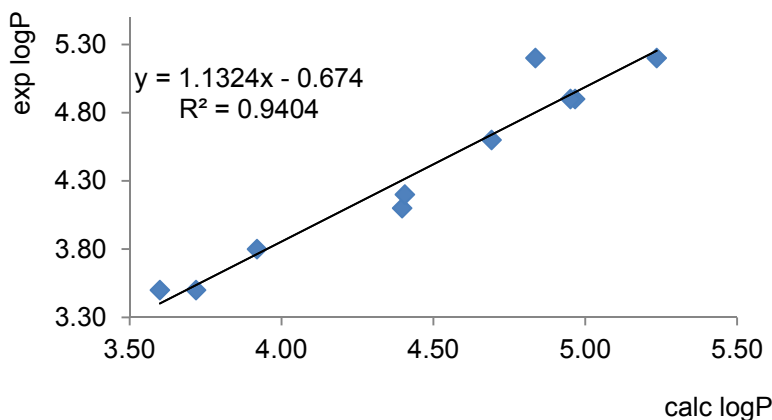


Figure 2. The plot $\log P_{\text{exp}}$ vs. $\log P_{\text{calc}}$. for the test set (external validation).

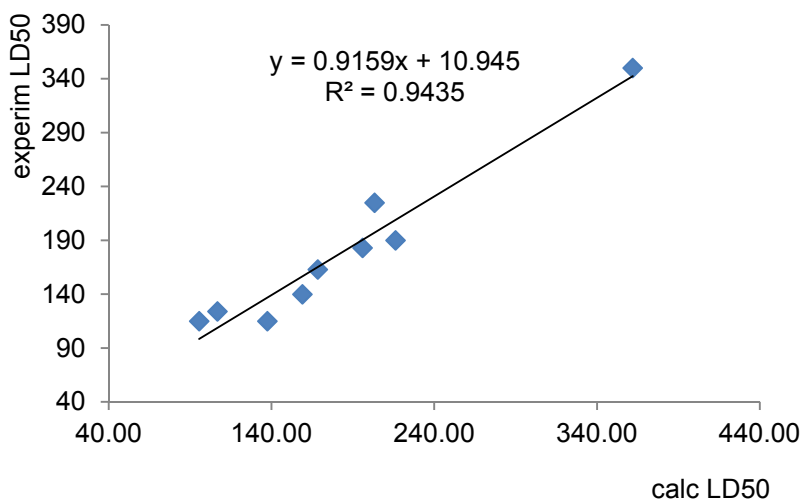


Figure 3. The plot $LD_{50\text{exp}}$ vs. $LD_{50\text{calc}}$. for the test set(external validation)

From Figures 2 and 3 one can see that our models show a good predictive ability.

(c) Similarity Cluster Validation

Validation can also be performed by using similarity clusters: each of the 10/9 molecules in the test set, is the leader of its own cluster, selected by 2D similarity among the 20/19 structures of the learning set (each cluster comprising about 12-15 molecules). The values of logP and LD_{50calc} were predicted by 10/9 new equations (the leader being left out) with the same descriptors as in Eqs. 5 and 8, respectively.

The monovariate correlation for logP

$$\log P_{\text{exp}} = -0.516 + 1.094 \times \log P_{\text{calc-clusters}} \quad (11)$$

$n=10, R^2=0.946, s=0.162, F=141.674$

is plotted in Figure 4.

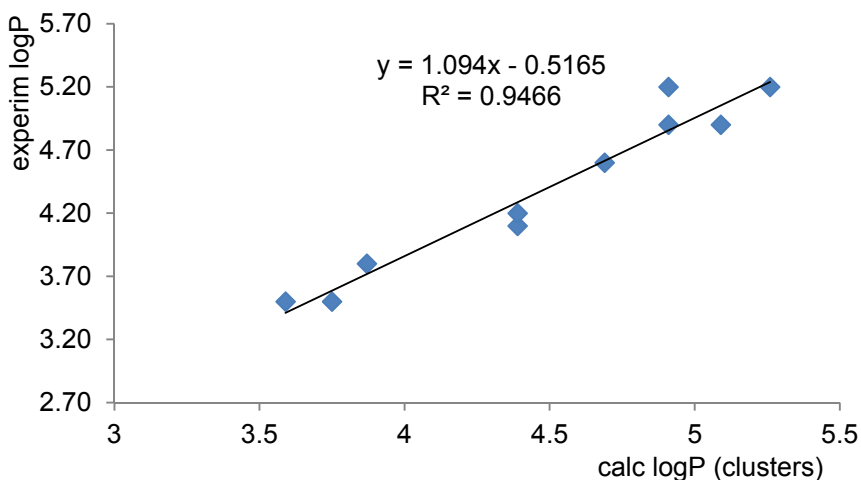


Figure 4. The plot logP_{exp} vs. logP_{calc} (by clusters of similarity) for the test set

The monovariate correlation for LD₅₀

$$LD_{50\text{exp}} = 10.99 + 0.914 \times LD_{50\text{calc-clusters}} \quad (12)$$

$n=9, R^2=0.951, s=17.707, F=134.87$

is plotted in Figure 5.

Prediction of logP ($R^2=0.946$), and LD₅₀ ($R^2=0.951$), is more accurate when using the similarity clusters, compared to the classical external validation of the model. We limited the model to three variables, keeping in mind the suggestions of Topliss and Costello [15].

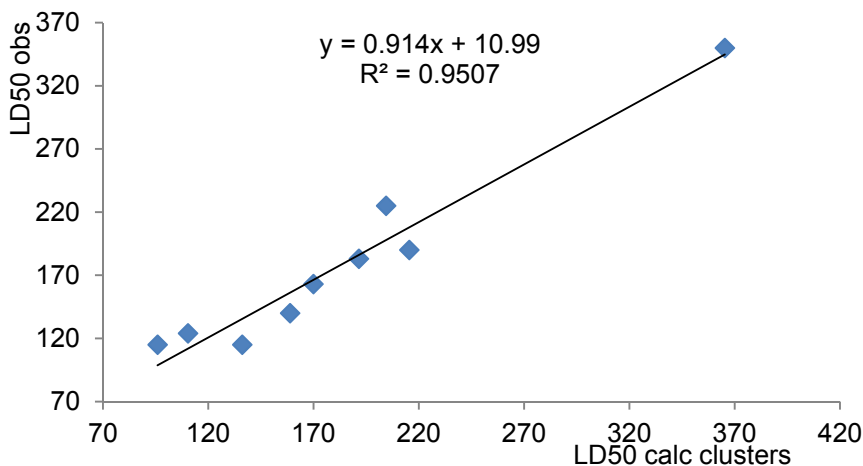


Figure 5. The plot LD_{50} vs. LD_{50calc} (by clusters of similarity) for the test set

CONCLUSIONS

A QSAR study for modeling $\log P$ and LD_{50} of a set of 30 phenothiazine derivatives, downloaded from some well-known databases, is reported. The approach is based on correlation weighting and alignment over a hypermolecule, that mimics the investigated correlational space. The best models, derived on the learning set of phenothiazines, were validated by leave-one-out test, in the external test set and in a version of prediction, based on clusters of similarity. The models were built up around the „sum descriptor” SD_i that collects the ligand topological informations, a linear combination of local descriptors CD_{ij} , weighted by correlation coefficients of fitting the ligands (*i.e.*, molecules of the learning set) over the hypermolecule. The other topological, global descriptors were calculated by TOPOCLUJ software program. The clusters of similarity ensured the „congeneric state” of molecules on which the prediction of property/activity is made for the molecules in the test set, thus surpassing the models found in the learning set and also in the test set, by external validation.

ACKNOWLEDGMENT

The authors are indebted to Prof. Dr. Mircea V. Diudea for valuable discussions and help in preparing the manuscript.

REFERENCES

1. M.V. Diudea, "Fenotiazine și medicamente structural înrudite", PhD Thesis, Inst. Chem. Cluj, **1979**.
2. S.M. Free, Jr, J.W. Wilson, *J. Med. Chem.*, **1964**, 7, 395.
3. H. Kubinyi, "QSAR: Hansch analysis and related approaches", R. Mannhold, Krogsgaard-Larsen P., Timmerman H. (Eds.), VCH Publishers, New York, **1993**.
4. M.V. Diudea, (Ed.), *QSPR/QSAR "Studies by Molecular Descriptors"*, NOVA, New York, **2001**.
5. M.V. Diudea, *MATCH Commun. Math. Comput. Chem.*, **1997**, 35, 169.
6. M.V. Diudea, *J. Chem. Inf. Comput. Sci.*, **1997**, 37, 300.
7. O. Ursu, M.V. Diudea, TOPOCLUJ software program, Babes-Bolyai University, Cluj, 2005.
8. C.D. Moldovan, A. Costescu, G. Katona and M.V. Diudea, *MATCH Commun. Math. Comput. Chem.*, **2008**, 60, 977.
9. A.T. Balaban, A. Chiriac, I. Motoc, and Z. Simon, "Steric Fit in QSAR" (*Lectures Notes in Chemistry*, Vol. 15), Springer, Berlin, **1980**.
10. A.A.Toropov, A.P.Toropova, *Internet El. J. Molec. Design*, **2002**, 1, 108.
11. A.A.Toropov, A.P.Toropova, *J. Mol. Struct. (Theochem)*, **2001**, 538, 287.
12. P. Willett, J.M. Barnard, G.M. Downs, *J. Chem. Inf. Comput. Sci.*, **1998**, 38(6), 983.
13. Gaussian 09, Gaussian Inc Wallingford CT, Revision A.1 (2009) Frisch MJ, Trucks GW, Schlegel HB, Scuseria GE, Robb MA, Cheeseman JR, Scalmani G, Barone V, Mennucci B, Petersson GA, Nakatsuji H, Caricato M, Li X, Hratchian HP, Izmaylov AF, Bloino J, Zheng G, Sonnenberg JL, Hada M, Ehara M, Toyota K, Fukuda R, Hasegawa J, Ishida M, Nakajima T, Honda Y, Kitao O, Nakai H, Vreven T, Montgomery JA, Peralta JE, Ogliaro F, Bearpark M, Heyd JJ, Brothers E, Kudin KN, Staroverov VN, Kobayashi R, Normand J, Raghavachari K, Rendell A, Burant JC, Iyengar SS, Tomasi J, Cossi M, Rega N, Millam NJ, Klene M, Knox JE, Cross JB, Bakken V, Adamo C, Jaramillo J, Gomperts R, Stratmann RE, Yazyev O, Austin AJ, Cammi R, Pomelli C, Ochterski JW, Martin RL, Morokuma K, Zakrzewski VG, Voth GA, Salvador P, Dannenberg JJ, Dapprich S, Daniels AD, Farkas Ö, Foresman JB, Ortiz JV, Cioslowski J, Fox DJ.
14. L. Jäntschi, LOO Analysis (LOO: leave one out), Academic Direct Library of Software, **2005**, Available at:
<http://l.academicdirect.org/Chemistry/SARs/SARs/loo/>
15. J.G. Topliss, R.J. Costello, *J. Med. Chem.*, **1972**, 15, 1066.

==ERRATUM==

STUDIA UBB CHEMIA, Volume 60 (LX), 4, 2015 (p. 179)

In the article entitled “CORROSION RESISTANCE OF LASER CLADDED NiCrBSi COMPOSITE COATINGS”, Authors I. Hulka, V.A. Serban, D. Utu, N. Duteanu, A. Pascu, I.C. Roata, the image in figure 6 must be replaced by the corrected version as shown below.

**CORROSION RESISTANCE OF LASER CLADDED
NiCrBSi COMPOSITE COATINGS**

I. Hulka¹, V.A. Serban¹, D. Utu¹, N. Duteanu¹, A. Pascu², I.C. Roată²

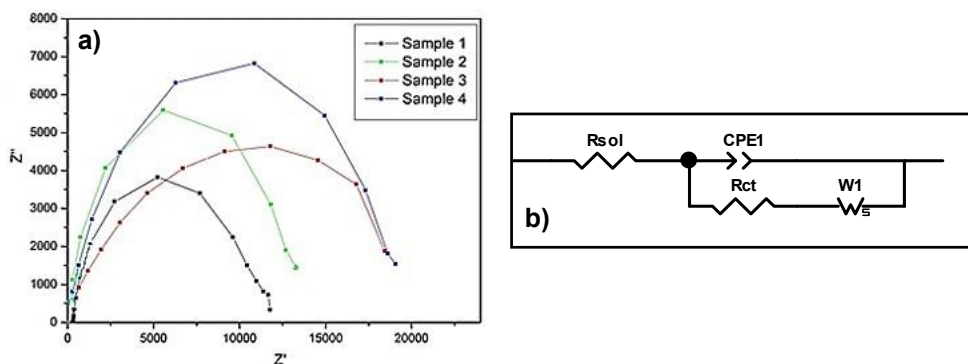


Fig. 6. Niquist plot (a) and equivalent circuit for spectra modeling (b)

STUDIA UBB CHEMIA, LXI, 1, 2016 (p. 319)
(RECOMMENDED CITATION)

==ERRATUM==

STUDIA UBB CHEMIA, Volume 60 (LX), 2, Tom I, 2015 (p. 161-167)

In the section References of the article entitled "*Groundwater chemistry rendering using Durov, Piper and ion balanced diagrams. Case study: the northern part of Sibiu county*", authors: Maria-Alexandra Hoaghia, Cecilia Roman, Claudiu Tanaselia, Dumitru Ristoiu, the reference 6 was corrected as follows:

6. M. Miclean, E. Levei, O. Cadar, M. Senila, I.S. Groza, *Carpathian Journal of Earth and Environmental Sciences*, **2013**, 8 (4), 93.